

NASA TECHNICAL MEMORANDUM



*N73-18866*

MSC-07219

NASA TM X-58106

NOVEMBER 1972

**CASE FILE  
COPY**

# 7th AEROSPACE MECHANISMS SYMPOSIUM

*Manned Spacecraft Center  
September 7 and 8, 1972*

NATIONAL AERONAUTICS AND SPACE ADMINISTRATION  
MANNED SPACECRAFT CENTER, HOUSTON, TEXAS 77058

**Page intentionally left blank**

1. Report No. <b>NASA TM X-58106</b>		2. Government Accession No.		3. Recipient's Catalog No.	
4. Title and Subtitle <b>7th AEROSPACE MECHANISMS SYMPOSIUM</b>				5. Report Date <b>November 1972</b>	
				6. Performing Organization Code	
7. Author(s) <b>William F. Rogers and Gordon Rysavy, MSC, Compilers; George G. Herzl, Lockheed Missiles and Space Co., Symposium Chairman/Editor</b>				8. Performing Organization Report No. <b>MSC-07219</b>	
				10. Work Unit No. <b>914-13-20-13-72</b>	
9. Performing Organization Name and Address <b>Manned Spacecraft Center Houston, Texas 77058</b>				11. Contract or Grant No.	
				13. Type of Report and Period Covered <b>Technical Memorandum</b>	
12. Sponsoring Agency Name and Address <b>National Aeronautics and Space Administration Washington, D.C. 20546</b>				14. Sponsoring Agency Code	
15. Supplementary Notes					
16. Abstract  <p>This document contains the papers presented at the 7th Aerospace Mechanisms Symposium, the purpose of which was to exchange information regarding the design, development, and operation of aerospace mechanisms. The more significant operational mechanisms problems and experiences from the Apollo Program and the unique mechanism subjects for future programs, such as the Apollo Soyuz Test Project, the space shuttle, and other related activities, are discussed. Problems and failures encountered with actual flight hardware are documented.</p>					
17. Key Words (Suggested by Author(s))  <ul style="list-style-type: none"> <li>· Aerospace Systems</li> <li>· Servomechanisms</li> <li>· Mechanisms</li> <li>· Devices</li> </ul>			18. Distribution Statement		
19. Security Classif. (of this report) <b>None</b>		20. Security Classif. (of this page) <b>None</b>		21. No. of Pages <b>328</b>	22. Price

**Page intentionally left blank**

**NASA TM X-58106**

**7th AEROSPACE MECHANISMS SYMPOSIUM**

**Sponsored By**

**NASA Manned Spacecraft Center  
California Institute of Technology  
Lockheed Missiles and Space Company, Inc.**

**Held At And Prepared By**

**NASA Manned Spacecraft Center  
Houston, Texas 77058  
September 7 and 8, 1972**

**Edited by George G. Herzl**

## NOTE

This document contains the papers presented at the 7th Aerospace Mechanisms Symposium, and it is intended only as a forum for the dissemination of the information contained therein. Responsibility for content and technical accuracy lies with each respective author. Prior to formal publication elsewhere, the data presented herein may not be used without the author's permission.

## FOREWORD

The 7th Aerospace Mechanisms Symposium, held at the NASA Manned Spacecraft Center, Houston, Texas, September 7 and 8, 1972, was sponsored jointly by the California Institute of Technology, Lockheed Missiles and Space Company, Inc., and the NASA Manned Spacecraft Center. For the past several years, the Aerospace Mechanisms Symposia have provided an excellent forum for the exchange of information regarding the design, development, and operation of aerospace mechanisms from the point of view of specialists.

The Manned Spacecraft Center was particularly pleased to host the 7th symposium because it provided a timely opportunity to specifically document and discuss some of the more significant operational mechanism problems and experiences from the Apollo Program and to consider a few of the more unique mechanism areas for forthcoming programs such as the Apollo-Soyuz Test Project, the space shuttle, and other related activity. This document is a compilation of the papers presented at the symposium and have been selected carefully by the paper-review panel for areas of current interest and applicability. These papers include problems and failures encountered with actual flight hardware.

In the relatively short span of both manned and unmanned space flight, it is clear that the role of mechanisms, which have to function and perform properly in the harsh environment of space and near space, is becoming an increasingly important and vital segment of spacecraft design. Therefore, it behooves us to make every effort to understand clearly and to disseminate available information in such problem areas. It is with this spirit and intent that this symposium has been sponsored.

Acknowledgment is made to the following individuals who were directly responsible for the organization and conduct of this symposium. The organizing committee and paper-review panel included Paul W. Bomke and John D. Ferrera, Jet Propulsion Laboratory; J. Lloyd Jones and Benjamin Beam, NASA Ames Research Center; George G. Herzl and Alfred L. Rinaldo, Lockheed Missiles and Space Company, Inc.; Frank T. Martin and Bowden W. Ward, Jr., NASA Goddard Space Flight Center; Ernest E. Sechler and David Welch, California Institute of Technology; and Aleck C. Bond and Caldwell Johnson, NASA Manned Spacecraft Center.

I particularly wish to acknowledge and thank Gordon Rysavy and William Rogers, NASA Manned Spacecraft Center; Anne Moiseff, Lockheed Missiles and Space Company, Inc.; and Elizabeth Fox, California Institute of Technology for their valuable assistance and efforts involved in the preparation and conduct of this symposium. Additionally, I wish to thank the authors and the numerous other individuals of the participating organizations who provided active support in the preparation of the symposium.

Aleck C. Bond  
Assistant Director for  
Chemical and Mechanical Systems  
Engineering and Development Directorate  
NASA Manned Spacecraft Center

## OPENING REMARKS

George G. Herzl  
Symposium Chairman

In the name of the symposium's organizing committee, I wish to welcome you to the 7th Aerospace Mechanisms Symposium. This symposium is sponsored by the California Institute of Technology, the National Aeronautics and Space Administration, and Lockheed Missiles and Space Company.

Theodore Von Kármán said in his autobiography "I suppose if one were to find an appropriate epitaph which attempted to summarize my life, a comprehensive one might be, 'He looked for the simple answers.' I believe the good Lord would appreciate the commentary." The same epitaph could well apply to any good mechanisms designer because simplicity is the very essence of aerospace mechanisms. It is in fact that which distinguishes mechanisms more than anything else from electronic counterparts which often contain hundreds of components to accomplish in a matter of milliseconds what a few levers, springs, and rods can do in seconds. The present economic realities in aerospace force the sponsors and users of the spacecraft to take a closer look to see whether milliseconds really count or whether it is more important to take advantage of the inherent advantage of mechanisms. The growing share of mechanisms in spacecraft is evident already, and I predict that mechanisms will "capture" an even greater share of the total aerospace effort.

We must maintain this momentum by demonstrating continually the superior performance of mechanisms in spacecraft. Also, we should continue to pool our experiences and exchange ideas; the Aerospace Mechanisms Symposia have proven to be a suitable forum for this purpose. At the same time, we should not hesitate to discuss less-than-perfect performance of mechanisms because that is the best way that I know to avoid similar difficulties in the future. I am pleased that we have at this symposium more papers on "anomalous behavior" of mechanisms than we had at any of the previous symposia.

Von Kármán described in several places in his autobiography the important work of Ernest Sechler of the California Institute of Technology. I am pleased to announce that Dr. Sechler and his colleague, David Welch, have joined our symposiums organizing committee and we welcome California Institute of Technology in cosponsoring the Aerospace Mechanisms Symposia. We intend to continue the sponsorship of a Government agency, university, and industry that we have found to be successful to date. We will hold our next meeting at the NASA Langley Research Center in September 1973. I would like to invite you to attend or, better yet, to present a paper, and share your experiences with us.

I wish to thank the authors for their efforts and I would like to encourage your aggressive and critical discussion of the papers presented. The interchange of ideas

at past Aerospace Mechanisms Symposia has played a role in improving the performance of our spacecraft and in preventing major problems and flight failures. I hope that this symposium will also provide a similar service to the United States aerospace effort.

## CONTENTS

Section	Page
FOREWORD . . . . .	vi
By Aleck C. Bond	
OPENING REMARKS . . . . .	vii
By George G. Herzl	

## SESSION I

### Session Cochairmen

C. C. Johnson NASA Manned Spacecraft Center	K. S. Bush NASA Langley Research Center
MECHANISM PROBLEMS . . . . .	3
By John K. Riedel	
THE APOLLO 15 DEPLOYABLE BOOM ANOMALY . . . . .	15
By Robert D. White	
DOCKING SYSTEM OF ANDROGYNOUS AND PERIPHERAL TYPE . . . . .	27
By V. S. Syromyatnikov	
A FOLDABLE 4.27-METER (14 FOOT) SPACECRAFT ANTENNA . . . . .	37
By Donald J. Starkey	
DYNAMIC ANALYSIS OF APOLLO-SALYUT/SOYUZ DOCKING . . . . .	47
By John A. Schliesing	
MECHANICAL COMPONENT SCREENING FOR SCANNER . . . . .	59
By J. L. Olson and W. J. Quinn	
RADIATIVE COOLER FOR SPACECRAFT . . . . .	69
By John E. McCullough	

## SESSION II

## Session Cochairmen

J. D. Schmuecker  
Jet Propulsion Laboratory

F. T. Martin  
NASA Goddard Space Flight Center

ZERO-GRAVITY TISSUE-CULTURE LABORATORY . . . . . 81

By James E. Cook, P. O'B. Montgomery, Jr., and Joseph S. Paul

FRANGIBLE GLASS CANISTERS . . . . . 91

By Richard Seifert

LUNAR ROVING VEHICLE DEPLOYMENT MECHANISM . . . . . 101

By Alex B. Hunter and Bryan W. Spacey

RADIOMETER-DEPLOYMENT SUBSYSTEM . . . . . 111

By Kevin M. Speight

APOLLO LUNAR MODULE LANDING GEAR . . . . . 123

By William F. Rogers

## SESSION III

## Session Cochairmen

D. Welch  
California Institute of Technology

O. Fedor  
NASA Kennedy Space Center

APOLLO 15 MAIN-PARACHUTE FAILURE . . . . . 137

By Donald D. Arabian and Joseph E. Mechelay

MECHANICALLY PRESTRESSED WINDOWS . . . . . 149

By William H. Keathley

APOLLO COUCH ENERGY ABSORBERS . . . . . 157

By Clarence J. Wesselski and Ralph E. Drexel

Section	Page
THE LUNAR CART . . . . .	169
By Glenn C. Miller	
LIQUID PUMP FOR ASTRONAUT COOLING . . . . .	181
By Maurice A. Carson	
THE APOLLO 14 DOCKING ANOMALY . . . . .	191
By Robert D. Langley	
DYNAMIC TESTING OF DOCKING SYSTEM HARDWARE . . . . .	203
By Wade D. Dorland	

**SESSION IV**

Session Cochairmen

<p><b>B. Beam</b> NASA Ames Research Center</p>	<p><b>H. T. Haynie</b> The Boeing Company</p>
PLY-TEAR WEBBING ENERGY ABSORBER . . . . .	215
By Geoffrey W. H. Stevens	
FLEXIBLE SOLAR-ARRAY MECHANISM . . . . .	233
By Merlyn C. Olson	
SCANNING MIRROR FOR INFRARED SENSORS . . . . .	251
By Richard H. Anderson and Sidney B. Bernstein	
MANIPULATOR TECHNOLOGY FOR THE SPACE SHUTTLE . . . . .	267
By E. Glenn Burroughs	
A FLYING EJECTION SEAT . . . . .	275
By R. H. Hollrock and J. J. Barzda	
A 928-M <sup>2</sup> (10 000 FT <sup>2</sup> ) SOLAR ARRAY . . . . .	287
By Dale E. Lindberg	
ATTENDEES . . . . .	305

**SESSION I**

**Page intentionally left blank**

## MECHANISM PROBLEMS

By John K. Riedel\*

### ABSTRACT

Too frequently during the design and development of mechanisms, problems occur that could have been avoided if the right question had been asked before, rather than after, the fact. Several typical problems, drawn from actual experience, are discussed and analyzed. The lessons learned are used to generate various suggestions for minimizing mistakes in mechanism design. These suggestions are intended to precipitate the right question at the right time; that is, before, rather than after, a test or flight failure.

### INTRODUCTION

From a viewpoint of direct involvement in the design and development of various aerospace mechanisms in the past few years, it is disconcerting to realize how often failures or malfunctions occur. When viewed with hindsight, these problems cause one to wonder, "how could we have overlooked that?" This question is not concerned so much with anomalies revealed during early development testing; these anomalies are to be expected and are even needed during the design evolution. Rather, it is the failures that occur downstream during qualification or flight testing that are of greatest concern. These are the failures that cause embarrassment and consternation and which will be the subject of this report. Several examples will be cited, not only to illustrate typical errors but, more important, the lessons learned, followed by suggestions intended to improve future performance regarding mechanisms design. In presenting these examples, the role of design (as opposed to test and analysis) will be emphasized because this is where the responsibility usually rests and the blame falls.

### TYPICAL PROBLEMS

#### Diaphragm Problem

Two problems that were encountered in the development of the radar augmentation device (RAD) (ref. 1) will be used as examples. In essence, the RAD is a self-inflating

---

\*Lockheed Missiles and Space Company, Inc., Sunnyvale, Calif.

sphere that is used as a large reflector to facilitate early acquisition by the ground-based radars. It is inflated with Freon that is released from a reservoir when a spring-loaded piercer punctures a metal diaphragm at the outlet of the reservoir. It was recognized that temperature would affect the vapor pressure of the Freon and, thus, the rate of inflation of the sphere. Experience had indicated that, if the rate of inflation was too fast, the sphere or balloon, would burst. Therefore, one test was conducted at elevated temperature to verify sphere-inflation performance at the upper temperature limit. Instead of getting rapid inflation, just the opposite was obtained. By investigation, it was subsequently established that the increased vapor pressure was sufficient to overcome the force of the spring used to drive the piercer. As soon as the piercer punctured the diaphragm the increased vapor pressure acted on it to force it back before full penetration of the diaphragm was achieved. This problem is illustrated in figure 1. Subsequent redesign, shown in figure 2, incorporated a hollow piercer; thus, the vapor pressure could not act on it to force it back.

### Orientation-Sensitivity Problem

On another occasion in the RAD program, a design flaw was discovered by "coming through the back door." In a test designed to evaluate improvement in packaging the sphere, the unit was mounted horizontally to eliminate the influence of gravity on sphere deployment. Deployment was satisfactory but, unaccountably, the rate of inflation was significantly slower than in all previous tests wherein the unit had been inclined downward. Subsequent investigation established that the design was sensitive to orientation. When the sphere was in the downward orientation, Freon entered the sphere as a liquid, whereas when the sphere was in the horizontal position, Freon entered the sphere as a vapor or gas. Thus, a much slower rate of inflation occurred when the sphere was in the downward orientation. This problem and its solution are illustrated in figure 3.

### Moisture-Absorption Problem

In another design application, it was necessary to extend two panels radially outward a short distance (approximately 7.62 centimeters (3 inches)) from the missile during boost flight. The mechanism worked in limited ground-based tests under simulated flight loads (accelerations) but malfunctioned in flight. Subsequent investigation and ground-based testing revealed a marginal design: the actuating spring was just barely strong enough (really, not quite strong enough) to overcome accumulated friction forces when under maximum g loadings. In the initial design, clearances were made generous, and the spring was thought to be stronger than necessary; thus, the friction problem was not addressed adequately. There was another contributing factor. The actuating rod was supported or guided by two nylon sleeve bushings. After the flight anomaly, the materials experts suggested that these bushings swelled under long (several months) exposure to a humid atmosphere and increased the friction. An "over-test" on the ground may have exposed the marginal nature of the design, but the test was not conducted until after the fact. Subsequently, design improvements were made to minimize friction.

To confirm the postulate that the hydrophilic property of nylon could have adversely affected the operation of the actuator, an accelerated moisture-absorption test was conducted by submerging the assembled actuator in a tank of hot water (333.15° K) for approximately 3 weeks. After soaking, the actuator would not function because the nylon bushings swelled to the extent that they squeezed the actuator shaft. Accordingly, Rulon C (a filled tetrafluoroethylene) was used in the bushings. Rulon C is unaffected by moisture and, in addition, has a lower coefficient of friction than does nylon. Quantitative measurements were made in a second accelerated moisture-absorption test in which bushings made both of nylon and Rulon C were soaked in hot water. Test results, shown in figure 4, are indicative that the wall thickness of the nylon bushings increased 2.5 percent, whereas the Rulon C bushings were virtually unaffected (actually shrank slightly). The original and new design configurations of the actuator are shown in figure 4.

### Series Of Problems With Module Launcher

In this example it was required that a module be mounted in a launcher in an off-center position inside a spinning body and, upon signal, be ejected from the launch tube by means of a spring that provided both linear and rotational motion to the module. After a short delay (approximately 3 seconds), the module functioned. The rotational motion produced spin stability to provide a favored orientation for the module. This subsystem of module and launcher was tested during the development program, but in the first test, the module was not ejected properly. Subsequent investigations revealed a sequence of errors.

The launcher was simply a tube that had generous clearance so that friction was not considered to be a problem. Two factors were overlooked here: the module did not come out smoothly, but tended to chatter in its travel out of the tube; and the module had a safe-arm device which, it should be noted, was always in the "safe" position during development testing of the ejection mechanism. The safe-arm device used three spring-loaded steel balls that were ejected radially to actuate the module when it was free of the launch tube. In the "safe" position, the balls were constrained physically from moving by the safe-arm device but, when in the "armed" position, the balls bore against the side of the launch tube. Both of the factors just mentioned introduced friction; this fact probably accounted for the flight failure. Subsequently, improvements were made to reduce friction. These improvements included a redesign of the safe-arm device so that the balls were ejected by centrifugal force caused by the module spin rather than by a separate spring; thus, friction on the inside of the launch tube was largely eliminated.

During this development, ejection tests were conducted vertically downward to eliminate the effects of gravity on the tumbling motion of the module. In flight tests, the module was ejected in a gravity-free environment. This environment (that is, lack of gravity), incidentally, invariably complicates ground-based testing and often leads to errors. In arriving at the true separation velocity, the effect of the force of gravity was subtracted, which, in some cases yielded a negative separation velocity, clearly an impossibility. This proved to be a testing error: the ejection spring was found to be time dependent (as is any spring); thus, the module actually was falling away from the spring.

At first, the rate of tumble was thought to be negligible because it appeared to be so small in the short time it was observed in the test movies. More careful data reduction, however, indicated that the module would be pointing almost backwards when it functioned, showing that the tipoff moment was unacceptably large and the spin stabilization was inadequate. Two design changes, supported by additional analysis, corrected these deficiencies: a "zero-length" launcher was designed (the last point of contact of the module with the lip of the launcher was at the center of gravity of the module) and a "flywheel" was added at the longitudinal center of gravity of the module to increase its rotational moment of inertia.

In making these changes, the diameter of the launch tube was enlarged; thus, the tube no longer restrained the safing balls in the module so that they were free to fall or be jarred out by logistic and boost environments before the signal to eject the module. Unfortunately, this rather obvious mode of failure was not realized until after the flight test when module function was not obtained. As mentioned earlier, a given magnitude of spin was required to eject the safing balls. During the failure analysis, it was realized that transverse shocks and vibration experienced prior to module release could produce sufficient force to free the balls and cause the captive module to function. A fall-away collar was added to correct this problem. In final evaluation tests, in which the module with this collar was ejected in the atmosphere, the module still underwent an unacceptable rate of tumble. Even though the analysis indicated the aerodynamic loads were negligible, subsequent tests were transferred to the vacuum chamber, wherein successful ejection was obtained. In subsequent flight tests, the device worked successfully. The original and final design configurations are shown in figure 5.

#### SUGGESTIONS FOR MINIMIZING MISTAKES IN MECHANISM DESIGN

As is obvious from the foregoing discussion, the design and development of a mechanism is not generally a one man or even a one department undertaking, but involves three main activities: design, analysis, and testing. However, the predominant or leading role inherently falls to the design group. If the mechanism does not perform properly, the blame, either in full or in part, ultimately falls on the design; even if circumstances permit or are created to spread and obscure this blame, it is of little consequence because, in the majority of the cases, it is up to the design group to resolve the problem.

If it turns out that the analysis or testing efforts have not adequately supported the design, the blame must be shared by the design group for not making the proper requests or for not challenging or properly monitoring these support efforts. Even in matters defined as problems in quality control and manufacturing, design generally becomes involved. What then can the design group do to minimize the type of mistakes described?

The problems just described occurred in spite of the fact that each design was formally reviewed periodically by a design-review committee. Generally, conceptual, interim, and final design reviews were held. These reviews uncovered some, but obviously not all, the weaknesses in the design. It is felt that, in addition to these periodic reviews, a means to provide a disciplined, continuous monitoring of the design is

needed. It is proposed that this be done through a small control group within the design group; for lack of a better name, this group can be called the Design Parameters Group (DPG) and would be responsible to the design leader or supervisor. This group should be activated at the outset of any new design effort and one of its main functions would be to ask the right questions in a disciplined rather than haphazard way. To accomplish this, it is suggested that the DPG should establish the following documents or checklist for each design subsystem and should administer the checklists on a continuing basis. These documents are the tools designed to precipitate pertinent questions before the fact, so that potential problem areas can be revealed before the mechanism fails to perform in qualification testing or end-item usage. The functions of the DPG are shown in figure 6.

### Design Parameters and Requirements Checklist

This checklist is a comprehensive list of the design requirements derived from systems and performance requirements. Many of these design parameters could be derived only with appropriate analysis, which would be done under the cognizance of the DPG. This list should be kept current as the design evolves and requirements change, and the list should be used as a checklist to ensure that the design meets each requirement. Then, a completed checklist should be manifested at each formal design review. An example of this checklist applied to the RAD is shown in figure 7.

### Design-Limits Checklist

As is illustrated in the preceding examples, failures often occur because no effort was made to determine how marginal the design was. The design limits checklist would contain a definition and a list of the design limits; thus, design margins would be shown. Of course, this procedure is almost always done in stress analysis but not in functional aspects of the mechanism. In many cases, analyses and testing would be required in order to complete this list; thus, the list would be used to point out where additional analysis and testing should be done. A simplified example of a partial design limits checklist is shown in figure 8.

### Test-Requirements Checklist

Test requirements should be generated by the design group and, indirectly, by the analysis group when test data are needed to supplement analysis. In conjunction with the administration of the design requirements, the DPG should prepare test requirements that would form the basis for test plans and requests. Then, the test results should be evaluated against the design requirements by the DPG. How such a checklist would be formulated is illustrated in figure 9.

### Failure-Mode-Analysis Checklist

As soon as the design is defined sufficiently, the failure-mode analysis should be made by the DPG in conjunction with quality-control personnel. The failure mode analysis checklist consists essentially of a systematic listing of all postulated modes

of failure that could occur and a statement of what has or will be done to prevent failures or to ensure that failures cannot occur. This checklist should be kept current, updated with each design change, and submitted to the design-review committee. How this checklist could be applied to the RAD is shown in figure 10.

### Why Won't It Work List

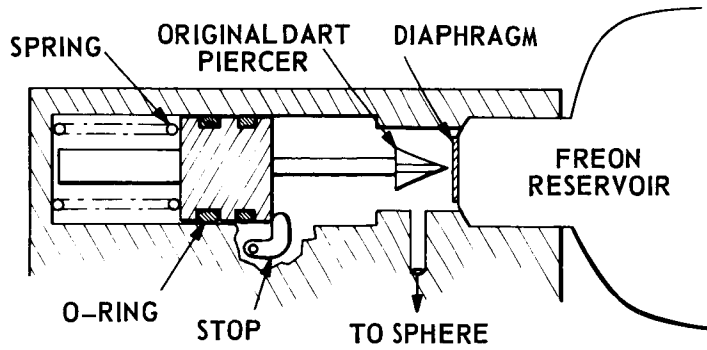
The critiquing engineer should list questions for each mechanism, asking what can or will keep the mechanism from working as intended; then, the critiquing engineer should obtain or provide the answers. Although this list will overlap the failure mode analysis checklist, it will supplement it by asking questions from a different viewpoint.

### CONCLUDING REMARKS

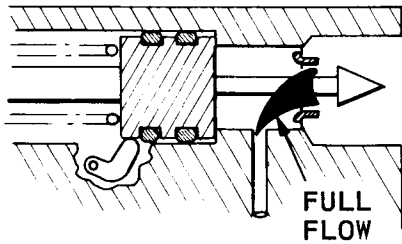
As was stated earlier, these checklists are intended to serve as tools to precipitate the questions that would uncover potential problems before the fact. To gain maximum benefit from the checklists, a proper or healthy attitude must be generated and maintained. Part of the task of the mechanism designer is to dispell the notion that "anybody can build a mechanism." The designer must convince critics (and helpers) that mechanisms are not so simple and trivial that development testing is not necessary. However, the designer has to develop a receptive attitude and guard against nurturing a defensive attitude. The designer should not be reticent in seeking expert help in specialized areas such as friction and lubrication problems and materials selection. Even in areas of his specialty, an independent review by other designers should not be discouraged.

### REFERENCE

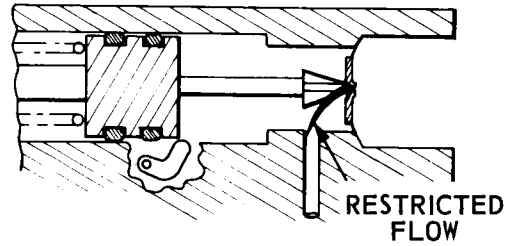
1. Riedel, J. K.: Radar Augmentation Device. Paper presented at the 6th Aerospace Mechanisms Symposium (Moffett Field, Calif.). NASA TM X-2557, 1972.



(a) Original valve assembly.

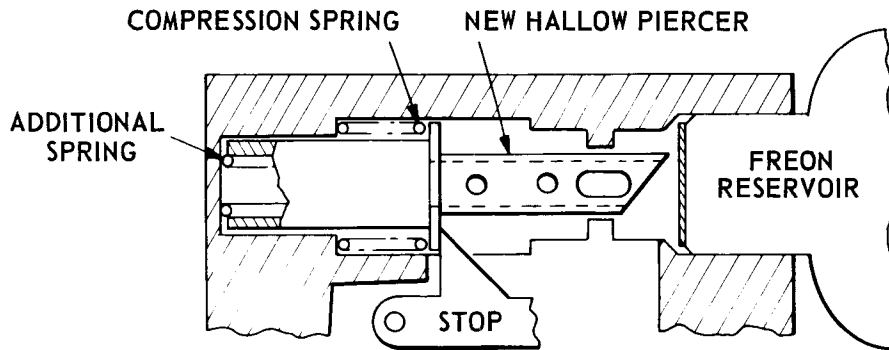


(b) Normal operation.

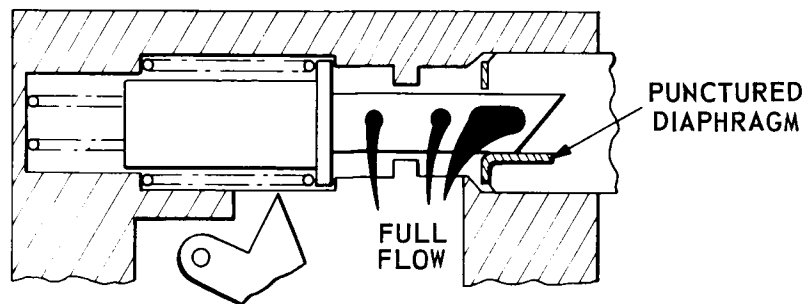


(c) Operation at elevated temperature.

Figure 1. - Illustration of the piercer problem.



(a) Cocked position.



(b) Fired position.

Figure 2. - Redesigned valve assembly.

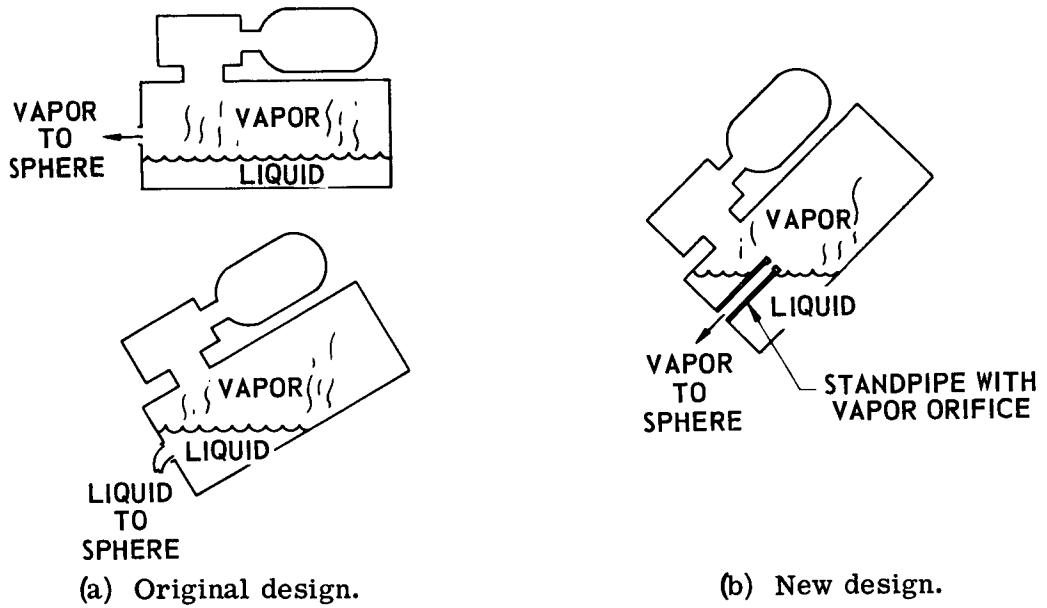


Figure 3. - Orientation problem.

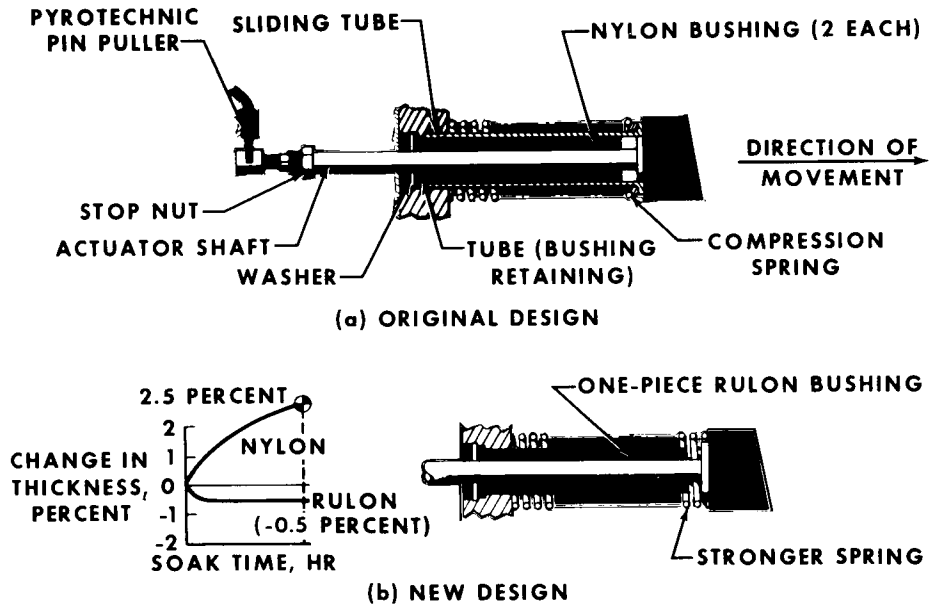


Figure 4. - Moisture-absorption problem.

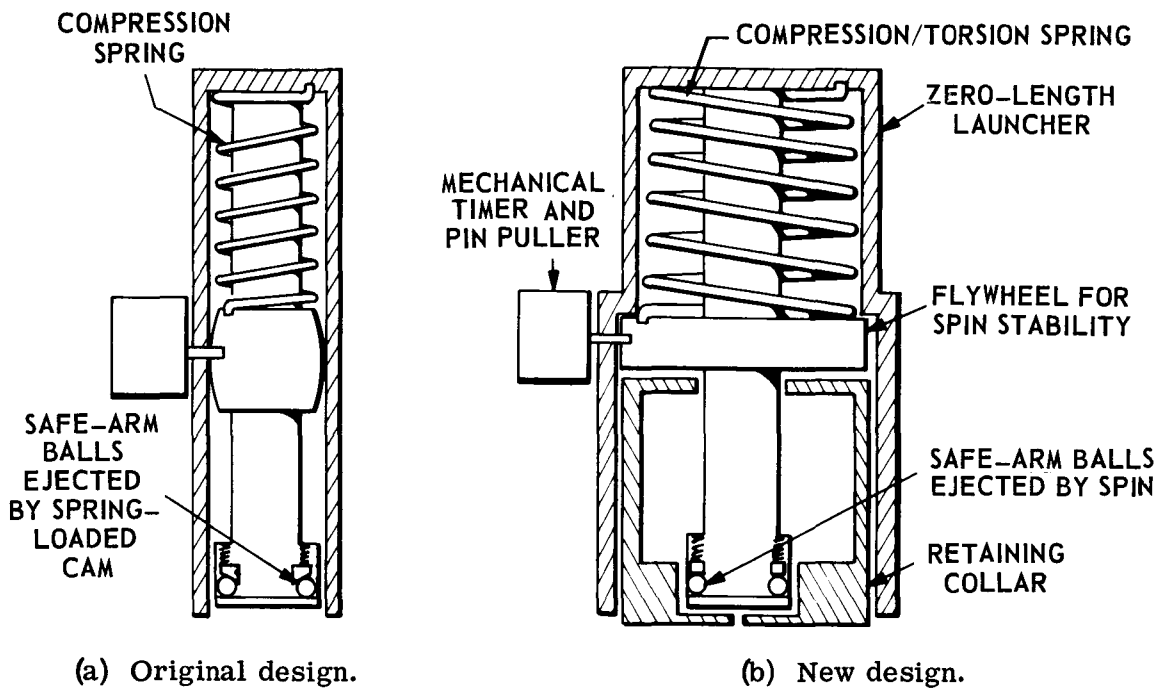


Figure 5. - Module-launcher problem.

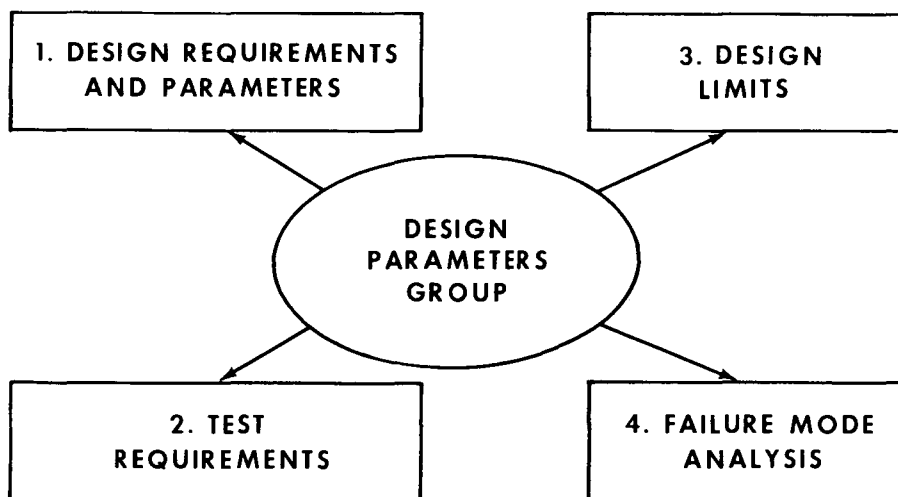


Figure 6. - Functions of the design parameters group.

SYSTEM REQUIREMENTS	DESIGN REQUIREMENTS	DESIGN SOLUTION
ALINEMENT (REACTION CONTROL SYSTEM) <ul style="list-style-type: none"> <li>● PASSIVE DEVICE</li> <li>● DEPLOY FROM RIGHT-HAND EQUIPMENT BAY</li> <li>● 1m<sup>2</sup> MINIMUM</li> </ul>	LARGE REFLECTOR SELF-ERECTING STEADY (REACTION CONTROL SYSTEM)	 <ul style="list-style-type: none"> <li>● 8-FT SPHERE</li> <li>● ALUMINUM</li> <li>● SMOOTH SURFACE</li> </ul>
TETHER TO RIGHT-HAND EQUIPMENT BAY	RAPID INFLATION ORDERLY UNFURLING	2-SEC FULL INFLATION ACCORDIAN AND PLEAT FOLDS
DISAPPEAR DURING ENTRY	CONSUME BY ENVIRONMENTS	NO METAL STRUCTURE MYLAR SKIN

Figure 7. - Design-requirements checklist.

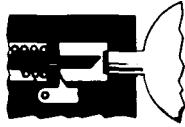
PARAMETER	LIMIT
RATE OF INFLATION SPIN 	DETERMINE BY TESTING <ul style="list-style-type: none"> <li>● MINIMUM RATE, TWIST AND TANGLE</li> <li>● MAXIMUM RATE, TEAR OR BURST</li> </ul> VARY SIZE OF ORIFICE
PIERCER PENETRATION 	DETERMINE MAXIMUM PIERCING CAPABILITY <ul style="list-style-type: none"> <li>● TEST PROGRESSIVELY</li> </ul> THICKER DIAPHRAGMS TEST TO FAILURE OR MAXIMUM

Figure 8. - Design-limits checklist.

<p><b>COMPONENT</b></p> <p><b>PIERCER MECHANISM</b></p> 	<p><b>TEST REQUIREMENT</b></p> <p><b>TEST SPRINGS</b></p> <p><b>BENCH TEST PIERCER PENETRATION</b></p> <p><b>FUNCTIONALLY TEST IN SYSTEM TEST</b></p>
<p><b>TETHER EXTENSION</b></p> 	<p><b>TEST VOLUTE SPRINGS</b></p> <p><b>FUNCTIONALLY TEST IN EXTENSION VACUUM WITH FREON</b></p>
<p><b>SPHERE INFLATION</b></p> 	<p><b>LEAK TEST, AND SO FORTH</b></p>

Figure 9. - Test-requirements checklist.

COMPONENT	ASSUMED FAILURE MODE	CAUSE	DESIGN ACTION
<p><b>PYROTIMER</b></p> 	<p><b>DOES NOT CUT PIN</b></p>	<ul style="list-style-type: none"> <li>● PYRO ELEMENT FAILS</li> <li>● PIN IS TOO HARD</li> </ul>	<p><b>PREVIOUSLY QUALIFIED</b></p> <ul style="list-style-type: none"> <li>● OVERTEST</li> <li>● INSPECTION</li> </ul>
<p><b>TETHER</b></p> 	<p><b>NO EXTENSION</b></p> <p><b>PARTIAL EXTENSION</b></p>	<p><b>LINKAGE DOES NOT RELEASE LID</b></p> <ul style="list-style-type: none"> <li>● HIGH FRICTION</li> <li>● INSUFFICIENT CLEARANCE</li> </ul>	<ul style="list-style-type: none"> <li>● TOLERANCE STUDY</li> <li>● VERIFY IN TEST LUBRICATE</li> <li>● TOLERANCE STUDY</li> <li>● INSPECTION POINT</li> </ul>
<p><b>PIERCER</b></p> 	<p><b>DOES NOT PUNCTURE DIAPHRAGM</b></p>	<ul style="list-style-type: none"> <li>● NO RELEASE</li> <li>● WEAK SPRING</li> <li>● AND SO FORTH</li> </ul>	<p><b>VERIFY IN TEST</b></p> <p><b>100 PERCENT TEST</b></p>

Figure 10. - Failure-mode-analysis checklist.

**Page intentionally left blank**

## THE APOLLO 15 DEPLOYABLE BOOM ANOMALY

By Robert D. White\*

### ABSTRACT

During the Apollo 15 mission, a boom with an attached mass spectrometer was required to retract periodically so that the instrument would not be in the field of view of other experiments. The boom did not fully retract on five of 12 occasions. Data analysis indicated that the boom probably retracted to within approximately 2.54 centimeters (1 inch) of full retraction. The pertinent boom-design details, the events in the mission related to the anomaly, a discussion of the inflight and postflight investigation of the problem, a discussion of the design changes to the boom mechanism as a result of the investigation, and subsequent flight performance are presented in this report.

### INTRODUCTION

While the Apollo 15 commander and lunar module pilot were on the lunar surface, the command module pilot completed 34 lunar orbits, operating scientific instrument module (SIM) experiments to obtain data concerning the lunar surface and the lunar environment. One of these experiments involved the use of a mass spectrometer that was deployed from and retracted into the SIM bay by means of a deployable boom mechanism. A boom was necessary because the experiment was used to detect released gases from the lunar surface and, therefore, had to be placed away from the immediate vicinity of the command/service module to minimize any contamination of the instrument by offgassing products of the vehicle. The boom was required to retract periodically so that the mass spectrometer would not be in the field of view of other experiments and also to allow firing of the service propulsion system engine. However, during the Apollo 15 flight, the boom did not fully retract on five of 12 occasions. The problem that occurred in flight, the postflight investigations, and the subsequent design changes and results are discussed in this report.

### DEPLOYMENT MECHANISM

Two experiments, a gamma-ray spectrometer and a mass spectrometer, were mounted on similar extendable/retractable boom mechanisms in the SIM bay of the Apollo service module (fig. 1). When deployed, the mass-spectrometer boom extended 762 centimeters (25 feet) and the gamma-ray boom extended 817.8 centimeters

---

\*NASA Manned Spacecraft Center, Houston, Tex.

(26 feet 10 inches). The mass-spectrometer unit that was attached to the end of the boom weighed approximately 11 kilograms (25 pounds). The deployment mechanism (including the jettison mechanism) had dimensions of 33 by 43 by 84 centimeters (13 by 17 by 33 inches) and weighed 41 kilograms (90 pounds).

The boom is formed of two tempered-steel tapes that are 14.2 centimeters (5.6 inches) wide and 0.03 centimeter (0.012 inch) thick. Before deployment, the tapes are stored flat on two motor-driven reels. As the tape is unreeled during deployment, it assumes its natural C-shaped cross section and joins the other tape to form a circular cross section boom 5.08 centimeters (2 inches) in diameter (fig. 2). The deployment cycle is terminated by allowing a roller follower on the extend limit switch (fig. 2) to drop through a slot cut in one of the steel tapes, opening the circuit to the extend winding of the reel-drive motors and a talkback indicator that is monitored by the command module pilot. The retraction cycle is terminated when the experiment mounting flange engages the retract limit-switch actuation rod and opens the circuit to the retract winding of the reel-drive motors and to the talkback indicator.

Cycling time of the mass-spectrometer boom assembly is a function of several factors (for example, temperature and available bus voltage). At a nominal 28 V dc, the boom assembly would take approximately 140 seconds for extension and 173 seconds for retraction. Boom-position-monitoring capability is provided by means of talkbacks. However, these boom-status monitors indicate full deployment, full retraction, boom in transit, and boom jettison only; intermediate boom positioning necessitates timing by the crewman.

The experiment is connected electrically to the SIM bay by means of a cable that is coiled around the boom at deployment (fig. 3) and that is stored within the boom-actuating mechanism housing (fig. 2) when the boom is retracted. The experiment power cable is a bundle of 20 electrical conductors and one coil spring wire having a total cross section of 1.3 centimeters (0.5 inch). The coil spring is included to control the location of the power cable and the diametrical size of the coils during extension and retraction. The pitch of the coiled cable reverses direction at the midpoint in the cable length so that there is no torsional effect from the spring on the experiment during extension and retraction or while extended and operating. The length of the power cable is approximately 1920 centimeters (63 feet), but, in the relaxed coiled configuration, the length is approximately 260 centimeters (8.5 feet). A force of approximately 4.5 kilograms (10 pounds) is required in order to compress or extend the coils from the relaxed position; however, the drive motors will not stall until an excess of 200 kilograms (440 pounds) is applied to the boom.

To guide the power cable into its storage volume during retraction, the mechanism housing is flared at the end and the experiment mounting flange has six fingers attached that act like scoops during retraction (figs. 2 and 3). The flare on the housing has cutouts so that the fingers can push the cable bundle past the housing lip.

Because the retracted experiment and its boom mechanism must be supported in the SIM bay for launch forces, the experiment and the boom are mounted on two rails that are supported by trusses from the bottom side of a SIM-bay shelf (fig. 4). These guide rails also allow the experiment to extend and then retract for support during space-flight acceleration forces with the service propulsion system engine. Linear bearings attached to the experiment pick up the tapered ends of the guide rails during retraction.

Because of the limited mechanical strength of the boom, it must be retracted before any service propulsion system engine firings to avert buckling of the boom, which could damage the service module. If the boom cannot be retracted because of a malfunction, the boom-actuating mechanism, the boom, and the experiment could be jettisoned. The spring-powered jettison mechanism is shown in figure 4. On proper circuit closure, the fusible wire actuator would release the restraining link, and the boom-actuating mechanism, the boom, and the experiment all could be jettisoned at a rate of approximately 213 cm/sec (7 ft/sec).

The mass-spectrometer installation in the SIM includes a thermal and contamination cover (figs. 4 and 5) that closes over the outboard face of the experiment. This protective cover opens with the initial motion of the boom mechanism during extension and closes with the final motion during retraction. The cover prevents heating and contaminant damage to the experiment that would result from reaction control system (RCS) jet firings and effluent dumps.

### FLIGHT ANOMALY

During the Apollo 15 flight, the mass-spectrometer boom mechanism was required to retract 12 times. On five of these occasions, the boom did not retract fully. Normally, the deploy/retract talkback indicator is gray when the boom motors are off and the boom is retracted or extended fully. The indicator is "barberpole" when the boom is either extending or retracting. However, because the indicator is wired in series with the drive motors, a half barberpole will usually show if the drive motors stall. When the motors stall, the current increases and causes a voltage drop. The voltage drop then causes the indicator to activate only partially to the barberpole position. The command module pilot noted this half-barberpole condition that indicated stalled motors and, therefore, incomplete retractions.

Telemetry data from the spacecraft electrical buses plotted with a time base indicated that the current driving the retract motors was normal on the five stall occasions until the boom was within 2 to 5 centimeters (0.79 to 1.97 inches) of full retract. At that point, the current increased from a nominal 3 to 4 amperes to the typical stall level of approximately 9 amperes.

A space cold soaking of the fully deployed boom and power cable preceded each anomalous retraction. In every case, after a warmup period in the sun, the boom could be retracted fully after first again extending it approximately a meter. Also, a special inflight test to investigate the boom anomaly was accomplished during the spacecraft coast back to earth. This test supported the theory that the malfunction was related to thermal conditions; that is, after a cold soak, the boom did not retract completely, but, after a subsequent hot soak, retraction was completed.

An inflight photograph of the extended boom (fig. 6) revealed that the power-cable coils remained circular but were not concentric to the boom and appeared to touch the boom on most of its length. The assumption had been made that in zero-g this sagging would not occur significantly because of the coiled spring in the power cable.

The extravehicular activity by the command module pilot to the SIM bay to retrieve film cassettes confirmed the assumption that the boom was within approximately 3 to 4 centimeters (1.18 to 1.57 inches) of full retraction. The boom had stalled before the extravehicular activity and was left in the stalled position for visual inspection by the command module pilot. He reported that the mass-spectrometer thermal cover was approximately 30 to 40 degrees open and that he could see only the tapered tip of the guide rail protruding from the experiment support bearing, as simulated in figure 5. This corresponds to a boom position of approximately 3.5 centimeters (1.38 inches) from full retract, as shown by the data in figure 7.

Although retraction problems occurred, the boom was always manipulated (sun exposure and short recycles) so that the experiment did not have to be jettisoned to allow SPS engine firings. Valuable mass-spectrometer data would have been lost if the stalled boom had been jettisoned. However, only a small percentage of the experiment data-gathering time was lost. The similar boom-deployment mechanism for the gamma-ray spectrometer worked normally throughout the Apollo 15 mission.

### PROBLEM INVESTIGATION

No postflight hardware analysis or testing could be conducted with the Apollo 15 boom mechanism because the service module that contained the SIM bay was jettisoned before earth entry. However, because gamma-ray-spectrometer and mass-spectrometer boom mechanisms were to be used on the Apollo 16 mission, an extensive anomaly investigation was conducted in an attempt to correct the problem. The investigation was based on the following list of most probable causes of the anomaly.

1. Cable bunching and jamming at the mechanism housing annulus opening
2. Cable sagging and bunching between flared housing and fingers or experiment bearing
3. Cable service-loop snagging on housing or support structure
4. Interference between guide rails and spectrometer bearing
5. Low-temperature stiffness of the power cable
6. Marginal adjustment or malfunction of the retract limit switch or the actuator rod to the switch
7. Interference between experiment and cover

The investigation started with the following analysis and testing.

1. A documentation review of all pertinent drawings, specifications, analyses, and discrepancy records was conducted to identify any irregularity that may have caused the retract anomaly.

2. A visual inspection of the Apollo 16 mass spectrometer and gamma-ray spectrometer was accomplished at the launch pad while the instruments were installed in the flight configuration. The inspection included a short extension and retraction of each assembly.

3. After return of the Apollo 16 mass-spectrometer boom assembly to the contractor, additional visual inspection and dimension verification were accomplished. In addition, short extensions and retractions were performed at room-ambient conditions under various orientations with respect to gravity to simulate worst-case cable-sagging conditions.

The major problem discovered was that of sagging in the power cable. On a few occasions, the sagging would allow the cable to bunch up and jam or snag between the flared housing and a guide finger or between the flared housing and an experiment support bearing. An abnormality of this kind is shown in figure 8.

This same cable-sagging problem had been observed during the original flight-qualification testing of the deployment mechanism, but most of the sag was attributed to the one-g environment, and the assumption was made that the sag would be confined within the flared housing and the guide fingers during zero-g conditions. Therefore, for the majority of the qualification tests, the cable was counterbalanced when the boom was cycled.

Also, in power-cable developmental tests that were conducted before the qualification testing, no stiffness change was detected in the cable coils when the coils were exercised at room temperature and at 188.15° K (-85° C). This fact was verified during the anomaly investigation.

## INVESTIGATION CONCLUSIONS AND CORRECTIVE ACTIONS

After all plausible causes for the Apollo 15 flight anomaly were examined, and based on the analyses and testing discussed in this report, the conclusion was reached that the problem occurred because of one of the following reasons.

1. Improper stacking of the power-cable coils into the annulus of the mechanism housing during retraction
2. Jamming of the power cable either between the experiment support bearing and the mechanism housing or between the guide fingers and the housing

The first possible cause cited could not be corrected in time to support the Apollo Program schedule. The housing annulus opening would have had to be redesigned and, possibly, the cable-coil diameter would have had to be decreased. These changes could not have been accomplished and requalified for flight in time for the Apollo 16

launch. However, for the second possible cause, several simple changes could be made to the existing design and could be tested within the schedule. The following changes were implemented.

1. Tab extensions were added to the flare on the mechanism housing (fig. 9).
2. A second cable clamp was added to retain the cable service loop better at the experiment interface (fig. 9).
3. The inboard experiment-support bearings were modified by adding a ramp to serve as a fairing during cable retraction (fig. 10).
4. The guide fingers on the experiment-mounting flange were extended where possible to improve gathering of a sagging cable (fig. 9). A similar change was made to the Apollo 16 gamma-ray-spectrometer deployment mechanism.

After these modifications were added, the Apollo 16 mass-spectrometer mechanism (with a prototype spectrometer) was tested at room-ambient and low-temperature conditions and at the low-temperature gradients in a vacuum simulating the worst-case low-temperature-gradient environment of lunar orbit. No test anomalies were experienced, and the mechanism performance was nominal.

The mass spectrometer deployment mechanism assembly was completely recycled through standard acceptance-test procedures before return to the launch pad. However, in the event the changes did not solve the problem for the next flight (such as improper stacking of the retracting cable), a proximity switch was also added to each of the spectrometer experiment mechanisms (fig. 10). This switch would indicate when the boom was within 30 centimeters (11.81 inches) of full retract even if the motors did stall. The boom is safe for an SPS engine firing within this 30 centimeters (11.81 inches), and this knowledge could prevent either experiment from being jettisoned if the boom did stall.

## CONCLUDING REMARKS

The Apollo 15 mass-spectrometer-deployment mechanism could not be returned for an evaluation to determine the cause of the flight anomaly. A postflight investigation revealed two probable causes; however, the flight schedule for Apollo 16 prevented any extensive redesign of the mechanisms. Only simple modifications could be added to the mechanisms in an attempt to avert the problem from occurring again and also to add a proximity switch to indicate when the boom was in a safe position for service propulsion system engine firing. These modifications were thought to be sufficient because Apollo 16 was the last spacecraft to use these spectrometer mechanisms.

The Apollo 16 mission proved that the changes were not adequate because both mass-spectrometer and gamma-ray boom mechanisms would not always retract fully when commanded. However, the proximity switches on both experiments always indicated they were retracted within 30 centimeters (11.81 inches), saving the experiments from being jettisoned while gathering data in lunar orbit. It is the opinion of this author that the basic problem was improper stacking of the cable into the mechanism

housing annulus during retraction; this should be recognized as a significant design problem. If similar concepts of long retractable booms that have an external cable are needed in future space efforts, an ample stowage area should be provided for the cable.

## DISCUSSION

D. D. Laine:

Are internal electrical cables being considered by the MSC for future booms of this basic cross-sectional configuration?

White:

There will be no booms with electrical cables used on any other Apollo flight, and I would say that it is too early to know this type of detail for the space-shuttle program.

A. B. Hunter, Jr.:

On the double C-spring boom mast, was there any resistance to twisting and was this a problem? Also, did the outer coiled cable impart any twist to the boom?

White:

The boom tapes did have restraints or clamps located at each end of the boom; however, it was known from ground-based testing that the boom would have 40° to 60° thermal twist. This twist was not a problem with the gamma-ray experiment but the mass spectrometer inlet scoop had to be redesigned. The external power cable did not cause a torsional problem while extended because the pitch of the coiled cable reversed direction at the cable-length midpoint to cancel the torsion from the coil spring.

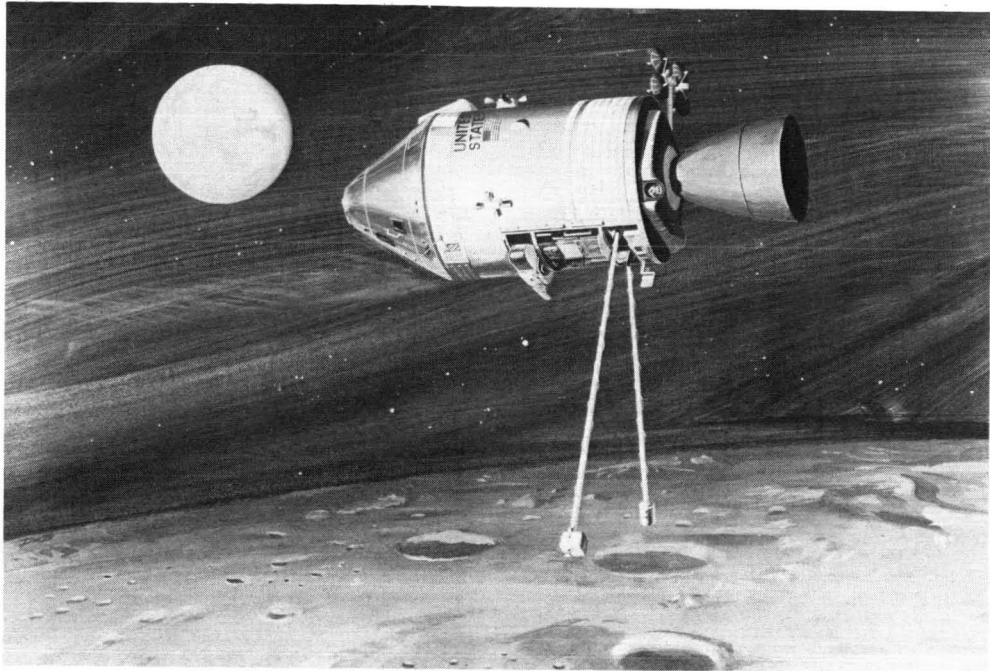


Figure 1. - Apollo SIM-bay experiments.

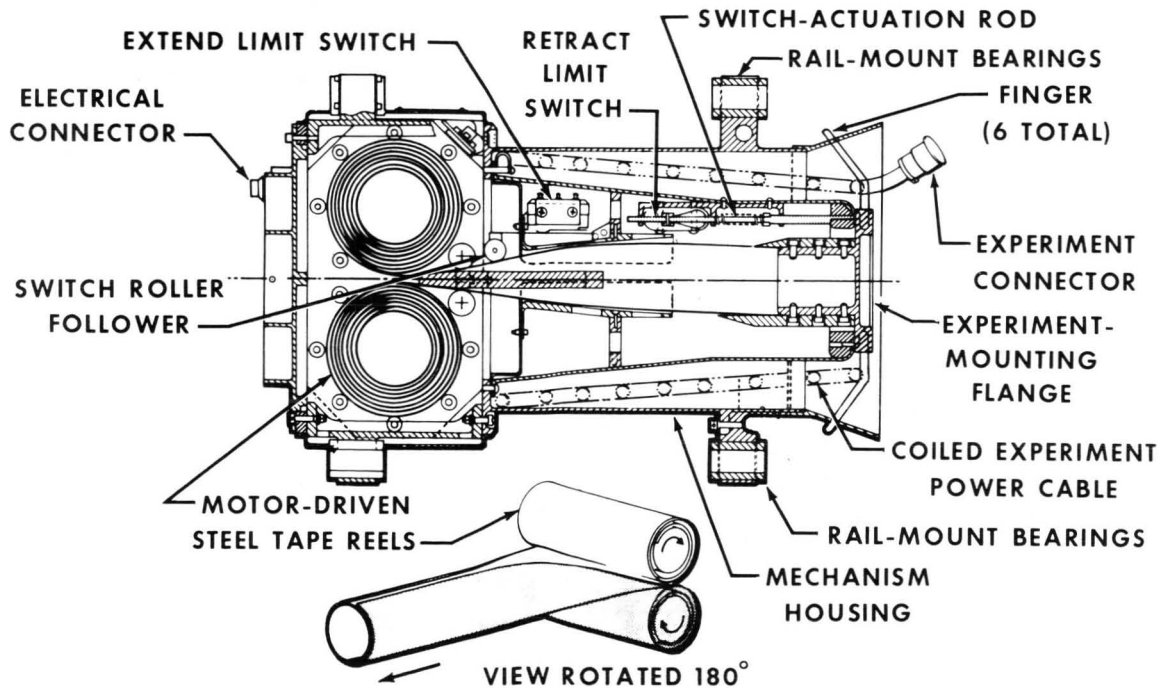


Figure 2. -Mass-spectrometer boom-actuating mechanism.

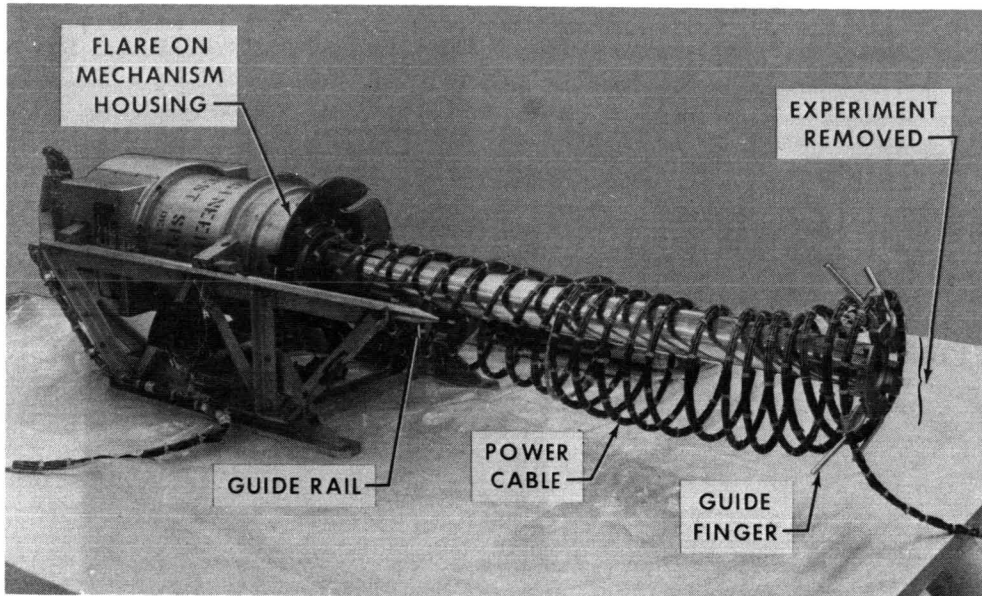


Figure 3. - Mass-spectrometer boom partially extended.

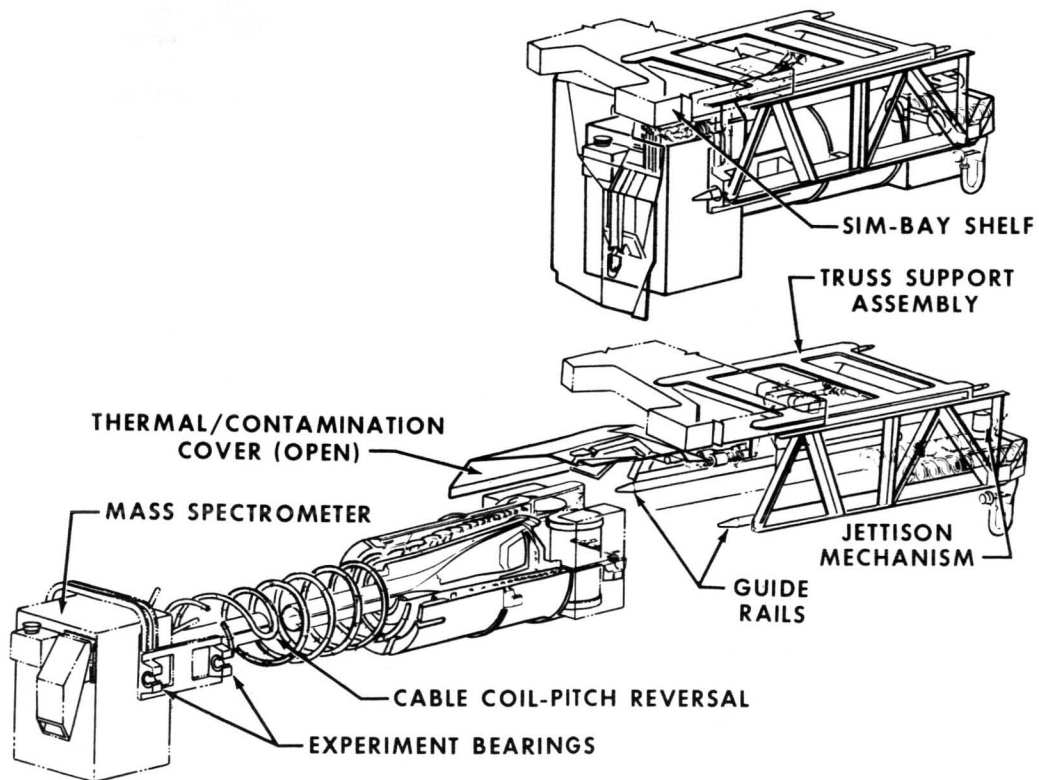


Figure 4. - Deployment mechanism and support structure.

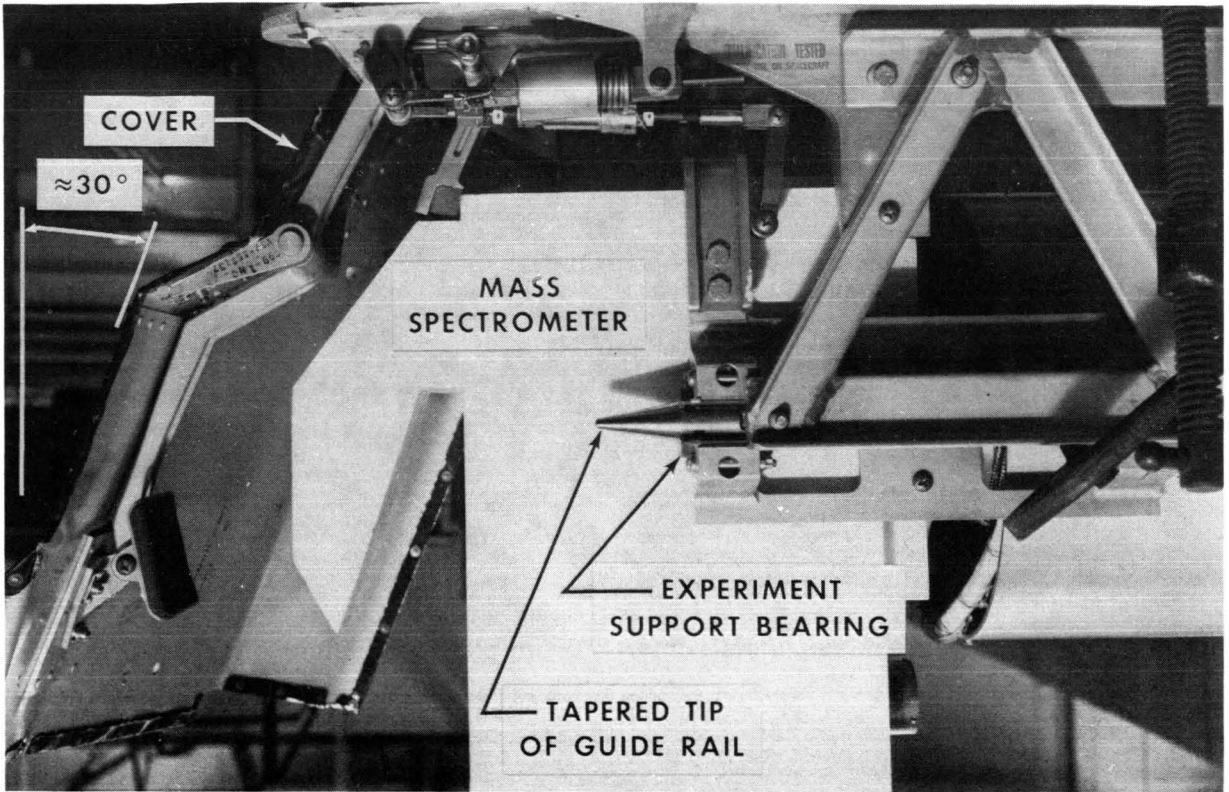


Figure 5. - Simulation of command module pilot observation.

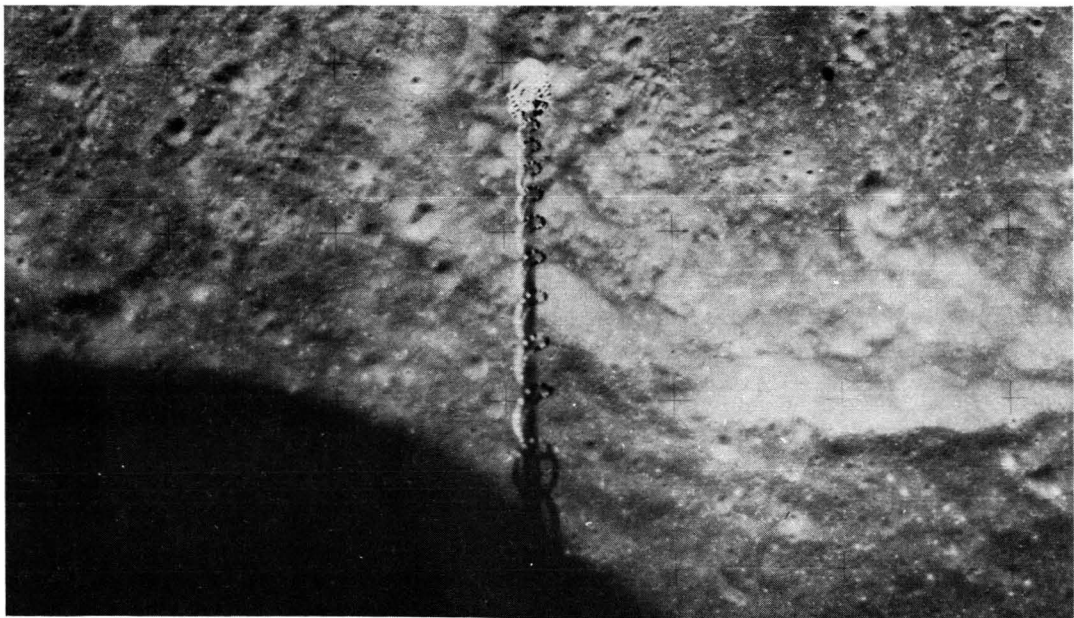


Figure 6. - Boom deployed in lunar orbit.

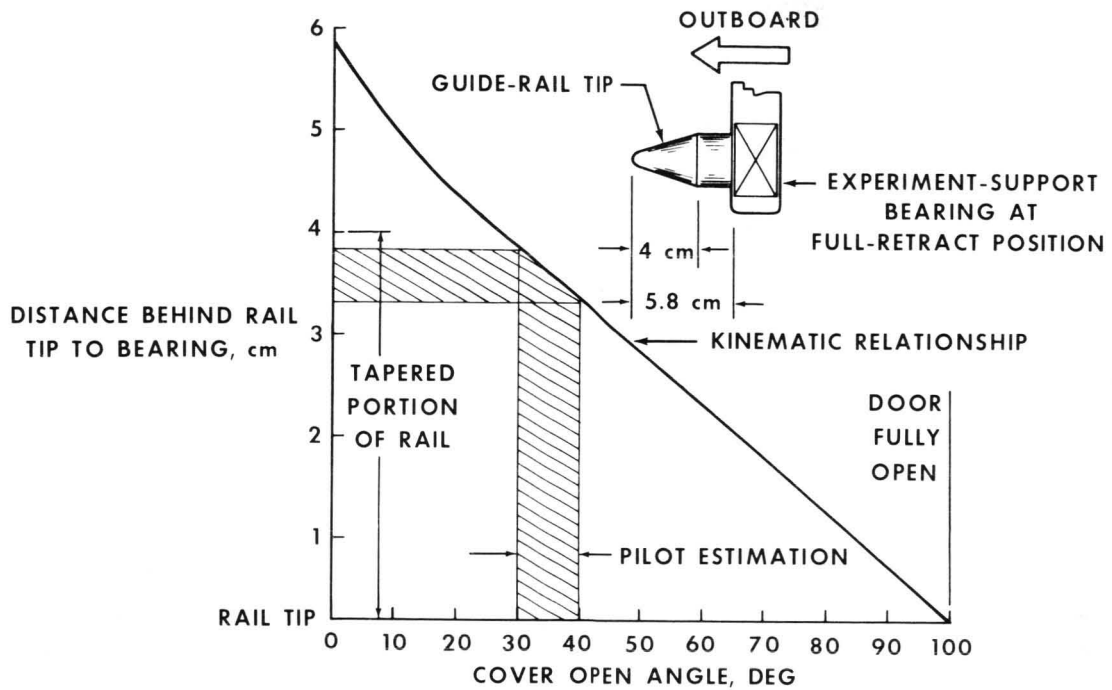


Figure 7. -Relationship of mass-spectrometer cover to bearing position.

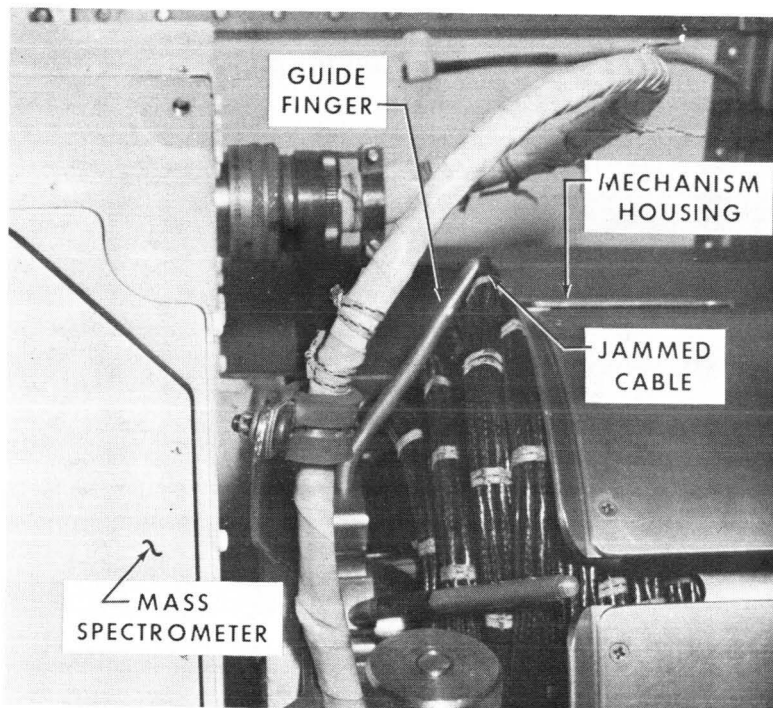


Figure 8. - Boom stall caused by jammed cable.

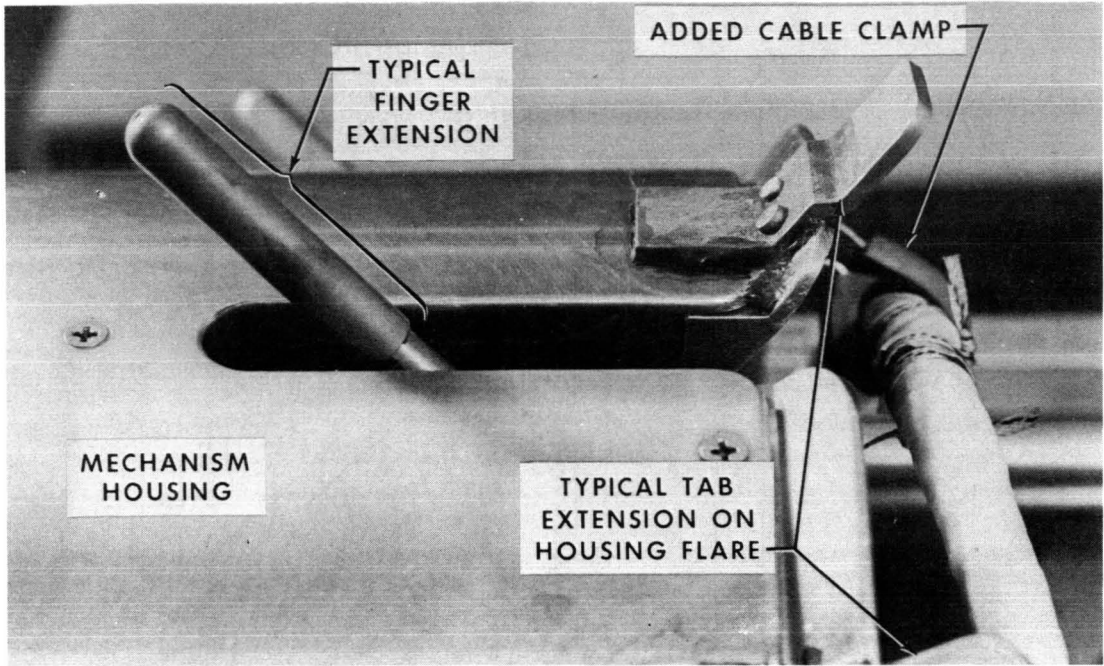


Figure 9. - Design changes to the deployment mechanism.

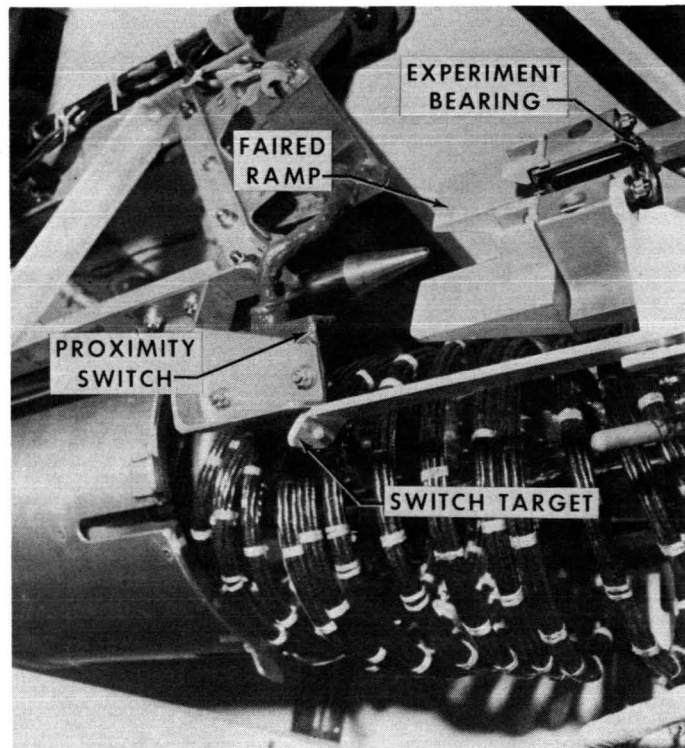


Figure 10. - Additions to the deployment mechanism.

# DOCKING SYSTEM OF ANDROGYNOUS AND PERIPHERAL TYPE

By V. S. Syromyatnikov\*

## ABSTRACT

Soviet and American space engineers have proceeded with creating compatible means for closing and docking spacecraft. It was decided to make a new advanced docking system of a peripheral and androgynous type. Because of a more complex design of the new-type docking mechanism, a number of technical problems arose. To a great extent, the solution of these problems depends on a chosen concept of the docking mechanism. The report deals with the docking system concept accepted by the Soviet engineers as the basis for further development. The description and structural arrangement of the docking system as a whole, its basic assemblies, and a kinematic scheme of the docking mechanism using a system of differentials are given. It should be noted that the experience that was gained from the development of previous docking systems was used to create a new type of docking system. The main problems to be solved in the course of designing and developing the advanced system are noted.

## INTRODUCTION

Having developed the proper docking systems and having realized the docking of spacecraft, Soviet and American space engineers proceeded with the creation of compatible docking systems which, if necessary, allow the spacecraft of both countries to dock with each other. The specialists came to an agreement that the design of the systems may be different and only such a minimum number of elements and parameters should be unitized that will ensure the docking of spacecraft. It is natural that, on the one hand, the designers of each country try to use the experience acquired in developing the docking means for previous projects and, on the other hand, they wish to improve these means. Moreover, they try to develop such equipment and structures of spacecraft that would meet tomorrow's tasks and could serve as the basis for solving more complex and multipurpose space-program problems than the present ones.

The docking system for joining spacecraft is a complex multifunctional assembly of the spacecraft. While developing such a system, many technical problems such as dynamics, kinematics, strength, thermal control, and so forth must be solved. The docking system for the Soyuz spacecraft and a further modification for the Soyuz-Salyut

---

\*Academy of Sciences, Moscow, U.S.S.R. This report was summarized at the 7th Aerospace Mechanisms Symposium by C. C. Johnson, NASA Manned Spacecraft Center.

space system is designed according to the principle that is called "probe-drogue." The docking systems for the Gemini and Apollo spacecraft are designed in accordance with the same principle. However, the specialists of both countries came to a conclusion that, unfortunately, the docking system having a probe and a drogue suffers from at least two substantial shortcomings. First, the probe and the drogue occupy the central part of the system; however, in most manned spacecraft it is expedient to use it for creating an intravehicular transfer tunnel. Second, when both parts of the system to be docked are alike and can operate both actively and passively, the ensurance of androgyny presents some difficulties.

Therefore, proceeding to the design of a new docking system, the specialists of both countries agreed to develop a system of a radically new peripheral and androgynous type. The docking mechanism of this system performing the main functions of joining spacecraft is located around the periphery of the docking ring. By means of thorough analysis is shown that, in solving many problems connected with the creation of the peripheral-type system, the experience and technology of the probe-droge-type docking system may be used successfully. This report deals with the description of the concept of the docking system of an androgynous and peripheral type that allows the solution of a number of technical problems of principle inherent in designs of this type.

## DOCKING SYSTEM CONCEPT

It is expedient to assume that each part of the docking system to be installed upon the spacecraft to dock and further referred to as a docking assembly consists of two main units: the docking ring with elements located on it (structural latches, electrical and hydraulic connectors, actuators, transducers, and so forth) and the docking mechanism, which, for the design considered, is located around the periphery of the docking ring. Although these two main units may be connected closely to each other, their functions are substantially different in essence and in the sequence of performance.

The general view of the active and passive docking assemblies is shown in figure 1, and the front view of these assemblies is shown in figure 2. As was stated, the docking assembly is designed to be androgynous. The identity of the active and passive assemblies is achieved by the use of the assemblies that have a common axis of opposite symmetry that coincides upon docking (axis I-III in figure 2). All of the mating elements of both the docking ring and the docking mechanism to be joined upon docking are placed symmetrically about this axis. The docking mechanism consists of a guide ring (located on six moving rods), a drive, and a system of kinematic links between the rods. The docking mechanism accomplishes impact attenuation, coupling, alinement and pulling of the spacecraft until contact. The docking ring houses the inter-face seal, structural latches, actuators, pushers, transducers, and other elements.

Before docking, the active spacecraft extends the guide ring into the extreme forward position. The ring of the passive spacecraft is placed into the extreme retracted position. Such a preparation would permit the accomplishment of all docking operations using the mechanisms of the active spacecraft only.

Structural joining of the docking rings that ensure sealing is accomplished, for this design, by means of a system of structural latches after the interfaces come into contact with the help of the docking mechanism.

The latches exert a preload that ensures the compression of the seal and the integrity of the interface under internal pressure and under all external loads that occur during flight in a docked mode. The desirability of a secondary link through the use of structural latches results from two factors. First, it permits the use of a low-power drive for latches having a small stroke (several millimeters) and a large force (approximately  $20 \times 10^3$  kilograms (20 tons)) at a comparatively small power of the docking-mechanism drive, which has a large stroke (several hundreds of millimeters) and significantly less force. Second, it allows an increase in the number of shackling points, which is necessary to provide for the sealing and integrity of the interface. The primary docking mechanism link in a joint mission can be used as a redundant safety link.

Sets of mechanisms, on board both spacecraft, capable of performing all docking and undocking operations must ensure higher reliability. In case of failure, the active-spacecraft docking mechanism can be turned into the passive mechanism by retracting the ring into the extreme rear position. In case of a complete failure, the possibility for its jettisoning and the use of reserve guides is provided (fig. 3).

In performing docking by the active spacecraft, some operations of docking and undocking can be accomplished by means of mechanisms of the passive spacecraft. The pyrotechnics can be used as a redundant means for undocking the spacecraft.

The docking ring shown in figure 2 has electrical and hydraulic connectors that are similar to those which were successfully used in the Salyut and Soyuz docking systems. These elements are connected at the final phase of pulling the spacecraft together by the docking mechanism. The electrical connectors in the interface permit, if necessary, the control of mechanisms (as well as other systems of the second spacecraft) and data exchange between the crews before the transfer hatches are opened.

The docking assemblies are self-contained units and can be mounted on various spacecraft, which significantly facilitates design, manufacture, development, and testing. This factor is particularly important in creating compatible designs.

The docking assemblies are equipped with a system of transducers, the signals of which carry data on performing docking and undocking operations to the pilot panel, through a telemetry system to the ground, and into the docking-system control device to provide the possibility for automatic performance of main operations. The automatic control and commutation device is mounted on the docking assembly to facilitate testing of the system as a whole.

## DOCKING MECHANISM

The "double ring and cone" principle employed in the docking mechanism is a novel concept. To attain attenuation in all degrees of freedom relative to the movement of spacecraft, the ring should possess six degrees of freedom in relation to the body.

The ring is mounted on six rods that are gimbaled both to the body and to the ring. In order to ensure the necessary freedom for the ring, all rods must have the capability of translational movement independent of each other. The rods should be provided with attenuators and a drive for further pulling of the spacecraft. In order to ensure alignment and pulling of the spacecraft without misalignment, the movement of all rods is synchronized.

The concept that was developed includes one drive for moving the ring, one attenuator for absorbing most of the energy, and a kinematic link between the rods through the system of differentials (fig. 4). Actually, the rods are screws equipped with ball-screw assemblies. Nuts of these assemblies are connected with each other and with the drive through five differentials that provide five degrees of freedom for the ring because of changes in the rod lengths (that is, to move along the lateral axes and rotate relative to three main axes). The drive has a self-adjusting clutch. When the clutch is slipping, the ring can move along the longitudinal axis in the sixth degree of freedom.

Thus, the clutch that has a stable slippage moment owing to a regulator provides the spacecraft-impact attenuation in the longitudinal direction and, at the same time, it is the drive-safety device that limits the force of pulling the spacecraft. The slippage moments in both directions may be different.

To return the ring to a mid position after its deflection, each differential is fitted with a spring-loaded mechanism that has a high value of preload in both directions. Such a value provides the precise, stable return of the ring to the mid position and holds it in this position.

In the general case, the spacecraft are misaligned just prior to the first contact. At impact, the active-spacecraft ring moves (because of guides) until it matches with the ring of the passive spacecraft. Simultaneously, the energy of the spacecraft relative movement in the lateral direction and the relative rotation is absorbed by the torsion of the springs. At the moment of matching the rings, three capture latches of the active-spacecraft ring are coupled with the latches on the body of the passive spacecraft.

After accomplishing the coupling and after absorbing the main portion of the impact energy of the longitudinal movement, the spacecraft are aligned by the spring-loaded mechanisms of differentials, which return the ring to the mid position when the friction clutch is slipping. For intensive damping of the spacecraft relative oscillations after coupling and for better energy absorption during the ring deflections at the first impact, electromechanical dampers (ref. 1) producing a force that is in proportion to the movement velocity of the rods, are connected to nuts of each rod. While the ring moves with the help of the drive, its speed can be within several millimeters per second (the impact velocity usually is equal to several hundred millimeters per second) and the dampers do not add an appreciable load on the drive.

Each differential has a mid-position transducer that corresponds to the mid position of the ring (along the corresponding coordinate). The transducers can indicate the initial extended and retracted positions of the ring without misalignment (in conjunction with a signal from the drive stop contacts), the completion of alignment, and the due course of pulling the spacecraft. If misalignments occur, signals from the transducers can be used in the docking-system control device and for transmitting data to the pilot panel and through the telemetry system to the ground for analysis.

To eliminate the ring misalignments in the course of pulling the spacecraft, the differentials may be fitted with controlled locks that prevent the differentials from mismatching. The necessity for such locks may become evident in the course of more detailed development and experimentation.

One of the most important problems in designing the docking mechanism of a peripheral type is the choice of possible ring deflections because this range determines primarily rod lengths, longitudinal dimensions of the assembly as a whole, and assembly as a whole, and assembly weight. To facilitate the coupling, it is advisable that the range of the ring deflections be equal to the corresponding maximum errors in the relative position of the spacecraft upon the initial contact and that the forces be minimum but, in this case, the docking-mechanism dimensions increase. The second limit case occurs when impact forces do not exceed maximum allowable limits, and the range of ring deflections is small and is determined by the magnitude of the stroke, during which maximum possible energy of impact is absorbed. Apparently, a rational solution of the problem is somewhere between these two limit cases. To solve the problem, it is necessary to conduct theoretical and experimental investigations of coupling dynamics.

## DOCKING RING

The body of the docking assembly with the docking ring is the primary structure which houses all other elements and units including the docking mechanism. The forward part of the docking ring contains a system of structural latches. This design uses the system of latches that was developed for the Soyuz docking system and it meets the androgynous principle. The system consists of eight latches that distribute the force to 16 points equally spaced around the docking ring. The system is actuated by one electric drive, has a closed cable loop between the latches, and has pyrotechnics for redundant undocking. The latch system functioned well during development and flight tests. Electrical and hydraulic connectors and spring-loaded pushers mounted on the docking-ring interface satisfy the androgynous principle as well.

To provide the guiding-pin operation with allowance made for tolerances or when the dimensions change because of temperature drops and strain, one of two pins or one of two sockets of the assemblies to be docked must be movable in the lateral direction. The androgyny of the assemblies is preserved by a lock on the guiding pin that is used for locking the pin of the active spacecraft.

Two types of rubber gaskets were developed to be used as an interface seal. They are similar for both assemblies and form two redundant seal rings. The first type consists of two half-rings of different diameters (fig. 2) connected by comparatively wide radial parts. When the docking rings contact, the half-rings come into contact with the metallic surface of the docking ring interface and the radial parts touch each other. The second type consists of two concentric rings that come into contact with similar rings of the second spacecraft upon sealing.

The docking ring must have special devices that would provide for the functioning of a system for pressurizing the interspace between the hatches of the docked spacecraft,

as well as systems for pressurization check and pressure release inside the interspace before undocking. When there are two gaskets, the space between them, which is of a very small volume, can be used to make a rough but very quick check.

The structure of the assemblies with hatches is shown in figure 1; a drive for opening it and a drive for pressurization are present. In addition, the provision is made for manual pressurization and hatch opening, both from inside and outside.

## USE OF THE EXPERIENCE ACQUIRED

In developing the docking-ring housing and the mechanisms, most parts of the Soyuz-Salyut docking system units are used. Some units of docking systems developed earlier (such as ball-screw pairs, electromechanical brakes, and the self-regulating brake) also were used in designing the docking mechanism. More detailed analysis, however, makes it possible to draw a closer analogy between the docking mechanism that has the system of differentials and the mechanism of the probe-drogue type used in the Soyuz spacecraft.

In spite of a very complex system of attenuation, alinement, and pulling that results from the necessity for moving the guide ring in six degrees of freedom, the principle of designing the systems is the same. First, the same kinematic elements are used for both attenuation and pulling, the friction brake being used both for absorbing the impact energy along the longitudinal axis and as the drive safety element. Second, lateral and angular viscoelastic attenuators are used that return the system to its initial alined position after damping. The advantages of such a system were mentioned in reference 2.

The analysis of the dynamics of the spacecraft impact through an attenuating system of the peripheral type also reveals that the impact process of this mechanism has some features in common with features of the probe-drogue-type system. The methods of computations developed earlier and some conclusions made on the basis of this analysis also can be used. However, docking dynamics is a specific subject and cannot be considered in a limited report.

According to one of conclusions derived from the dynamic analysis, it is expedient to create a substantial difference in forces produced by the longitudinal attenuator and the lateral viscoelastic attenuators, which is ensured by the friction brake. In this case, the advantage of the differential kinematic link between rods becomes evident. Translational movement of the active-assembly ring occurs only after complete coupling with the passive one, and the quantity of this movement is small, even at maximum closing velocity. This quality of the attenuating system simplifies the choice of the required range of possible ring deflections and, finally, reduces the assembly dimensions.

## CONCLUDING REMARKS

The present description of the concept of a peripheral and androgynous type docking system, which the U.S.S.R. specialists took as a starting point for further work, is based on the results received in the initial phase of its development. Much design, development, calculational, and experimental work should be carried out to create such a system. However, preliminary design and subsequent work make it possible to say with sufficient degree of reliability that it is possible to create a docking system meeting the requirements and recommendations given in technical specifications that were determined by the Soviet specialists together with their American colleagues. Joint efforts and mutual information exchange will promote the advance of the spacecraft technology.

## REFERENCES

1. Syromyatnikov, V.S. : Docking-Mechanism Attenuator with Electromechanical Damper. Paper presented at 5th Aerospace Mechanisms Symposium (Greenbelt, Md.). NASA SP-282, 1971.
2. Syromyatnikov, V.S. : Docking Devices for Soyuz-Type Spacecraft. Paper presented at 6th Aerospace Mechanisms Symposium (Moffett Field, Calif.). NASA TM X-2557, 1972.

## DISCUSSION

J. H. Parks:

It is beyond the scope of your comments, but could you comment on any problems to date or any anticipated problems related to such things as dimensional-tolerance specifications and so forth? This question is in consideration of the fact that the Soviets use the metric system and our working drawings still tend to involve the inch-foot-pound system.

C. C. Johnson (for Syromyatnikov):

At one of our first meetings with the Soviet engineers, we jointly agreed to use the International System of Units in all interfacing situations. We had some misgivings but, in practice, there has been little inconvenience and no confusion. However, neither the Soviets nor we feel comfortable with the newton; we both continue to express force in weight units.

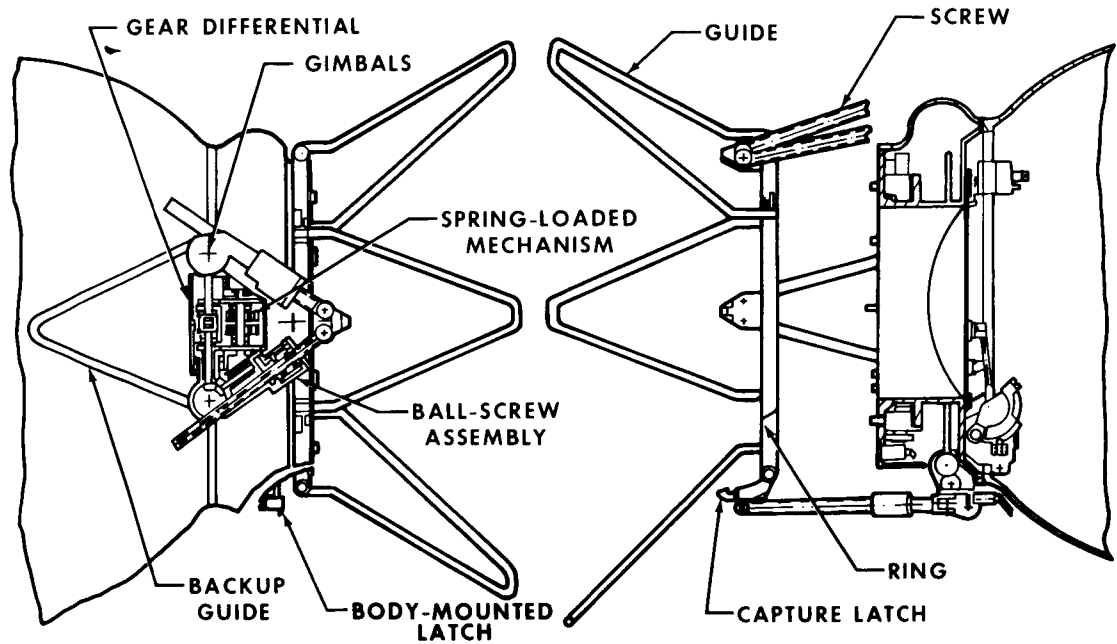


Figure 1. - General view of the active and passive docking assemblies.

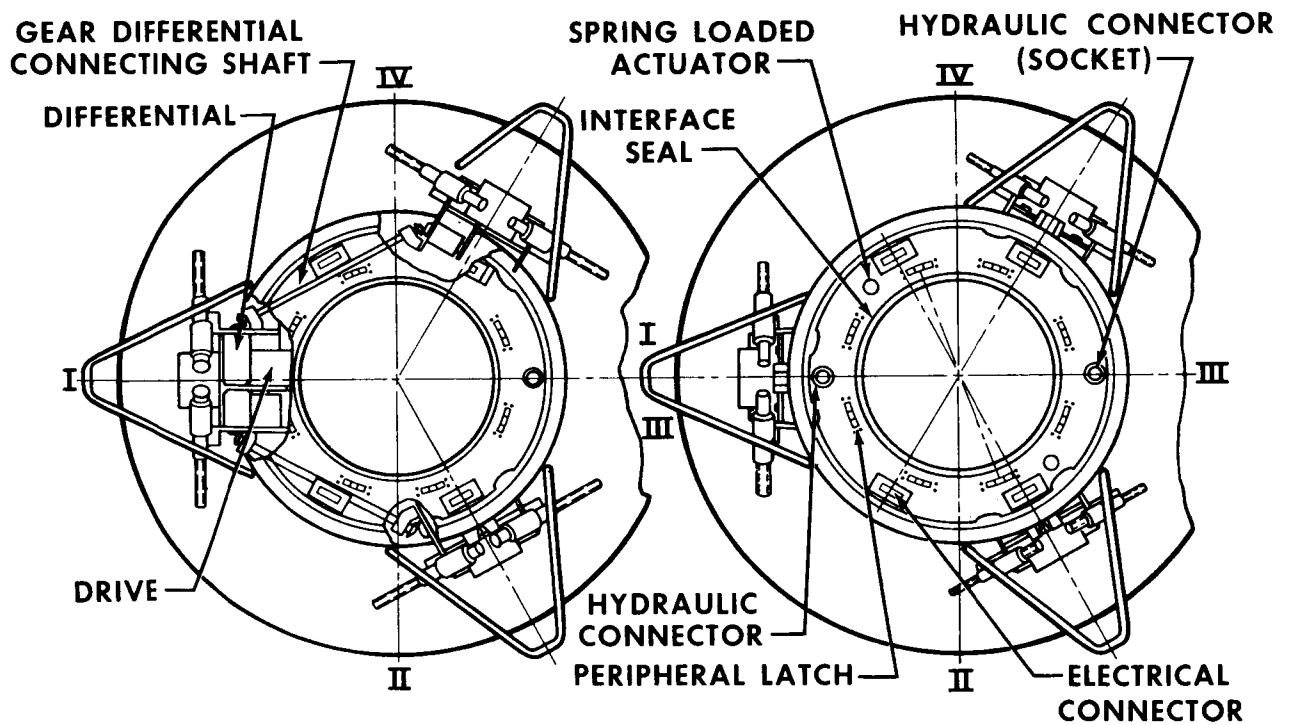


Figure 2. - Front view of the active and passive docking assemblies.

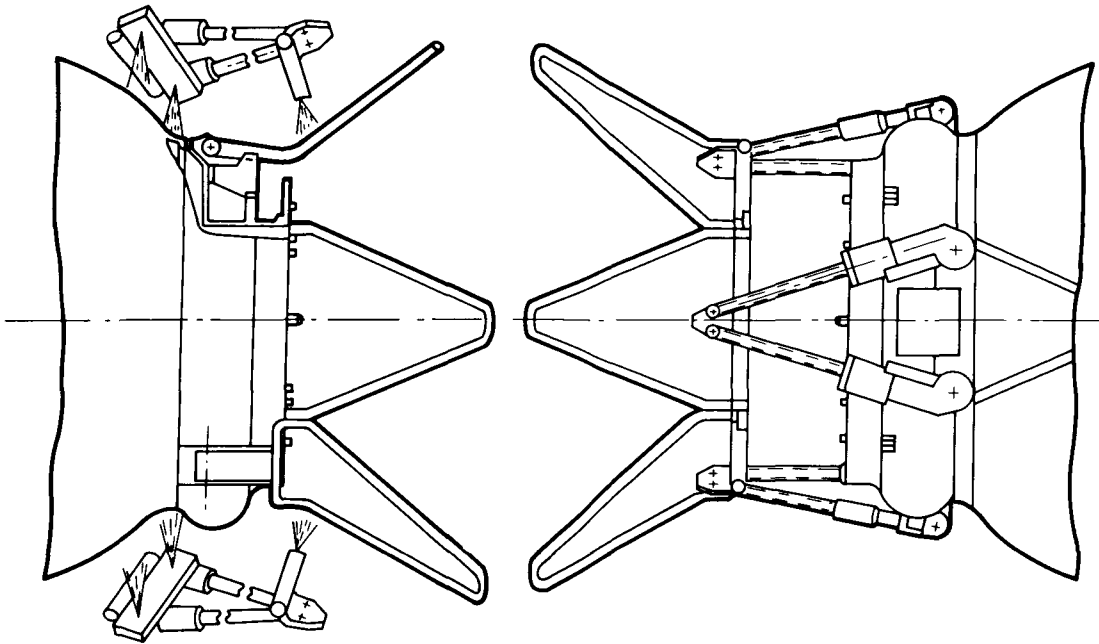


Figure 3. - Emergency assembly jettisoning and docking preparation.

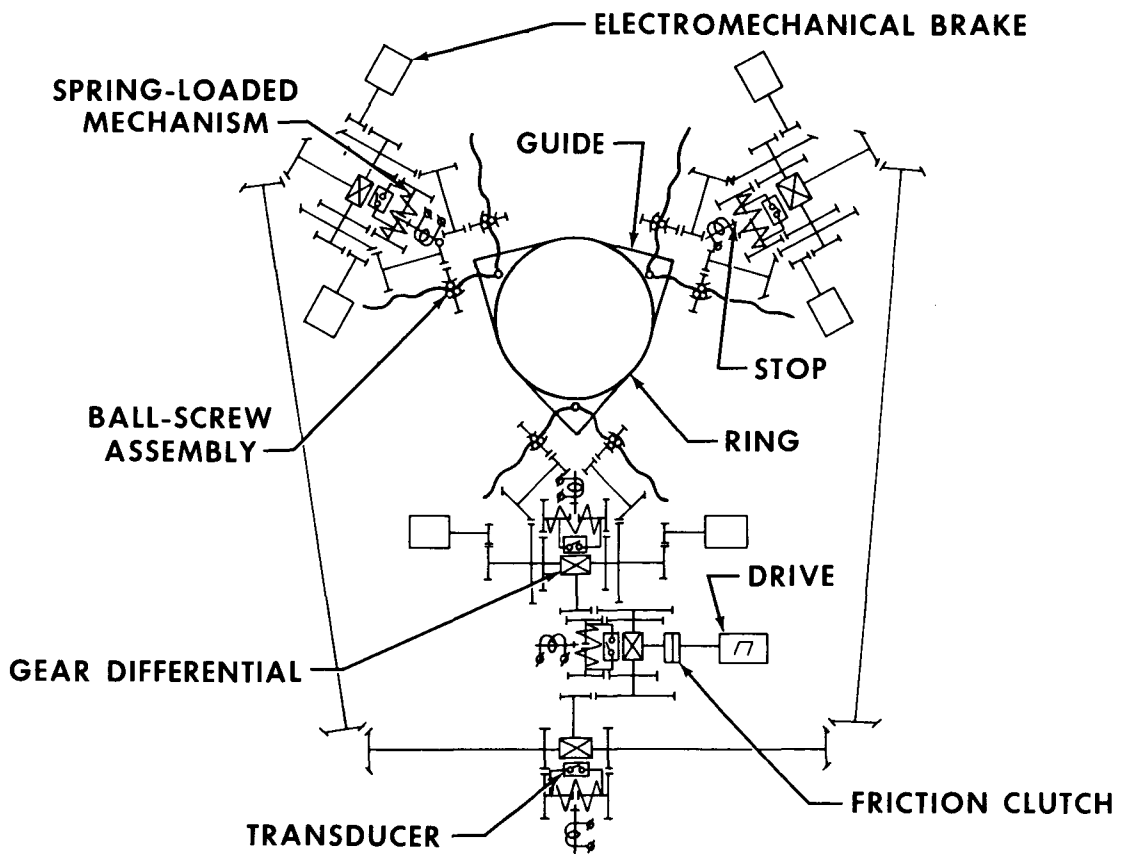


Figure 4. - Assembly synchronization.

**Page intentionally left blank**

## A FOLDABLE 4.27-METER (14 FOOT) SPACECRAFT ANTENNA

By Donald J. Starkey\*

### ABSTRACT

The problems and solutions associated with the design, fabrication, and testing of a large, lightweight, radial-rib, folding, spacecraft antenna reflector are discussed in this report. The antenna reflector was designed as a highly efficient communications system for outer-planet missions extending as far as approximately

$59.839 \times 10^{11}$  meters (40 astronomical units) from the sun. The methods used to obtain a lightweight precision rib surface, the evaluation and fabrication of the metallic reflector mesh surface, and the surface-evaluation techniques used on the assembled antenna reflector are included in this report.

### INTRODUCTION

The design, analysis, fabrication, assembly, and testing of a lightweight, foldable, radial-rib, parabolic antenna reflector was undertaken to establish that the weight and volume requirements of future outer-planet missions could be met while maintaining antenna-surface accuracy to comply with the communications criteria. The primary effort was concentrated on the mesh-covered area of the reflector because that area comprised the majority of the total reflector surface. An analytical prediction and the subsequent verification of the mesh surface (when it was subjected to the interactions inherent in the antenna design) were included. The structural, gravitational, and thermal interactions on the mesh surface also were analyzed.

### DESIGN REQUIREMENTS

The need for a highly efficient antenna design became evident during an outer-planet-mission study early in 1969, when the following design requirements were placed on the antenna reflector.

1. Weight: 16.8 kilograms (37 pounds)
2. Deployed diameter: 4.27 meters (14 feet)
3. Stowed diameter: 1.57 meters (62 inches)

---

\*Jet Propulsion Laboratory, Pasadena, Calif.

4. Stowed height: 1.98 meters (78 inches)
5. Feed access: 0.61 meter (24 inches)
6. Surface accuracy: 0.89 millimeter root mean square  
(0.035 inch root mean square)
7. Deployment: one-g field
8. Temperature range: 366.45° to 33.15° K  
(93.3° to -240° C)
9. Focal length/diameter: 0,42
10. Natural frequency: 8-hertz lateral  
3-hertz torsional
11. Gain: 49 decibels
12. Feed system: Cassegrainian

#### ALTERNATIVE CONCEPTS

An industry search was initiated in 1969 to determine the antenna designs that were available to fulfill the design requirements. Two designs considered were an antenna flex-rib and an expandable-truss antenna. The flex-rib, radial-rib-type antenna is folded by wrapping the carpenter-tape-shaped ribs and copper-plated Dacron reflector mesh circumferentially around the hub. The extendable-truss design has many triangular, deep-truss modules that are hinged at and fastened together with spider joints. This design involves the use of a Chromel-R mesh that is fastened to the concave side of the truss network by means of a system of cables and springs.

An evaluation of these antennas concluded that either could fulfill most of the future outer-planet needs. Both antennas provided limited feed-access area, and the flex-rib design appeared to have a lower natural frequency than required in the torsional mode. Because both antennas would have required an extensive developmental effort to satisfy all requirements, they were not considered further.

A third antenna design (the radial rib) was then investigated. This design evolved from an antenna that was proposed for a Mariner vehicle in the early 1960's. The radial-rib-antenna design satisfied all the requirements and provided a good base on which to check the evaluation analysis of the surface conformance of any parabolic antenna. When the design details for the radial-rib antenna were completed, it was discovered that a company concerned with radiation research had also designed and built a similar radial-rib antenna that had a small hub and constant-section tubular radial ribs that are folded forward around the feed. Because investigation showed that that antenna would have also required extensive redesign in the hub area to meet the design requirements, the Jet Propulsion Laboratory version was pursued.

## RADIAL-RIB ANTENNA

### Hub

The Jet Propulsion Laboratory radial-rib-antenna-reflector structural configuration (fig. 1) was based on a stiff central hub. This hub provides the hinge support points and the rib adjustment surfaces for the 48 radial ribs, together with the mounting surface for the central dish, the deployment mechanism, and the forward subdish support structure. The outer-planets spacecraft configuration required that the antenna be offset from the spacecraft geometric centerline to correct a center-of-gravity imbalance. Accounting for this antenna offset, the hub diameter was sized at 1.37 meters (54 inches), which held the folded antenna components inside the given envelope. It was advantageous to use a large central dish because it would be far easier to build a large, precise, central-dish surface instead of having to control the mesh-covered surface. In addition, the hub size had to be reasonably large to provide for the 0.61-meter (24 inch) central feed-access hole. Also, the minimum hub circumferential length had to be large enough to allow assembly space for the 48 rib hinges. Sizing the hub, using these criteria, provided sufficient volume for the rib-deployment mechanism that was selected.

### Ribs

The hub sizing and the deployed antenna diameter provided the end points for determining the rib lengths. Accounting for the parabolic contour, the final rib length was 1.56 meters (61.58 inches). The aluminum ribs (fig. 2) were formed from a round, tubular cross section as a trade off between the structural and thermal requirements. Because this antenna was to be pointed at a continually receding sun, the thermal-design group preferred flat, thin-plate ribs to minimize thermal gradients that would in turn reduce the thermal distortions. The structure-analysis group preferred greater depth than width to increase the stiffness of the ribs in the highest-stress direction. The round, aluminum, tubular cross section was chosen as a compromise that would keep the thermal gradients through the ribs and the resulting thermal distortions within an acceptable level. It also provided the ribs with adequate structural stiffness to withstand the handling and flight loads.

For weight reduction and structural efficiency, the rib diameters were tapered from 2.79 centimeters (1.10 inches) at the hub to 0.95 centimeter (0.375 inch) at the outer end. This tapered-tube configuration, while being structurally efficient, provided an almost insurmountable fabrication problem. The 0.51-millimeter-wall (0.020 inch) aluminum tubes were passed through a compressive roller die in five separate steps to obtain the full taper, which produced many dogleg bends and apparently extensive surface defects. Upon completion of the initial tapering process, a precise internal mandrel was placed inside the tapered tubes and the compressive roller die was again passed over the full length of each tube. The result was a perfectly tapered straight tube. An etching process removed the surface defects, which were very small, and the final tubes were perfect.

It became evident early in the rib-development program that it would be very difficult and extremely costly to contour a tapered tubular rib to a precise  $\pm 0.25$ -millimeter (0.010 inch) parabolic shape. The solution that evolved was to add a machinable surface to the concave side of the tubular rib, once the rib had been contoured by hand to within 0.29 centimeter (0.125 inch) of the nominal parabolic shape. This machinable surface was an inverted T-section fastened to the tubular rib. The T-section was then machined to a precise contour in a horizontal mill while the rib assembly was held in as close to a free state as possible. The result of this precision contouring operation was that, in the worst case, the rib shape was less than 0.15 millimeter (0.006 inch) from nominal.

The 48 radial ribs and hub provide the principal structural support for the total reflector-surface area. Therefore, most of the structural and thermal analysis was concentrated on the hub and ribs.

### Mesh Evaluation

The material chosen to cover the radial-rib area of the reflector was a gold-plated Chromel-R yarn formed into a mesh using a tricot weave. This mesh material is commonly used as the reflective surface in lightweight folding antennas. The mesh material has many problems for space applications but was chosen primarily because of its availability. The Chromel-R material is readily available in fine filament form because it is commonly used in wire-wound resistors and it has a very high strength (180 klb/in<sup>2</sup>). The wire filaments can be formed into several yarns. The one chosen for this application had seven wires per strand. The available tricot-mesh patterns also vary. A mesh pattern of 7 ends/inch appeared to be cost effective for this application. The unplated Chromel-R mesh, as woven, has a much higher radio-frequency (RF) loss (0.3 compared with 0.1 decibel) than was required to meet the RF efficiency goal. To reduce the RF losses in the mesh to an acceptable level (0.1 decibel), the mesh was electroless gold plated, temporarily solving the mesh RF loss problem but creating a materials problem.

The electroless gold is very brittle and will not adhere to the passive Chromel-R wire. When the mesh is flexed during fabrication and antenna furling, the gold cracks and tends to flake off, reducing the RF efficiency of the mesh slightly in addition to creating a contamination problem. Several alternatives were investigated to solve the gold-flaking problem. The first was using electrolytic gold plating. The applied gold from this process is quite ductile but still does not adhere to the Chromel-R. This increased ductility reduced the gold cracking and subsequent flaking but was still considered unsatisfactory. A second alternative involved materials that had low RF losses without being plated. Several precious-metal alloys were woven into a mesh and tested for RF reflection losses. One silver-base material most nearly met the RF reflection criteria but was not readily available in large quantities and had a somewhat lower strength, which could result in greater mesh-surface deviations.

Tests were performed on the gold-plated Chromel-R mesh to establish its physical properties for the antenna-surface analysis. Such data as the effective Young's modulus of the mesh, stiffness, strength, and thermal expansion were needed to analyze and predict the mesh shape when it is placed on the antenna ribs. Because of the compliant nature of the mesh and the interaction between the two orthogonal directions, these physical characteristics were difficult to determine. Instead of precise quantities, ranges were established for most of the unknowns, which proved sufficient for analyzing the mesh shape.

Tests were run to establish the desired tension field for the mesh by tensioning the mesh to various values in the two orthogonal directions and checking the RF reflection efficiency, in addition to the mechanical out-of-plane distortions. Once the mesh tension range was established, the next problem was to determine a ratio between the two orthogonal tensions that would result in the least geometric surface error and still not adversely deflect the ribs. The ratio was set at 1 to 3, low in the radial direction and high in the circumferential direction. The higher the tension ratio, the lower the geometric surface error. In actuality, the circumferential tension is limited on the upper end by deformation in the mesh loops, thereby reducing or eliminating the compliant feature of the mesh, which could result in large local thermal distortions. The radial lower tension limit is also bounded because the mesh surface has a tendency to wrinkle as this value is reduced.

### Mesh Reflector Fabrication

Once the tension ratio was established, the fabrication of the mesh skirt was begun. The uncut mesh panels were stretched over a rectangular frame. The pattern was marked on the stretched mesh, and the gores were cut out. The marked edges were matched and then fastened together by sewing. Sewing techniques were developed using both a metallic and an organic thread. The metallic thread is a must for long-term space missions. The poor availability of a good-quality metallic thread that was compatible with a specially modified sewing machine made development of this technique difficult. The only metallic thread that finally proved satisfactory had a Teflon coating. Both the metallic and organic sewing techniques were used to assemble the full mesh skirt. The skirt was then stretched to match the ribs, and, once the match was made, the tension ratio was again at the proper value.

### Deployment Mechanization

Several deployment mechanization schemes were studied: a drum, pulley, and cable mechanism; several bar-linkage arrangements; and an individual rib-deployment design. The linkage-and-cable devices were abandoned because of their complexity and the limitation that they remain almost wholly within the hub envelope. The individual rib-deployment scheme was incorporated; it consisted of a pair of constant-force springs located at each rib (fig. 3).

## ANALYSIS

The analysis effort was concentrated on the reflector-surface evaluation and was initiated by developing a computer program that would mathematically describe the antenna-reflector surface. The analysis was continued by estimating the error sources, determining the thermal effects, and establishing the deployment dynamics. The reflector surface to be analyzed was composed of a compliant mesh material that was placed in biaxial tension and supported by a semistiff parabolic structure.

### Reflector Surface

The variable inputs to the reflector-surface evaluation program are the mesh tensions, major and minor diameters, numbers of support elements (ribs), and the geometric shape of the rib elements. The program was designed to optimize all these elements so that the final antenna-reflector surface would have the lowest possible geometric surface error. The computer program begins with a parabolic-rib support structure and modifies the rib shape to minimize the mesh pillowing effect (geometric surface error). This process is continued until a minimum surface deviation is achieved. The mesh tension is then removed mathematically by the program while accounting for the rib-support structural stiffness, and the resultant is the rib free-state manufacturing geometry. This analysis has been verified through the use of antenna-segment test fixtures that provide for membrane tension variations and will accommodate any compliant membrane material. The program, when applied to the 4.27-meter (14 foot) 48-rib antenna, yielded a maximum geometric error of 0.57 millimeter root mean square (0.022 inch root mean square).

### Error Analysis

An error analysis was developed early in the design of this antenna. The error budget was established as a design goal and appeared to be reasonable. At that time, a 0.51 millimeter root mean square (0.020 inch root mean square) was assigned as the geometric error. The remainder of the errors were assigned maximum values and were root mean squared to determine the resultant surface error. The number assigned to the mechanical rib-surface deviations was  $\pm 0.25$  millimeter (0.010 inch); for deployment repeatability,  $\pm 0.25$  millimeter (0.010 inch); and for thermal distortion, 0.13 millimeter (0.0005 inch). All these numbers were determined on the basis of experience with prior error magnitudes associated with similar components on past developments. These errors were combined as follows to provide the following surface accuracy capabilities.

$$\Sigma = 0.51 \text{ mm} + \left[ (0.25)^2 \text{ mm} + (0.25)^2 \text{ mm} + (0.13)^2 \text{ mm} \right]^{1/2} = 0.89 \text{ mm}$$

$$\Sigma = 0.020 \text{ in.} + \left[ (0.010)^2 \text{ in.} + (0.010)^2 \text{ in.} + (0.005)^2 \text{ in.} \right]^{1/2} = 0.035 \text{ in.} \quad (1)$$

## Thermal Analysis

The antenna was developed for a mission that proceeds into deep space away from the earth and sun. This type of trajectory would result in an antenna temperature of approximately  $366.15^{\circ}\text{K}$  ( $93^{\circ}\text{C}$ ) near earth and then it would be cooled steadily to a temperature of  $33.15^{\circ}\text{K}$  ( $-240^{\circ}\text{C}$ ) near Neptune. This temperature condition was complicated because directly behind the antenna and at one edge of the spacecraft was located a group of radioisotope thermoelectric generators, which have a surface temperature of  $533.15^{\circ}\text{K}$  ( $260^{\circ}\text{C}$ ). As the spacecraft travels farther away from the sun, the radioisotope thermoelectric generators have a more pronounced thermal effect on the antenna. By the time the spacecraft is approaching Neptune, the thermal gradient across the antenna dish could be as large as  $513.15^{\circ}\text{K}$  ( $240^{\circ}\text{C}$ ), resulting in thermal distortions and subsequent surface deviations significantly above the acceptable values. The solution was to place a multilayer, superinsulation thermal blanket behind the dish to thermally isolate it from the generators. In addition to the generator isolation, the thermal blanket reduced the thermal gradient through the depth of the ribs by providing reflected solar energy to heat the back sides.

The thermal analysis, assuming a thermal blanket covering all the back of the reflector, resulted in a maximum antenna-surface distortion of 0.18 millimeter (0.007 inch) throughout the mission, which could be further reduced to almost zero by an inflight focal-point movement of 2.8 millimeters (0.11 inch). The focal-point movement is equivalent to best fitting a new parabola through the distorted antenna surface.

## Deployment Analysis

The deployment dynamic analysis was initiated using the redundant constant-force springs as a given parameter. These springs were sized so that each would deploy a rib and mesh against gravity from a vertically downward orientation to a horizontal position. Once each rib had a pair of these springs applying the full deployment force and the antenna was positioned so that the ribs had a gravitational assist, the deployment velocity was much too great. The analysis showed that the yield strength of the ribs would be exceeded at the instant they hit the stops on the hub. Reducing the spring force or removing the redundancy was considered as a solution, but this was inconsistent with the project requirements. However, the final solution was to add a rotary-shear viscous damper on every fourth rib. This damper was designed and built and reduced the deployment velocity to an acceptable level.

## OPERATION

### Surface Evaluation

The operational phase of antenna development initially included three parts: RF testing, surface adjustment, and deployment repeatability.

## Radio-Frequency Testing

A brief study revealed two primary concerns associated with RF testing: (1) the unsymmetrical rib deflections in the gravitational field and (2) the wind load deflections. Any analytical predictions for these effects would have to be verified through extensive testing that would be time consuming and, therefore, costly. These predictions were not fully evaluated. The wind deflection could be eliminated through the use of an RF transparent dome, and the gravitational droop could be alleviated through the use of a special support structure. This special test equipment was not available at the Jet Propulsion Laboratory, and the constraining support structure, if used, could lead to higher RF efficiencies than are obtainable in space. Because this type of testing at the Jet Propulsion Laboratory would be wasteful of resources, the whole RF testing idea was eliminated.

## Surface Adjustment

Because a fixture had been assembled to adjust the antenna surface, it seemed reasonable to try to measure the antenna-surface deviations with the same fixture. Once the rib tips were positioned mechanically, a proximity sensor was installed on the fixture to measure the surface variations. The data reduction from this operation proved to be very unsatisfactory. A closer evaluation showed that the proximity sensor not only measured the air-gap variations but also the variations in the gold-plating quality. A second mechanical measurement was tried using a dial indicator. This scheme also proved to be unsatisfactory because the pressure from the dial indicator deflected the rib and mesh surface in varying degrees. It became evident that one way an antenna surface could be measured to within the required precision was through a noncontacting process such as photogrammetry. This type of measurement technique has another advantage in that the antenna surface can be measured in the face-up and face-down position; and, by averaging these two measurements, the gravitational distortions are theoretically reduced to zero. This technique was not pursued because of budgetary limitations. A third measuring technique, using a depth micrometer and an electrical-contact indicating device, was used with good results. This measuring system is limited in that it is only good for determining the antenna-surface deviations in one orientation.

## Deployment Repeatability

Because of the low sensitivity of the initial measurement system, it seemed almost impossible to get a precise number for the deployment repeatability. The initial deployment tests resulted in rib-tip deviations in the 1.27- to 2.54-millimeter (0.050 to 0.100 inch) range. An investigation showed that in addition to the measurement problem, two mechanical conditions caused these large variations. The constant-force deployment springs were inadvertently positioned so that when the ribs were fully opened and adjusted, the spring force was nearly zero (small preload). Secondly, the hub cone seats for the rib adjustment screws had some mechanical deviations that kept the ribs from fully seating against the stops. Once these conditions were corrected and the micrometer measuring system was used, the rib-deployment repeatability tests provided deviations in the 0.25-millimeter (0.010 inch) range as predicted.

## CONCLUDING REMARKS

Designing, building, and testing the 4.27-meter (14 foot), lightweight, folding antenna reflector verifies that the technology exists to fulfill the future outer-planet-mission requirements. The design uses a compliant mesh material in conjunction with a semi-stiff support structure. This concept has several advantages. The surface distortion resulting from unsymmetrical surface heating is all but eliminated, the mesh provides a very low-weight-per-unit area reflector material, the mesh folds up easily and does not take a permanent set, and varying the mesh tension over a wide range does not result in significant surface distortions. The antenna described has the capability of satisfying the initial set of outer-planet requirements. By incorporating a false-rib technique in the design, the total surface error could probably be reduced by half. A complete surface evaluation was curtailed because of a subsequent reduction in the estimated future planet communication requirements.

## DISCUSSION

J. K. Riedel:

You mentioned that tapering the ribs caused a problem. What was the problem and, in view of the problem, would you recommend not tapering the ribs?

Starkey:

The problem was a result of the taper per unit length in conjunction with a wall-thickness decrease. The degree of taper per unit length using aluminum tubing turned out to require the use of a new process. Similar tapering had been performed many times in the past on stainless-steel tubing with excellent results; however, the aluminum required that a completely new manufacturing technique be worked out. The technique for tapering aluminum tubes from 1.1 inch in diameter down to 0.38 inch in diameter in 61.5 inches of length has now been developed and it provided excellent results. I would not hesitate to recommend the tapered tubes for any similar application now that the manufacturing technique has been developed.

W. A. Stewart:

Please indicate the maximum deviation in the surface. Also, please indicate the relationship among deviation permitted, rib spacing, and the antenna frequency.

Starkey:

The maximum deviation was approximately 0.070 inch. This antenna was designed for a frequency of 8.4 GHz. The rib spacing or number of ribs directly affects the surface deviations. The greater the number of ribs, the more precise the resulting surface. This design required 48 ribs to obtain a geometric surface deviation of 0.020 inch root mean square.

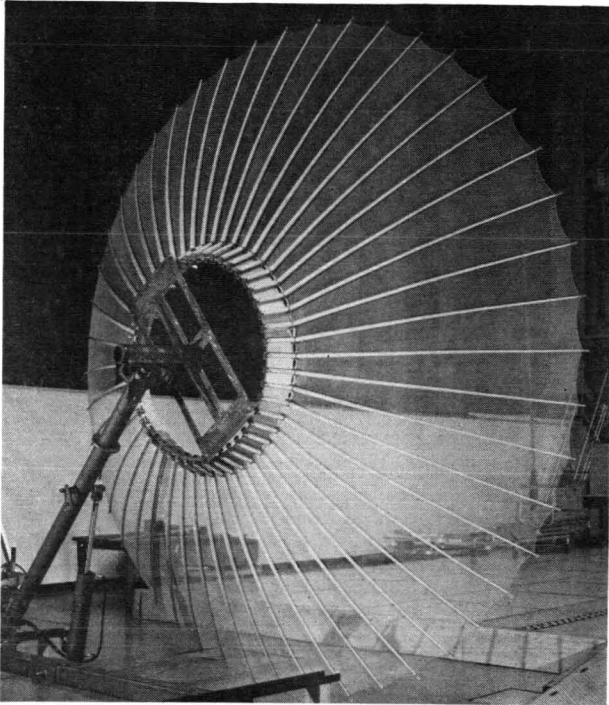


Figure 1. - Antenna reflector.

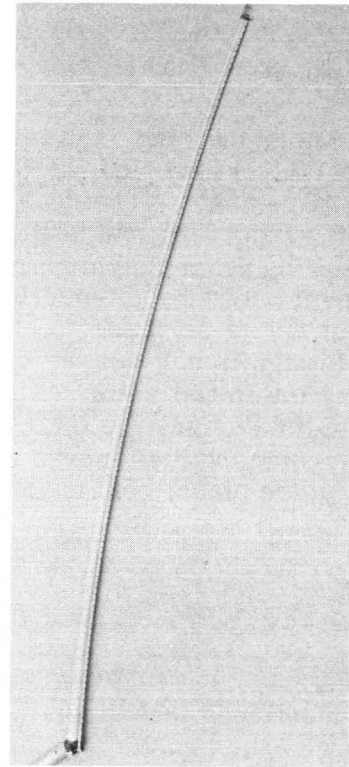


Figure 2. - Antenna rib.

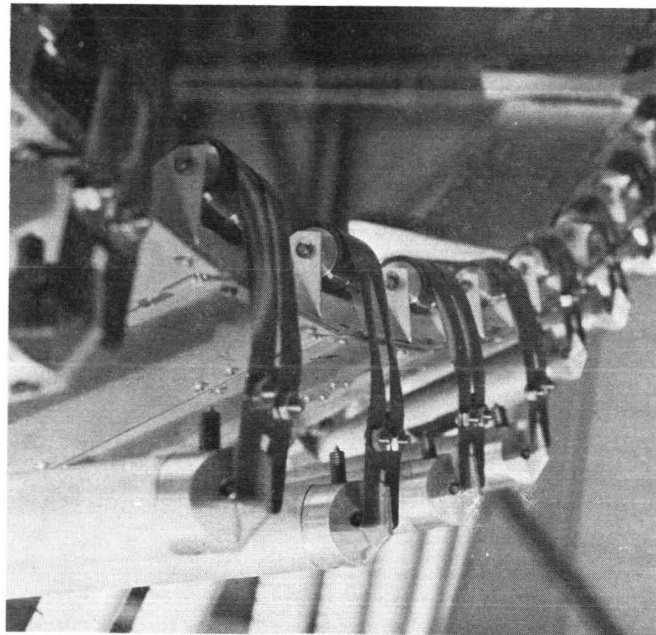


Figure 3. - Deployment mechanism.

## DYNAMIC ANALYSIS OF APOLLO-SALYUT/SOYUZ DOCKING

By John A. Schliesing\*

### ABSTRACT

The use of a docking-system computer program in analyzing the dynamic environment produced by two impacting spacecraft and the attitude control systems is discussed in this report. Performance studies have been conducted to determine the mechanism load and capture sensitivity to parametric changes in the initial impact conditions. As indicated by the studies, capture latching is most sensitive to vehicle angular-alinement errors and is least sensitive to lateral-miss error. As proved by load-sensitivity studies, peak loads acting on the Apollo spacecraft are considerably lower than the Apollo design-limit loads.

### INTRODUCTION

International cooperation in space exploration has resulted in the possibility of an international rendezvous and docking mission (IRDM). The proposed IRDM will be flown by a modified American Apollo command and service module (CSM) and a modified Soviet Soyuz space vehicle. A docking module (DM) will be attached to the CSM to serve as an airlock for crew interchange and as an adapter section for mounting the international docking mechanism (IDM) (fig. 1). The Soyuz space vehicle will be fitted with a geometrically compatible docking mechanism. An important purpose of the IRDM is to validate physically the docking-mechanism design for use on future spacecraft, such as the American space shuttle. To ensure that the IRDM will be performed successfully, a digital-computer simulation of the docking dynamics has been developed. The use of the computer program in supporting the design and development of the docking system is discussed in this report.

The IDM design information used in the studies presented herein was furnished by William K. Creasy, Larry P. Ratcliff, and Thomas O. Ross of the NASA Manned Spacecraft Center.

---

\*NASA Manned Spacecraft Center, Houston, Tex.

## SYMBOLS

$A_c$	effective working area of attenuator piston
$A_o$	area of attenuator orifice (fig. 5)
$c$	coefficient of discharge for attenuator orifice
$E$	energy absorbed by stroking attenuators
$F_a$	resultant axial force of attenuator
$F_{d_i}$	viscous damping force for $i$ th attenuator
$F_f$	attenuator-stroking friction magnitude
$F_s$	attenuator spring load (fig. 4)
$L$	initial lateral misalignment <sup>a</sup>
$V$	initial axial closing velocity <sup>a</sup>
$V_{s_i}$	stroking velocity of $i$ th attenuator
$W$	initial lateral velocity <sup>a</sup>
$\theta$	initial pitch-yaw angular alinement <sup>a</sup>
$\rho$	damping-fluid density
$\phi$	initial roll misalignment <sup>a</sup>
$\Omega$	initial angular velocity <sup>a</sup>

## DESIGN CRITERIA

The design of the docking hardware has been directed toward satisfying performance requirements and geometry constraints. The basic performance requirements of the IDM are to capture-latch the docking vehicles, to attenuate and to limit the relative translational and rotational excursions at the docking interface, to aline the docking

---

<sup>a</sup>Measured relative to the target-body coordinate system.

vehicles, to draw the vehicles together, to connect structurally and to seal the interface, and to undock and to separate the vehicles. The IDM must be capable of satisfactory performance using the following set of docking-interface initial-impact criteria.

1. Axial closing velocity, m/sec            0.05 to 0.3
2. Lateral velocity, m/sec                 $\pm 0.1$
3. Lateral alinement, m                     $\pm 0.3$
4. Pitch-yaw angular alinement, deg       $\pm 7$
5. Roll alinement, deg                     $\pm 7$
6. Angular velocities, deg/sec            1

Geometrically, the IDM must provide an 800-millimeter-diameter (31.49 inch) clear passageway and must fit within the launch shroud of the Salyut spacecraft.

### INTERNATIONAL DOCKING MECHANISM

The IDM is a completely androgynous system, assuming that the mechanism on one of the spacecraft is fully retracted and passive (fig. 2). The active IDM consists of a guide ring, three guides, three capture latches, three body-mounted latches, six attenuators, eight structural ring latches, and a cable-retraction system. During a docking attempt, the active IDM guides intermesh with the passive IDM guides, creating a centering effect. If the impact energy is sufficient, the attenuator geometry of the active IDM will comply, allowing the spring-loaded capture latches of the active IDM to latch the body-mounted latches of the passive IDM. The relative kinetic energy, remaining after capture-latch, is nulled by the six attenuators. The stored energy in the attenuator springs returns the IDM to the initial configuration, facilitating alinement between the docking vehicles. Initiation of the cable-retraction mechanism draws the vehicles together, engaging the structural latches and rigidifying the docking interface.

### COMPUTER SIMULATION

To ensure that the IDM is capable of performing the tasks satisfactorily, an all-digital three-dimensional simulation of the IDM dynamics has been developed. Referred to as the ring-finger docking-dynamics program (RFDD), the computer program simulates the dynamic environments produced by the interaction of the guide-ring docking systems during collision, by the use of the automatic attitude control systems, and by the use of astronaut translational-control inputs.

Simulated forces produced by the interaction of the docking system are classified as guide-ring-interaction forces, capture-latching forces, and attenuator forces. In the simulation, the guides and guide ring are considered to be linear elastic members.

During a docking attempt, the guide edges of the active and passive IDM interfere geometrically. At each interference point, the interference distance is determined, enabling the computation of the elastic loads. The interaction load is assumed to be normal to the contact edges. The active IDM guides can contact and force the passive IDM guides and guide ring; the passive IDM guides can do likewise. Relative motion between the DM interface and the active guide ring causes the attenuators to stroke.

The attenuators attach to the DM and guide ring (fig. 3). The force in an attenuator is simulated in the RFDD as a function of the instantaneous stroke and velocity. The force is divided into three components: spring force ( $F_s$ ), damping force ( $F_{d_i}$ ), and seal friction force ( $F_f$ ).

$$F_a = F_{d_i} + F_s + F_f \left( \frac{V_{s_i}}{|V_{s_i}|} \right) \quad (1)$$

A typical spring force-stroke function is illustrated in figure 4. The curve represents a preload of 44.5 newtons (10 pounds), a pneumatic spring in compression, and a non-linear equivalent structural spring in tension. The damping force  $F_{d_i}$  is given as

$$F_{d_i} = \frac{\rho A_c^3}{2} \left( \frac{V_{s_i}}{c A_o} \right)^2 \quad (2)$$

where  $\rho$ ,  $A_c$ ,  $V_{s_i}$ ,  $A_o$ , and  $c$  are fluid density, attenuator-piston-cylinder area, attenuator velocity, orifice area, and coefficient of discharge. The orifice area is given as a function of attenuator stroke (fig. 5). It is assumed that the seal friction force is constant and that it opposes the stroking motion. In addition to orifice damping, the attenuators contain a pressure regulator to limit maximum dynamic loads in regions of extremely small orifice area.

The capture latches are simulated in the RFDD as elastic restraints at the geometric-latch locations shown in figure 3. Once the capture latch engages the body-mounted latch, a latch restraint is enforced during an attempted docking. The capture latches develop tension loads normal to the plane of the interface.

#### CAPTURE-LATCHING DYNAMICS OF THE INTERNATIONAL DOCKING MECHANISM

The compliance motion necessary to capture-latch the IDM can be visualized as four simultaneous motions consisting of relative translation parallel to the interface

that centers the docking systems, relative roll indexing of the two systems, axial translation toward capture latch, and relative pitch-yaw rotation that aligns the interfaces. Generally, the vehicle dynamics resulting from the impact forces result in the first three types of interface motion. The vehicle-interface motions reduce the amount of IDM attenuator compliance and lower the amount of resulting attenuator energy absorption; however, the resulting relative pitch-yaw rotational motion of the docking vehicles usually is divergent from the desired rotational motion of aligning the docking interfaces. The undesirable rotational motion and the initial pitch-yaw rotational error must be compensated for by stroking of the supporting attenuators. This stroking absorbs a significant amount of the kinetic energy needed for capture-latching.

## IDEALIZED CASE

The following idealized case illustrates the attenuator-design problem of accommodating the required compliance with little energy absorption or storage. The IRDM vehicles contact at a minimum closing velocity (0.05 m/sec) and maximum pitch-yaw interface angular misalignment ( $7^\circ$ ). For this case, the available kinetic energy is 11.1 joules. Assuming that one pair of attenuators actively comply to accommodate the misalignment, the average force  $F_a$  in the attenuators must not exceed 52 newtons (12 pounds), or the 11.1 joules of relative kinetic energy will be absorbed before the IDM rings are in position to capture-latch. The attenuator preload must be at least twice as large as the seal friction to overcome the seal breakout force and to align the vehicles after capture-latch. Even if the damping force is neglected and it is assumed that the attenuators resist compliance with a constant force equal to the preload and seal friction, the resulting bounding values for the preload and seal friction are extremely small: 34.6 newtons (8 pounds) and 17.3 newtons (4 pounds).

## RESULTS

### Attenuator Optimization

Analytical capture-performance studies of the IDM, in which the varying nature of  $F_a$  is taken into account, were conducted with parametric variation in the components of  $F_a$ . As indicated by the studies, an improvement in capture performance can be achieved if the seal-friction and spring preload are lowered from the initial design estimates. As a result, the seal friction and attenuator-spring preload requirements were reduced to 22.25 newtons (5 pounds) and 44.5 newtons (10 pounds). Although still in excess of the 52-newton (12 pound) minimum requirement cited for the earlier sample, the total of these values was considered to be as low as is practical. Alternate attenuator designs to reduce the axial stiffness have been rejected because of complexity and corresponding reliability problems. Within practical design constraints, the design of the IDM has evolved in order to optimize the overall capture performance.

## Capture-Latching Sensitivity Studies

Digital-computer simulations of the IRDM have been conducted to determine capture-latching sensitivity to parametric changes of the initial contact conditions. The results of the study are presented in figures 6 to 8. In the study, capture-latching capability was investigated as a function of parametric variations in axial closing velocity and state-position-error parameters. Reduction in axial closing velocity reduces capture-latching capability because the relative kinetic energy required for compliance of the active IDM is reduced as a function of the square of the axial closing velocity. Also, increases in state-position error reduce capture capability because the active IDM must comply more to achieve capture latching.

Axial velocity  $V$  and miss distance  $L$  were varied parametrically; the remaining state parameters  $W$ ,  $\theta$ ,  $\Omega$ , and  $\phi$  initially were set equal to zero (fig. 6). As indicated by the results, the capture-latching performance of the IDM is insensitive to miss distance within the range of allowable axial velocity. Little relative kinetic energy is dissipated by the attenuators because the vehicle motion following impact aligns the interface. In the IRDM, the moment arm to the center of mass of each vehicle is large, permitting small lateral forces at the docking interface to rotate the vehicles into alinement.

Axial velocity  $V$  and roll misalignment  $\phi$  were varied parametrically; the remaining state parameters,  $W$ ,  $\theta$ ,  $\Omega$ , and  $L$  initially were set equal to zero (fig. 7). As demonstrated by the results, the IDM is sensitive to relative roll misalignments when the axial velocity  $V$  is small. Two factors influence the sensitivity: the attitude control system and the small rotational-moment arm about the centerline of the vehicle. The CSM attitude control system maintains the initial relative-roll error, forcing the IDM to rotate and to stroke the attenuators. In addition, the small rotational-moment arm about the centerline of the vehicle decreases the amount of natural relative-roll motion induced by impact. This decrease forces the IDM to comply in roll by stroking the attenuators.

Axial velocity  $V$  and relative pitch-yaw rotational error  $\theta$  were varied parametrically; the remaining state parameters  $W$ ,  $\Omega$ ,  $\phi$ , and  $L$  initially were set equal to zero (fig. 8). As indicated by the results, the capture-latching performance of the IDM is sensitive to  $\theta$  when the axial velocity is small. These results are in agreement with the previous discussion on attenuator-compliance requirements for pitch-yaw misalignments.

Addition of state-velocity error, radial-velocity state parameter  $W$ , and angular-rate state parameter  $\Omega$  will reduce the given IDM capture performance because the attenuator system must attenuate the relative motion induced at the interface by these parameters.

## CONCLUDING REMARKS

The early development of a digital-computer simulation of the IDM has been a valuable tool in the design of the IDM. Use of the program to study the sensitivity of

impact loads and capture performance to variations in design parameters has resulted in a simple reliable design that has known performance characteristics. As demonstrated by the performance studies, the IDM capture capability is most sensitive to vehicle angular-alinement errors when the axial closing velocity is near the minimum criteria value and is least sensitive to lateral-miss error for all values of axial closing velocity.

## DISCUSSION

J. W. James:

Because this docking-mechanism configuration can be installed identically on any spacecraft, is it generally believed that this may be the last new docking mechanism to be designed?

Schliesing:

A primary purpose of the Apollo/Soyuz Test Project is to validate the design concept for possible use on advanced missions. This, of course, leaves open the possibility of using other docking mechanism configurations. In addition, the NASA is studying the feasibility of using manipulator systems to dock and to handle cargo.

J. E. Price:

Complexity is often a product of overly optimistic and an overabundance of design requirements. In establishing the requirements for the docking mechanism, how have you limited the number of basic functions to something that is manageable.

Schliesing:

The requirements presented for the docking mechanism were limited to only those that are related to dynamic analysis, namely performance and impact criteria. The overall design requirements are much more numerous.

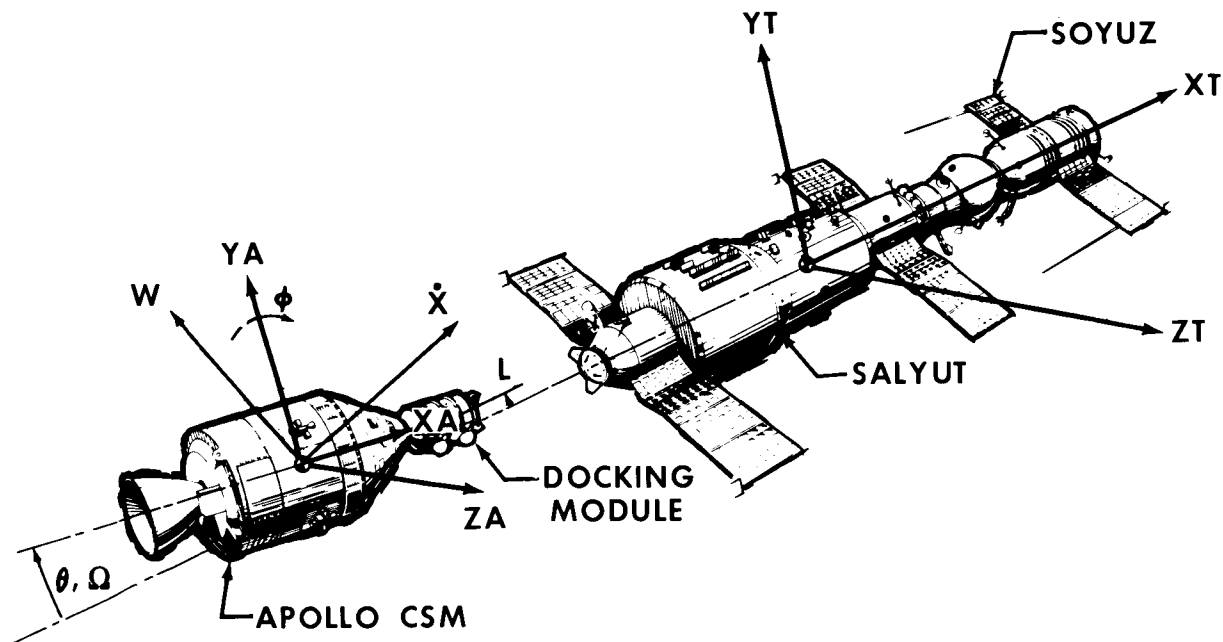


Figure 1. - Apollo-Salyut rendezvous and docking test mission.

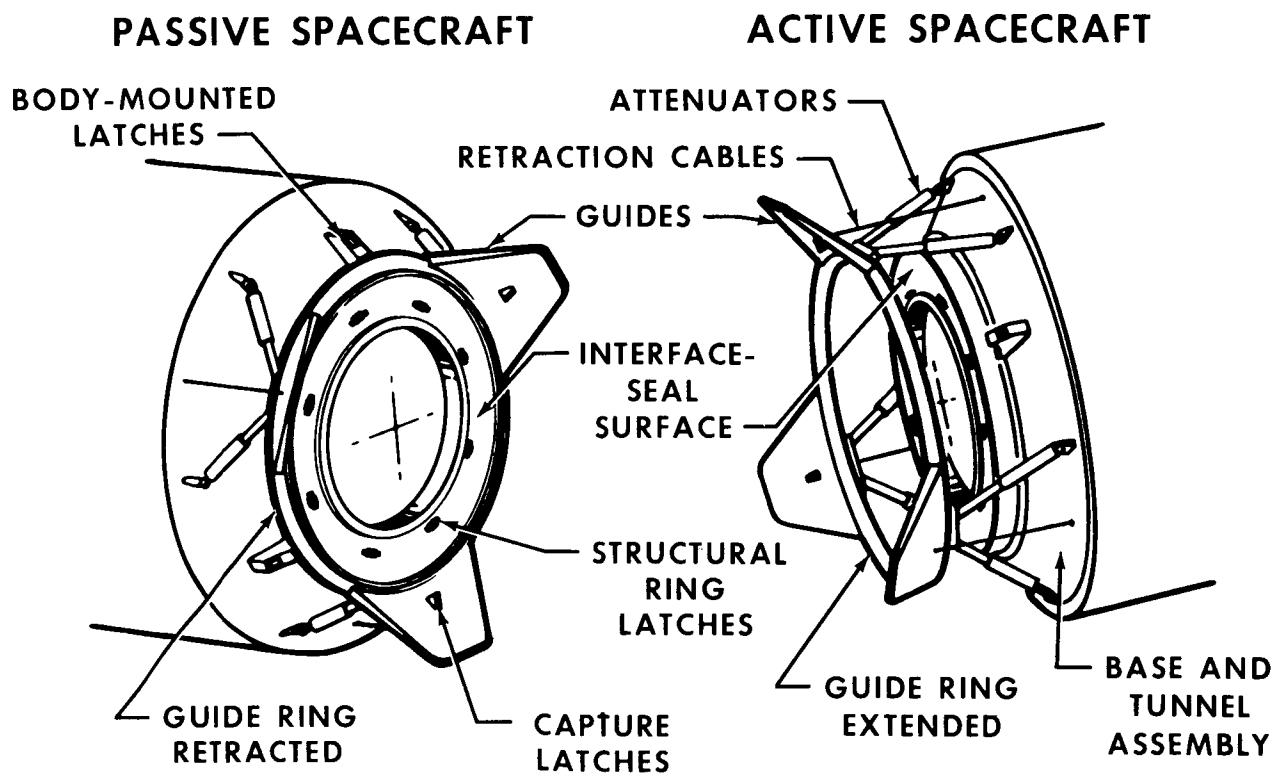


Figure 2. - International docking mechanism.

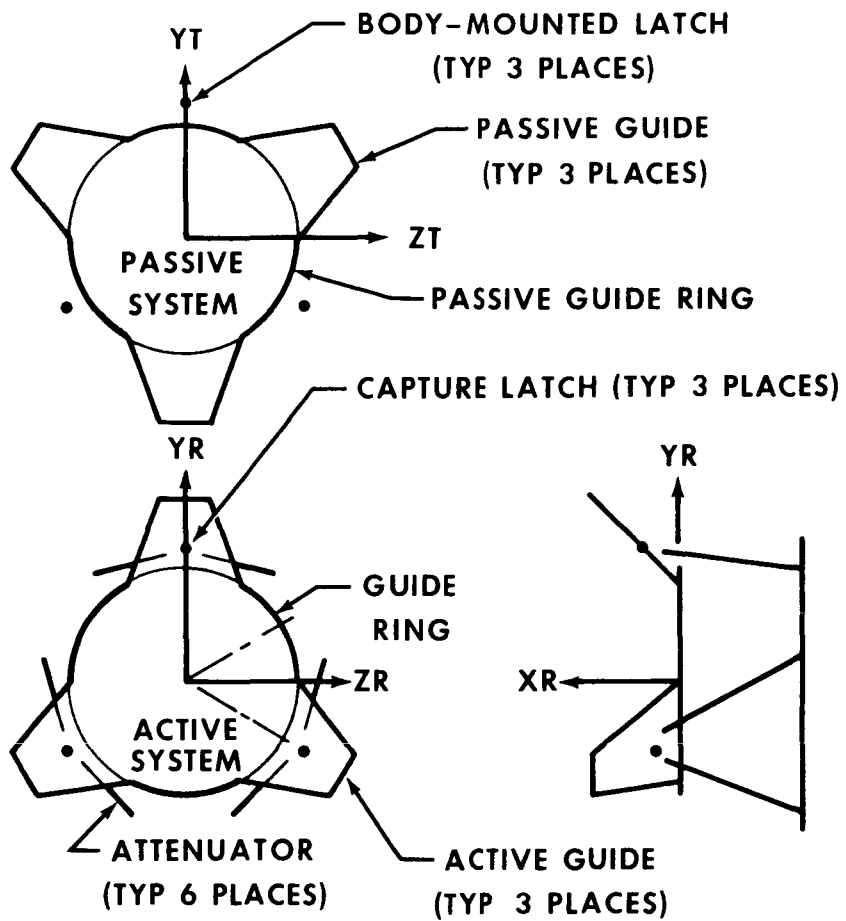


Figure 3. - Schematic of international docking mechanism.

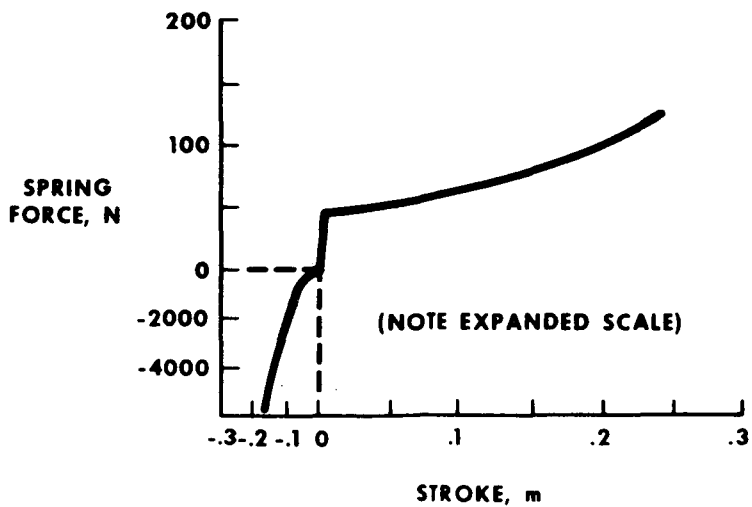


Figure 4. - Attenuator spring force.

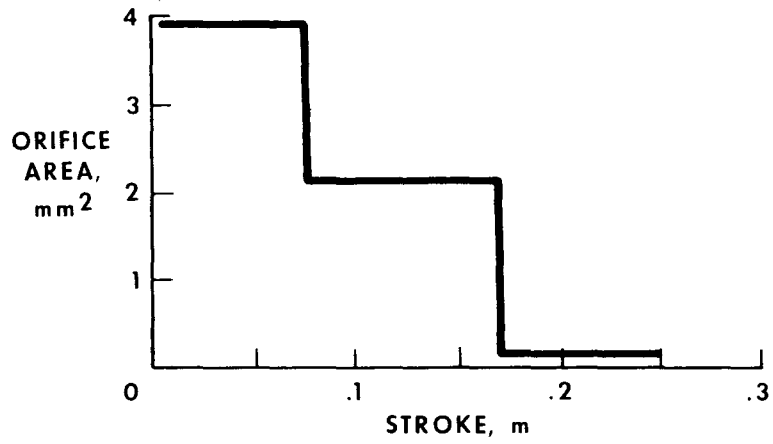
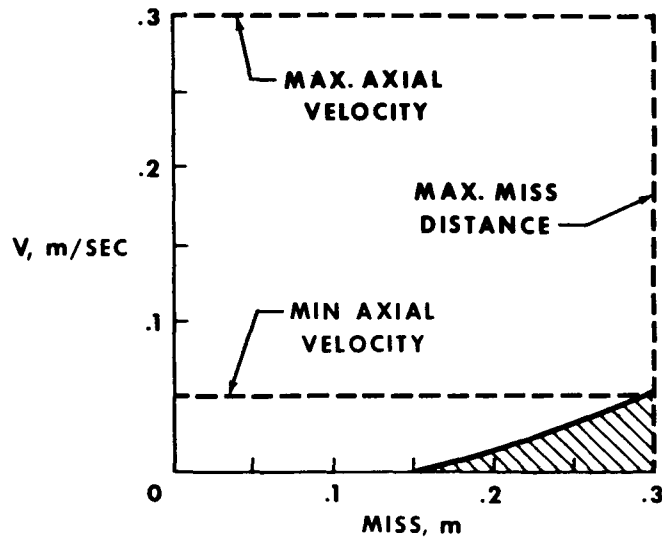
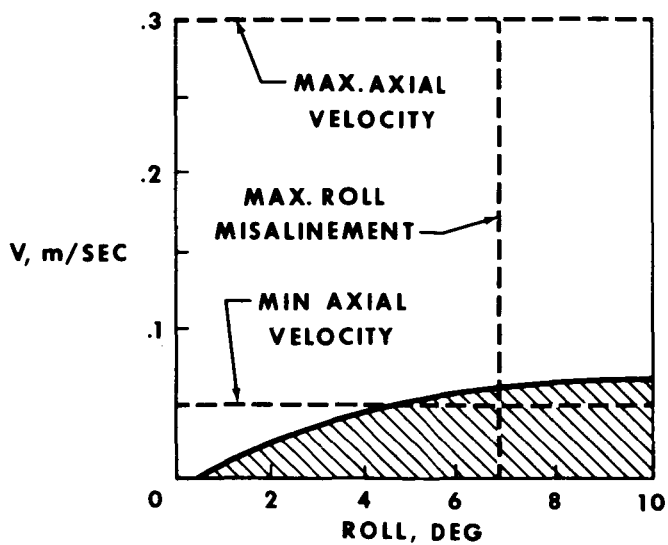


Figure 5. - Attenuator orifice area.



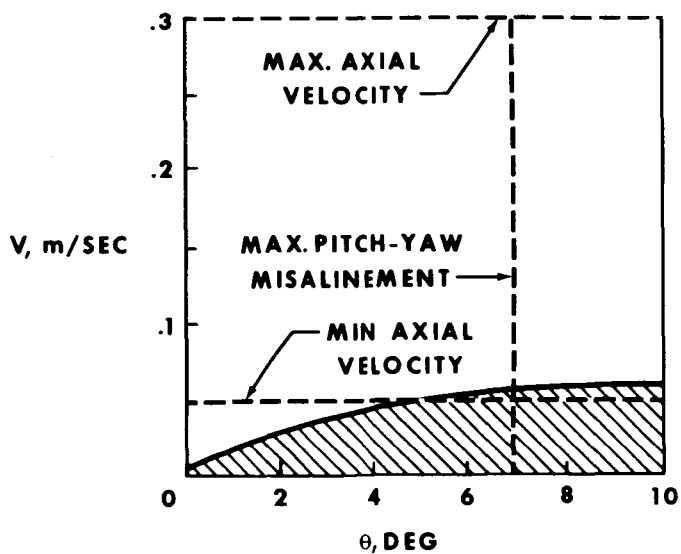
 LOW CAPTURE LATCHING PROBABILITY AREA

Figure 6. - Axial velocity compared to miss distance.



 LOW CAPTURE LATCHING PROBABILITY AREA

Figure 7. - Axial velocity compared to roll misalignment.



 LOW CAPTURE LATCHING PROBABILITY AREA

Figure 8. - Axial velocity compared to pitch-yaw misalignment.

**Page intentionally left blank**

73N18872

## MECHANICAL COMPONENT SCREENING FOR SCANNER

By J. L. Olson\* and W. J. Quinn\*

### ABSTRACT

The critical mechanical components of the scan mirror mechanism are described and their evaluation and screening procedures are discussed. A bumper/damper unit is used in the design to reverse motion of the mirror and effect scan and retrace cycles. A wear evaluation was conducted on the bumper impact surfaces that established nylon 6-10 as an acceptable material. The elastomeric dampers were subjected to thermal vacuum tests for condensables and outgassing as well as parametric life tests. The flexure pivots that support the mirror were tested to establish a curve of stress plotted as a function of cycles to failure for rotational operation. The pivots met the life requirement of 150 000 000 cycles at a  $\pm 2.9^\circ$  amplitude during fatigue testing. Screening procedures have been established for dampers and flexure pivots to obtain flight quality components.

### INTRODUCTION

As the Earth Resources Technology Satellite travels along its polar orbit, a multispectral scanner (MSS) mirror mechanism scans a nominally symmetrical east-west swath reflecting an image of the earth surface into the scanner optical system. The image format is 185.2 by 185.2 kilometers (100 by 100 n. mi.) from the 926-kilometer (500 n. mi.) circular orbit. The assembly consists of the mirror and the devices that impart necessary rotation. The components that are subject to wear and fatigue are the flexure-pivot suspension and bumper/damper units that reverse the rotation at the limits of travel. The wear characteristics of the bumper pads and the fatigue characteristics of the dampers and flexure pivots were determined. Because redundancy cannot be used, screening procedures were established to identify potential early-life failures for the dampers and flexure pivots.

This report presents the results of one phase of research conducted at Hughes Aircraft Company under contract number NAS 5-11255, from NASA Goddard Space Flight Center.

---

\*Hughes Aircraft Company, Culver City, Calif.

## SCAN MECHANISM DESCRIPTION

The relative position of the components that were evaluated in the MSS scan mirror assembly are shown in figure 1. The scan mirror mechanism includes the following components.

1. A nickel-plated beryllium mirror with reinforcing ribs
2. Two flexure pivots, which suspend the mirror and allow the mirror to rotate about the pivot axes
3. An aluminum support structure to which the mirror, the pivots, and the rest of the components are attached
4. An electromagnetic drive assembly with the coil mounted on the supporting structure and an armature mounted on the mirror
5. An electronic driver that energizes the coil over an appropriate portion of the retrace cycle
6. An optical switch that turns off the coil when the mirror reaches the center of the retrace cycle
7. Two bumper/damper units that act at each end of the scan interval to change the direction of rotation of the mirror and dissipate the energy of the impacts. Each unit (fig. 2) consists of a bumper cup with nylon impact surfaces, a spring suspended bumper, and two dampers. Two units are used so that the forces acting on the mirror produce a couple that will turn the mirror around with only a slight force on the flexure pivots. This feature minimizes rotation of the mirror about an axis perpendicular to the pivot axes (cross-scan jitter).

## BUMPER MATERIAL

The four candidate materials chosen were linen-phenolic, per federal specification L-P-509 (Type 2, Grade L); low-moisture nylon, per L-P-410 (Composition 6-10); Teflon-filled polycarbonate (Lexan); and polyurethane from two suppliers. In the MSS application, the most important characteristics the material must have are good wear and impact resistance, suitability for adhesive bonding, and suitability for use in the space environment.

Nylon was selected as the bumper material. The bumper pads are bonded in place using an epoxy-polyamide film adhesive that has a shear strength of  $27.58 \times 10^6 \text{ N/m}^2$  (4000 psi) and provides control of bond line thickness.

There were two test conditions used during the bumper-wear tests on a prototype bumper assembly configuration. The first condition was an impact velocity of 38.10 cm/sec (15 in/sec), which is comparable to that developed in the scan mirror mechanism. This is accomplished by introducing a 0.10-millimeter (0.004 inch) gap between the bumper and each of the impact surfaces on the bumper cup and by driving

the cup at a rate of 90 hertz. The second condition was an impact force in the shape of a half sinewave with a peak amplitude that was 20 percent greater than the force developed in the flight hardware. This is achieved by driving the cup 0.69 millimeter ( $\pm 0.027$  inch, which includes the 0.004-inch gap) so that the bumper deflection that compresses the bumper spring and displaces the dampers is 0.58 millimeter ( $\pm 0.023$  inch).

The greater impact forces that were applied provide a conservative estimate of the wear rate that can be expected in the application. The technique that was used for measuring the amount of wear was to scribe a grid pattern on the nylon pads with the depth of the scribe mark being approximately 0.038 millimeter (0.0015 inch). A baseline measurement of the surface using a Talysurf machine was made before the initiation of the test. Subsequent measurements traversing the same paths were made at regular intervals for comparison to the baseline. The amount of wear was calculated by the change in the depth of the scribe lines. The test results for the nylon material are presented in figure 3, which shows the Talysurf traces of the surface contour at the beginning of the test (baseline) and after 142 000 000 cycles. Comparison of the traces show that the amount of the surface wear was less than  $5.08 \times 10^{-3}$  millimeters (0.2 mils, which is substantially less than the allowable wear of  $50.8 \times 10^{-3}$  millimeters (2 mils)). In addition to determining the material wear characteristics, this test program showed the integrity of the bond between the nylon and the aluminum bumper cup.

## DAMPERS

### Requirements

Two elastomeric dampers operate with a precompressed spring on each side of the scanning mechanism as shown in figure 2. These dampers dissipate energy by shear distortion. The dampers must displace approximately 0.48 millimeter ( $\pm 0.019$  inch) during each cycle of the required life. The design goal for a pair of dampers originally was established at 0.350 N-sec/cm (0.20 lb-sec/in.) at an excitation frequency of 125 hertz. This frequency corresponds to the nominal 4-millisecond turnaround time on the scanner mechanism. Two types of damper designs finally were considered. The device that was developed by the contractor was a simple rectangular configuration using a silicone elastomeric material. The device from a commercial producer was cylindrical in shape and also used a silicone elastomer. The ultimate selection of the dampers required for the scanner mechanism was based on the results of thermal vacuum and cycling tests.

### Evaluation Tests

Checks were made during the thermal vacuum test for condensable materials after 4 days at the real-time temperature and in a vacuum environment of  $1.33 \times 10^{-4}$  N/m<sup>2</sup> ( $10^{-6}$  torr). For a silicone damper to pass this test, a postcure at elevated temperature was required. From the results of tests on the Surveyor, it had been determined that silicone elastomers postcured at 449.80° K (350° F) showed the least change from the initial physical properties while still reducing the outgassing to an acceptable level. Tests were made on dampers as they were received and on dampers that had been

subjected to postcures at sea level. The dampers that were designed by the contractor were found to require 10 days at 449.80° K (350° F) while the vendor parts required 5 days at 449.80° K (350° F). After these bakeouts, both the parts designed by the contractor and the vendor parts had less than a 0.1-percent weight loss during the 4 days and had no oily deposits or condensables that could be found during the test.

Life tests were performed on dampers of both designs. An apparatus was designed that would simultaneously test six pairs of dampers. The life test was conducted with a cyclic shear displacement amplitude of 0.58 millimeter ( $\pm 0.023$  inch). This displacement is approximately 20 percent greater than actually produced during impact in the scan mirror mechanism. Three pairs of commercial dampers and three pairs of the dampers designed by the contractor were tested in the condition in which they were received, and two additional pairs of both designs were tested after an elevated temperature postcure. Dampers were test cycled under the conditions of no prestress, a 0.76-millimeter (0.030 inch) compression prestress, and a 1.17-millimeter (0.046 inch) shear offset prestress. These mounting variations were evaluated to determine the effect they would have on the damper fatigue life. No fatigue failures occurred and the damping changes were comparable; therefore, no prestress was used in the system. The postcured dampers were harder and had higher damping constants. At equal displacements, the postcured dampers are receiving a higher stress under the test conditions than the dampers in the condition in which they were received. The actual values of the damping constant compared to the number of test cycles for two pairs of dampers from the commercial source that were postcured are shown in figure 4. The dampers maintained a constant damping value within 5 percent. As a result of the vacuum tests and life testing, the dampers of the cylindrical design were selected for use on the flight system.

### Screening Criteria

Specifications were generated to provide the necessary controls and screening procedures. The manufacturer is required to produce parts from one controlled lot of materials. After receipt, the dampers are subjected to a postcure at 489.80° K (350° F). As a lot-acceptance test, 10 percent of the lot are tested for condensables and outgassing. Each device that is used in the system has the damping characteristics measured on a pair basis.

## FLEXURE PIVOTS

### Description

Two flexure pivots provide the suspension points for the scan mirror. These pivots must withstand the launch environment and subsequently operate at  $\pm 2.9^\circ$  rotation for 150 000 000 cycles. The flexure pivots are commercially available devices. They are  $90^\circ$  symmetrical two-strip pivots, in which one of the strips has been divided for increased lateral rigidity. The stationary portion of the pivot is brazed to one cylindrical barrel, while the rotating portion of the pivot is brazed to the other cylindrical barrel. The flexing elements bend to allow rotation of one barrel with respect to the other. The flexure elements are stamped from close tolerance, cold-rolled spring stock of type 420 stainless steel. Flexure pivots do not have a fixed center of rotation.

The amount of the change of center of rotation during rotational displacement of one sleeve with respect to the other is termed centershift. The flexure pivots being used are 15.9 millimeters (5/8 inch) in diameter and of the  $\pm 15^\circ$  design. The flexing strips are 0.34 millimeter (0.0135 inch) thick.

### Vibration Tests

The two important tests that these parts must pass before being included in any flight system are vibration and cycling life testing. The pivots used on MSS have passed successfully tests that simulate the launch environment. Vibration tests were conducted on an early engineering model and later on the systems with the final design. The early vibration testing is critical with a flexure-mounted system, as launch excitations close to the natural frequency of the pivot/mirror system can result in extremely high gravity loads. There is negligible inherent damping in flexural pivots, and this results in high transmissibilities of input vibration levels. The mechanism was designed originally with 12.7-millimeter (1/2 inch) diameter pivots, and had to be redesigned to accept stiffer 15.9-millimeter (5/8 inch) diameter pivots in order to pass this test.

### Life Tests

To demonstrate compliance with the system cycling life requirements, it was necessary to determine the fatigue-life characteristics of the flexure pivots. A test program to produce a curve of stress as a function of cycles to failure for the parts was performed (fig. 5). The equivalent angle is included on the right of the figure for the  $\pm 15^\circ$  pivot design, and also the MSS operation required is noted.

The expression used to calculate the stress for pure rotation is

$$S = \frac{Et}{2L} \Theta$$

where  $S$  = stress,  $E$  = material modulus of elasticity ( $1.99 \times 10^{11}$  N/m<sup>2</sup> ( $29 \times 10^6$  psi) for 420 CRES),  $t$  = flexure thickness,  $\Theta$  = angle through which the pivot is rotated (in radians), and  $L$  = effective flexure length.

The test grouping is typical of fatigue testing. Some scatter in results is expected because of the inhomogeneous nature of metals and the tolerances in manufacturing the parts. These particular pivots closely follow the life curve that is predicted by the manufacturer data. Also, previous life tests of different size pivots (ref. 1) indicate that the MSS design requirements are below the endurance limit of the pivot material.

### Screening Requirements

In addition to meeting life and environmental requirements, the pivots must meet critical parameters regarding mirror support. Two pivots from each manufacturer lot are subjected to destructive static-load test and to a metallurgical examination. Each

pivot is visually examined with both a conventional microscope and a small diameter borescope for surface defects. Pivots are examined for evidence of burrs, nicks, or scratches that might reduce the strength or life of the part. Each pivot is subjected to a dye-penetrant inspection for evidence of surface and subsurface cracks. All flight pivots are subjected to a radial load of 978.56 newtons (220 pounds) to test for defective braze joints.

To ensure minimum stress and satisfactory mirror alinement under scan conditions, each pivot is tested for center-shift and torsional spring rate at  $\pm 3^\circ$  rotation. Then, pivots are paired so that they have closely matched torsional spring rates, and, when rotated, the center shifts are the same magnitude and in the same direction. Matched pairs of pivots that passed all visual and physical tests were used in the flight units.

### CONCLUDING REMARKS

To achieve state-of-the-art performance of a complex instrument, consideration of each detailed element is required. This must be followed by evaluation and screening of the critical ones before final selection and use. The identification and removal of potential early-life failures is an important factor in meeting overall system performance requirements. The qualification and screening of critical materials and mechanical devices such as dampers and flexure pivots is particularly important in applications such as the multispectral scanner, because redundancy cannot be used as readily for mechanical devices as it is for electronics.

### REFERENCE

1. Olson, J. L. ; The Evaluation of Flexural Pivots to Meet Critical Performance and Life Requirements. Rep. 70-DE-76, ASME, May, 1970.

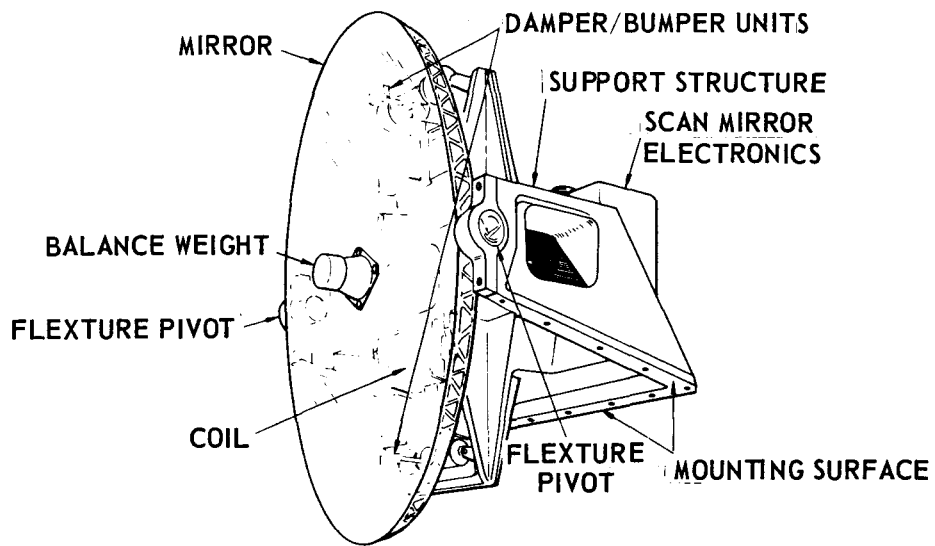


Figure 1. - Scan mirror mechanism.

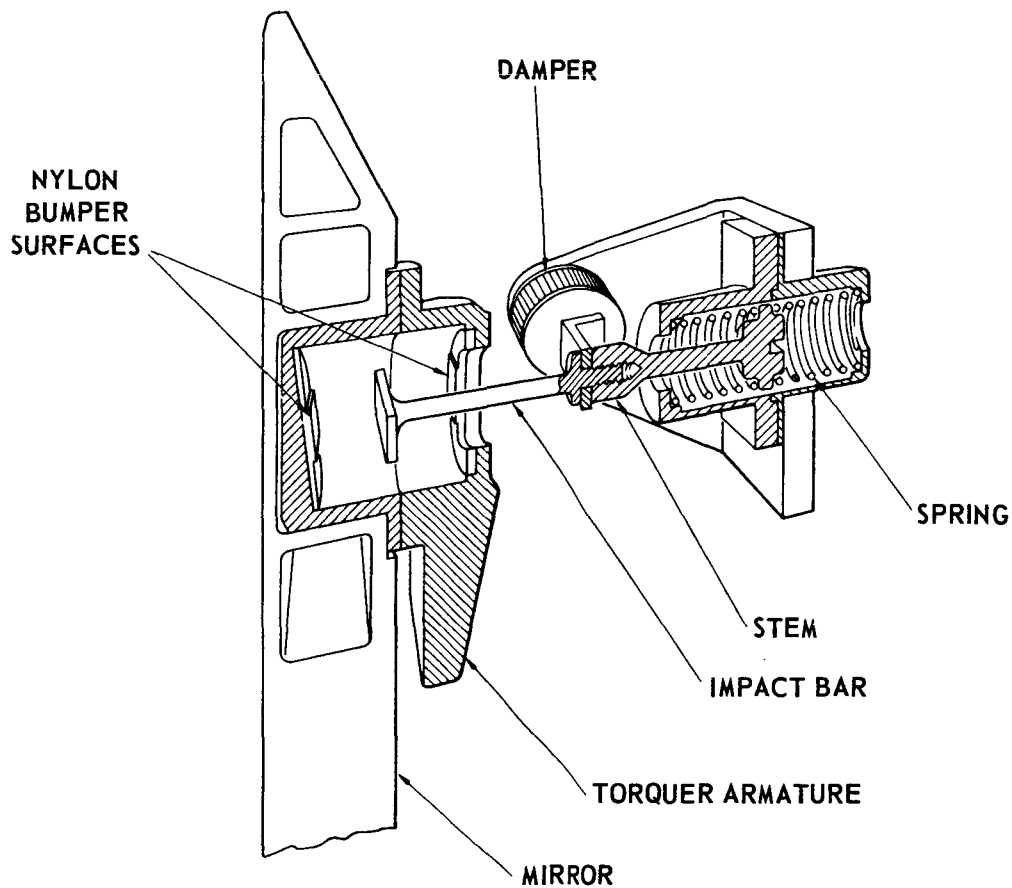
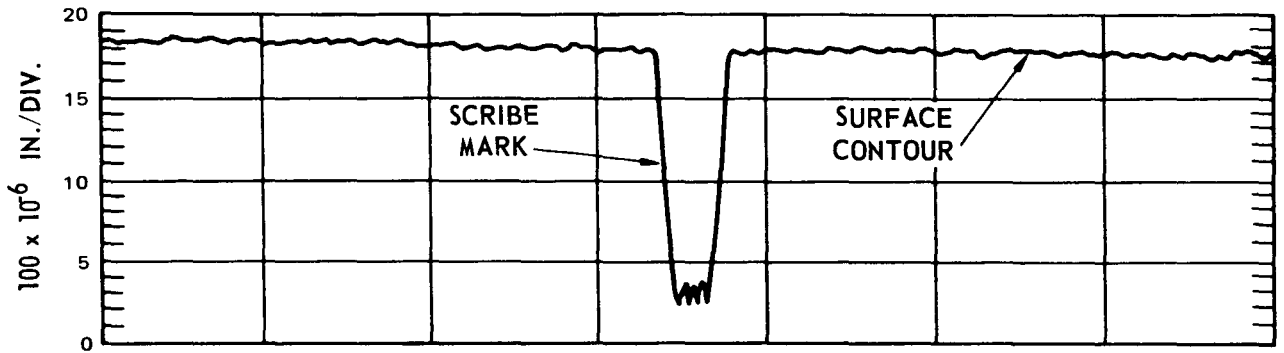
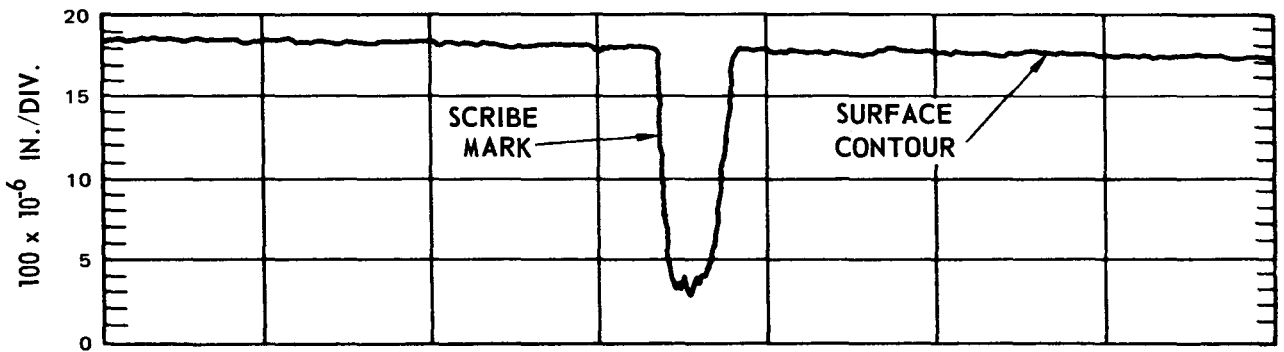


Figure 2. - Bumper/damper unit.

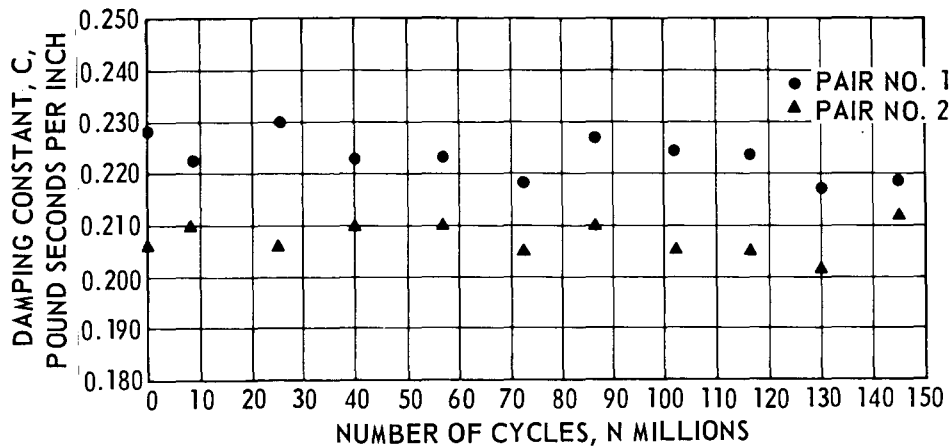


(a) Baseline.



(b) After 142 000 000.

Figure 3. - Bumper surface wear.



NOTE: DAMPING TEST FREQUENCY = 144

Figure 4. - Damping as a function of life.

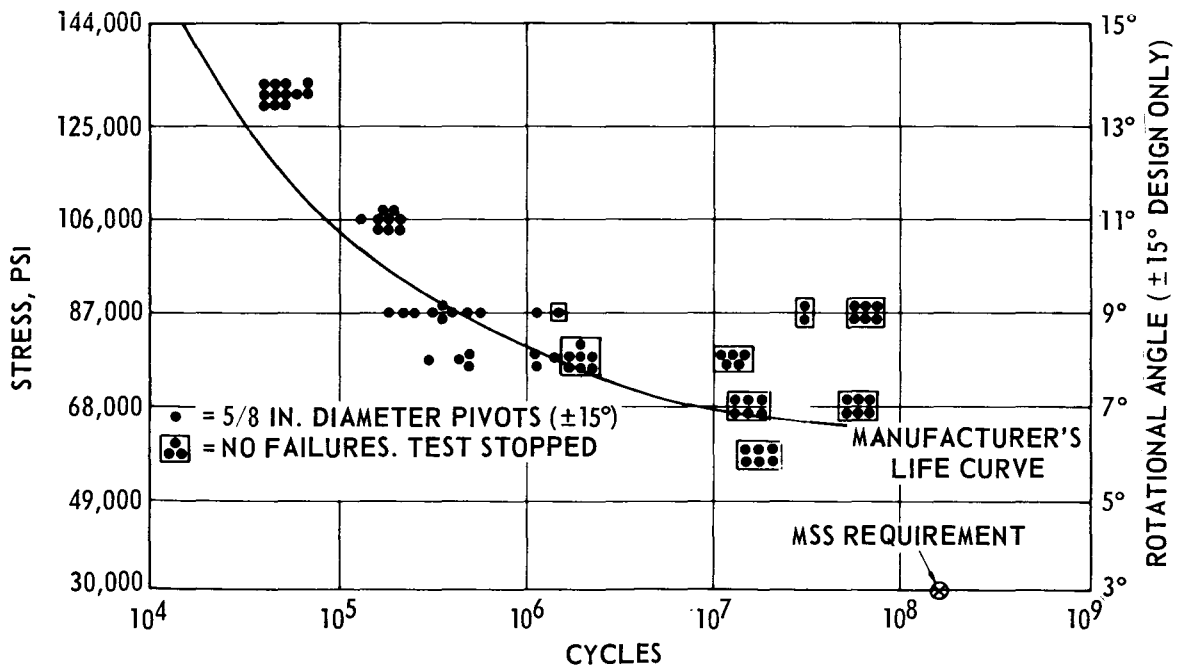


Figure 5. - Flexure pivot fatigue test results.

**Page intentionally left blank**

## RADIATIVE COOLER FOR SPACECRAFT

By John E. McCullough\*

### ABSTRACT

The design, construction, and testing of a passive radiative cooler that provides solutions to the design problems of withstanding mechanical stress, achieving the required thermal isolation, and maintaining optical alinement, cleanliness, and integration with the spacecraft are described in this report.

### INTRODUCTION

The passive radiative cooler provides a simple, reliable means of maintaining a detector in a satellite-borne optical system at its required cryogenic operating temperature. This device is able to cool a low-power-dissipation optical detector to temperatures of approximately  $100^{\circ}$  K by virtue of its ability to radiate more thermal energy to deep space than it receives from other parts of the spacecraft, the sun, and the earth.

For maximum thermal isolation, mechanical connections between the radiator and the spacecraft must be minimized. This is normally achieved by the use of guy-wire supports or nonmetallic structural elements with a large length-to-cross section ratio. However, these traditional types of supports for cryogenic components are not appropriate for supporting radiative coolers because they cannot withstand the dynamic environment of launch and they cannot provide the precise alinement of the detector relative to associated optical components. Additionally, nonmetallic materials are sources of optical-system contaminants like water vapor or volatiles that evolve under space-vacuum conditions.

### DESIGN CRITERIA

The complete design specification for a passive radiative cooler suitable for spacecraft use must include the following requirements as a minimum.

1. Mechanical requirements
  - a. Survive launch and orbit-insertion mechanical environment
  - b. Maintain optical alinement of cooled elements and orientation with respect to the remainder of the optical system
  - c. Use dimensionally stable materials

---

\*Arthur D. Little, Inc., Cambridge, Mass.

- d. Operate reliably
- e. Have minimum weight
- 2. Thermal requirements
  - a. Be able to reach required temperature levels while viewing deep space
  - b. Reject heat inputs from the spacecraft (both radiative and conductive) as well as radiant thermal inputs from planetary and solar sources
- 3. Optical requirements
  - a. Maintain optical element spacing and alinement at operating temperatures
  - b. Position optical elements to allow focus adjustment and secure locking in final position
  - c. Maintain cleanliness of optical elements before and after orbit insertion
  - d. Duplicate the properties of an optical-quality mirror with the radiative-energy reflecting surfaces
- 4. Vacuum and cryogenic requirements
  - a. Use construction materials suitable for space environments
  - b. Consider the material properties at cryogenic temperatures
  - c. Use thermal-insulation techniques that are equivalent to multiple-reflective-layer insulation systems

## DESIGN

The design philosophy of the cooler described in this report is that a surface thermally isolated from its mounting will radiate thermal energy to deep space, eventually reaching cryogenic temperature levels. However, to reach these temperatures, the surface must be shaded from sunlight and be oriented such that it cannot "see" portions of the spacecraft or earth that act as sources of energy radiated back to the cooling element.

The basic right conical configuration and size of the cooler discussed in this report were derived using thermal-analysis techniques from basic requirements of operating temperature, bias-power heat load, location on the spacecraft, spacecraft configuration, and orbit parameters. The mechanical design of the cooler started with the subsequent shape and size requirements so generated as well as limits on the allowable heat leak or flow of thermal energy between the mounting surface and the cooling element. The design presented in this report results from consideration of all of the design criteria.

## Support Element

From previous experience in the design of cryogenic equipment, it was known that the design of the support elements was the most critical aspect of the whole cooler design problem. The support elements must be rugged enough to survive extreme mechanical environments yet have very low thermal conductance. Additionally, they must maintain precise alignment of the cooler stages, such that a detector mounted on the innermost element of the cooler would maintain accurate alignment with respect to the associated optical system attached to the cooler's outermost element. Three supports are used to locate each stage. The supports are located in the plane of the supported component center of gravity to eliminate eccentric dynamic loading. All major components of the cooler were designed as bodies of revolution because this shape was most convenient for the reflective interior of the outer stage and also because this configuration is easily manufactured by standard fabrication equipment, has high stiffness per unit weight, and can be readily analyzed to determine deflection under load and natural frequency modes.

## Radiative Cooler

The radiative cooler (fig. 1) consists of three major components: an outer stage, an inner stage, and a mounting ring. The outer stage is a truncated cone, the large end of which is open and flanged around the rim. The inner stage, which is mounted inside the small end of the outer stage, consists of a structural disk and a cover plate that is bolted to it. The mounting ring surrounds the outer stage and provides a means for mounting the radiator to the associated optical system. The inner stage is supported within the outer stage at three equally spaced points around the perimeter, with its center of gravity in the plane of the support elements. The latter unique design provides strong mechanical support at room temperature, so that the cooler will withstand the shock and vibration of launch, and high thermal resistance in the space environment. The outer stage is positioned within the mounting ring by three similar support elements in the plane of its center of gravity.

## Optical Design

The optical detector is attached to the structural disk of the inner stage, facing toward the small end of the conical outer stage. The detector can be inserted into or removed from the cooler assembly simply by removing the inner-stage cover plate. The lens system used in conjunction with the detector is attached to the outer stage with the aid of a lens holder. Threads on the exterior surface of the lens holder mate with a tapped section in the outer-stage structure; for focusing adjustment, the lens holder can be moved axially with respect to the detector by rotating it in the appropriate direction.

## Thermal Design

The interior surface of the outer stage is highly polished to minimize radiative thermal-energy transfer to the inner stage and to reject solar energy that strikes the cooler at angles nearly perpendicular to the axis of the cooler. The outer flange area

of the outer stage serves as a heat radiator by virtue of its special  $\alpha/\epsilon$  thermal control coating. Except for this flange, the outer stage is covered by a multiple-reflective-layer blanket, which passes between the outer stage and mounting ring to reduce radiative heat transfer to the outer stage from the cooler surroundings.

When the radiative cooler is exposed to a low-temperature heat sink in vacuum, it radiates thermal energy to this sink from the inner- and outer-stage surfaces. Temperature reductions in the two stages cause the support elements to decouple, resulting in an additional temperature drop. The outer-stage element reaches an equilibrium temperature when its total conductive and radiative heat inputs balance its total radiative output to the heat sink. Similarly, the inner-stage equilibrium temperature will reflect a balance between its total radiative and conductive heat inputs and its radiative output.

To achieve an inner-stage temperature of approximately 100° K, heat inputs to both stages must be minimized in every way possible. For this reason, multiple-reflective-layer radiative insulation is used around both the inner and outer stages, and very fine 0.10 to 0.13 millimeter (0.004 to 0.005 inch) electric wiring is used to convey signals from the detector to the terminal strip on the mounting ring. These wires are typically stainless steel and are encased in Teflon tubing in such a way that they can withstand severe mechanical stress without breaking.

All construction materials used in the cooler are space qualified, and the quantity of nonmetallic materials is minimized. In addition, all parts are scrupulously cleaned before final assembly to maintain the cleanliness of the optical system contained within and to minimize the evolution of adsorbed contaminants from component surfaces. Volatiles emitted by cooler components could easily render the optical system inoperative by coating the elements with condensed vapor or ice.

## FABRICATION TECHNIQUE

The major components of the radiative cooler (fig. 2) were machined from solid billets of 6061-T6 aluminum. This material was chosen because it has good mechanical properties, can be readily machined to precise tolerances with standard equipment, is readily available in large billets of uniform temper and homogeneity, can be made dimensionally stable through heat treatment, and is a suitable substrate for nickel plating and polishing. Machining these components from solid billets has proved to be the best way to avoid encountering material nonhomogeneities during fabrication, especially in the conical reflector surface.

After rough machining to within 2.54 millimeters (0.10 inch) of final size, the inner- and outer-stage components were subjected to a thermal stabilization to guarantee dimensional stability during repeated thermal cycling from room temperature to cryogenic temperatures (less than 100° K (-280° F)). After thermal stabilization and final machining of the major parts, the parts were positioned relative to one another in their final configuration and holes for the three support elements were line bored in the inner and outer stages. In this way, precise alinement of the two stages and the mounting ring was achieved and proper functioning of the support element was ensured.

The conical interior surface of the outer stage was prepared for optical polishing in the following way. First, it was polished to remove the majority of machining marks. Next, it was electroless nickel plated. Finally, it was polished with standard optical lapping materials; the technique used was an automated process that was developed especially for polishing conical surfaces to a quality approaching that of an optical mirror.

The evolution of this polishing technique was guided by visual comparison of the polished surface with reference surfaces having the desired reflective qualities. This comparison was made by replicating the polished surface and comparing this to replicates of high-quality optical surfaces (mirror or flats) as well as replicates from surfaces with known thermal control or reflective characteristics. This comparison was made by visual examination of photomicrographs of the replicates made at magnifications as much as 25 000 times, using electron-beam microscopy techniques.

## ASSEMBLY

Cooler assembly started by building up the inner stage. Following this, the inner stage was positioned within the outer stage by three support elements so that its concentricity relative to the outer stage was held within 0.038 millimeters (0.0015 inch) T.I.R.

After a multiple-reflective-layer blanket was placed over the outer stage, the mounting ring was positioned by its support elements so that the concentricity of the mounting ring relative to the outer stage was maintained within 0.025 millimeters (0.001 inch) T.I.R.

The internal electrical wiring of the cooler was connected to a terminal block bolted to the mounting ring; pins on the terminal block are readily accessible for connection to the associated optical-system wiring.

After the detector was inserted in the central counterbore of the inner stage and bolted in place, the detector leads were soldered to adjacent terminals on the inner-stage structure. Finally, the inner-stage cover was bolted in place, completing the cooler assembly.

## TEST PROCEDURE AND RESULTS

The fully assembled radiative cooler (fig. 3) was thermally tested in a vacuum chamber equipped with a liquid-nitrogen-cooled shroud. The cooler was oriented so that only its forward portions viewed this heat sink, while the rear portions were surrounded by a shroud maintained at room temperature. With this apparatus, successful operation of the cooler can be verified and temperature achievement measured. These data can be extrapolated by thermal-modeling techniques to predict orbital thermal performance.

Data on temperature as a function of time were taken for the inner and outer stages during the cooldown process. Thermal equilibrium was reached approximately 24 hours after the chamber was evacuated, and the shroud temperature was reduced to liquid nitrogen levels. At equilibrium, the temperatures of the inner and outer stages were 102° and 178° K, respectively.

Following thermal testing, the cooler was mounted to a test fixture and subjected to mechanical environment testing, which consisted of flight-acceptance-level sine and random vibration. The random vibration portion of this specification produces 11.3g root mean square acceleration for 2 minutes in each axis. During this testing, the cooler was covered with a large, clean plastic bag to protect it from ambient contamination. The cooler was free to move in all directions without contacting the bag or causing undue motion of the bag.

After this acceptance-level vibration test, the cooler was again mounted in the thermal-vacuum chamber for final optical focusing adjustment and system characterization. The lens mounted on the outer stage was focused by rotating the lens-holder component with a special drive tool mounted on a shaft passing through a rotary feed-through in the vacuum-chamber wall while the cooler was at operating temperature. After focusing, the most sensitive axis of the detector optical system was established using a special translatable infrared source and commensurate optical-measuring equipment.

During these measurements, it was established that the maximum radial movement of the detector axis relative to the lens axis was less than 0.025 millimeter (0.001 inch) as the cooler went from room temperature to operating temperatures. Axial motion of the detector relative to the lens vertex was found to be approximately 0.025 millimeter (0.001 inch) over the same temperature range. No contamination was detected on the optical system after extensive thermal and mechanical testing of this unit.

#### CONCLUDING REMARKS

The radiative cooler described is a simple, rugged device with proven capability for maintaining satellite-borne optical detectors at temperature levels of 100° K. It is a passive device with intrinsic high reliability that can be readily integrated and aligned with precise optical systems. The design and the materials used in the construction of this cooler promote long trouble-free operating life in the space environment with maximum protection of the low-temperature optical elements from contamination.

## DISCUSSION

A. L. Wade:

What information do you have about the criticalness of the contamination of the cold surfaces in orbit? Also, what material was used for support between the inner and outer stages?

McCullough:

The orbital performance information that we are able to talk about is not complete enough to draw conclusions about possible contamination phenomena. We have been cleared to talk about only those aspects of the cooler design that I have presented.

R. L. Samuels:

Was surface-finish deterioration during orbital lifetime investigated?

McCullough:

Yes, the finishes that we selected are considered to be as good as any available for the maintenance of the required thermal properties during extended exposure to the space environment.

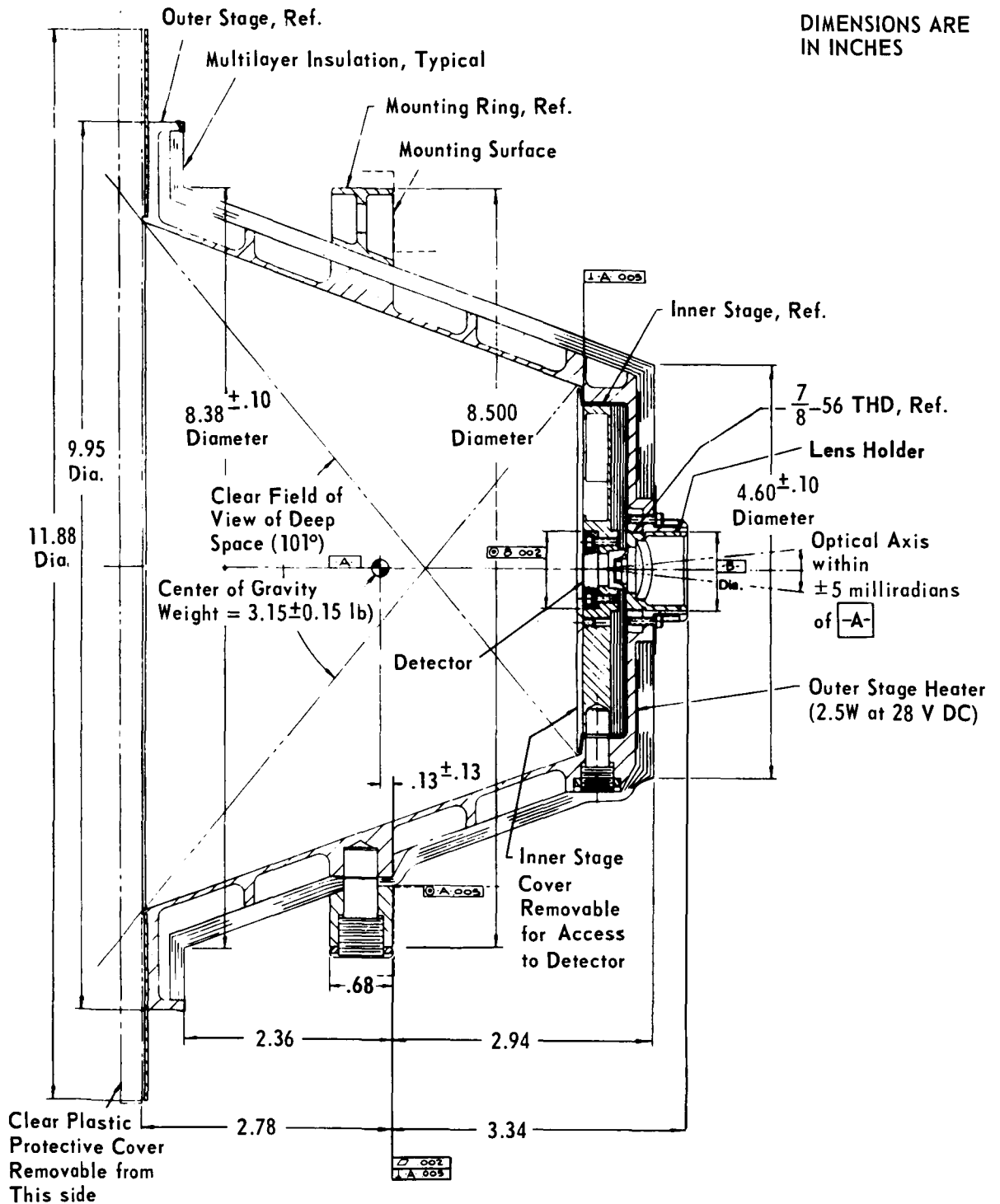
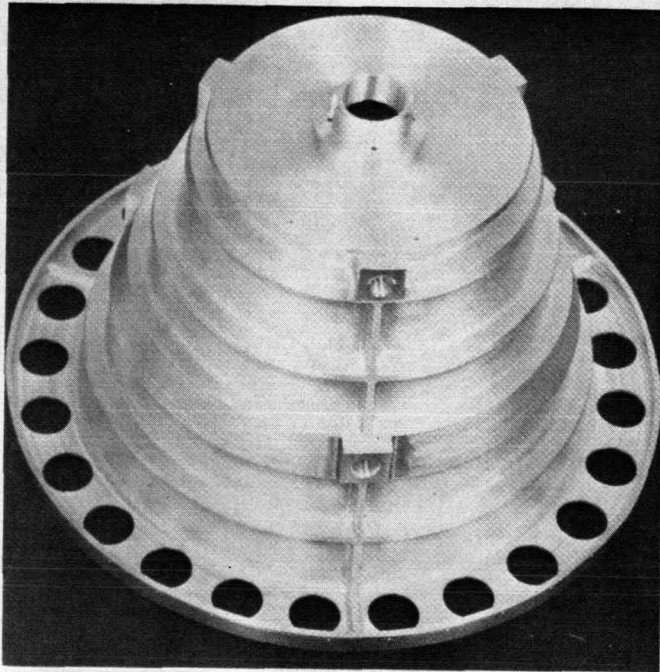
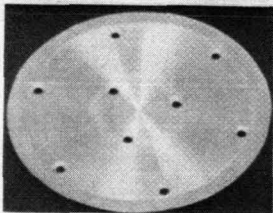


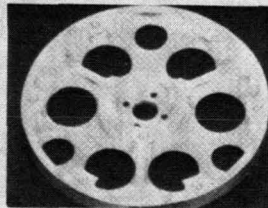
Figure 1. - Radiative cooler assembly.



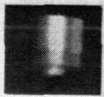
Outer Stage



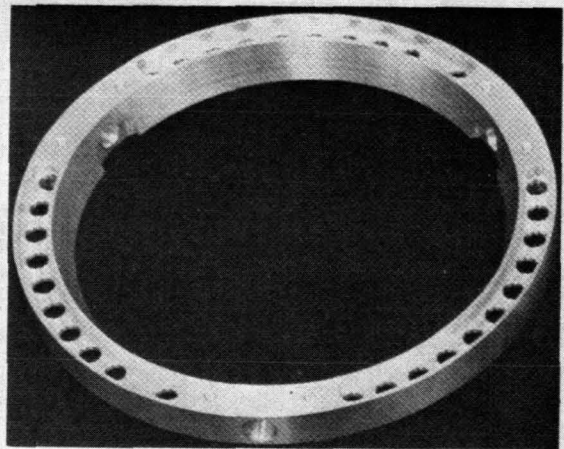
Inner-Stage Cover



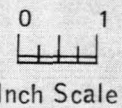
Inner Stage



Lens Holder



Mounting Ring



Inch Scale

Figure 2. - Radiative cooler major components.

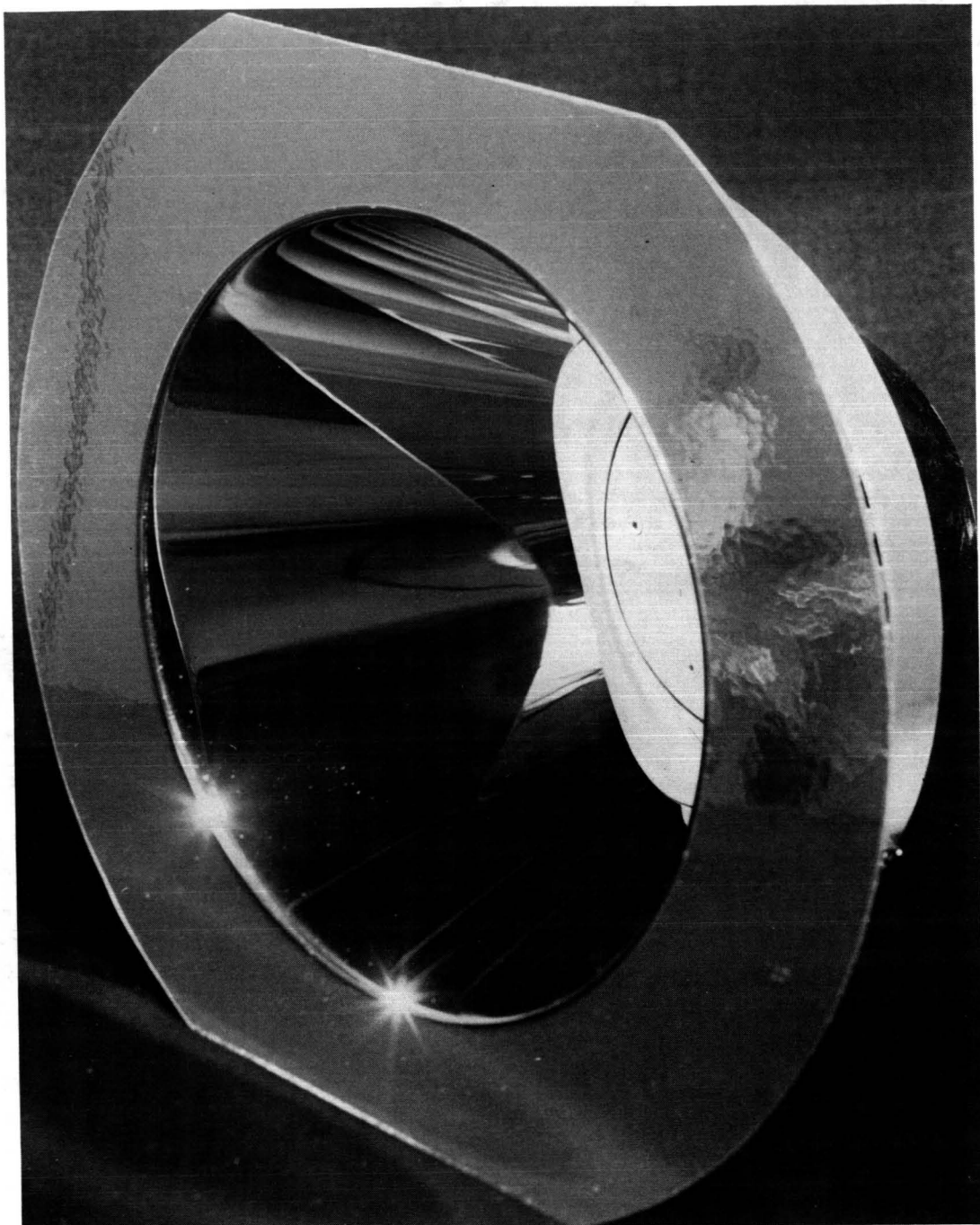


Figure 3. - Passive radiator for detector cooling.

**SESSION II**

**Page intentionally left blank**

## ZERO-GRAVITY TISSUE-CULTURE LABORATORY

By James E. Cook, P. O'B. Montgomery, Jr., and Joseph S. Paul\*

### ABSTRACT

Hardware has been developed for performing experiments to detect the effects that zero gravity may have on living human cells. The hardware is composed of a time-lapse camera that photographs the activity of cell specimens and an experiment module in which a variety of living-cell experiments can be performed using interchangeable modules. The experiment is scheduled for the first manned Skylab mission.

### INTRODUCTION

It is possible that the removal of gravity for an extended period of time will have significant effects on living organisms. These effects may be manifested at the cellular level because this is the fundamental biological element in all living systems.

Living cells are studied routinely outside the living system by supplying them with oxygen and suitable nutrients, by maintaining their temperature, and by protecting them from toxic and disease-causing agents. This process is known as tissue culture. Typical experiments include microscopic observation of the tissue-culture cells, measurement of rates of nutrient usage, and observation of the effects of chemical, radiation, disease-inducing agents, and many others.

A small, automated tissue-culture laboratory has been developed for the National Aeronautics and Space Administration (NASA) that will be used to perform a variety of experiments designed to determine the effects of the zero-g environment on living cells.

The laboratory was designed to achieve two major objectives: to produce time-lapse movies of living cells and to perform a variety of cell experiments by injecting various liquids into the nutrient media. All data are to be analyzed after recovery of the flight package.

As with most equipment developed for space flight, the laboratory-hardware design is restricted by the usual limitations of size, weight, and power; at the same time, high reliability and safety standards must be maintained. In addition, the biological compatibility of materials and the necessity to sterilize components at a high temperature are major constraints.

---

\*University of Texas Southwestern Medical School, Dallas, Tex.

We wish to thank Harry Jarrett and Richard Summers for contributions to the design of the equipment.

## DESCRIPTION

The laboratory is enclosed in an airtight package that weighs 11 kilograms and occupies  $0.015 \text{ m}^3$ . Switches on the faceplate of the package (fig. 1) are operated by the crewmen in flight to initiate operations and, with the aid of indicator lamps, to check equipment performance.

Internally, the package is divided into two operationally independent sections to accomplish the two major objectives. The two divisions are the camera-microscope section and the experiment module. The camera-microscope section and the relative location of the experiment module are illustrated in figure 2. Space between the two sections is provided for the addition of circuit boards and timers. A container slips over the entire assembly and joins with the front panel to form an airtight enclosure. All penetrations of the panel by switch shafts and windows are sealed with O-rings.

### Camera Microscope

The camera-microscope section consists of two independent systems. One system photographs specimens through a 20-power microscope and the other system photographs through a 40-power microscope. Each microscope, including the lamp used to illuminate the specimen, is only 7 by 4 by 2.5 centimeters in size. The phase-contrast image produced by the microscope is projected through a tube and is reflected by a mirror onto the film. The mirror can be rotated, permitting an observer to view the image and to focus the microscope during ground-based checkout. A locking device is provided to hold the objective lens in position after focusing. No shutter is required because the lamp is turned off after each exposure.

The camera operation (fig. 3) is unusual in that film registration is accomplished by using photocells to sense sprocket-hole position in the film instead of using the usual sprocket wheels or claws. This arrangement reduces weight and eliminates troublesome film loops and takeup-reel slip clutches. It is limited in speed, however, because it requires the takeup reel to stop for each frame. Periodically, an internal timer turns on the microscope exposure lamp for a short period of time to expose one film frame. As the lamp turns off, a pulse is generated that triggers a silicon controlled rectifier (SCR). The SCR completes a circuit that allows the film-takeup drive motor and registration lamp to operate. The motor advances the film until a small light beam shines through the next sprocket hole and strikes the phototransistor. The phototransistor output switches on a transistor connected across the SCR. The SCR stops conducting because of the shunt path, but the transistor maintains the circuit until the edge of the sprocket hole again interrupts the light path, turning off the transistor and stopping the motor. Now, the cycle is ready to be repeated for the next frame.

Film for the camera is supplied from a replaceable film pack that has two rolls of 16-millimeter film that is 100 meters long. Normally, the photographic rate is 5 frames/min for 40-minute intervals twice each day throughout the 28-day mission.

Each microscope holds a living-cell specimen grown in a 0.05-cm<sup>3</sup> chamber formed by a gasket sandwiched between two glass disks. Tubes are attached to the gasket for use in injecting fresh liquid nutrient media and for removing waste media. The chamber is kept in a heated block that is thermostatically controlled to maintain body temperature (310.15° K or 37° C).

Cells suspended in a liquid medium are injected into the chamber. After a few hours, the cells settle into a thin layer and firmly attach to the lower glass disk. Then, the chamber may be installed in a microscope in any position. The thin layer of cells forms a flat plane on which the objective lens is focused.

Fresh nutrients are supplied twice a day from a cylindrical reservoir containing a piston. The piston forces fresh media into the chamber and forces waste media into the volume on the back side of the piston. The piston is advanced by a motor that rotates a lead screw on which the threaded piston rides. Separate media-pump reservoirs are provided for each specimen chamber. Timing of the camera cycles and the media-pump advance is controlled by a commercially available, self-powered, tuning-fork watch movement that operates switch contacts.

### Experiment Module

This module section is constructed so that various hardware modules can be installed in the basic package to perform a variety of experiments. The module is enclosed in a sealed container, which provides redundancy in case the outer enclosure seal is lost. Two different modules have been designed. One module, termed a biopack, has been designed to inject various radioactive tracers (or labels) into specimen chambers after several days of cell growth in a zero-g environment. Then, the labels are rinsed out and the cells are preserved with a fixative solution for analysis after recovery of the equipment. Analysis includes the measurement of the incorporation of the radioactive compounds by the cells.

The cell-growth curve module is designed to grow cells in several chambers. At predetermined intervals, the chambers automatically fill, one at a time, with a fixative that is used to preserve the cells. Upon return of the package, a growth curve will be constructed by counting the cells in each chamber and tabulating the number according to the day they were preserved. Any shifts in this curve compared with ground-based control experiments may be a result of the zero-g environment.

### Biopack Module

The biopack module is installed in the package with one experiment assembly removed (fig. 4). The module consists of two experiment assemblies, one of which labels, rinses, and fixes the cells on the fourth day after launch. The other module labels the cells on the 10th day after launch. The label/rinse/fix cycles are initiated by the astronauts. The experiment assemblies are identical except that the 10-day media-supply pump is longer. Both assemblies can be removed from the drive-train portion of the module for sterilizing and filling with biological materials.

Each experiment assembly has 12 chambers that are used for maintaining living cells. The chambers are connected in series so that, for feeding twice a day, fresh media are forced into chamber 1 and the contents of chamber 1 are forced into chamber 2 and so on through chamber 12. Enough media are provided from a media-pump reservoir to change the media in all 12 chambers each time the cells are fed. This feeding process is performed automatically until either 4 or 10 days after launch. On these days, an astronaut will operate a switch to begin the label/rinse/fix cycle of the appropriate biopack.

In order to label, rinse, and fix the cells, the equipment must perform the following operations in sequence.

1. Shift a valve in the chamber block to disconnect the series fluid path and to connect individual chambers to separate pump reservoirs containing label and rinse solutions.
2. Inject the various radioactive labels into the proper chambers.
3. Rinse out the labels after a predetermined time.
4. Return the chamber valves to the series feed position.
5. Inject the fixative into all chambers.
6. Shut off power to the experiment assembly.

The label and rinse pump reservoirs are constructed from a solid block containing 11 bores (one of the 12 chambers is not labeled). A piston and a lead screw are installed in every bore. Initially, each piston is positioned so that the reservoir volume on one side holds  $2\text{ cm}^3$  of a label solution. Rinse solution fills the  $7\text{-cm}^3$  volume on the other side. Tubing connects the two ends of each pump to the proper chamber. As the piston is advanced, the label solution is forced into the chamber and the chamber contents are forced into the rinse-solution side of the pump. Reversing the piston forces the rinse through the chamber into the end of the pump that originally contained the label.

All of the various pumps and valves are driven by means of a single drive motor (fig. 5). In order to select which device is driven at a given time, an escapement mechanism is used. The motor rotates a shaft that would be free to slide along its axis if it were not restrained by the escapement. A spring on the shaft keeps the escapement pressed against a stationary pin. Initially, a gear attached to the shaft is aligned to drive the media pump. Twice each day, the internal timer starts a media-advance cycle. This cycle is terminated by a cam switch after the proper number of revolutions. When the astronaut is ready to begin the label/rinse/fix cycle, he rotates a front-panel switch causing the motor to run in reverse. This reversal rotates the escapement enough to allow it to slip a short distance past the stationary pin. The spring forces the shaft and drive gear forward to engage the gear that drives the chamber-valve shifting mechanism. The motor continues to drive until a limit switch terminates the cycle. The motor direction is changed for each succeeding step to engage the proper gear at the right time.

When the drive gear shifts, it may not engage properly at first, but a few degrees of rotation will allow the gears to mesh. This drive normally operates only a few times during testing and flight and the motor speed is only 20 revolutions/min. Test units have been subjected to hundreds of operations without any significant wear. This system is smaller, lighter, and less complex than a comparable system that has electromechanical clutches or numerous motors.

A pump similar to the media pump (but smaller) is used to supply the fixative solution. The fixative is introduced through the same series path that the media flowed through. A selector valve is repositioned when the chamber valves are first shifted, connecting the fixative pump to the fluid lines and disconnecting the media pump.

### Growth-Curve Module

The growth-curve module consists of two identical, independent assemblies. Each assembly provides nine cell-culture chambers installed in a temperature-controlled holder (fig. 6). The specimens are fed automatically by means of a media pump. Media pass through the preheater (a reservoir attached to the heated holder) before entering the chambers.

A tape program reader, driven by the media-pump motor, uses a Mylar tape that is punched with two rows of holes. Microswitch actuators ride on the tape and drop into the holes. One row of holes determines the amount of media for each feeding, and the other row initiates cycles to inject fixative into one chamber at a time. Usually, fixation will be programmed to occur at 2-day intervals.

Fixation is accomplished in the following manner. Upon command by the programmer, the fixative-pump motor begins to drive a sector gear. The sector gear rotates a fixing valve  $22.5^\circ$ , then disengages. This rotation connects lines from a fixative pump to the chamber to be fixed and disconnects the chamber from the media-supply lines. As the motor continues to run, the sector gear engages a gear on the fixative pump. Fixative is injected and the cycle is terminated by a cam switch on the motor. This cycle is repeated to fix the other chambers. One of the nine chambers is not fixed but is returned with the cells alive so that they can be subcultured upon return to earth.

Each time a specimen is fixed, it no longer requires feeding. The tape programmer terminates the media-pump cycle sooner so that only media enough for the remaining unfixed chambers will be supplied.

### DESIGN PROBLEMS

When living cells are maintained and studied in test tubes, bottles, and so forth, they are said to be studied "in vitro." The term literally means "in glass." Most tissue culture is still performed "in glass" because most glass is nontoxic to the cells. A few other materials, such as Teflon and silicone rubber, are used routinely. The development of the flight equipment required considerable research to find materials that have properties of nontoxicity, structural strength and stability, machinability, heat resistance (for sterilizing at  $393.15^\circ\text{K}$  or  $120^\circ\text{C}$ ), and flame resistance (for use

in manned spacecraft). Clear sulfuric-acid-anodized aluminum (type 6061) is used extensively because it has all of the properties just noted and it is light in weight. Care must be exercised to prevent scratching the surfaces, however, because unanodized aluminum is toxic. The toxicity of each lot of material must be tested before use because minor changes in its manufacture can make it unusable. For example, "nontoxic" epoxy can be lethal to cells if curing-agent proportions are varied.

Another problem encountered when performing tissue culture in zero-g is bubbles in the fluids. Normally, gravity holds fluids in contact with cells, and bubbles are of little consequence. Because in zero-g the location of bubbles cannot be predicted, it is necessary to build fluid systems so that bubbles may be removed during filling operations. The use of materials, such as silicone rubber, that have a high permeability to gases is restricted because gas leakage will cause bubbles to form after a period of time.

### CONCLUDING REMARKS

Many new techniques for performing tissue culture have been devised in the development of zero-g tissue-culture equipment. Several of the techniques can be adapted to laboratories on earth. These techniques would be of particular value in long-term experiments to eliminate daily manual care and, by using closed systems, to reduce the risk of contamination.

### DISCUSSION

K. M. Speight:

What type of motor is used in the main drive?

Cook:

Direct-current brush-type generators are used. Because our package is sealed, we do not operate in the pure-oxygen atmosphere of the command module.

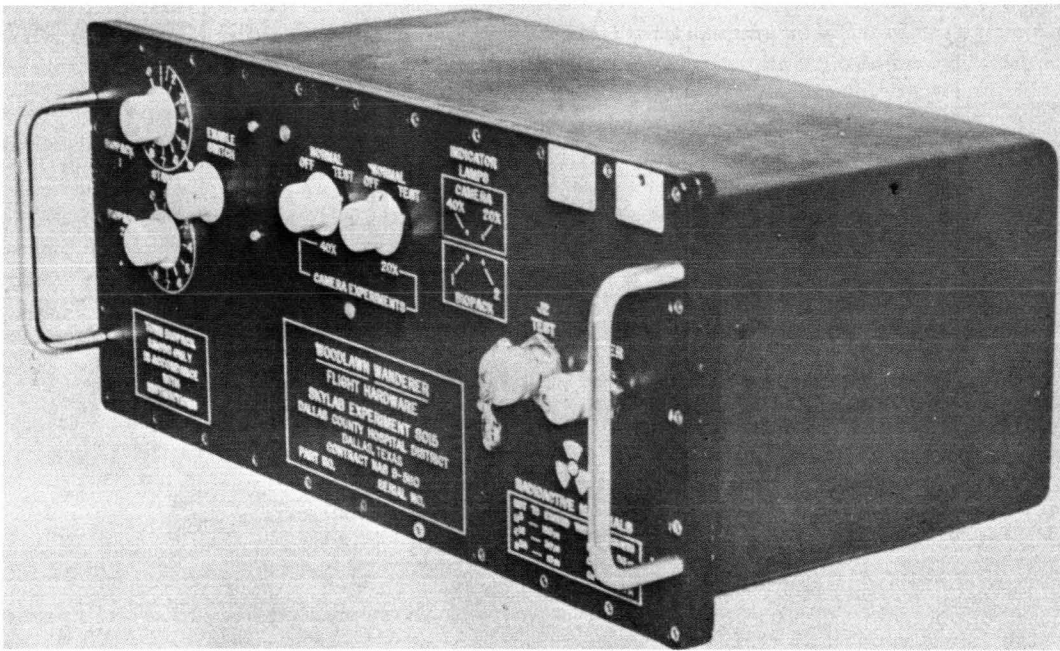


Figure 1. - Flight-hardware package.

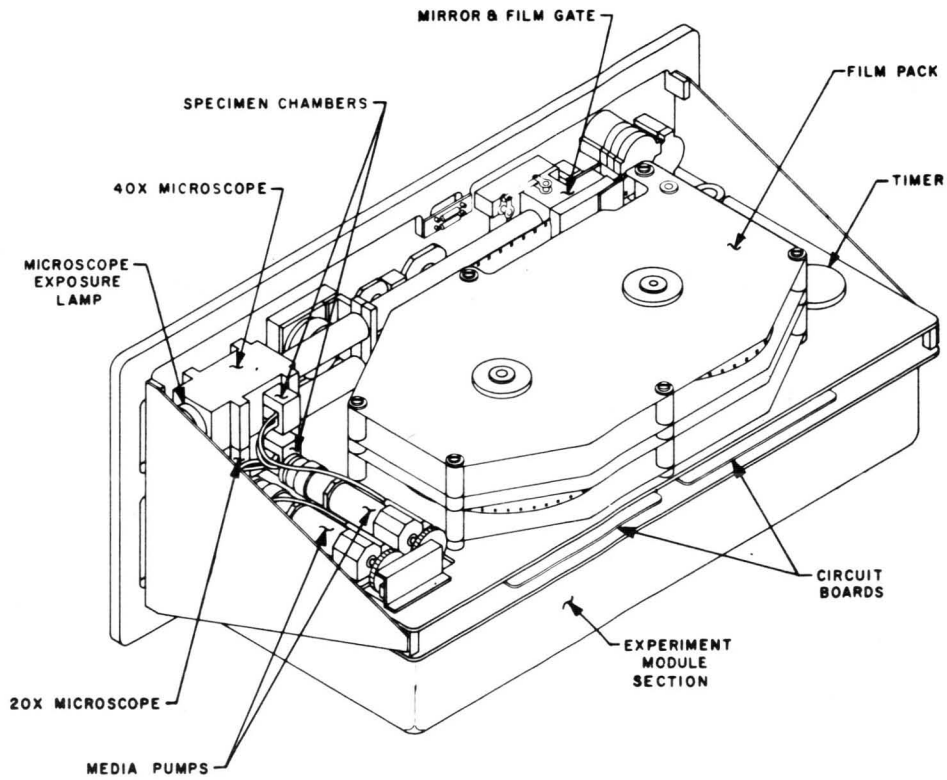


Figure 2. - Camera-microscope section.

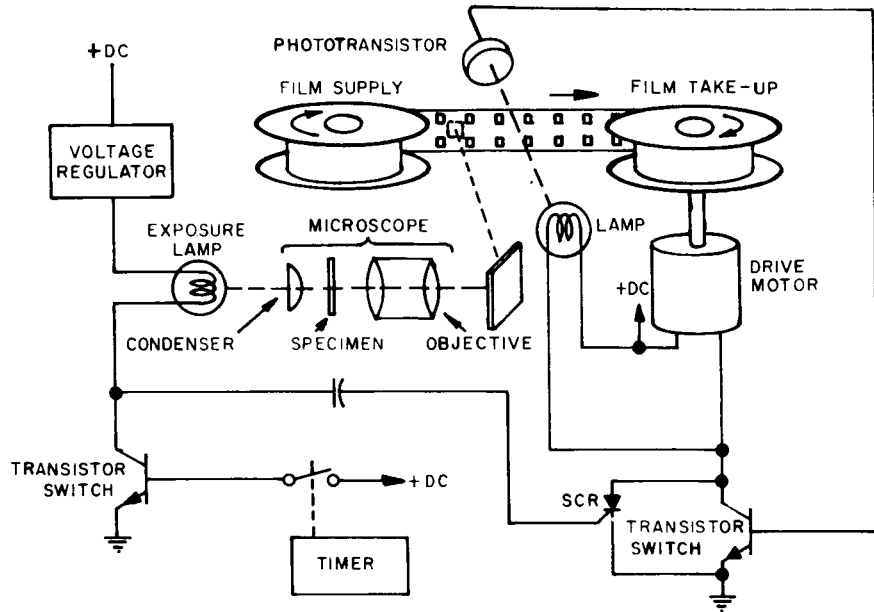


Figure 3. - Microscope-camera diagram.

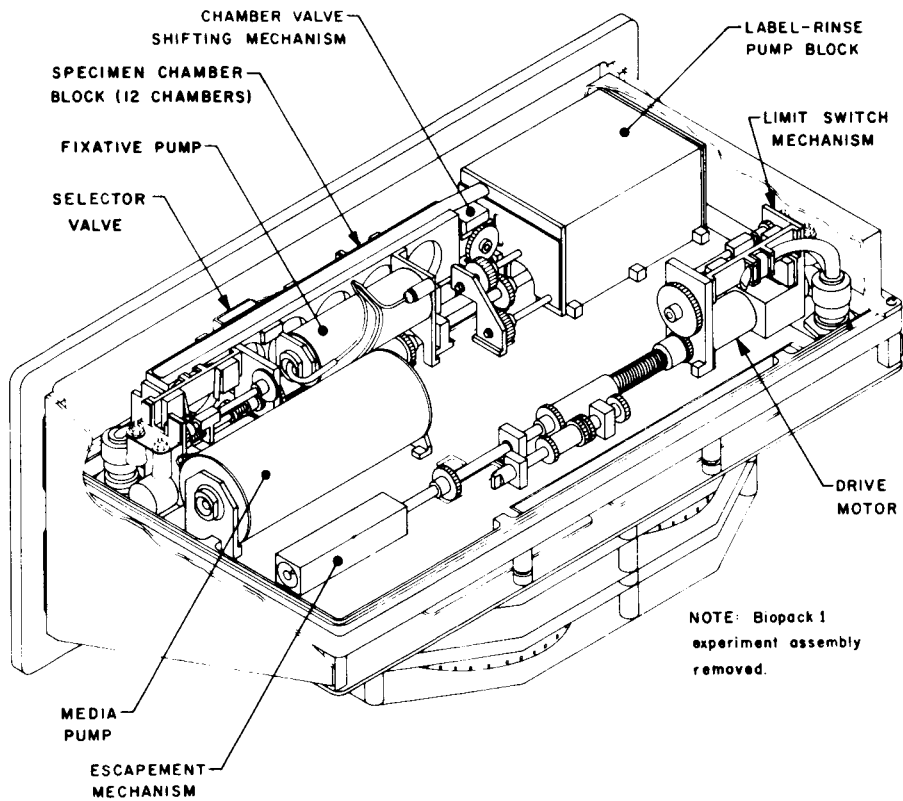


Figure 4. - Biopack experiment module.

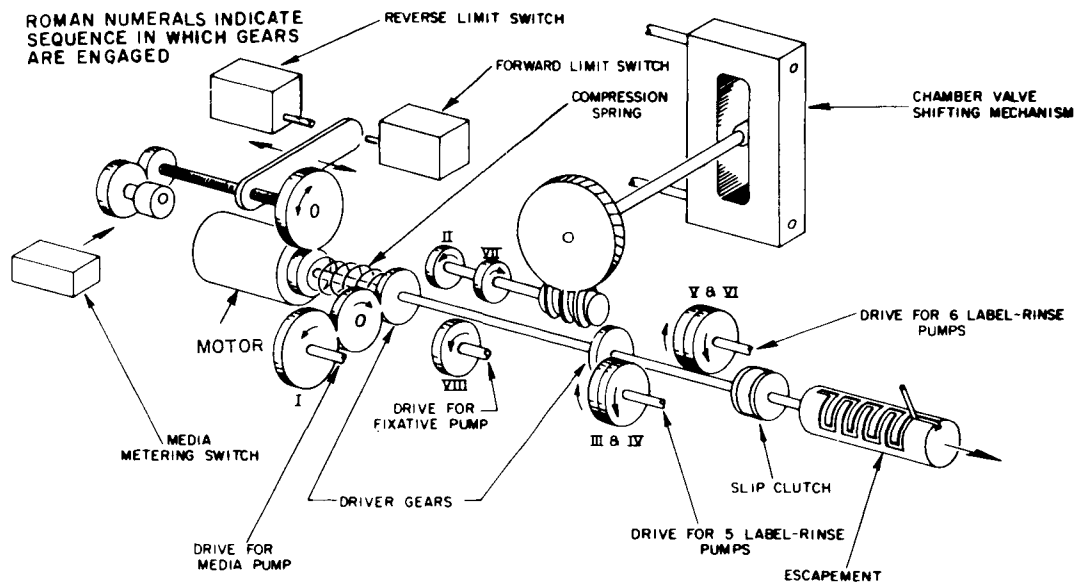


Figure 5. - Biopack drive train.

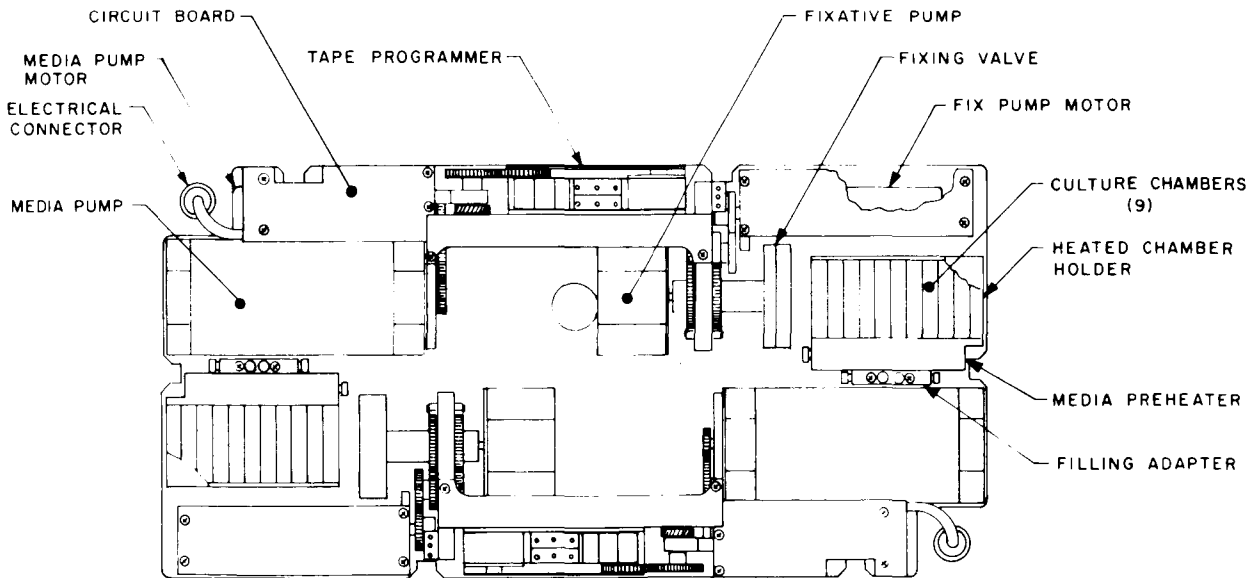


Figure 6. - Growth-curve module.

**Page intentionally left blank**

## FRANGIBLE GLASS CANISTERS

By Richard Seifert\*

### ABSTRACT

The need for a canister that can release its contents without disturbing the contents dynamically is discussed. The solution of this problem by the use of a frangible glass canister is presented. The basic theory applicable to frangible glass and the method of initiating a command flaw are discussed. A brief description of the test program and the results of a flight test are presented.

### INTRODUCTION

In one program, there was a requirement that a payload be deployed in space in a manner which would impart only negligible dynamic disturbances upon release. The payload should be ejected from a standardized launch tube that would be flown for test purposes on a Nike-Hydrac sounding rocket. The internal and external dimensions of the launch tube were fixed and governed the external dimensions for the payload-carrying device (that is, a canister that houses the payload). The obvious solution was to carry the payload inside the previously developed canister, for which the launch tube had been designed (fig. 1). This approach was tried during a test program.

The assistance provided by Morris Creel, Tracor, Inc., and Gary Goodman, Owens-Illinois, and their associates is gratefully acknowledged, as well as their ideas on the detailed development aspects of this design concept, test, and implementation of the device.

### ALTERNATE CONCEPT

In addition to a propelling device, the existing canister consists of two metallic cylindrical half shells that are held together by several fasteners, locking two tongue-and-groove joints that are separated by  $180^\circ$  and that extend the full length of the cylinder. Separation of these half shells is accomplished by redundant pyrotechnic means. The tongue-and-groove joint is constructed so that it accommodates a small column insulated delay (SCID) line. The gas pressure resulting from the burning of the SCID is used to shear the fasteners, rupturing the cylindrical canister. The gases propel the separated halves away from the payload.

---

\*Aerospace Corporation, San Bernardino, Calif.

Although the existing metallic canister could easily accommodate the payload, in the test program mentioned earlier it was demonstrated that the canister would not meet the most important requirement: excessive dynamic disturbances were not to be imparted to the payload. It was evident from the beginning that the propagating SCID separates the canister halves near the point of entry into the tongue-and-groove joint before it arrives at the opposite end. Tests showed that each canister-half end deflects outward from the longitudinal centerline because of the thin-wall construction, and becomes banana shaped. This action causes the escaping gases to impinge on the payload, imparting motion to it. Although the duration of this event is very short, it is sufficient to impart dynamic motion beyond tolerable limits to the released payload.

## FRANGIBLE GLASS CANISTERS

The foregoing tests resulted in an investigation to find a new canister design that would not subject the internal payload to a detrimental dynamic environment. A solution was found: use a specially treated glass tube that has a uniform wall thickness. A fused lithium-alumina-silicate glass exists that, when subjected to an ion-exchange process, results in a rearranged molecular structure. The process consists of immersing the so-called "green" glass tube in a heated bath for a certain length of time. Near the surfaces, the small lithium ions are exchanged for larger sodium ions, in effect producing three layers in the glass-tube wall. Both outer layers are in compression; the middle layer is in tension (fig. 2).

Two principles are used to develop the strengthened frangible glass canister. First, glass is much stronger in compression than in tension. Second, almost all failures in glass result from a surface defect that acts as a tensile-stress riser. Chemically strengthened glass is processed to incorporate a residual compressive stress in the surface layers of the glass; this stress is balanced by tensile stresses in the interior of the glass wall. The forces in the thin layers of highly compressed glass can be balanced by relatively low tensile stresses in the thicker middle layer. Because the tensile stress is relatively low and is contained in the interior of the glass thickness, spontaneous failure resulting from the presence of tensile forces is inhibited. The residual stress distribution in this glass is shown in figure 3.

Command failure results when the outer layer, containing the high residual compressive stress, is penetrated; an imbalance of forces in the glass wall results. The stored tensile stress is relieved, resulting in rapid fracture of the glass. The stored energy is sufficient to result in multiple forked fractures that dice the glass into very small fragments. In a tube configuration, the fragments are forced outward radially as the highly compressed surface layers attempt to expand to relieve the residual internal-stress condition.

## CONFIGURATION

For the intended application, the glass was produced in open-ended-tube configurations. The cylinders were produced with a carefully controlled wall thickness ( $0.127 \pm 0.005$  centimeter ( $0.050 \pm 0.002$  inch)), without excessive outer or inner

waviness, and in the lengths required (fig. 4). The existing specification is for glass fragments to have an area of less than 0.65 square centimeter (0.10 square inch), with the stipulation that no fragment exceed 0.95 centimeter (3/8 inch) in the largest dimension. The unrestricted radial dispersal rate of the glass fragments has been defined as follows.

1. No more than 10 percent of the fragments may have a velocity of 0 to 1.22 m/sec (0 to 4 ft/sec).

2. Ninety percent of the fragments must have velocities in excess of 1.22 m/sec (4 ft/sec). Although not in the specification, the cracking propagation rate for the glass-tube length and wall thickness applicable in this case was approximately 134.15 m/sec (440 ft/sec).

## GLASS FRANGING

Having established that a suitable glass tube could be produced, a suitable means of initiating the glass-franging process had to be found. As usual, conventional methods were tried at first. These consisted of building pins (or "pingers") of various hard materials, varying front cone angles, varying shank diameters, and driving the pins from various distances toward flat frangible-glass specimens. These tests were unsuccessful. Pins either broke or deflected when contacting the glass surface. Because of a very tight schedule, it was decided not to pursue an investigation into possible unusual alloys that would maintain structural integrity and act as successful pingers for the glass. It was decided to use a diamond-tipped pin to shatter the glass. Both the diamond and its mounting had to be controlled carefully. The diamonds that were used were unicrystals and, therefore, were susceptible to shattering if the cleavage planes were not oriented properly with respect to the tip radius. The result of this development is shown in figure 5.

The installation of this franging pin in the housing is shown in figure 6. The SCID is routed around the circumference of the franging-pin shank, which is held in position by means of a shear pin. The SCID is initiated by the rocket motor through the use of a timer and redundant delays. When the motor burns, the resulting gases act on the franging-pin shoulder, creating a force adequate to shear the small pin. Now, the gas is permitted to act together with an expanding coil spring. Working together, these forces propel the franging pin forward into the glass with sufficient force to penetrate the thin compression layer. In turn, this initiates the cracking process. Two franging pins, 180° apart, were incorporated in the final design. These pins strike the glass simultaneously from the inside. To obtain a high-reliability franging process, it was decided to position the diamond-tipped pins near the tube end where a metal backing existed on the outside of the glass wall. It was shown that the propelling forces on each pin not only caused complete penetration of the glass but, in fact, impacted this metal backup. An empty glass cylinder before initiation of the franging process is shown in figure 7. The glass particles are shown moving away radially in figure 8. The second picture was taken a few milliseconds after the franging pin impacted the glass.

Other tests, involving the same fringing system, were performed to determine correct standoff distances between the retained pin and the glass surface, with and without a metal backup behind the point of diamond impact, and using various thicknesses of treated glass. The force required to initiate the fringing process was determined experimentally to be approximately  $27.58 \times 10^7$  N/m<sup>2</sup> (40 000 psi) which, in this case, is achieved by controlling the gas force, the spring force, and the diamond-tip radius. The velocity distribution of the glass particles also was obtained experimentally by placing 8.89-centimeter-diameter (3.5 inch diameter) containers side by side (in a pie shape) on the floor of a chamber, starting at the point in line with the glass canister centerline. Inspection of these containers after a fringing test demonstrated a concentration of particles in a circular band, as had been predicted.

It should be noted that, during one of the tests in this series, a frangible-glass canister inadvertently was permitted to fall free from a height of approximately 35 feet before it impacted into 15.24 centimeters (6 inches) of polyurethane. The glass canister did not break as a result of the fall, and X-rays revealed no damage to it or to the fringing device that had been installed.

### CONCLUDING REMARKS

When all tests were completed, flight articles were assembled and installed in the sounding rocket. The canister and the fringing system were successful during a flight test. This was demonstrated conclusively by tracking of the payload, which could operate only when it was released from the canister.

### DISCUSSION

T. G. Harrington:

Do you have any test data to verify that no glass particles moved inboard? How were data obtained?

Seifert:

Glass-particle motion was, in fact, as stated: 10 percent had velocities 0 to 4 ft/sec; 90 percent moved away at rates in excess of 4 ft/sec. The data were obtained by collecting of particles at the bottom of the chamber in the containers that were visible in the movie. No particles were found in the containers on the chamber floor located in line with or near the canister centerline.

W. E. Oakey:

In your movie, some of the glass fragments appeared to be approximately 2 inches long. Were they in fact this long, or were you able to meet the 3/8-inch maximum-dimension requirement?

Seifert:

The fragments were all of the specified dimension. The first camera was quite close to the test specimen and fragments appear larger than they are in reality.

**W. A. Stewart:**

Please comment on the appearance of "shock" waves at the outer edges of expanding glass.

**Seifert:**

If the film is viewed at a slower speed, the cracking propagation is visible in an orderly manner. The fringing over the entire cylinder length is visible in 3 frames, whereas the movie was taken at 10 000 frames/second. What is visible in the movie does not represent a shock wave. It is visible indication of already created particles moving away from the portion of the canister which is still undisturbed.

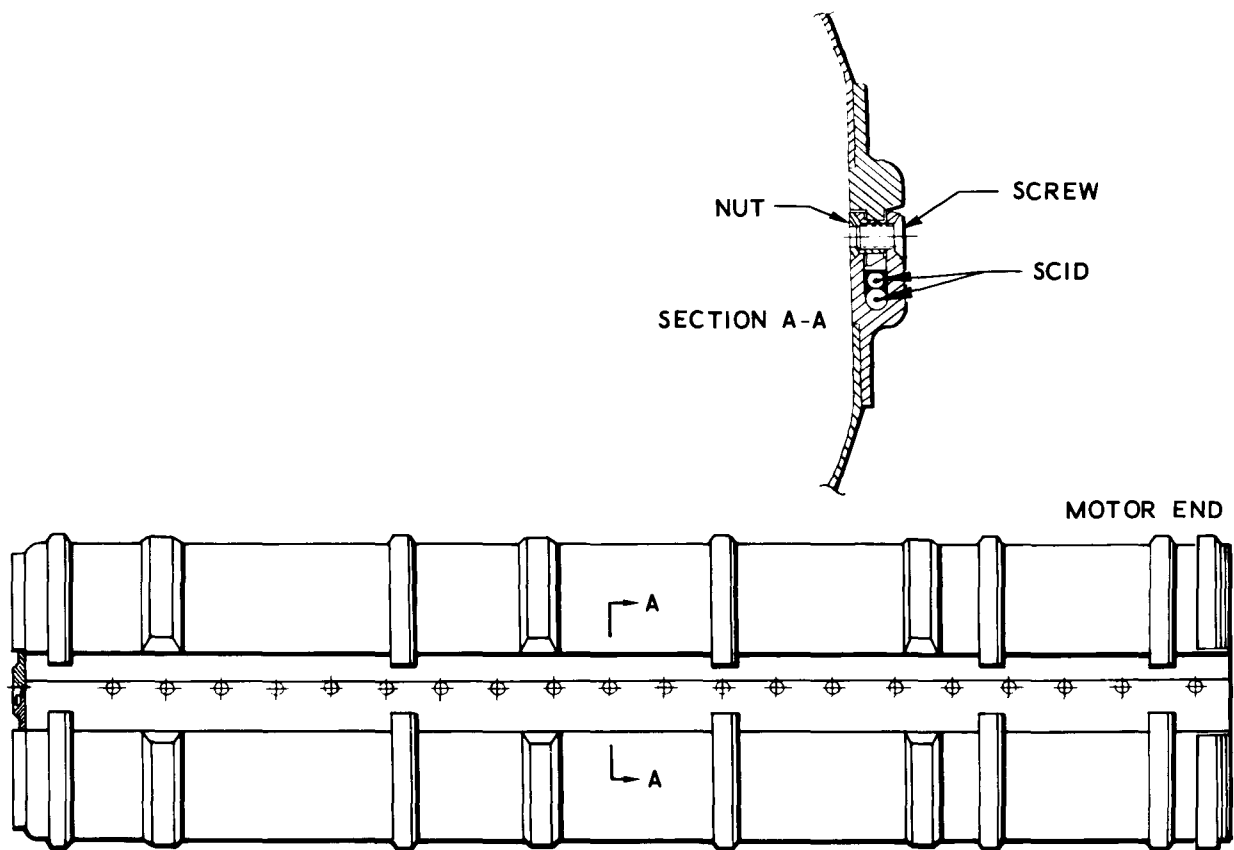


Figure 1. - Metallic canister.

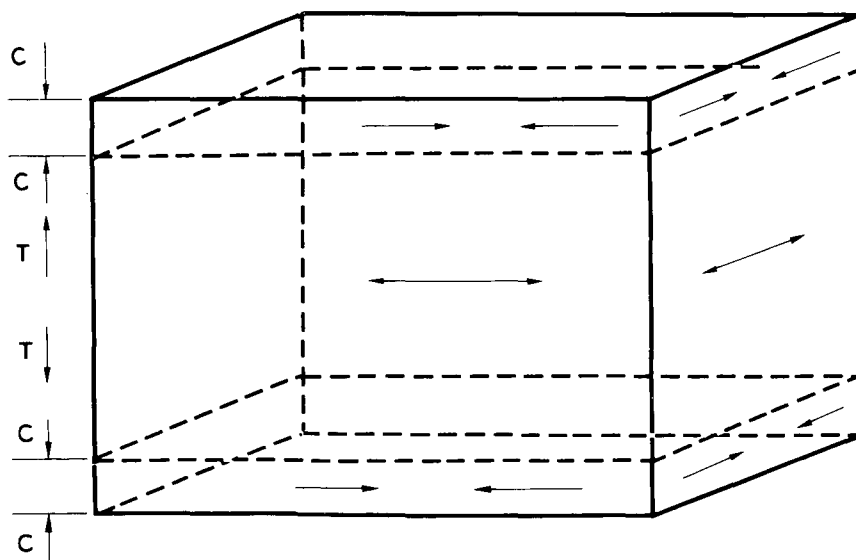


Figure 2. - Idealized stress layers in chemically strengthened glass.

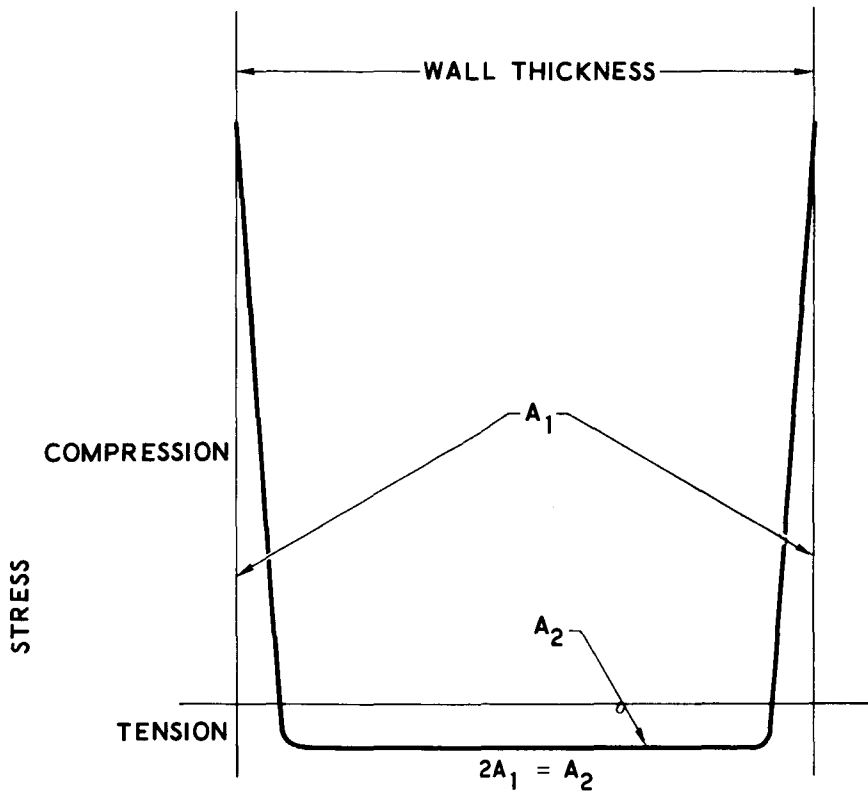


Figure 3. - Residual stress distribution in chemically strengthened glass.

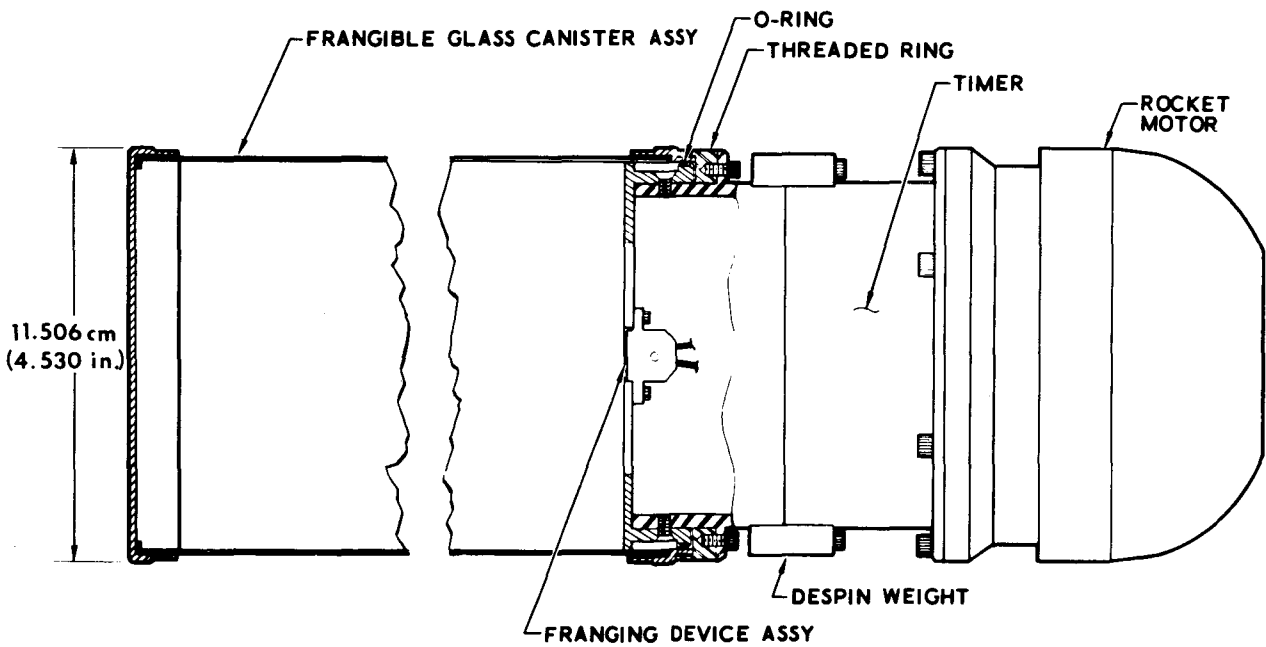


Figure 4. - Glass canister.

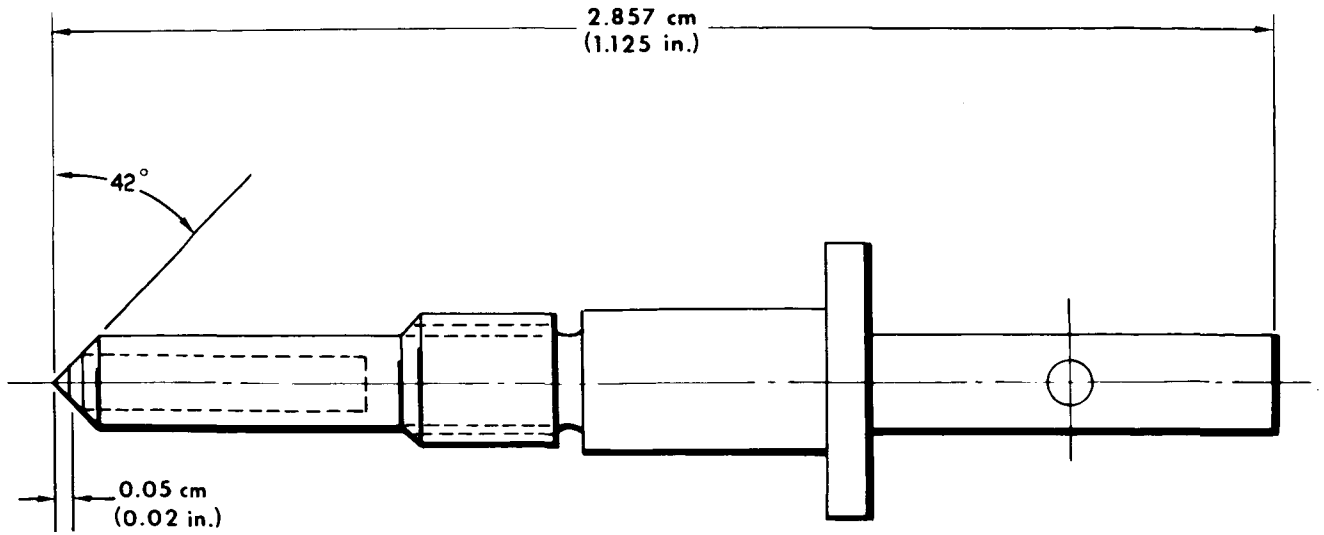


Figure 5. - Diamond-tipped fringing pin.

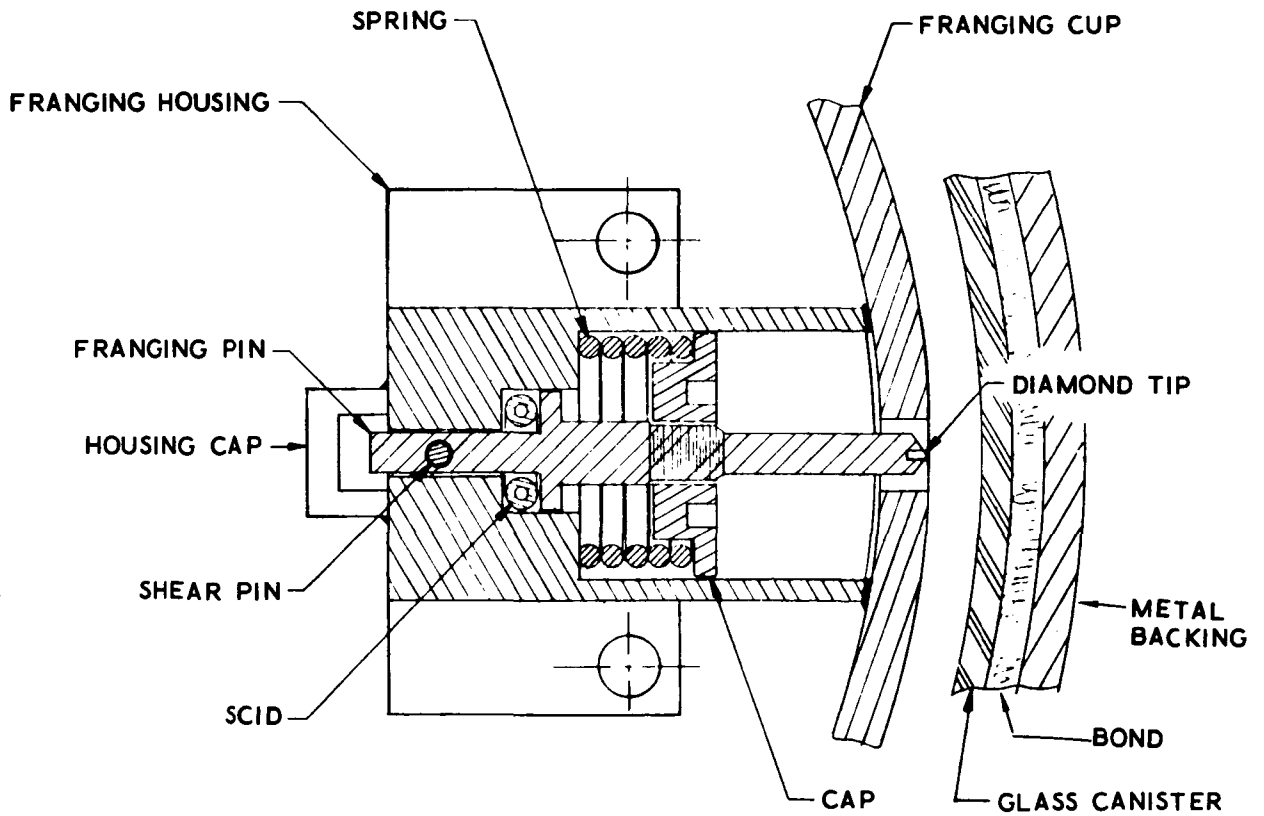


Figure 6. - Pinger installation.

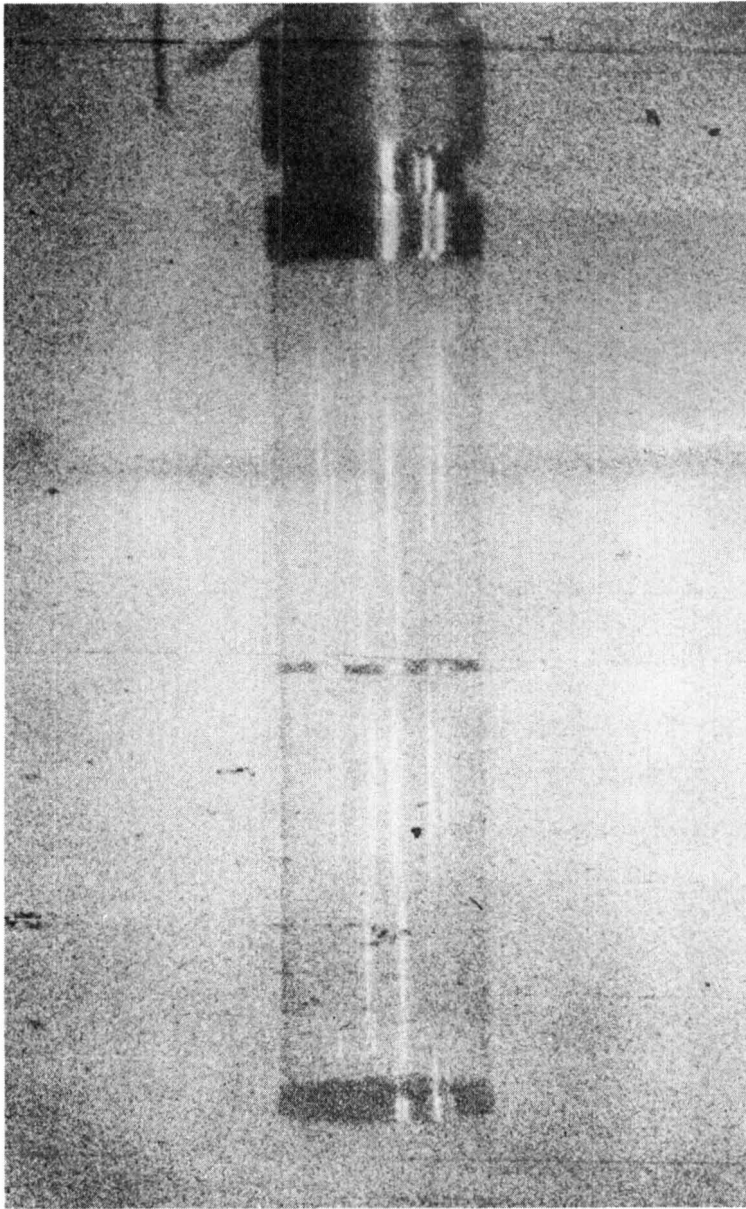


Figure 7. - Glass cylinder before fringing.



Figure 8. - Glass cylinder undergoing fringing.

**Page intentionally left blank**

73N18876

## LUNAR ROVING VEHICLE DEPLOYMENT MECHANISM

By Alex B. Hunter\* and Bryan W. Spacey\*

### ABSTRACT

The space support equipment that supports the lunar roving vehicle during the flight to the moon and permits the vehicle to be deployed from the lunar module onto the lunar surface with a minimum amount of astronaut participation is discussed in this report. The design and evolution of the equipment are discussed. The success of the overall lunar roving vehicle design, including the space support equipment, was demonstrated on the Apollo 15 and 16 missions.

### INTRODUCTION

The lunar roving vehicle (LRV) is designed to provide transportation on the lunar surface for two astronauts and their equipment in support of lunar-exploration missions (fig. 1). The LRV is a manually controlled vehicle equipped with navigation instruments, systems-monitoring instruments, and independent four-wheel drive and suspension system and is powered by two silver zinc batteries. The LRV is transported to the lunar surface in an open quadrant of the lunar module (LM) and secured by space support equipment (SSE). The LRV is manually deployed by the astronauts and loaded with communications and scientific apparatus as required to perform specific missions.

One of the foremost design features of the LRV is the method of stowage in the LM and deployment on the lunar surface. Design specifications required that the LRV be folded to 50 percent of the initial length and 70 percent of the initial width (fig. 2) and to retain deployment capabilities that require a minimum of astronaut effort on the lunar surface.

### FOLDING AND STOWAGE

The LRV is stowed in the folded configuration in the LM in a triangularly shaped envelope 1.78 meters wide, 1.65 meters high, and 0.94 meter deep (figs. 2 and 3). The LRV is secured in this bay to three structural hardpoints and positioned by tripods

---

\*The Boeing Company, Huntsville, Ala.

mounted to the front of the LRV center chassis (point 10A, fig. 4) and a support tube (item 21, fig. 3) attached from the bay to the rear of the center chassis. The tripods are discarded after deployment.

The LRV is prevented from unfolding by pin-and-clevis type latches between the center-chassis vertical console post and the forward and aft chassis. These latches are released by cables on the saddle fitting during the deployment sequence. The saddle fitting is attached to the forward chassis by a similar latch that is released by the astronaut after deployment. The wheels are held in the folded position by aluminum struts between the wheel drive motors and the corresponding chassis. These struts are released by cable assemblies within the individual chassis when the chassis is within  $10^\circ$  of the fully unfolded position.

Two torsion springs are used to unfold the forward chassis while torsion bars unfold the aft chassis and the wheels. The aft torsion bar is at the neutral position with the chassis folded up approximately  $80^\circ$ . Therefore, it not only unfolds the chassis but decelerates and reduces the dynamic loading before chassis latching in the unfolded position. The chassis are latched in the unfolded position automatically by spring-loaded shear pins, two in each of the four chassis hinges.

### DEPLOYMENT REQUIREMENTS

The following are the requirements for deploying the LRV on the lunar surface.

1. The capability must exist to deploy the LRV when the LM is at any attitude within  $14.5^\circ$  of vertical, on a  $6^\circ$  maximum lunar slope, and with the lower LM bay hard points from 0.356 to 1.58 meters from the lunar surface. The worst-case condition occurs if one leg of the LM is in a hole 0.61 meter deep.
2. The capability must exist for LRV deployment between the adjacent LM legs within a specified ground envelope that allows astronaut clearance between the LRV and LM legs for LRV separation.
3. The capability must exist for LRV deployment by the 2-man crew with minimum effort, under full control, within 15 minutes. The following limitations were placed on the motions required of a suited astronaut: arm motion (hand-over-hand pull is preferable to turning a rotating crank or pushing) and gripping capability of a gloved hand. Pull in a free-standing condition on the lunar surface is limited to 120 newtons (27 pounds force).

### ALTERNATE DEPLOYMENT CONCEPTS

The initial concept was a system that would deploy the LRV onto the lunar surface automatically with a single pull of a D-shaped handle. Test and analytical results soon indicated that this system would not deploy the LRV repeatedly within the required confidence level. Modifications were then made that added discrete stops to the

deployment sequence, and additional handle pulls were required after each stop to continue deployment. This semiautomatic system was fully space qualified but was abandoned primarily because of the dynamics and complexity of the required deployment steps. Other drawbacks were the difficulty of deployment demonstration of a full-weight LRV under earth-gravity conditions and the possible difficulty in deploying under certain malfunction conditions. Therefore, a decision was made by the NASA Marshall Space Flight Center (MSFC) to initiate the design of a system called the manual SSE in parallel with the design of a semiautomatic system. The initial concept of a manual system was proposed by the MSFC; however, the design of this system was a joint effort between the MSFC and the LRV contractor.

## SEMIAUTOMATIC SYSTEM

The first LM/LRV interface limited the points of contact to three (items 2 and 12, fig. 3). To use these hardpoints, the SSE required a window-frame structure from which the remaining SSE and the LRV were to be supported. Further refinements resulted in discarding this frame and allowing the LRV to be supported by the LM structure with additional low-load LM-to-SSE attachment points.

The original LRV deployment concept was that the folded LRV would pivot out of the LM bay around the two lower hardpoints (item 2, fig. 3) while controlling the movement with cables from the top of the LM bay to each side of the LRV center chassis (points 4A and 4B, fig. 4). These cables were to be controlled by constant-force springs. Next, walking hinges were added (item 4, fig. 3), a mechanism that automatically transferred the point of LRV rotation during deployment from the lower LM hardpoint/LRV tripod interface (point 2A, fig. 4) to the walking-hinge/center-chassis interface (point 4C, fig. 4). In effect, this moves the point of rotation of the entire folded LRV out from the LM approximately 30 centimeters, allowing the forward chassis and wheels to clear the LM bay during deployment. Also required was an assembly of telescoping tubes (item 5, fig. 3 and point 14A, fig. 4) pivoting about attachments between the lower LM hardpoints and terminating at a saddle fitting (item 7, fig. 3) attached by a clevis-pin arrangement to the front of the LRV forward chassis. By adjusting cables and timing the release of various latches, this system then would completely unfold the LRV in midair and lower the entire vehicle to the surface. The constant-force springs were later replaced with velocity-controlled rotary dampers to ensure LRV deployment at a fairly constant velocity. The "rotary dampers" were essentially rotary escapement mechanisms attached to cable drums. Developmental testing soon indicated that it was not practical to deploy the LRV under fully automatic control. Then, the automatic system was converted to semiautomatic status by the addition of a fixed-length center deployment cable and a second D-shaped handle mechanism sequentially released by the center cables. This system was also subject to various dynamic problems, and a decision was made to develop a manually controlled system in parallel with the described semiautomatic SSE.

## MANUAL SYSTEM

The manual system was to use as much of the semiautomatic equipment as practical because of the time constraints. The following changes were made to the semiautomatic SSE.

1. The three rotary dampers were replaced with two worm-gear, cable-drum mechanisms (items 13 and 14, fig. 3). These mechanisms use selflocking worm gears attached to the deployment cable drums and are actuated by a reel of nylon tape large enough to be gripped by the gloved astronaut so that this equipment can be operated within the capability of the astronauts for hand-over-hand pull.
2. The center telescope-tube saddle assembly was modified to require only one center deployment cable (item 8, fig. 3), which performs all required unlatching functions as well as stopping the rotation of the vehicle forward chassis at  $45^\circ$  and then lowering the front wheels to the lunar surface.
3. The D-ring mechanism (item 1, fig. 3) was modified to remove D-ring 2 and to require only a single pull of D-ring 1 to unlatch the vehicle. Thus, only one ascent to the LM porch is required in order to initiate deployment.
4. The placement of the deployment cable reels was changed from separate interface points on the LM to the SSE upper diagonal (item 15, fig. 3), and the diagonal was modified by the addition of cantilevered outriggers (item 16, fig. 3) to help absorb deployment-cable shock loads.
5. All this equipment could be operated within the capability of the astronauts for hand-over-hand pull with the deployment tape large enough to be gripped by astronaut gloves.

These changes resulted in the final deployment system used by the Apollo 15 and 16 astronauts on the lunar surface.

## DEPLOYMENT SEQUENCE

The following deployment sequence was used. Each step is referenced to parts of figure 4.

1. The protective LM thermal blanket is removed from the bottom of the LRV, and deployment tapes are laid out for easy access (part 1).
2. The astronaut ascends the LM ladder and pulls the D-ring to release the attachment pins (part 1). The pushoff spring then will revolve the LRV out around the lower hardpoints, its velocity controlled by the rate of astronaut pull on the right-hand deployment tape (part 2). At  $15^\circ$  of LRV rotation, the point of rotation will transfer from the lower hardpoints to the walking hinges (part 3). At this point, the necessity may occur for the second astronaut to pull on a deployment cable to help the LRV over

center. Therefore, current procedures require that this cable be manned by the second astronaut for all deployment activities. This cable is attached to the rear of the aft chassis and over the top of the LRV center chassis and its use is required in certain LM landing attitudes.

3. At  $45^\circ$  of rotation, the cable from the center braked-reel assembly to the telescopic-tube saddle becomes tight (part 4), releasing the forward and aft chassis locks. (It starts with a fixed amount of slack.) The aft chassis and wheels then deploy by spring action (parts 5, 6, and 7). This is the only dynamic motion in the manual SSE deployment. The forward chassis is prevented from deploying at this time by antireverse latches on the telescopic-tube assembly.

4. The LRV center chassis then continues to rotate, still controlled by the right-hand deployment tape, until the rear wheels touch the lunar surface (parts 8 and 9). The center chassis is unlocked from the walking hinge by means of a cam-actuated latch at approximately  $70^\circ$  of chassis rotation but will not move out from the walking hinges as long as tension is on the steel deployment cables (part 9).

5. With the rear LRV wheels on the surface, continued pull on the right-hand deployment tape puts slack in the steel deployment cables and allows the center chassis to move out of the walking hinges and the forward chassis and wheels to deploy by means of spring action (part 11). The steel deployment cables are then released from the center chassis and discarded.

6. The astronaut then pulls on the left-hand deployment tape, which controls the center steel deployment cable and lowers the front of the LRV to the surface (parts 11, 12, and 13). A pull on the saddle-release cable then releases the telescopic-tube saddle from the LRV (part 14), completely freeing the LRV from the LM. Then, the contingency deployment cable, aft wheel-lock tethers, and SSE tripods are removed from the LRV by the action of quick-release pins and are discarded.

#### DEPLOYMENT TESTING AND ANALYSIS

All LRV components were subjected to static and dynamic analysis and to testing in a vacuum at high and low temperatures as well as under ambient conditions. Some critical components were tested functionally while coated with a layer of simulated lunar dust.

With the exception of short 1/6-weight flights in a KC-135 aircraft, there is no way to simulate a lunar-gravity environment, and the deployment system depends on the force of gravity and inertia to operate. Therefore, the deployment system was analyzed by a computer program that simulated lunar deployment conditions. This program was checked by changing the parameters to a 1/6-weight, 1/3-inertia LRV and by comparing the resulting simulated deployments with actual deployments performed with a special 1/6-weight, 1/3-inertia test LRV.

During this program, the SSE was subjected to developmental, qualification, and acceptance tests. The following areas were included in the tests.

1. Static and dynamic structural load tests.
2. Vibration tests through the complete envelope in the three basic attitudes while the SSE was supporting a full-weight LRV (vibration test vehicle).
3. Deployment from the required deployment angles of the LM with the LM at both maximum and minimum heights and with the deployment surface at the required slant angles. These tests were run with the 1/6-weight test unit for dynamic deployment and with the full-weight qualification-test LRV for clearance and envelope determination.
4. Thermal-vacuum testing and deployment of the 1/6-weight unit under actual lunar conditions of vacuum and temperature after cold soak in space environment and with a one sun thermal environment.
5. Drop test using the qualification vehicle installed in a flight-configuration LM. This test simulated interface integrity during the lunar-landing phase.

During the testing just described, the following requirements were met.

1. Deployment from any LM angle within a  $29^\circ$  conical angle from vertical
2. A 0.356- to 1.58-meter ground clearance below the LM hardpoints
3. A  $6^\circ$  maximum ground slope
4. The LRV center-of-gravity location restraint in the LM bay
5. Thermal: mean temperature LM/LRV attachment points of  $200^\circ$  and  $395^\circ$  K
6. Vacuum:  $1.33 \text{ by } 10^{-7} \text{ N/cm}^2$  ( $10^{-5}$  torr)
7. Deployment in a thermal vacuum within 15 minutes

#### SIGNIFICANT DESIGN FEATURES

Some of the design features that differentiate the SSE design from a normal design for this type of mechanism are as follows.

1. The use of rigid tubing (item 6, fig. 3) rather than cables to pull lock pins, requiring only one lock instead of individual locking pins.
2. The use of very loose clevis joints on the release mechanism to preclude the need for rod-end bearings.

3. The use of controlled friction at the gear faces of the braked-reel assembly to make a self-locking worm drive from a worm drive that could normally be back-driven with full lubrication. This was accomplished by running a clean bronze worm gear with a dry-film,  $\text{MoS}_2$ -lubricated, hardened-steel worm.

4. The use of graphite-filled nylon bearings with aluminum shafts throughout the gearbox.

#### CONCLUDING REMARKS

The overall success of this design was demonstrated on the Apollo 15 and 16 missions.

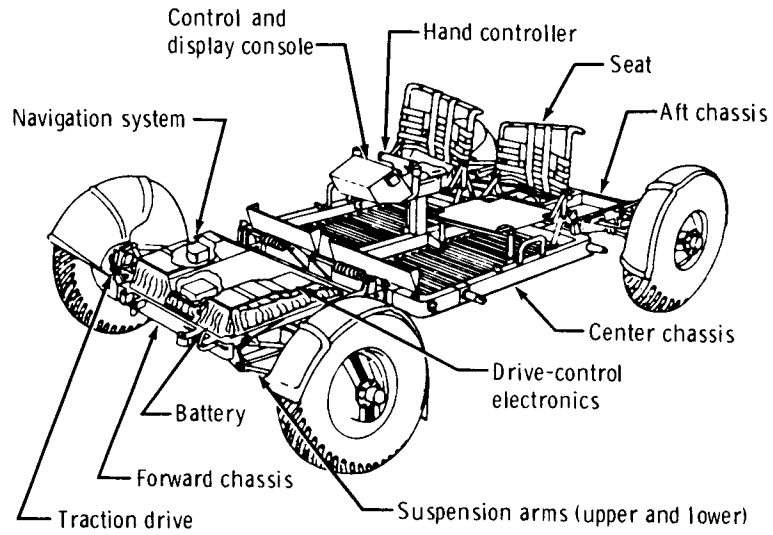


Figure 1. - Lunar roving vehicle, unfolded.

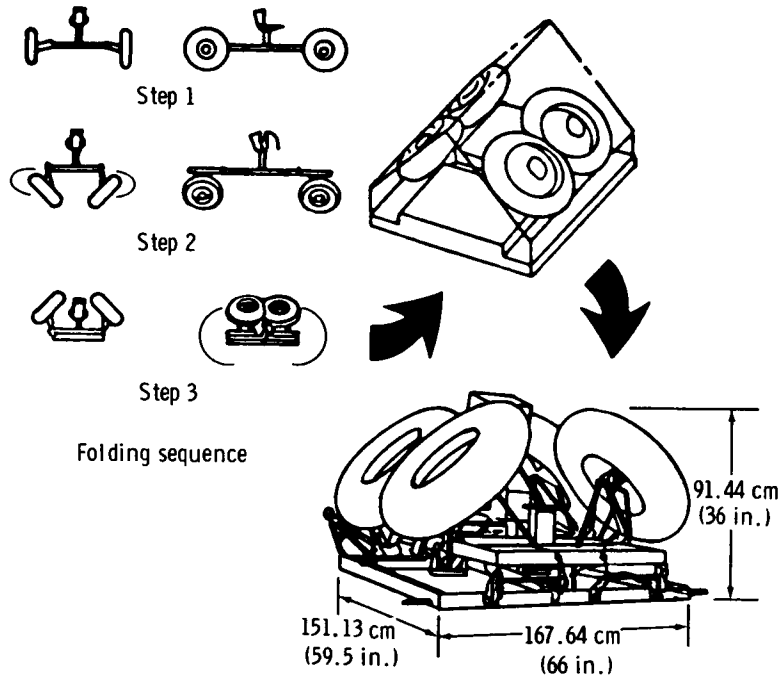
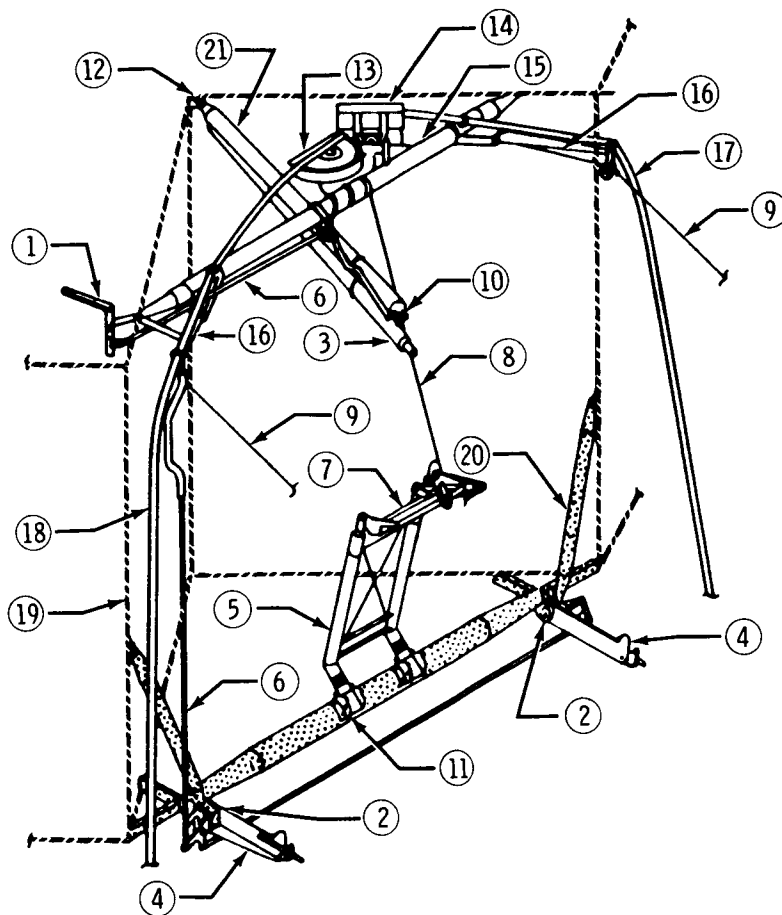


Figure 2. - Lunar roving vehicle, folded.



- |                            |  |
|----------------------------|--|
| ① D-handle mechanism       | ⑬ Center braked-reel assembly                                |
| ② Lower LM hardpoints      | ⑭ Side double-braked-reel assembly                           |
| ③ Pushoff spring assembly  | ⑮ Upper diagonal   |
| ④ Walking hinges           | ⑯ Upper diagonal outriggers                                  |
| ⑤ Telescopic tube assembly | ⑰ Right-hand deployment tape<br>(for side deployment cables) |
| ⑥ Release-system mechanism | ⑱ Left-hand deployment tape<br>(for center deployment cable) |
| ⑦ Saddle assembly          | ⑲ Outline of LM bay  |
| ⑧ Center deployment cables | ⑳ LM structure   |
| ⑨ Side deployment cables   | ㉑ Support tube   |
| ⑩ Upper release pin        |  |
| ⑪ Antireverse latches      |  |
| ⑫ Upper LM hardpoint       |  |

Figure 3. - The LM-mounted space support equipment.

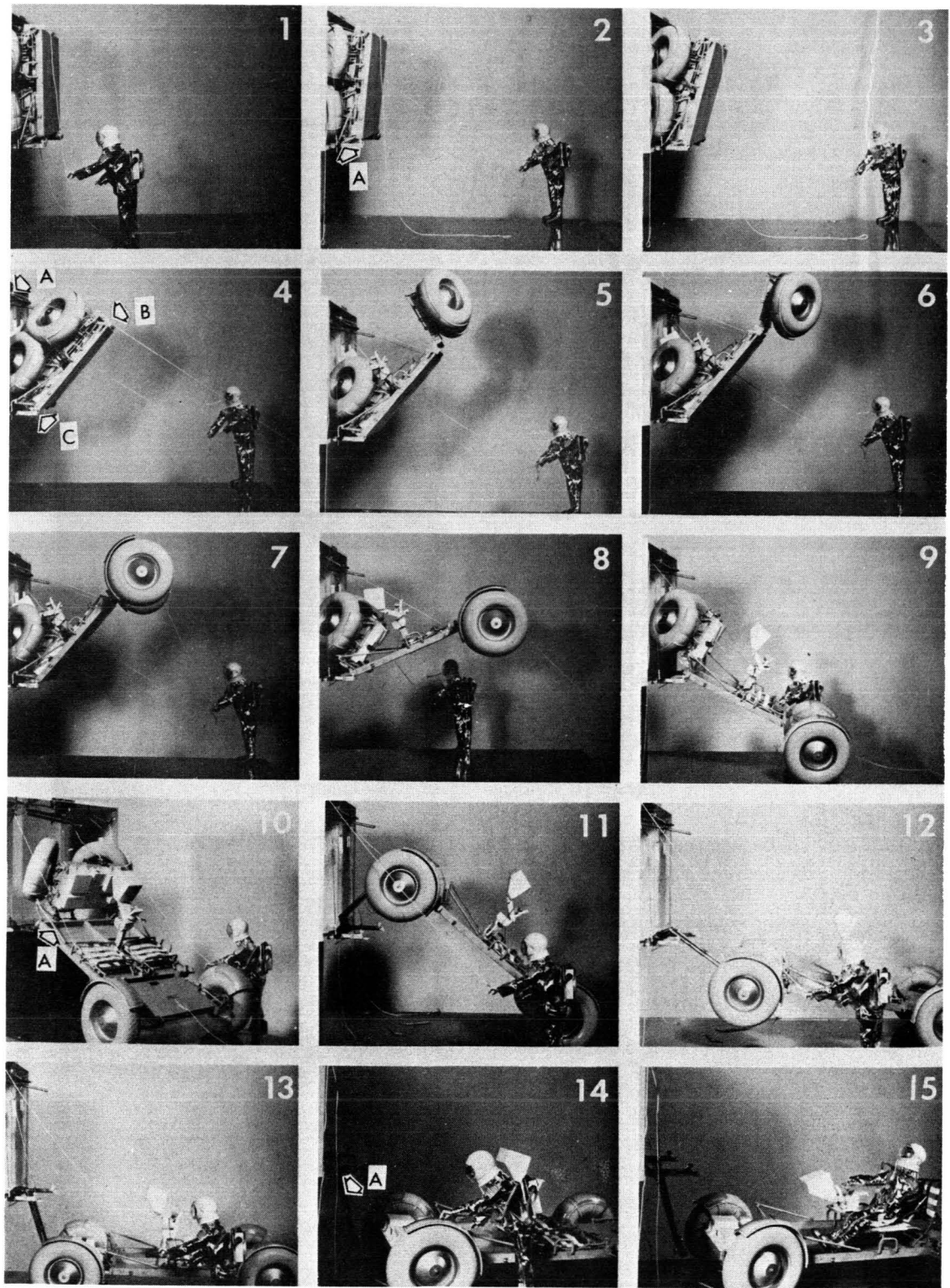


Figure 4. - Lunar roving vehicle, deployment sequence.

## RADIOMETER-DEPLOYMENT SUBSYSTEM

Kevin M. Speight\*

### ABSTRACT

A radiometer-deployment subsystem for the Nimbus E spacecraft has been designed, developed, and qualified for space use. The dimensions of the radiometer are 0.9 meter square by 0.1 meter, and it weighs 32 kilograms. Rigidly secured to the spacecraft during launch, the radiometer is deployed when the spacecraft reaches orbit. Deployment is achieved without permitting any portion of the radiometer to intersect the field of view of the infrared horizon scanner. This accomplishment necessitated a nonlinear deployment profile, which was accomplished by using a four-bar linkage composed of arms, cams, pivots, and steel tapes.

### INTRODUCTION

The electrically scanning microwave radiometer (ESMR) deployment subsystem is designed to support the ESMR during spacecraft launch and to deploy or to retract the ESMR upon command. This subsystem is a portion of the Nimbus E weather satellite scheduled for launch later this year (fig. 1). During spacecraft launch, the radiometer is held securely in a vertical position with pyrotechnically activated bolts. The earthward side of the radiometer (waveguide surface) is held against the structure in such a way as not to damage the radiometer. The radiometer bolts are released in orbit, and the radiometer is deployed to a near-horizontal position. A major requirement of this subsystem is that of never allowing the radiometer or any of the supporting equipment to enter the field of view of the attitude control system horizon scanner. This requirement led to a design using cams and tapes, which would cause the radiometer to counterrotate about the deployment arms as the arms were driven to the deployed or retracted positions. Essentially, the principle involved is that of a four-bar linkage mechanism.

---

\*General Electric Company, Valley Forge, Pa.

## DESIGN CRITERIA

The ESMR deployment subsystem was designed to meet the following requirements.

1. Deploy and retract radiometer upon command
2. Deploy/retract time: 4 to 6 minutes
3. Deploy/retract in such a way as not to interfere with infrared scanner field of view or the volume swept by solar paddles
4. Mechanism weight: 15.9 kilograms maximum
5. Spacecraft power not required to keep radiometer deployed or retracted
6. Deploy to a position accuracy of  $\pm 1^\circ$
7. Required motor power: 12 watts maximum
8. Natural frequency stowed (locked) shall be greater than 65 hertz
9. Natural frequency deployed shall be greater than 1.3 hertz

## DESCRIPTION

### General

The ESMR deployment subsystem consists of a rigid support structure that houses the drive mechanism, drive shaft, lower cams, tape-adjustment device, positive stops (for the deployment arms), retract limit switches, and associated telemetry thermistors and cabling. The drive mechanism contains a two-phase ac servomotor and gearhead, a magnetic hysteresis brake, a ball-detent clutch, a torque-out device (soft coupling), the associated cabling, a position potentiometer, and the deploy limit switches. Attached to each end of the drive shaft is a deployment arm. At the radiometer end of each arm is the upper pivot assembly, consisting of a torsion spring, the upper cam, a position potentiometer, and the radiometer-attachment fittings.

As the deployment arms are driven from a position of  $10^\circ$  off spacecraft vertical to a position of  $120^\circ$  off spacecraft vertical, the tapes bear against the upper and lower cams, causing the tapes to pull the radiometer in a counterrotating fashion to the desired deployment profile. As the tapes unwind from the upper cams, they wind on the lower cams. When the arms reach the  $120^\circ$  position, they bear against positive stops, causing the soft coupling to wind to a predetermined torque level and to trip the deploy limit switch that removes power from the motor. The magnetic hysteresis brake prevents the radiometer from leaving the fully deployed position. The radiometer is shown in the retracted, the partially deployed, and the deployed positions in figures 2, 3, and 4. The large yokelike structure is part of the counterbalance.

## Drive Assembly

The drive assembly consists of an aluminum housing that contains the motor/gearhead, clutch, and soft coupling (fig. 5). The overall housing dimensions are 10.1 centimeters by 10.8 centimeters by 12.7 centimeters.

### Motor/Gearhead

The motor/gearhead unit utilizes a size 11, two-phase servomotor capable of delivering  $2.83 \times 10^4$  dyne-centimeters (0.4 ounce-inch) of torque (with brake attached) at stall when energized with 27-volt root mean square, 400-hertz square wave. Power dissipation under this condition is less than 6 watts per phase. The motor bearings are class ABEC 7 with balls and races of 440C stainless steel. The bearing retainers are made of bleached cotton-based phenolic and are vacuum impregnated with SF-50 silicone fluid.

Attached to the motor is a 8203:1 gearhead composed of six stages of spur gearing and a planetary output system. The gear material is 17-4 PH stainless steel with Micro-X nitriding to increase surface hardness. All bearings containing metallic retainers or full complement bearings are packed with G300 SC silicone grease to 25 percent of the available volume. The gearhead bearings all have balls and races of 440C stainless steel. The gear lubricant is also G300 SC silicone grease.

Attached to the opposite end of the motor is a magnetic hysteresis brake, which develops a constant drag equivalent to  $0.7 \times 10^4$  to  $1.0 \times 10^4$  dyne-centimeters (0.1 to 0.14 ounce-inch) of torque. The brake consists of a permanent magnet rotating inside a cobalt ring to maintain the soft coupling-locking torque by preventing backdriving of the geartrain.

The motor/gearhead is capable of continuously driving a load of  $56.5 \times 10^6$  dyne-centimeters (800 ounce-inches) at a base-plate temperature of  $298.15^\circ \text{K}$  ( $25^\circ \text{C}$ ). The static load rating is  $106 \times 10^6$  dyne-centimeters (1500 ounce-inches). This device has an output speed of  $160^\circ$  to  $200^\circ/\text{min}$  at a load of  $13.5 \times 10^6$  dyne-centimeters (192 ounce-inches). The motor/gearhead pinion joins a beryllium copper gear lubricated with dry-film metallic-bonded molybdenum disulfide. Six clutch-housing retainer mounts are an integral part of this gear. Each mount contains a compression spring, a plunger, and a clutch ball. Dyflon bushings are pressed into each end of the gear. Through the bushings, the gear is supported on a 0.635-centimeter 440C stainless-steel intermediate shaft.

The intermediate shaft is an integral machined part with the clutch plate. The shaft contains 30 equally spaced conical detents on one side and reaction pins for three soft coupling springs on the other side. The shaft is supported on both ends by Dyflon bushings (asbestos-filled Teflon). The output pinion is made of Society of Automotive Engineers (SAE) 4340 with a hardness of Rc 50 and is isolated from the shaft with Dyflon bushings. This gear is an integral machined part with three leaf-spring mounts and a spring preload arm. The total gear is covered with a black oxide coating to retard corrosion. This output pinion is coupled to a beryllium-copper segment gear, which transmits the torques to the main output torque tube. This stainless-steel tube transmits the torques to the center of the output shaft, which, in turn, is coupled to both arms.

## Clutch

The simple ball-detent-type clutch uses 440C stainless-steel-ball actuators, 0.476-centimeter standard hardened 440C stainless balls, and 302 stainless-steel-coil compression springs packaged in an aluminum case. The actuators and the balls are dry lubricated with a phenolic resin-bonded molybdenum-disulfide coating to prevent cold welding. Each clutch-housing assembly is calibrated to 5.45 kilograms by use of laminated shims. In an engaged position, the coil springs are operating at 50 percent of the allowable stress level; in the slip condition, they operate at 75 percent of the allowable stress level. Maximum compressive stresses occur during clutch slip when the spherical ball is pressed against the hardened flat clutch plate, at which time 60 percent of the maximum-allowable Hertzian stresses are achieved. The clutch is calibrated for  $113 \times 10^6$  dyne-centimeters (100 inch-pounds) of torque, and the main purpose of the clutch is to protect the gearhead during ground handling. The clutch also serves as a protective overload device during space deployment or retraction. A single failure of any of the six clutch assemblies will result in a clutch torque greater than the maximum-anticipated deployment torques.

## Soft Coupling

When the radiometer is in the deployed position, the soft coupling takes up the backlash in the system and maintains a positive force by pressing the arms against hard stops. After the arms have engaged the stops, the motor continues to drive until the soft coupling has reached a preset deflection, providing a torque of  $62.2 \times 10^6$  to  $79 \times 10^6$  dyne-centimeters ( $186 \times 10^6$  to  $237 \times 10^6$  dyne-centimeters at the main drive shaft). When the desired torque level is reached, a limit switch is actuated to remove power from the motor. The spring action is developed by three double-leaf springs made from beryllium copper.

## Arms, Tapes, and Cams

The deployment arms are fastened to the drive shaft at one end and, through a pivot assembly, to the radiometer-attachment fittings at the other end. The pivot assembly (fig. 6), consisting of the upper cams, the Dyflon bushings, and the torsion springs, provides a positive torque about the radiometer pivot, which maintains tension in the tapes and provides the force for the angular motion of the radiometer during retraction. The torsion springs are made from chrome vanadium and coated with molybdenum disulfide. Each of the two springs produce a torque of  $13.6 \times 10^6$  dyne-centimeters (12 inch-pounds) at the retracted position and  $21.5 \times 10^6$  dyne-centimeters (19 inch-pounds) at the deployed position.

The tapes are made from a cobalt-nickel alloy called Elgiloy. This nonmagnetic material provides a high resistance to set, fatigue, and corrosion. The tapes measure 0.01 centimeter by 0.96 centimeter by 0.92 meter and provide an ultimate tensile strength of  $2 \times 10^9$  newtons/meter<sup>2</sup> (300 000 psi).

As the radiometer deploys, the Elgiloy tapes bear against the stationary lower cams and the rotating upper cams. The cams are cut so that the counterrotating motion of the radiometer prevent it from entering the field of view of the infrared scanner.

### Flexible Cables

The electrical interface to the radiometer is made through two flat flexible cables. The cables were designed to be flexible, electrically shielded, and impervious to ultraviolet radiation. The basic cable consisted of highly stranded circular copper conductors imbedded in a soft silicone rubber; a layer of Kapton was then put over the cable. The Kapton provides exceptionally good puncture resistance. A radio-frequency shield was then added over the Kapton, and the entire cable was covered with a fiber-glass boot. The fiber-glass was impregnated with black silicone rubber for ultraviolet radiation protection. The radio-frequency shield was soldered directly to the connector shells at both ends.

### TESTING

A counterbalance was attached to the radiometer to facilitate deployments in a one-g field. The counterbalance consists of a large yoke, which attaches to the radiometer side fittings and permits movement within the yoke. Steel cables were run through pulleys mounted in the 10.36-meter (34 foot) ceiling of the high-bay area and then were run to a dead-weight. A balance within 0.91 kilogram (2 pounds) was achieved.

Vacuum-thermal testing is done with a lightweight dummy radiometer and dumb-bell weights cantilevered off the deployment arms. The prototype deployment subsystem was successfully vacuum-thermal tested for qualification. The temperatures were cycled between the limits of 262.15° to 318.15° K (-11° to 45° C) and deployments were made at the temperature plateaus. The testing was performed at a pressure of  $1.33 \times 10^{-4}$  N/m<sup>2</sup> ( $10^{-6}$  torr) for a duration of 6 days. The prototype subsystem was also installed on a structural-dynamics model spacecraft, and the spacecraft vibrated with both sinusoidal and random inputs. The flight deployment subsystem was also successfully vacuum-thermal tested for 6 days at  $1.33 \times 10^{-4}$  N/m<sup>2</sup> ( $10^{-6}$  torr) at the temperature levels of 265.15° to 313.13° K (-8° to 40° C).

### CONCLUDING REMARKS

A unique radiometer-deployment subsystem has been designed, developed, and qualified for use on the Nimbus E weather satellite. The flight subsystem is presently being integrated into the spacecraft.

## DISCUSSION

**J. H. Parks:**

Requirements for ground-test simulation of such zero-gravity deployment devices frequently impose loading conditions such that these loads can become the governing loads for sizing of structural components. Did such a problem arise in your design?

**Speight:**

Yes. Many of the load-bearing elements of the design were sized according to the stresses developed with the system deployed in a 1-g field without the aid of a counterbalance. For instance, the Elgiloy tapes are sized to support in excess of 227 kilograms of tensile load, whereas only 4 kilograms are required in flight.

**R. J. Peterson:**

Did you consider using a harmonic drive to achieve the high reduction of the gearhead?

**Speight:**

Both a harmonic drive and a wobble-type drive were considered in the conceptual phase of the design. A conventional gearhead of the type previously flight proven on earlier Nimbus vehicles was selected for reliability, cost, and expediency reasons.

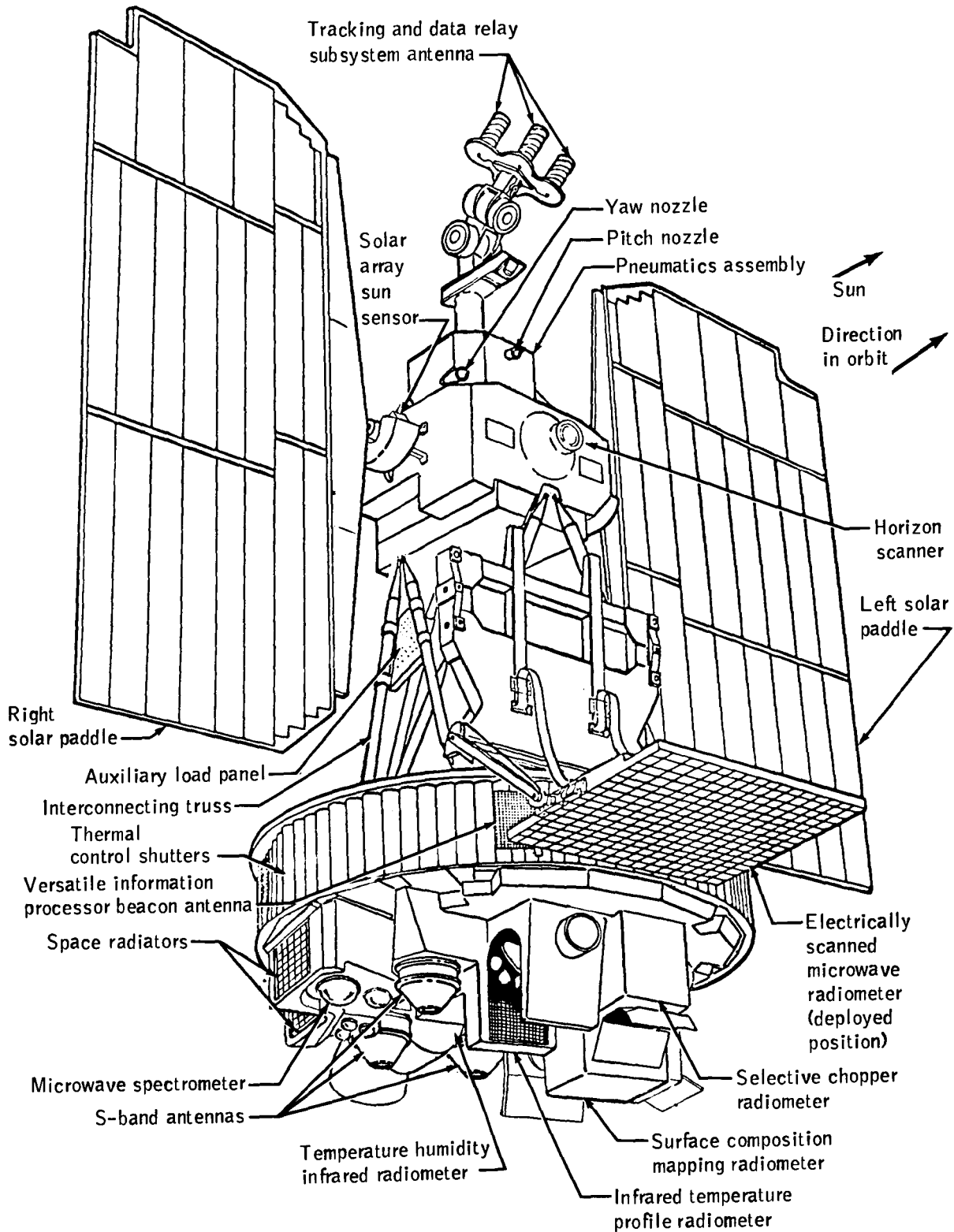


Figure 1. - Nimbus E satellite.

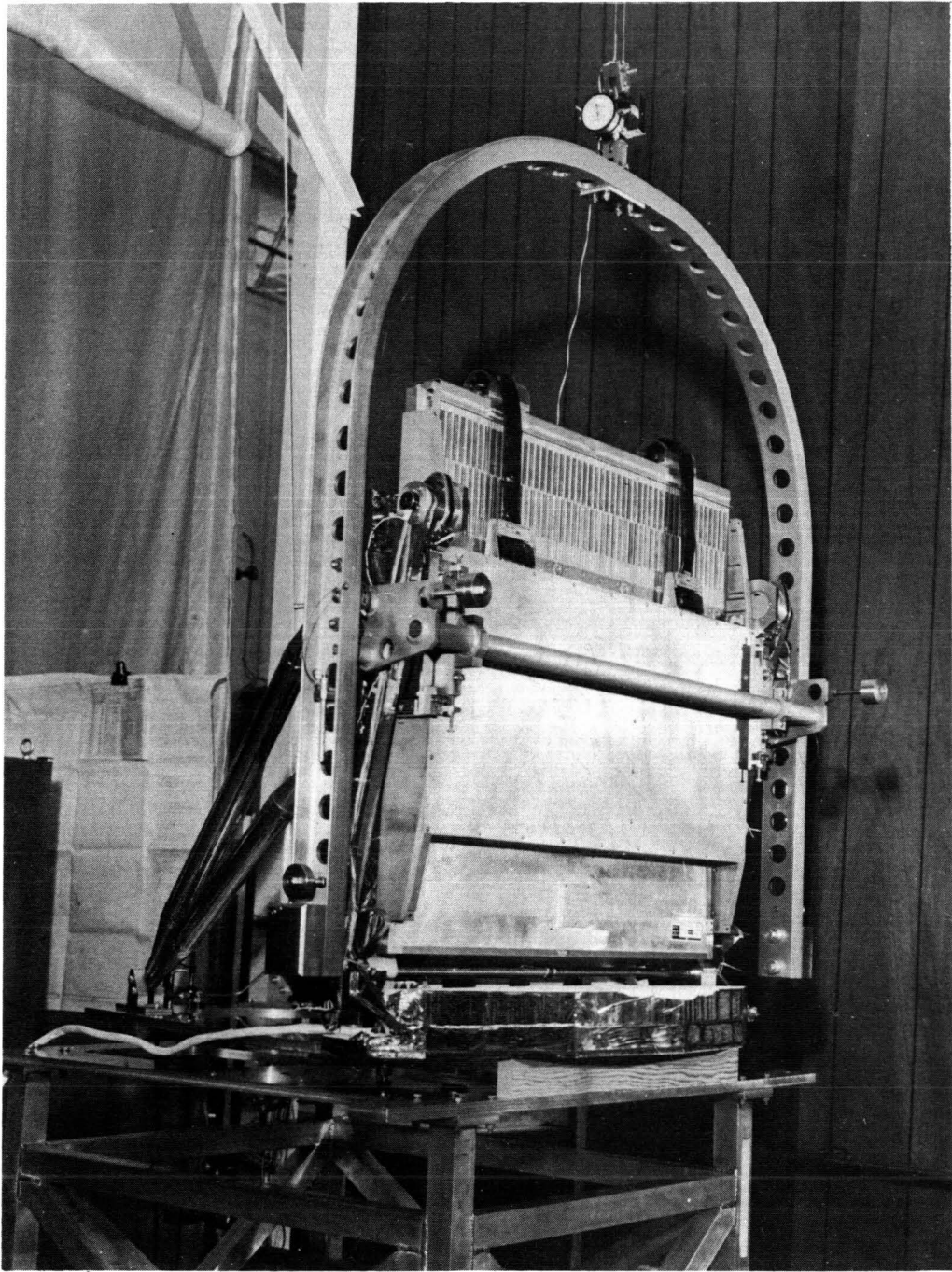


Figure 2. - Retracted radiometer.

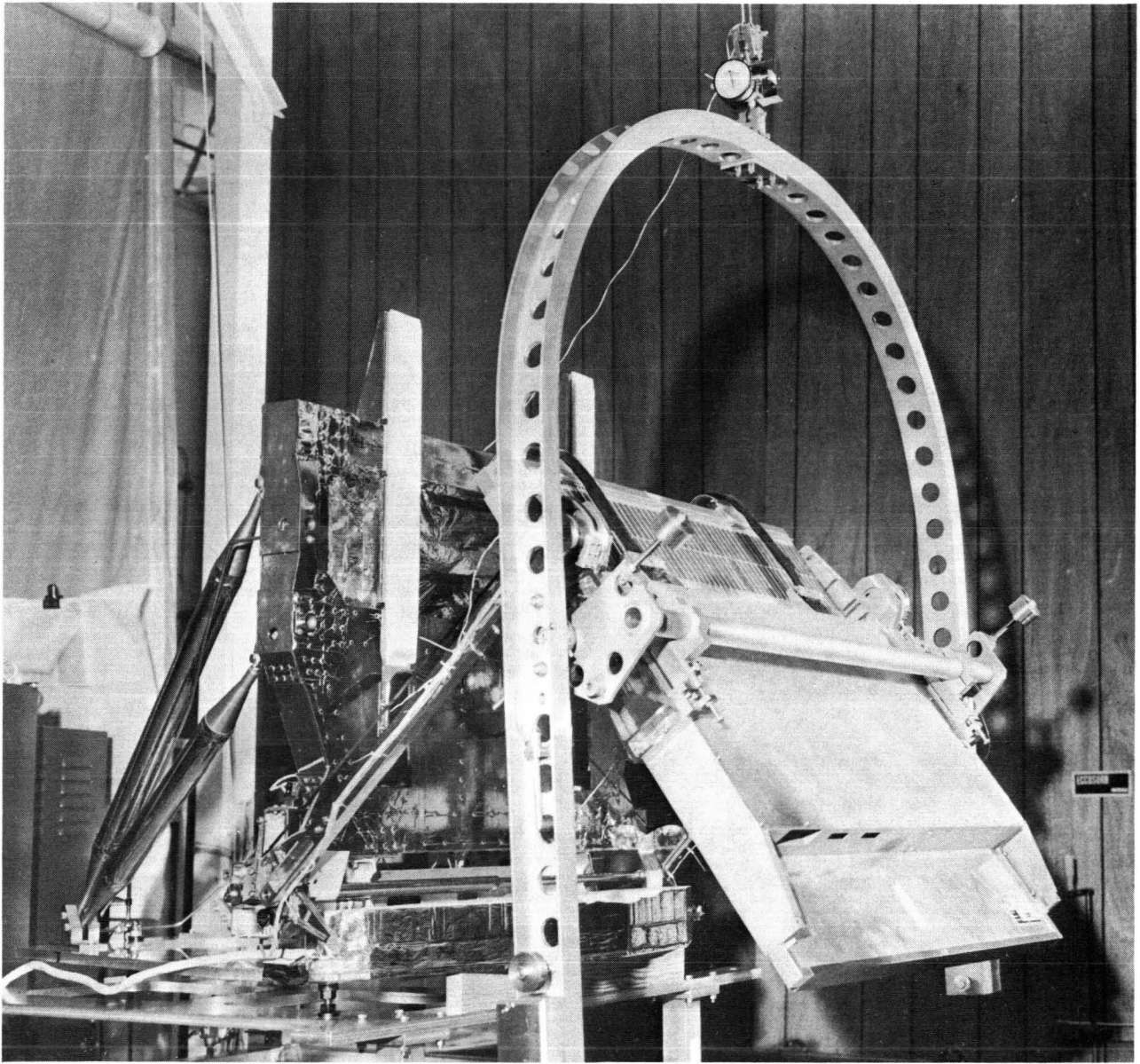


Figure 3. - Partially deployed radiometer.

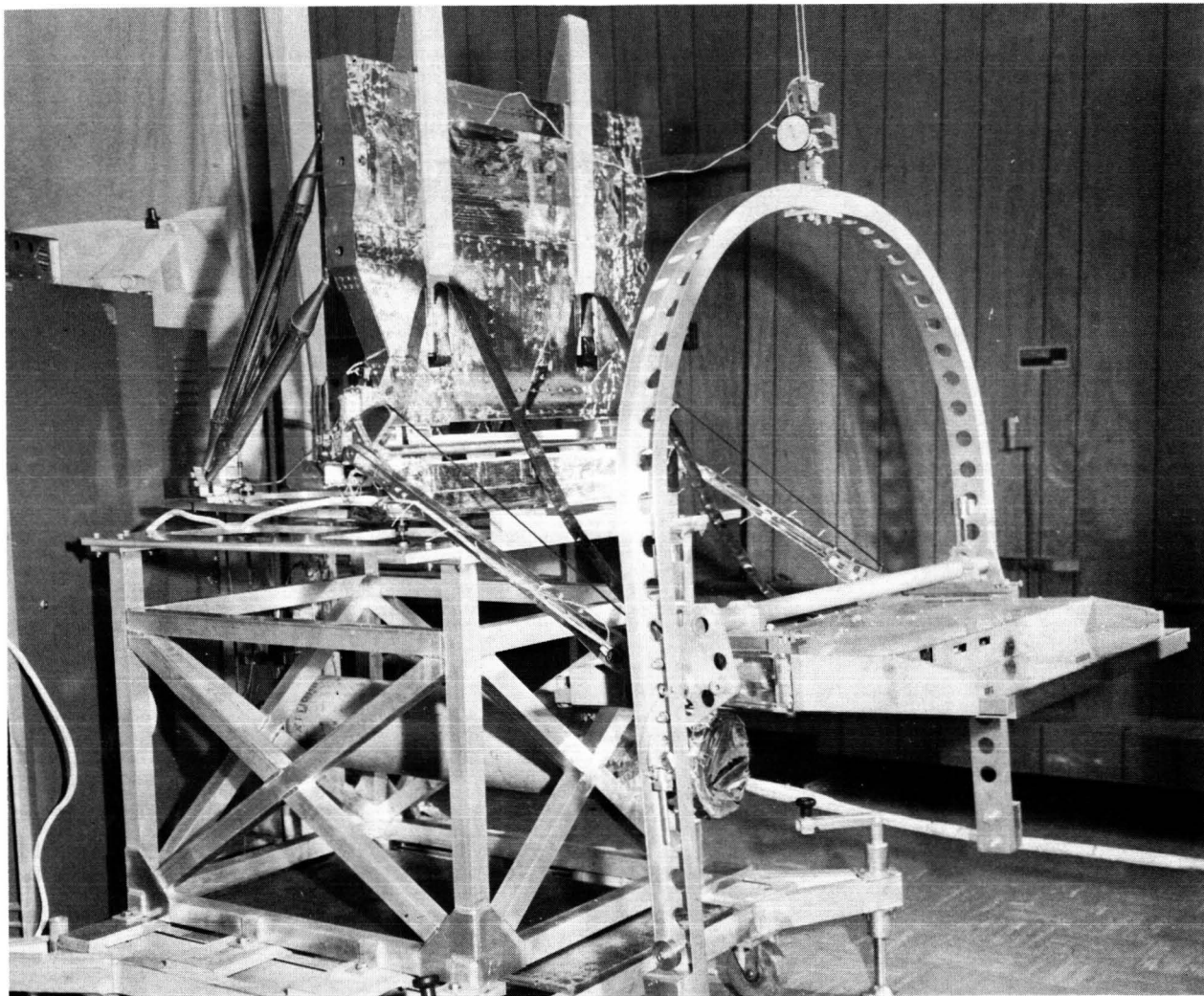


Figure 4. - Fully deployed radiometer.

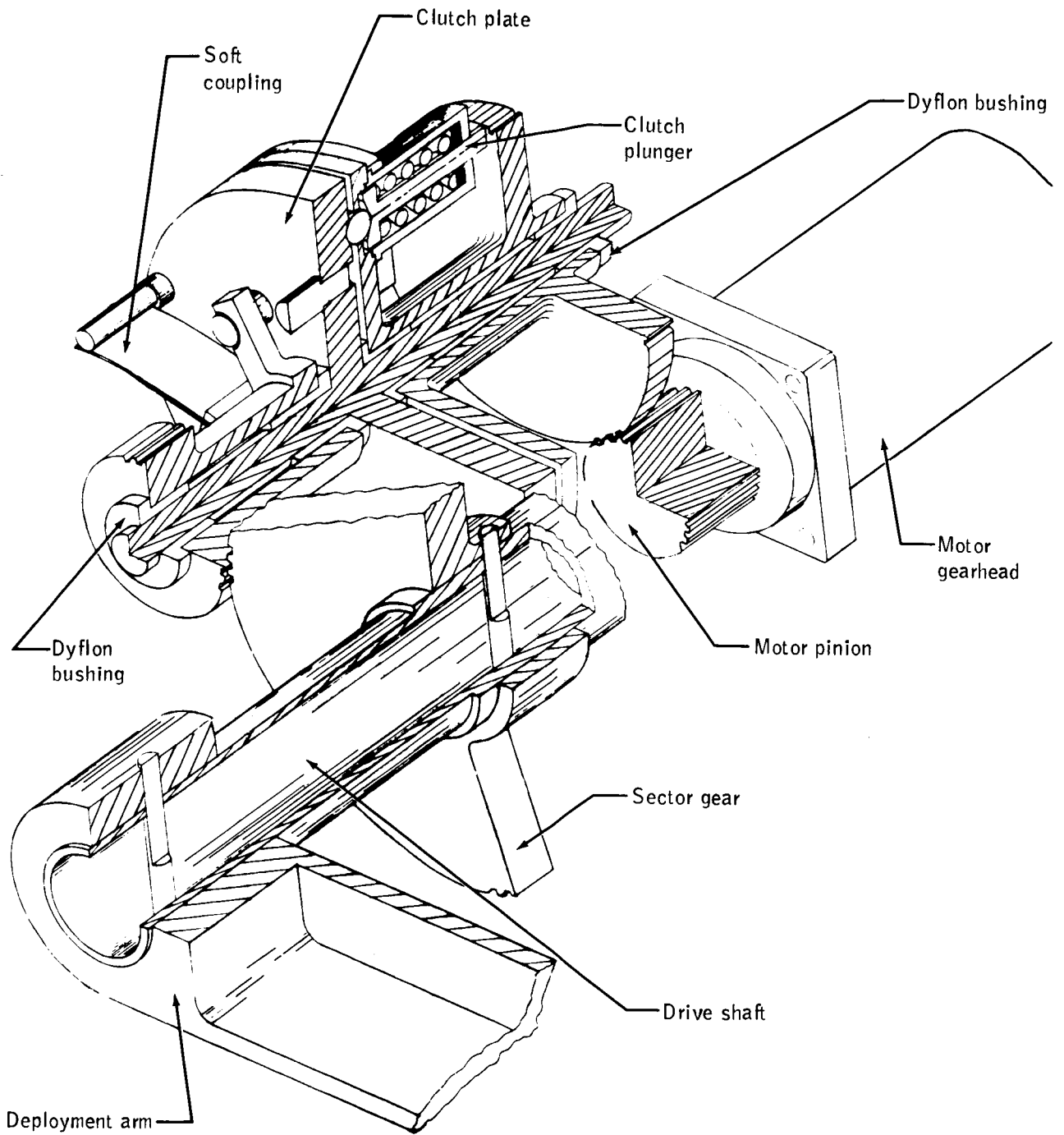


Figure 5. - Electrically scanning microwave radiometer drive assembly.

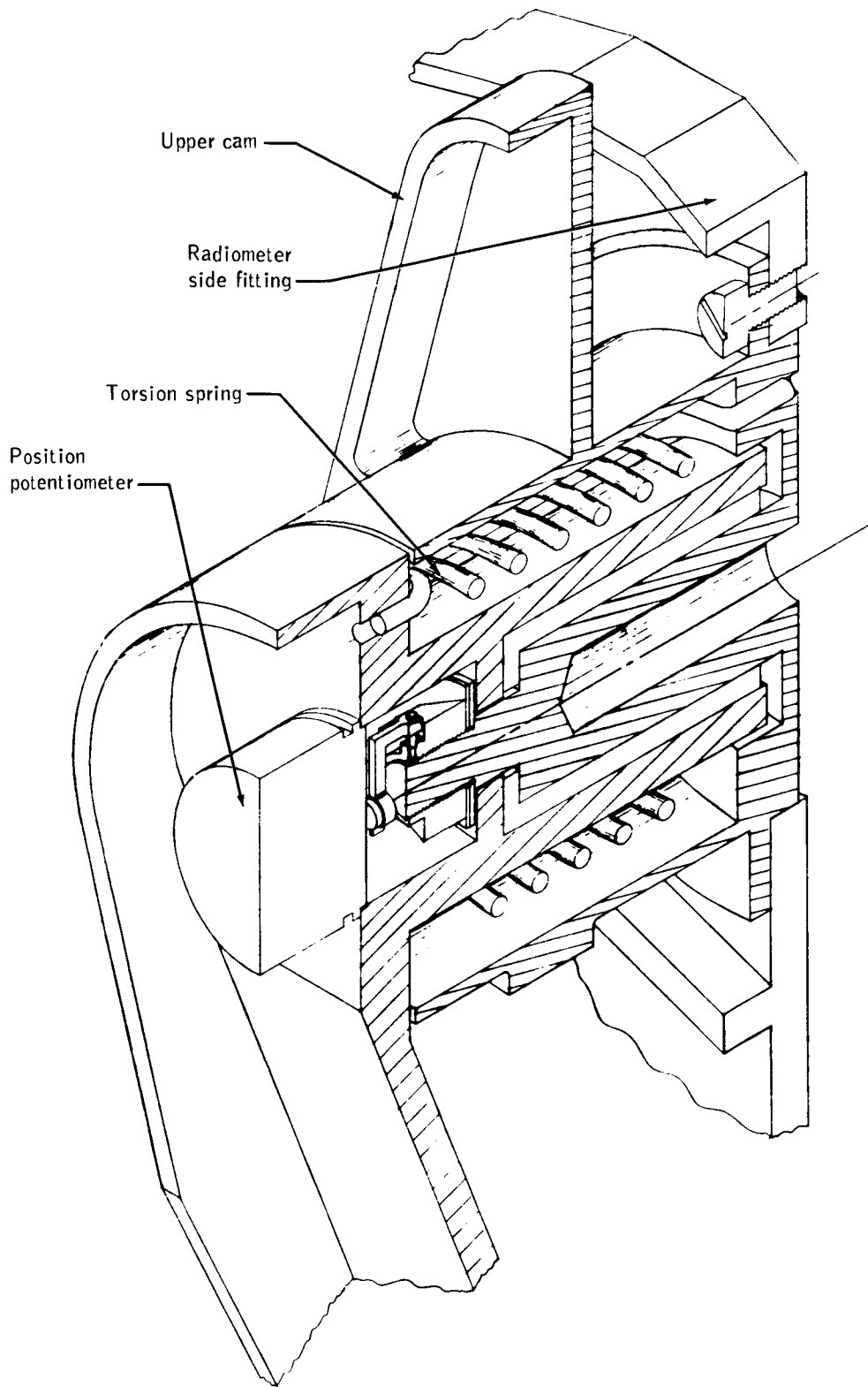


Figure 6. - Upper pivot assembly.

73N/8878

## APOLLO LUNAR MODULE LANDING GEAR

By William F. Rogers\*

### ABSTRACT

The Apollo lunar module landing-gear flight-performance results and three principal gear development problems are discussed in this report. In evaluating the lunar module touchdown performance, strut stroking and toppling stability are the prime factors and are governed primarily by touchdown velocity and surface slope at the touchdown point. Flight results are shown to be well within design values, and the landing-gear has performed successfully in all landings.

### INTRODUCTION

The landing of the lunar module (LM) on the surface of the moon is one of the crucial events of the Apollo mission. During touchdown, the LM landing gear brings the vehicle to rest while preventing toppling, absorbing the landing impact energy, and limiting loads induced into the LM structure.

The purpose of this report is to summarize the landing-gear flight-performance results and some of the problems encountered during development. Three important development problems are discussed: (1) use of a statistical approach to determine realistically the touchdown stability when worst-case combinations of parameters showed unacceptable performance, (2) a significant increase in thermal insulation that was required just before the first lunar landing, and (3) development of the strut bearing.

### GENERAL DESIGN REQUIREMENTS

The landing-gear-subsystem hardware-design requirements may be divided into three general categories: structural, mechanical, and landing performance. The categories are summarized in table I, and the listed items constitute the general standards that were used in determining the adequacy of the landing-gear-subsystem design. The criticality of the landing gear is apparent. Structural or mechanical failure during touchdown could result in loss of life, depending on the mode of failure and whether any attempted ascent-stage abort during landing proved to be successful. Failure to achieve proper touchdown conditions or failure to land in an area of specified lunar-surface topography could result in an unstable landing or in structural failure because of over-stroking a strut.

---

\*NASA Manned Spacecraft Center, Houston, Tex.

## CONFIGURATION DESCRIPTION

The Apollo 11 LM on the lunar surface is shown in figure 1, which illustrates the overall LM and landing-gear configuration. A landing-gear assembly, in both the stowed and the deployed positions, is shown in figure 2, and the major components are shown in figure 3. Each of the four separate landing-gear assemblies has energy-absorption capability provided by honeycomb cartridges in the single primary and the two secondary struts. The deployment truss serves as a structural-mechanical assembly between the landing-gear struts and the descent-stage structure. Each landing-gear leg is retained in the stowed position by a pyrotechnic uplock device. When the device is fired, a titanium strap that is attached to the primary strut and the descent stage is severed, which allows the landing gear to be deployed and locked by mechanisms on each side of the landing-gear assembly.

The primary strut (fig. 4), which is attached to the LM descent-stage outrigger assembly, consists of a lower inner cylinder that fits into an upper outer cylinder to provide compression stroking at touchdown. The footpad, which is attached to the lower end of the inner cylinder by a ball-joint fitting, is approximately 0.91 meter (3 feet) in diameter and is designed to support the LM on a  $0.69 \text{ N/cm}^2$  ( $1.0 \text{ lb/in}^2$ ) bearing-strength surface as well as to maintain sliding capability after having impacted rocks or ledges during touchdown. Attached to each of three of the footpads is a 1.73-meter (68 inch) probe designed to sense lunar-surface proximity and to signal the LM pilot so that he can initiate descent-engine shutdown. The secondary struts (fig. 5) also have an inner and an outer cylinder and are capable of both tension and compression stroking. Detailed descriptions of the landing gear may be found in references 1 and 2.

## LANDING-GEAR DEVELOPMENT PROBLEMS

### Statistical Landing Performance

A major change in the treatment of the landing-performance input parameters occurred as a result of the descent-engine thrust-decay time history. For design purposes, a thrust-decay time of approximately 0.5 second had been assumed. However, a thrust decay of several seconds, which was an extremely destabilizing influence at touchdown, was evident in the actual descent-engine firing data. When the actual thrust-decay time history was combined in a worst-case way with other touchdown parameters, the LM toppling-stability boundary lay well within the design velocity envelope, as illustrated in figure 6. For acceptable stability within the range of touchdown velocities considered, this boundary must lie outside the design envelope. Attempts to reduce the engine thrust-decay time by hardware changes were unsuccessful; therefore, the manner in which the touchdown parameters were combined for design was investigated as a potential solution.

Investigation of the touchdown parameters from piloted simulations revealed that the initial conditions at touchdown did not combine in a worst-case fashion. Furthermore, sufficient data were available to treat the data statistically. Another parameter

that affects touchdown performance significantly is the lunar-surface topography. To make the analysis as realistic as possible, a statistical description of the lunar surface, which consisted of general surface slopes and surface protuberances and depressions, was derived from Lunar Orbiter photography. Descriptions of potential Apollo landing sites were formulated, and the most severe site, based on general surface slope, was chosen for the analysis. The results of the analysis, which are shown in figure 6, indicate the degree of risk involved at touchdown. The analysis showed that the chances of fully stroking any strut was only one in a thousand and that the probability of an unstable landing on slopes of  $12^\circ$  or less was two in a thousand landings. The probability of an unstable landing, when considering all slopes in the landing site, was somewhat higher but was still acceptable. Although these probabilities are based on a Monte Carlo statistical analysis, considerable conservatism is involved. The stability analysis is based entirely on constrained-footpad-type landings; that is, footpad sliding is not considered in calculating toppling stability. For the calculations of stroking, the energy-absorption characteristics of the lunar soil are not considered except for friction as a result of footpad sliding. Furthermore, the statistical surface description is based on the Apollo site that has the most severe topography of the Apollo landing sites originally considered. Finally, no crew selectivity was assumed to be involved in choosing the touchdown point within the landing site. Actual landings on the lunar surface have verified the conservatism involved. All landings have resulted in footpad sliding, the lunar soil absorbed a large percentage of the impact energy, and the LM crews have been able to use some judgment in choosing a landing site in spite of the dust encountered before touchdown. This analysis, which was used to certify the adequacy of the LM landing performance, constituted a criterion change because of the method of combining design parameters.

#### Thermal Insulation

Landing-gear thermal insulation must maintain the landing-gear temperatures at or below design levels to ensure positive structural margins of safety and proper mechanical operation during deployment and landing. Furthermore, temperature control of the honeycomb energy absorbers within specified limits is necessary to preclude large variations in crush-load levels. A summary of the history of the landing-gear thermal-insulation weights is provided in table II.

A significant thermal-design problem was caused by the effects of descent-engine-plume heating near the lunar surface. A few months before Apollo 11, test data indicated that heating rates on the landing gear were much higher than anticipated. At approximately the same time, the LM flight crew expressed a desire to have the option of using either the probe mode or the pad mode for landing. The probe mode is the primary procedure for LM touchdown and consists of descent-engine shutdown initiation after probe contact with the lunar surface but before footpad contact. The pad mode is considered a backup landing mode in which engine thrust is terminated after footpad contact. Inclusion of the pad mode resulted in even higher predicted heating rates for the landing gear. Consequently, the Apollo 11 landing-gear thermal-insulation weight was increased to 31.03 kilograms (68.4 pounds), as shown in table II. A refined analysis allowed reduction of the landing-gear-insulation weight on subsequent vehicles so that it represents approximately 8 percent of the total landing-gear weight. This particular problem illustrates a hardware change made as a result of improved test data and a change in operational procedures.

## Primary-Strut-Bearing Design

An important design detail in the landing gear is that of the primary strut bearings (fig. 4). The bearing friction must be maintained within close tolerances because it accounts for 10 to 20 percent of the total force in the strut, thereby affecting both structural loads and landing performance. The friction depends on the bearing shape and the clearances, which are temperature dependent. Many component and gear-assembly tests were conducted to optimize the bearing friction. The effects of configuration on the effective coefficient of friction, which varies from approximately 0.05 on a flat surface to approximately 0.21 as the effective value based on the side load at the footpad, are illustrated in figure 7. Because footpad side load determines the bearing normal load, it is important to base the friction on the footpad load as well as to realize that the effective coefficient differs considerably from the actual coefficient based on normal force at the bearing. Additionally, thermal analysis must ensure that a positive clearance always exists between the bearing and the strut, thereby eliminating the possibility of very large axial loads as a result of binding. This development problem illustrates the importance of attention to detail in the landing-gear mechanical design.

## FLIGHT-PERFORMANCE RESULTS

Before the Apollo 11 mission, LM landing performance and landing-gear functional operation had been demonstrated by analysis and by extensive ground tests. During these tests, the landing gear was exposed to all significant flight environments, including vehicle drop tests under simulated lunar-gravity conditions. Landing-gear deployment has been successfully accomplished on eight Apollo missions. Of the five lunar landings attempted, all were successful. The landing-gear touchdown-performance results may be summarized by considering two of the pertinent parameters, surface slope at the touchdown point and touchdown velocities, which are summarized in figure 8. In all cases, the touchdown velocities were within design limits. The actual slopes at the touchdown point are compared with the landing-site slope statistics used in the touchdown analysis. The slope curves may be interpreted by choosing a particular slope (for example,  $11^\circ$ , the Apollo 15 touchdown slope at Hadley-Apennine) and reading the corresponding value of approximately 95 percent on the ordinate. This states that 95 percent of the slopes at this landing site are  $11^\circ$  or less. For all landings, vehicle attitudes and angular rates during touchdown have been low, indicating very stable landings.

Gear stroking in all landings has been minimal. The lunar soil has absorbed an estimated 60 percent of the touchdown energy through footpad penetration and sliding, resulting in secondary-strut tension stroking of about 10 centimeters (4 inches). A small amount of primary-strut stroking has occurred in some instances.

## CONCLUDING REMARKS

Problems encountered during the development of the LM landing gear have been solved, and at no time did the availability of landing-gear hardware jeopardize the Apollo Program schedule. The problems were solved by various means, some by hardware changes and some by criteria changes when such changes had a rational basis. It is concluded that the landing gear met the Apollo design requirements and that development problems were solved before flight.

## REFERENCES

1. Hilderman, R. A.; Mueller, W. H.; and Mantus, M.: Lunar Module Alightment System. Aerospace Mechanisms, vol. 1, part A, G. Herzl, ed., Lockheed Missiles and Space Corp., 1970, pp. 201-210.
2. Rogers, W. F.: Apollo Experience Report — Lunar Module Landing Gear Subsystem. NASA TN D-6850, 1972.

## DISCUSSION

J. T. Hinricks:

Ultimately, what material was selected for primary-strut bearings?

Rogers:

The primary-strut bearings are made of aluminum and are coated with a molybdisulfide dry-film lubricant.

TABLE I. - GENERAL DESIGN REQUIREMENTS

Category	Requirement
Structural	<p>Withstand loads and conditions imposed by the natural and induced environments</p> <p>Maintain strut loads within the LM structural design requirements</p>
Mechanical	<p>Deploy and lock down in lunar orbit</p> <p>In the stowed position, clear the S-IVB stage and the LM adapter during the ejection maneuver</p>
Landing performance	<p>Provide sufficient energy-absorption capability at touchdown</p> <p>Provide adequate toppling stability at touchdown</p> <p>Provide sufficient clearance on lunar surface to avoid impact of descent-stage structure, tanks, and plumbing (descent-engine skirt allowed to crush on surface contact)</p> <p>Maintain tilt angle within specified limits for ascent-stage lift-off</p>

TABLE II. - LANDING-GEAR THERMAL-INSULATION WEIGHT HISTORY

Approximate date	Weight, kg (lb)	Remarks
Nov. 1964	3.63 (8)	Thermal-paint estimate; no thermal blankets or plume shielding defined
Mar. 1967	≈9.98 (22)	Reaction control system plume-impingement requirement
Feb. 1969	13.34 (29.4)	Apollo 9 mission, actual
May 1969	13.34 (29.4)	Apollo 10 mission, actual
June 1969	31.03 (68.4)	Apollo 11 mission, actual; weight change caused by thrust until footpad contact and increased heating rates on landing gear
Nov. 1969	29.44 (64.9)	Apollo 12 mission, actual
Apr. 1970	17.10 (37.7)	Apollo 13 and subsequent missions, actual

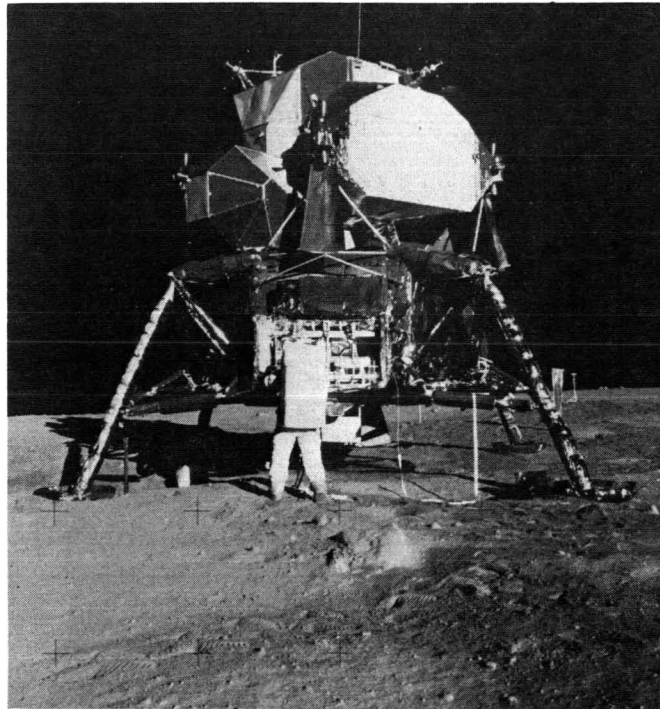


Figure 1. - Apollo 11 LM on the lunar surface.

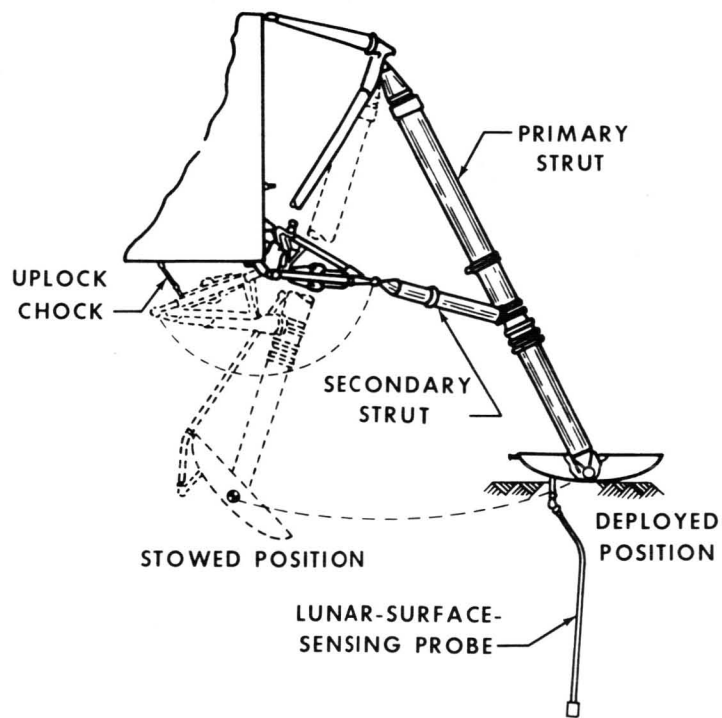


Figure 2. - Stowed and deployed positions of the landing gear.

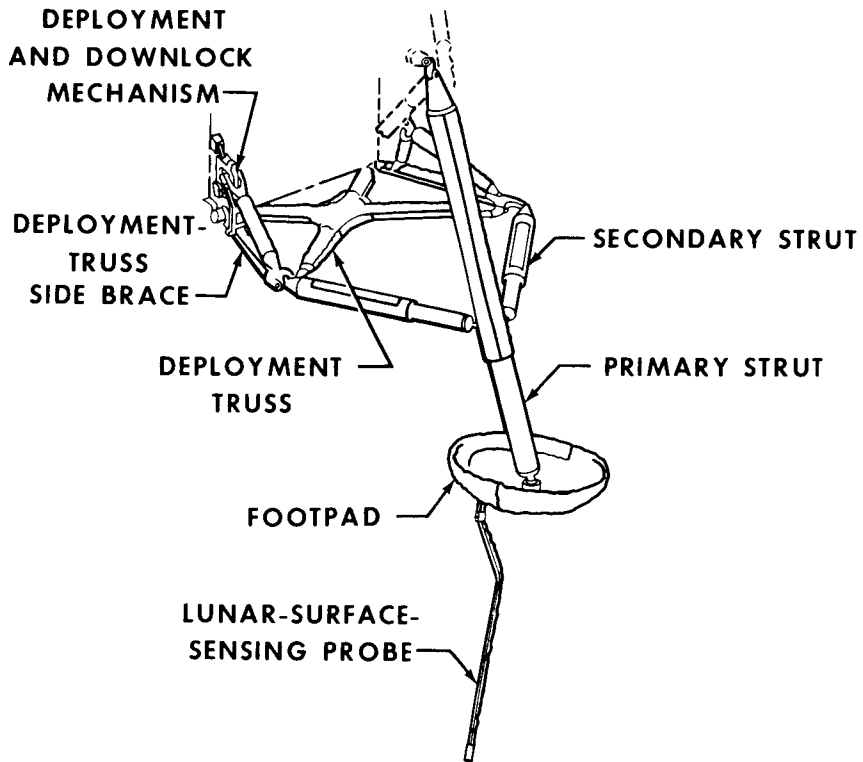


Figure 3. - The LM landing gear.

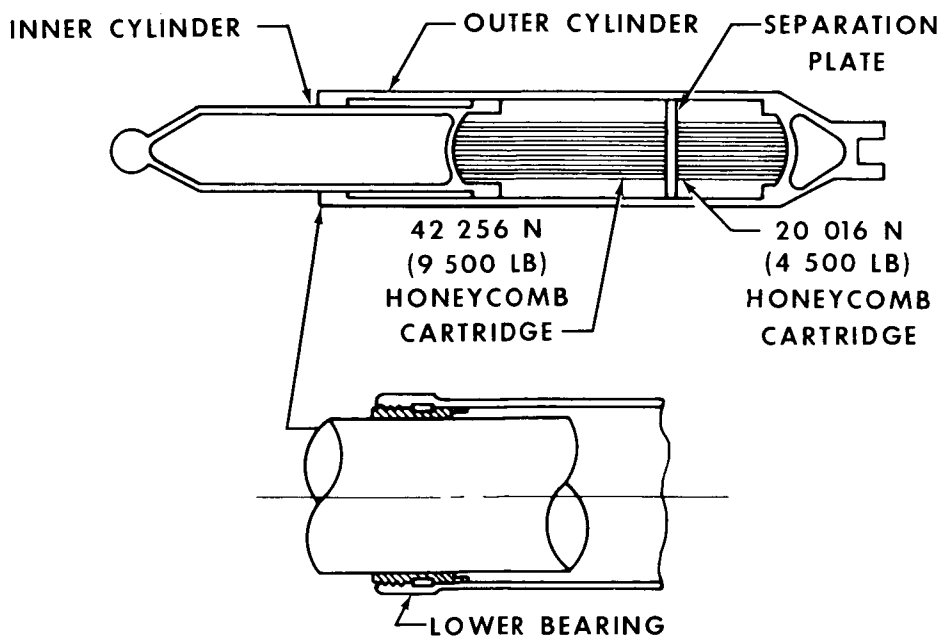


Figure 4. - Landing-gear primary strut.

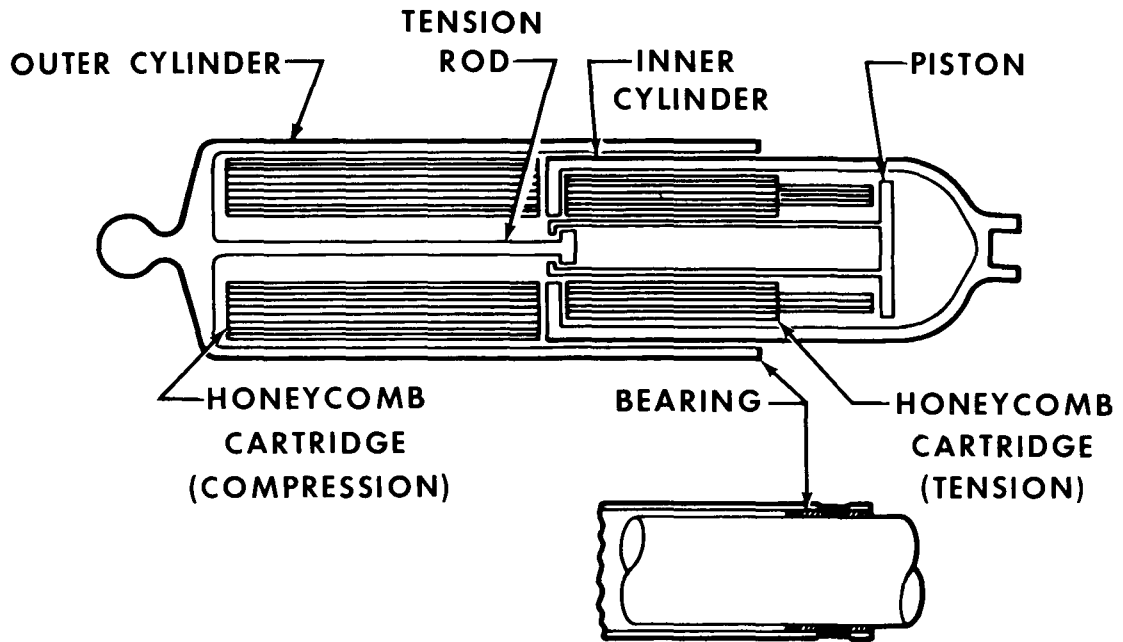


Figure 5. - Landing-gear secondary strut.

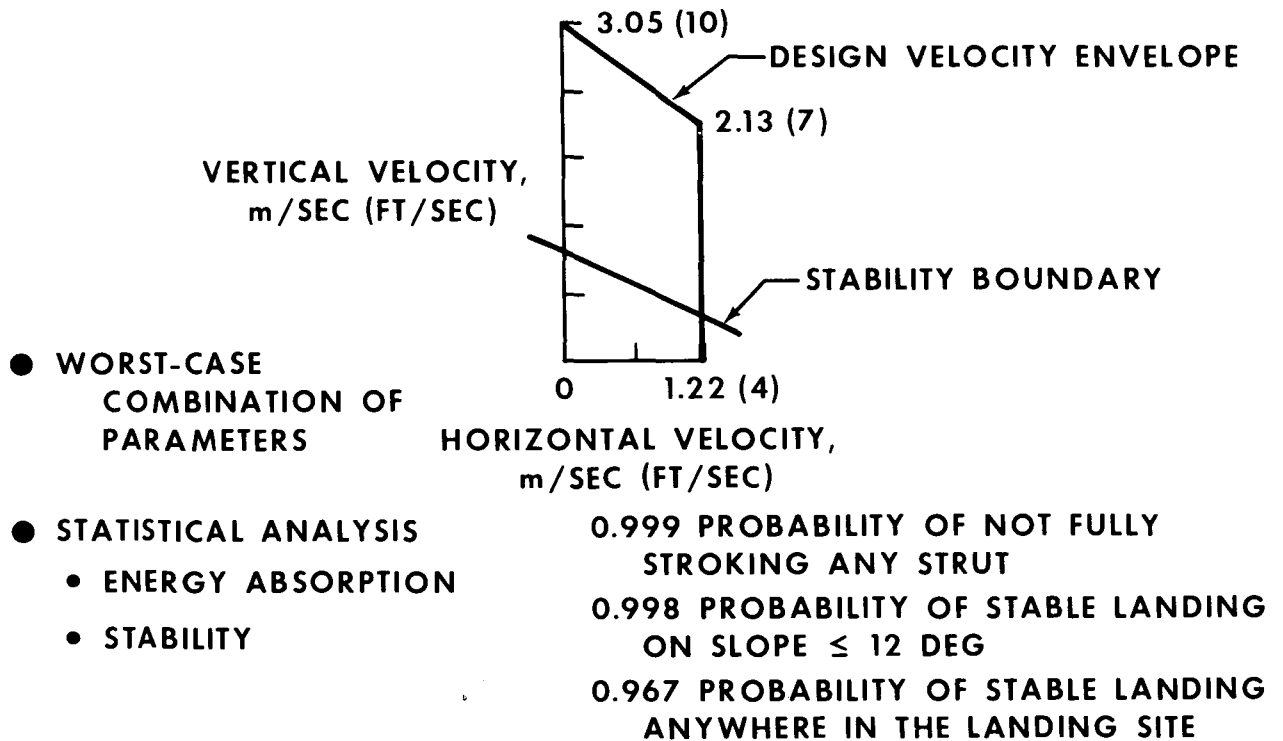


Figure 6. - Landing-performance analyses.

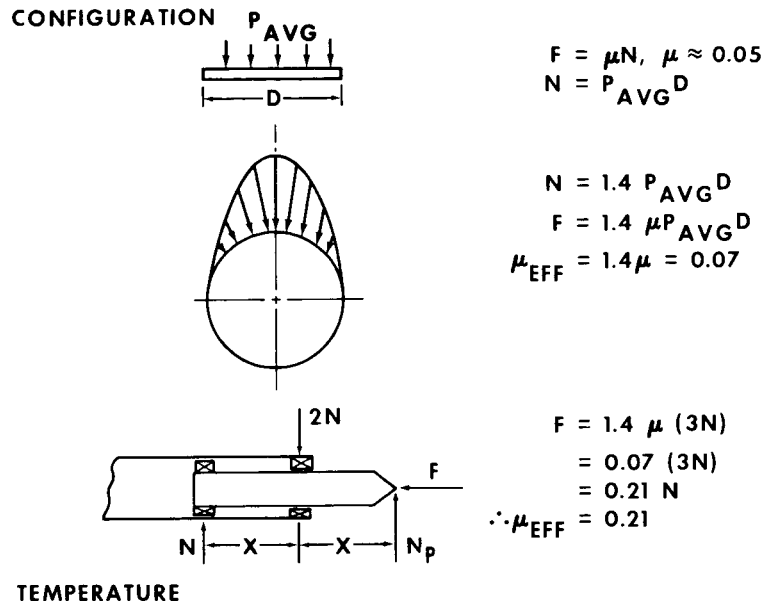


Figure 7. - Strut-bearing friction.

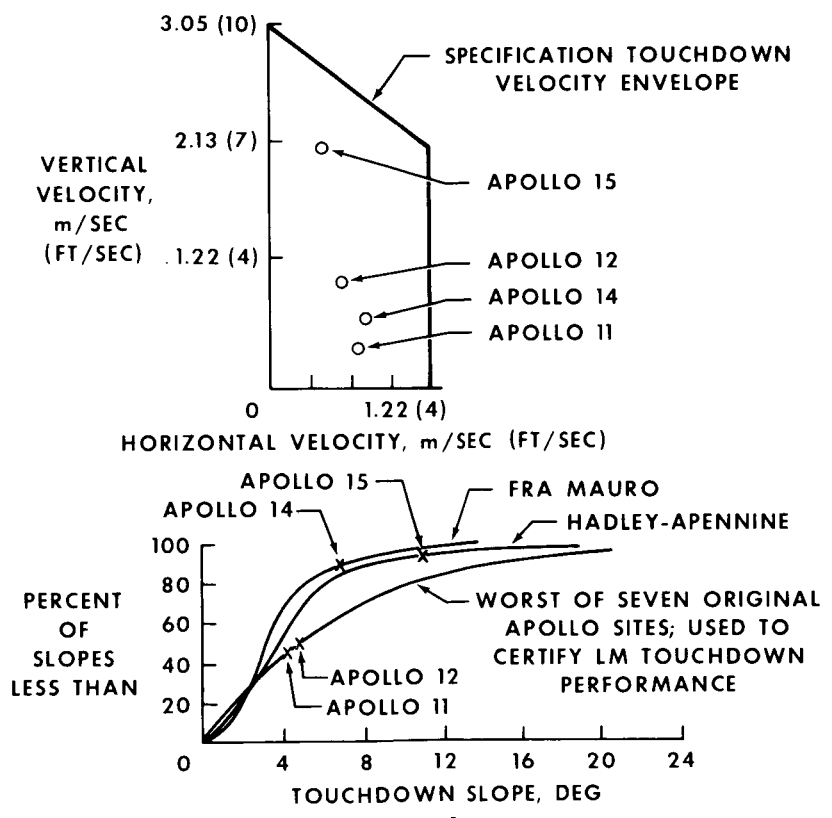


Figure 8. - The LM flight-performance results.

**Page intentionally left blank**

## **SESSION III**

**Page intentionally left blank**

## APOLLO 15 MAIN-PARACHUTE FAILURE

By Donald D. Arabian and Joseph E. Mechelay\*

### ABSTRACT

In the investigation of the failure of one of the three main parachutes of the Apollo 15 spacecraft, which collapsed at approximately 1825 meters after operating properly from deployment at 3050 meters, three conditions considered to be possible causes of the failure were produced. The suspect conditions were the proximity of the forward heat shield that passed the spacecraft at approximately 1825 meters, the dumping of the reaction control system hypergolic propellants at approximately 1825 meters, and the failing of a riser link found on a recovered parachute. (The failed parachute was not recovered.) The remaining two parachutes functioned as planned and averted a catastrophic failure. In this paper, the highlights of the investigation and the conclusions concerning the cause of the failure are discussed.

### INTRODUCTION

One of the three main parachutes of the Apollo 15 spacecraft collapsed at approximately 1825 meters altitude after operating properly from deployment at 3050 meters. Immediately after the successful recovery of the Apollo 15 crewmen, an investigation was conducted to assess the data, to perform tests and analyses as required to identify possible causes of the problem, and to define the corrective action necessary to preclude the occurrence of the incident on future flights. In this paper, the highlights of the investigation are summarized. The paper also shows how wrong conclusions concerning the cause of a problem can easily be reached if all of the available information is not weighed carefully during the course of the investigation.

### DESCRIPTION OF EVENTS

The three main parachutes of the Apollo 15 spacecraft deployed and inflated properly at approximately 3050 meters altitude. Films show that all three parachutes disreefed and opened fully in the proper sequence. The spacecraft and its parachutes were obscured by clouds at approximately 2135 meters altitude. On emerging from the clouds at approximately 1825 meters altitude, one of the three main parachutes was deflated,

---

\*NASA Manned Spacecraft Center, Houston, Tex.

as shown in figure 1. The spacecraft and parachute system descended in this configuration to water landing. The three parachutes were disconnected and one of the good main parachutes was recovered.

The failure occurred abruptly. At about the altitude and time of the failure, the forward heat shield was in proximity to the spacecraft, and the reaction control system propellant-depletion firing was almost completed. An inspection of the recovered parachute showed that one of the six riser links had a broken stud and three others had cracks. Therefore, the investigation of the failure was focused on the reaction control system propellant-depletion firing, the forward heat shield, and the failed links.

## DATA GATHERING AND ANALYSIS

The initial efforts of the investigation team were concentrated on accumulating and assessing the spacecraft data, evaluating the photographic and television coverage, and inspecting the recovered parachute and the forward heat shield. The spacecraft data and the associated events are shown in figure 2. The time of the anomaly was determined from the X, Y, and Z accelerometer data and the associated rapid rate changes. The data show that the command module reaction control system depletion firing was completed approximately 3.5 seconds before the anomaly, as determined from an abrupt rise in the reaction control system manifold pressure. This change occurs when the pressure regulators abruptly close, as a result of the reaction control system tank bladders being collapsed. The completion time of the fuel (monomethyl hydrazine) dump that follows the depletion firing was determined by calculating the amount of fuel remaining at the end of the depletion firing (approximately 2.72 kilograms, using the known flow rate of the fuel through the engines). The 4.7-second duration of the fuel dump overlaps the time of the anomaly occurrence. The start of the reaction control system purge occurred 8.3 seconds after the anomaly, as determined from the spike in the pyrotechnic bus voltage and the immediate decreases in the reaction control system pressures.

The two most significant items of photographic data obtained were the television tape, which indicated that the forward heat shield was in the vicinity of the spacecraft at the time of the anomaly, and the photographs shown in figures 1 and 3, which show the spacecraft parachute system damage when the spacecraft was relatively close to landing. The photographs show that

1. Three of the risers are taking the load.
2. There is no evidence of flailing suspension lines.
3. Two of the damaged riser lines appear to be full length.
4. Approximately two-thirds of the suspension system appears to be missing.
5. No significant canopy damage is visible.

The inspection of the forward heat shield revealed no damage that could be attributed to contact with the parachute system or the spacecraft. The initial inspection of

the recovered parachute showed only that it was not the one that had collapsed. Approximately 1 week after the first inspection, a second inspection was conducted, and a broken riser/suspension-line connector link was found after the Dacron bootie that protected it had been removed. Two to 3 weeks later, a closer examination of the Dacron riser protective cover (fig. 4) and the Dacron connector-link booties showed evidence of heat.

## FAILURE ASSESSMENT

The investigation was directed toward the three most likely causes of the parachute failure.

1. The forward heat shield was suspected of causing the damage because of its close proximity to the spacecraft during the time period in which the failure occurred.
2. The broken riser/suspension-line connector link that was found on the recovered parachute indicated the possibility of broken links in the failed parachute.
3. The command module reaction control system propellant-depletion firing had just been completed and fuel expulsion was in progress at the time of the failure, indicating the possibility of damage from the propellants.

The analyses and tests performed to investigate each possibility are presented.

### Forward Heat Shield

Trajectory analysis. - The landing sequence was initiated at a nominal altitude of 7315 meters with jettisoning of the forward heat shield (fig. 5), which is used to protect the parachute system. Immediately after separation of the heat shield from the command module, a 2.19-meter-diameter parachute was mortar deployed from the forward heat shield, an action that augments separation of the heat shield from the command module. Following a drogue- and pilot-parachute deployment sequence, the main parachutes are deployed and decelerate the command module to its final descent velocity of approximately 9 m/sec. The descent rate of the 172-kilogram forward heat shield is approximately 31 m/sec.

A trajectory analysis was performed to determine if the forward heat shield could have contacted the main parachutes. The analysis shows that the spacecraft and the forward heat shield were at the same altitude at 1735 meters, with a miss distance of approximately 46 meters. This conclusion correlates with observations of the recovery personnel. Further, the analysis indicates that, at landing, the spacecraft and the forward heat shield were approximately 200 meters apart. This figure is in agreement with the estimated separation distance of 275 meters on the water, as observed by the recovery personnel. Based on wind-profile trajectory simulations (assumed deviations of plus or minus 1.0 m/sec), the forward heat shield could have contacted the spacecraft parachute system at an altitude near 1825 meters.

Photographic analysis. - A close examination of the television record of spacecraft descent on the main parachutes shows the forward heat shield below the spacecraft in a frame recorded approximately 2 seconds before the anomaly occurred. By correlation with a later frame that shows both the parachute and forward heat shield, by direct measurement of the separation distance between the two objects, and by measurement of the known parachute dimensions, the vertical separation distances between the forward heat shield and the spacecraft were determined.

By an extrapolation of the forward heat shield trajectory and a comparison of the trajectory with the spacecraft trajectory, the forward heat shield would have intercepted the spacecraft 10.5 seconds before the spacecraft data indicate that the parachute failure occurred. Therefore, the photographic analysis conclusively proved that the forward heat shield could not have caused the failure.

In addition, tests were performed that were designed to assess the damage to the parachute system and the command module from forward heat shield impact. These tests show the damage to be acceptable; therefore, the decision was made to retain the current forward heat shield/parachute system.

#### Riser/Suspension-Line Connector Links

The discovery of the failed link on the recovered parachute (fig. 6) resulted in an extension of the investigation in order to identify the process that caused the connector link to fail and to determine if such a failure could have occurred and resulted in the parachute failure observed during the Apollo 15 landing. Microscopic inspection of the broken stud (fig. 7) indicated that stress corrosion or hydrogen embrittlement may have caused the link failure, or that it may have been caused by some other indeterminate means. The material used in the studs (4130 steel alloy) is susceptible to cracking when it is highly stressed and immersed in salt water. This process can cause stress corrosion. Hydrogen embrittlement can occur in the plating operation during the manufacturing process. The plating produces hydrogen that causes the embrittlement if the subsequent heat treating is improper.

Tests were performed on the connector links in an attempt to determine if either stress corrosion or hydrogen embrittlement was the process that caused the link failure. These tests included sustained-load tests to determine if hydrogen embrittlement was present; stress-corrosion tests to determine if salt-water corrosion could have induced the failure; over-torque tests of the studs to determine if tolerance buildup of stresses could have caused the problem; and hypergolic propellant exposure to determine if propellant exposure could have caused the observed flaws. The results of the tests and the metallurgical examinations performed were inconclusive in isolating the failure mechanism.

It was not known whether a single failed link could cause the parachute to collapse. To answer this question, ground parachute tow tests were conducted by failing one, two, and three links of an inflated parachute. Inflation was obtained by towing a parachute into the wind. When the canopy was fully inflated and stable, selected risers were severed. These tests showed that the parachute will remain fully inflated and provide

normal drag with one of its six riser legs severed. When two or more adjacent riser legs are severed, the canopy will collapse and lose at least two-thirds of its load-carrying capability.

According to these results, two connector links must fail simultaneously to satisfy the abrupt load change calculated from the data of figure 2. It is highly unlikely that this situation occurred because of the low-load condition at the time of failure (35 percent of the opening shock load). Assuming that the collapsed parachute did have two failed links, load still would have been carried by the fractured links. This fact was demonstrated by testing of the recovered failed link in which the link withstood two complete mission load cycles.

### Command Module Reaction Control System

Early in the investigation, the command module reaction control system was suspect because the propellant-depletion firing had just terminated and excess fuel was being expelled when the abrupt load change indicated in figure 2 occurred. Furthermore, at the time of the load change, the damaged parachute was in a position over a pair of the reaction control system engines. The spacecraft had been loaded fuel-rich to circumvent a problem encountered on an earlier Apollo flight in which the parachute system had been damaged by oxidizer. Inquiries that led to this fuel-rich procedure indicated that dumping only fuel through the engines would not be dangerous. This conclusion had been reached based on a limited test firing of 5 seconds, and it was not recognized that this firing time was not of sufficient duration to heat the engines to a point at which the fuel would ignite.

Later in the investigation, evidence of melting was found on the Dacron protective covering of the fabric riser and the connector link booties on the recovered parachute assembly. As a result, a closer examination was made of potential heat sources.

A test was conducted which showed that fuel on the parachute risers and suspension lines could easily be ignited by a hot wire and, once ignited, would cause the risers to fail within a few seconds. The next questions concerned what possibility existed that fuel could get on the lines and what would ignite the fuel. To answer these questions, a test was conducted to investigate the effects of cold, flowing raw fuel through a hot engine. The test firings consisted of a series of hot firings of 10 to 45 seconds in duration, each followed by a 5-second fuel cold flow (using approximately 0.27 kilograms of fuel). In every case, the raw-fuel expulsion sequence produced burning outside of the engine. Burning fuel vapor, burning fuel droplets, and some unburned fuel were observed during these tests. The flame front existed as far as 2.4 meters from the engine exit plane, and unburned fuel was sprayed as far as 3 meters horizontally from the engine and then ignited by burning droplets. In flight, the burning fuel could be diverted upward into the risers by the free air stream.

Following this test, movies of a development test of the command module reaction control system firing that was performed in 1969 were reviewed. The movies clearly showed flames spewing from all of the reaction control system engines after the depletion firing sequence. The question arises as to why this failure did not occur on other

Apollo flights in which the fuel-rich propellant loading was used. After the parachute-location characteristics during the previous missions had been researched, it was determined that the parachute location is arbitrary and that, unfortunately, during the Apollo 15 descent, the failed parachute was oriented over the engines for several seconds during the fuel-expulsion sequence.

When the burning-fuel test results are combined with the available data (for example, the abrupt load change, the location of the parachute at the time of the failure, the damage to the parachute system as determined from the photographic coverage, and the timing of the fuel expulsion) and weighed against the forward heat shield and the broken stud as possible causes, all of the evidence indicates that the burning reaction control system fuel was the cause of the failure.

### Conclusions of Failure Assessment

The results of the analyses and tests lead to the following conclusions.

Burning of raw fuel (monomethyl hydrazine) that is being expelled during the later portion of the reaction control system depletion firing can exceed the temperature limits of parachute riser and suspension lines located over the thruster engines and can cause extensive damage to a parachute.

The failure of a single connector link has little effect on the load-carrying capability of a parachute and was not the cause of the parachute collapse.

The forward heat shield did not cause the damage to the parachute.

### CORRECTIVE ACTIONS

Corrective actions for the reaction control system include landing with the propellants on board for a normal landing and biasing the propellant load to provide a slight excess of oxidizer. Thus, for the low-altitude abort land landing, burning the propellants when the parachutes are deployed will subject the parachutes to some acceptable oxidizer damage but will eliminate the dangerous burning-fuel conditions. The suspension-line connector-link material has been changed to Inconel 718 to eliminate the requirement for plating, and the link-stud threads are rolled rather than machined to improve the metallurgical properties of the material.

### CONCLUDING REMARKS

Two major points can be emphasized as a result of the investigation of the Apollo 15 parachute problem. The first point is that existing information should be thoroughly analyzed before an integrated operational system is established. The Apollo 15 parachute problem could have been prevented if the implications of existing reaction control system ground-test data had been completely understood. The solution

to the earlier problem in which the spacecraft was loaded fuel-rich to prevent the parachutes from being damaged by oxidizer was acceptable insofar as the reaction control system and the oxidizer problem were concerned. However, the solution created different conditions that resulted in an unacceptable environment for the parachute landing system.

The second point is that, in cases in which the data are limited, more than one set of conditions may satisfy the questions raised. The probability of reaching a wrong conclusion is increased when data are limited. In the case of the parachute anomaly, three likely causes of the failure existed. If certain bits of telemetry, visual, timing, and photographic data had not been available, the wrong conclusion could have been reached. It is important to weigh all available information carefully during the course of the analysis.

Aside from the investigative effort, the importance of basic design considerations cannot be overemphasized. The interfacing effects of operational systems should be thoroughly analyzed and understood early in the program. Test programs should be developed to verify the integrity of the integrated systems. In short, it is more profitable to apply engineering man-hours to the development of operable and compatible systems than to the resolution of systems problems.

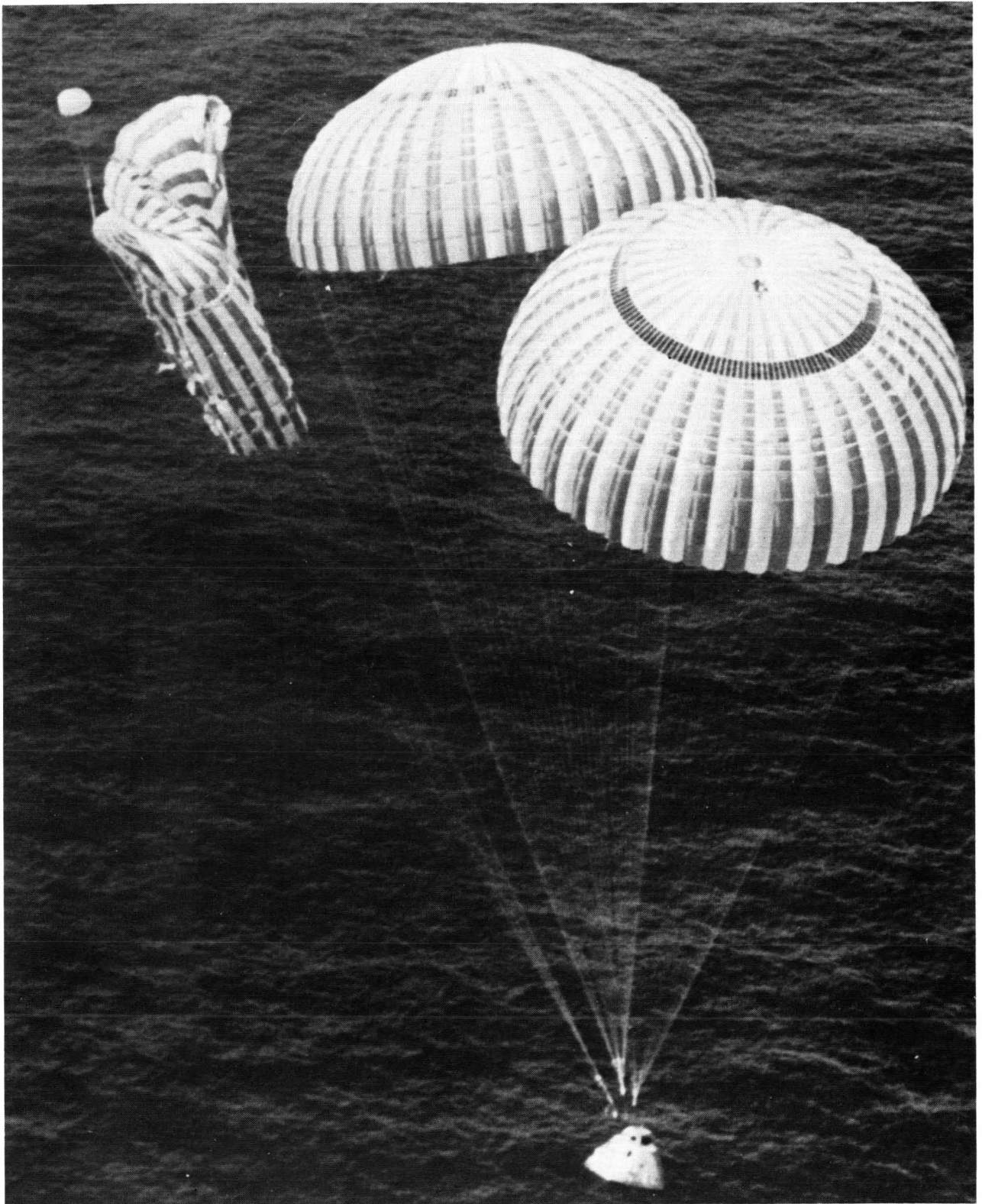


Figure 1. - Spacecraft descending with one main parachute failed.

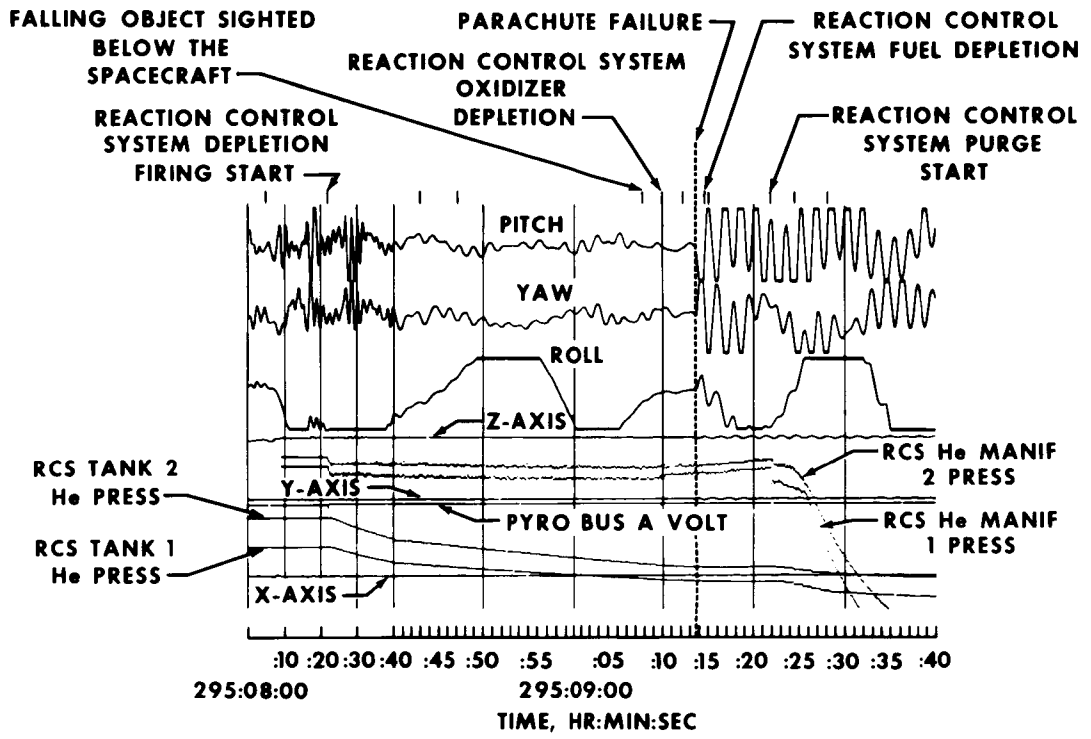


Figure 2. - Sequence of events during descent on the main parachutes.



Figure 3. - Parachute-riser damage during final descent.

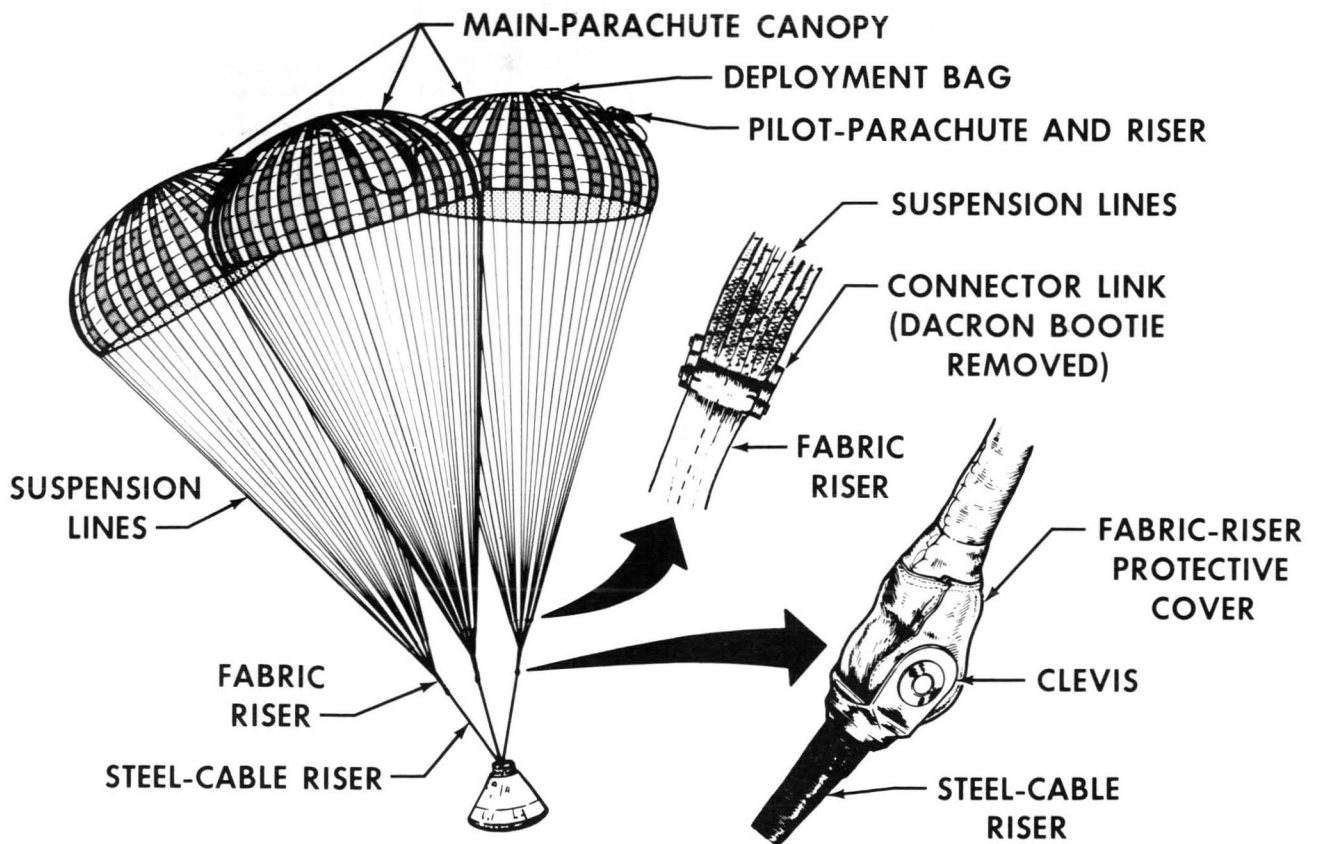


Figure 4. - Parachute system configuration.

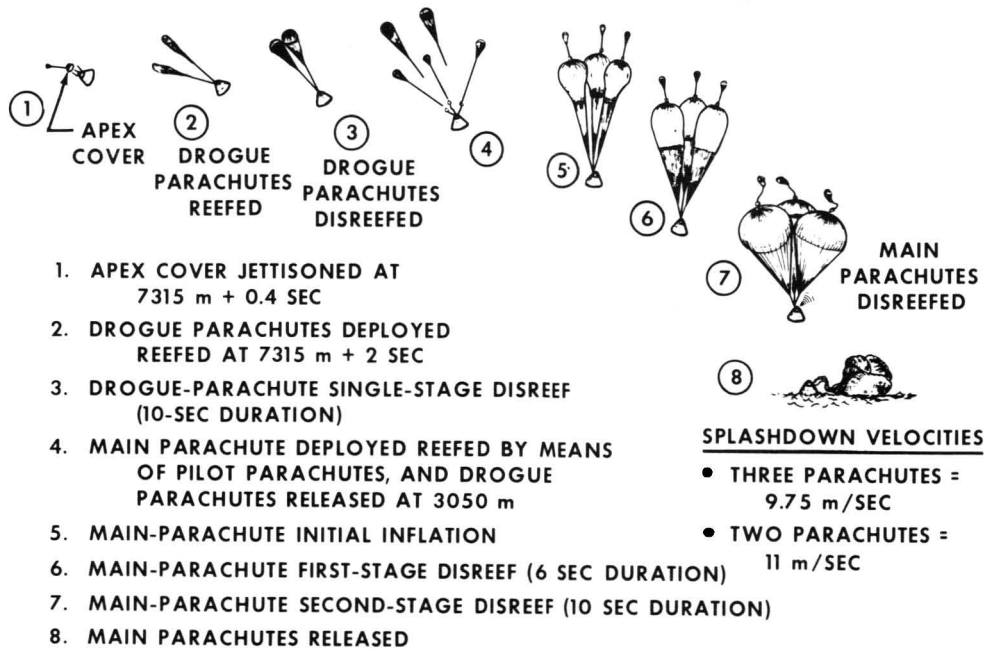


Figure 5. - Earth landing system normal sequence.

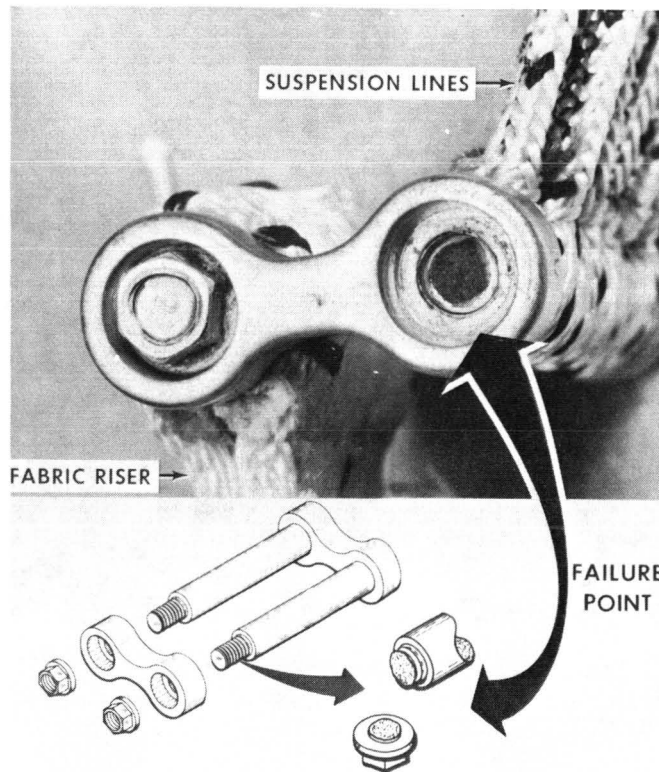


Figure 6. - Main-parachute connector-link failure.

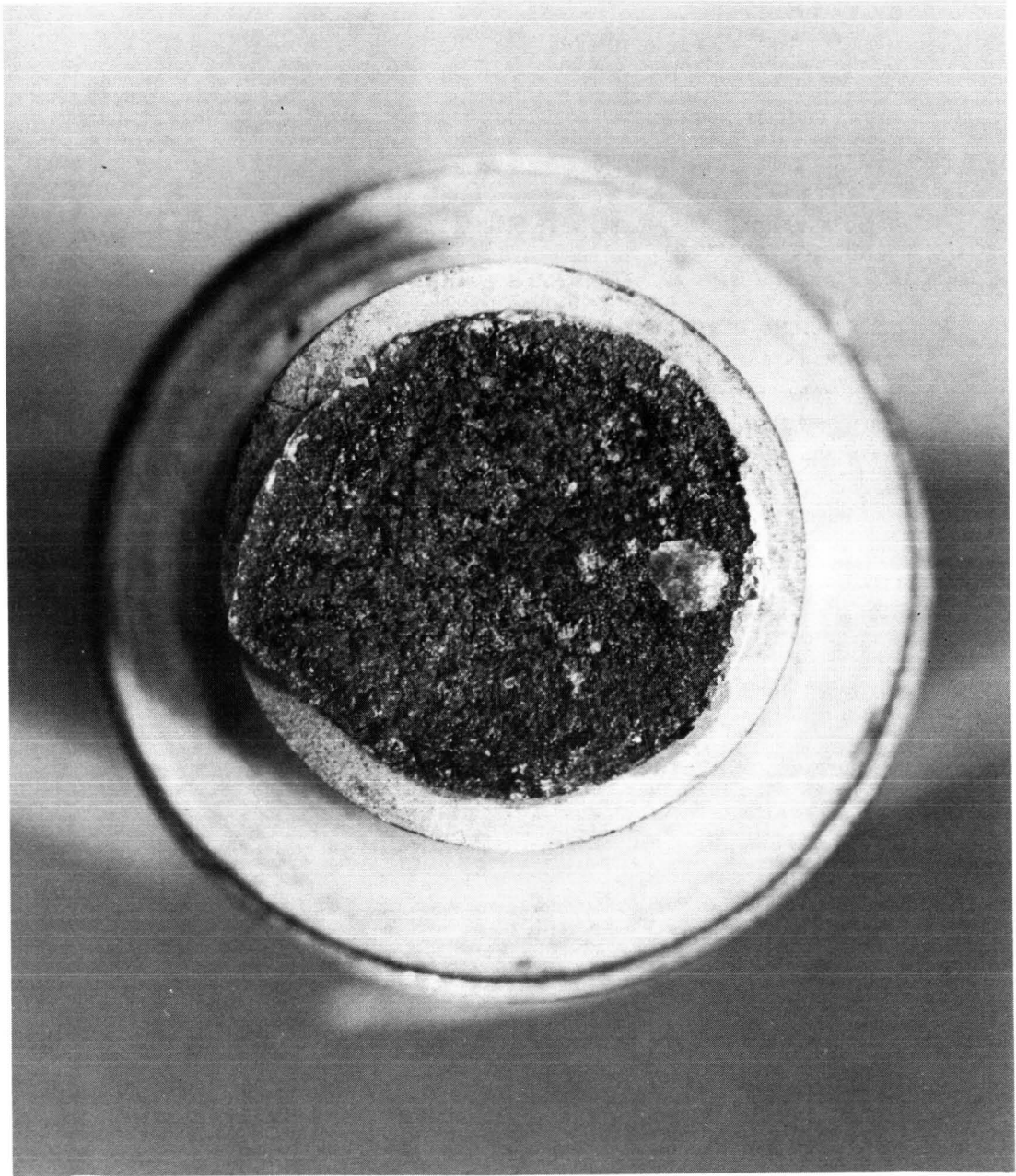


Figure 7. - Enlarged view of broken stud.

## MECHANICALLY PRESTRESSED WINDOWS

By William H. Keathley\*

### ABSTRACT

Microscopic cracks are present in the surface of any mechanically finished glass. Because glass does not yield, these surface cracks are the source of stress concentrations that can cause crack propagation and ultimate glass failure.

Mechanically prestressing glass, by means of placing a metal ring (in tension) around the periphery of the glass, eliminates this problem. The interference fit between the ring and the glass fixes the glass in a state of uniform compression. When the glass is subjected to a pressure loading, the compressive prestress prevents tension loading of the outer surface and, therefore, eliminates the tendency for propagation of surface imperfections.

### INTRODUCTION

Spacecraft windows have been round, rectangular, triangular, flat, and curved. The glasses have been made of quartz, aluminosilicate, pyrex, leaded glass, and many other materials. Some glass has been chemically tempered, some thermally tempered, and others annealed. Many "windows" would not even be recognized as such. Telescope lenses, viewports in experiment packages, or any piece of glass that, if broken, would deplete the pressure in a habitable portion of the space vehicle must be considered windows. For example, the Skylab contains 29 such "windows."

Glass is a very strong material. Tests on fine glass fibers have indicated breaking strengths of  $690\,000\text{ N/cm}^2$  (1 000 000 psi) or more. This is difficult to believe by anyone who has dropped a drinking glass. However, there are sound technical reasons for this apparent discrepancy. Glass develops surface flaws that may be seen easily or that may be so small as to be undetectable visually. These surface flaws are the source of stress concentrations when the surface is placed in tension and the bottoms of these slight imperfections are subjected to extremely high loads. Unlike ductile metals, glass does not yield and relieve these stress concentrations. The surface flaws propagate in a futile attempt to relieve the load and continue to propagate until rupture is complete. When glass is placed in compression, these flaws tend to close and have no tendency to grow.

---

\*NASA Manned Spacecraft Center, Houston, Tex.

A method has been developed for mechanically prestressing glass. Glass is placed in a state of high uniform compression. Then, when the window or viewport is subjected to a pressure load, the glass bows outward and relieves some of the compression induced by the prestressing. By properly selecting the amount of preload, the glass will never be subjected to a tensile load, and the surface flaws will have no tendency to propagate.

The contributions of Clarence J. Wesselski and Charles M. Vibbart, NASA Manned Spacecraft Center, are acknowledged gratefully.

## SYMBOLS

a	radius
h	thickness
P	pressure
$P_u$	ultimate rupture pressure
Q	reaction force
$\nu$	Poisson ratio
$\sigma_{pl}$	preload stress
$\sigma_u$	modulus of rupture

## DESIGN AND FABRICATION

### Materials

For economic reasons, all developmental work has been with Pyrex glass; however, quartz will be used for flight glass. All tests on Pyrex are assumed applicable to quartz.

Mechanically prestressing glass is accomplished by placing a highly stressed metal ring around the periphery of a circular piece of window glass. The edge of the glass is polished and the corners of the glass are rounded to prevent local stresses when installing the ring.

The working temperature range required for spacecraft windows is  $173.15^\circ$  to  $394.15^\circ$  K ( $-100^\circ$  to  $121^\circ$  C). This temperature range makes thermal compatibility between the glass and the ring mandatory in order to maintain uniform compression in the glass. Because the coefficient of thermal expansion of quartz is  $0.56 \times 10^{-6} \Delta L/L/^\circ C$ , the material that was selected for the ring was an alloy of

36 percent nickel (Invar) that has a coefficient of thermal expansion of  $0.50 \times 10^{-6} \Delta L/L/^\circ C$ . The inside diameter of the ring was ground to a  $2.54 \times 10^{-6}$ -centimeter (16 microinch) finish to prevent further local stresses in the glass. Invar was used in the annealed condition because only thin sections could be obtained in the cold-worked condition.

### Installation

The installation of the ring on the glass may be the key to the mechanical prestressing of glass. The original intention was to install the ring by thermal expansion because the ring-material expansion rate jumps sharply at approximately  $300^\circ C$ . However, the ring oxidized heavily at installation temperatures, it was difficult to center the glass, and some yielding of the ring occurred caused by the load increasing as the ring contracted onto the glass while the ring was still at an elevated temperature.

The alternate method of installation is to press the ring over a tapered mandrel and then onto the glass. This method seems to be severe but no problems have been encountered when using properly prepared parts. The edge of the glass is polished, the corners of the glass are rounded, and the inside diameter of the ring is ground. The mandrel, the ring, and the glass are lubricated thoroughly with spray Teflon; then, the ring is pressed on. The forces required for installation of a 22.2-centimeter (8.75 inch) diameter ring are approximately 31 000 newtons (7000 pounds force) for sliding friction and 35 000 newtons (7900 pounds force) for static friction.

### ANALYSIS

The rupture pressure of the window glass before prestressing is a function of the tensile load and the amount of time under tensile load. As was stated, the microscopic imperfections in the surface under tension propagate until failure occurs. A rigorous analysis, using fracture mechanics, is necessary to predict the test results accurately. A simple analysis will be used, omitting the time factor and assuming a simple supported edge condition. Using a modulus of rupture  $\sigma_u$  of  $4200 \text{ N/cm}^2$  (6100 psi) and a Poisson ratio  $\nu$  of 0.2, the ultimate rupture pressure  $P_u$  of the glass (fig. 1) is

$$P_u = \frac{8h^2 \sigma_u}{3\nu a^2 \left( \frac{3}{\nu} + 1 \right)}$$

$$P_u = 42.8 \text{ N/cm}^2 \text{ (62 psi)}$$

When the compression ring is added to the glass (fig. 2), the rupture pressure is increased in proportion to the amount of compression applied to the glass. When the preload (compression) equals  $3110 \text{ N/cm}^2$  (4500 psi),  $\sigma_{pl}$ , the rupture pressure is

$$P_u = \frac{8h^2}{3\nu a^2 \left(\frac{3}{2} + 1\right)} (\sigma_u + \sigma_{pl})$$

$$P_u = 74.5 \text{ N/cm}^2 \text{ (108 psi)}$$

### TEST RESULTS

Failure of the windows during hydrostatic testing is indicative of the value of prestressing. These windows have zero tension up to  $27.6 \text{ N/cm}^2$  (40 psi) and should support this pressure indefinitely. At pressures greater than  $27.6 \text{ N/cm}^2$  (40 psi), the outer surface goes into tension and failure becomes a function of load, time under load, humidity, and several other factors, just as with an ordinary window.

The first hydrostatic test (table I) was conducted on a window equipped with a 4340 steel ring (fig. 3). The pressure when cracking occurred was  $62 \text{ N/cm}^2$  (90 psi) and resulted in the crack pattern shown in figure 4. In the control test on a window without a ring, the window blew out completely at a pressure of  $34.5 \text{ N/cm}^2$  (50 psi).

The second test on a prestressed window resulted in the window cracking at a pressure of  $61 \text{ N/cm}^2$  (88 psi); then, an attempt was made to make the window blow out. By the use of a hand pump, the pressure was raised to  $83 \text{ N/cm}^2$  (120 psi). The window would not be blown out at this pressure and the pressure could not be increased because the leak rate was equal to the pumping rate. The third test was conducted using an electrically driven gear pump. The cracking pressure on this test was  $69 \text{ N/cm}^2$  (100 psi) and was higher than on the previous tests because of the faster pumping rate and the amount of time under load. After the window cracked, the center of the window blew out at a pressure of  $86 \text{ N/cm}^2$  (125 psi).

A thermal-cycle test was conducted to verify the theory that compatible thermal-expansion rates between the ring and the glass prevent the window from cracking around the edges as a result of localized stresses. The test was conducted with atmospheric pressure on one side of the window and a vacuum on the other side. The window assembly was thermally cycled from room temperature to  $173.15^\circ$  to  $394.15^\circ \text{ K}$  ( $-100^\circ$  to  $121^\circ \text{ C}$ ), and then back to room temperature. There was no trace of cracking of the glass.

## CONCLUDING REMARKS

A mechanically prestressed window will maintain cabin pressure even when the glass is cracked and can withstand eight times the normal working pressure of the spacecraft before the glass will blow out. The surface imperfections that result from mechanical finishing of the glass cannot propagate and cause failure. The use of mechanically prestressed windows, that have apparently unlimited life expectancy, should make them extremely attractive for use on long-term missions. Currently, planned testing includes meteoroid-impact studies, high-mass impact (accidental bumping), and continued hydrostatic and thermal testing.

Mechanically prestressed windows for use on future spacecraft can be of the highest optical quality because glass selection and glass finishing are independent of structural considerations. A single-pane prestressed window will be superior to conventional multipane installations because it has less light-transmission loss, because it has fewer surfaces, and there is no condensation between panes. The use of prestressed windows is not limited to spacecraft; it can be used on any structure in which glass must support a pressure load (for example, underwater vessels, vacuum chambers, and airplane cabins).

## DISCUSSION

R. J. Peterson:

Are you able to prestress noncircular windows?

Keathley:

We have made no attempt to prestress noncircular windows.

G. W. H. Stevens:

Are there any problems related to size and compression loads that affect the vibration responses of windows and buckling when windows are subjected to acceleration loads?

Keathley:

At this time I do not know.

TABLE I. - HYDROSTATIC TESTS ON 22.2-CM (8.75 IN.) DIAMETER WINDOW<sup>a</sup>

Test	Cracking pressure, N/cm <sup>2</sup> (psi)	Blowout pressure, N/cm <sup>2</sup> (psi)	Ring material and interference, mm (in.)	Compression load on glass, N/cm <sup>2</sup> (psi)	Comments
Control test	34.5 (50)	34.5 (50)	--	--	Slow pressurization
1	62.0 (90)	--	4340 Steel 1.12 (0.044)	2880 (4180)	Did not pressurize beyond cracking
2	60.7 (88)	82.8 <sup>+</sup> (120 <sup>+</sup> )	17-4 Stainless 0.94 (0.037)	3100 (4500)	Leak rate exceeded pumping rate at 82.8 N/cm <sup>2</sup>
Control test	56.5 (82)	56.5 (82)	--	--	Very high pumping rate
3	69.0 (100)	86.3 (125)	17-4 Stainless 0.94 (0.037)	3100 (4500)	Very high pumping rate

<sup>a</sup>Clear-view diameter was 19.1 cm (7.5 in.) on all tests.

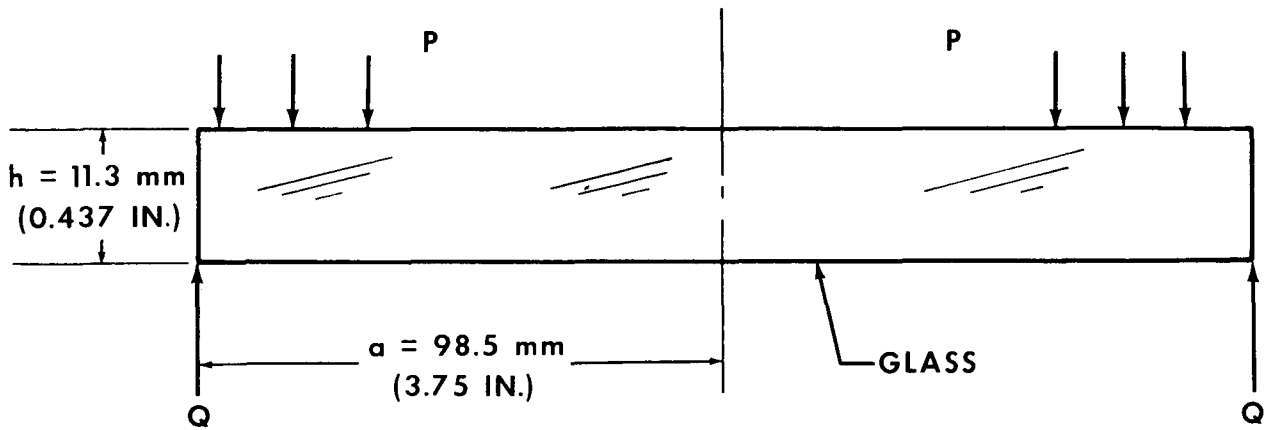


Figure 1. - Force diagram for test without compression ring.

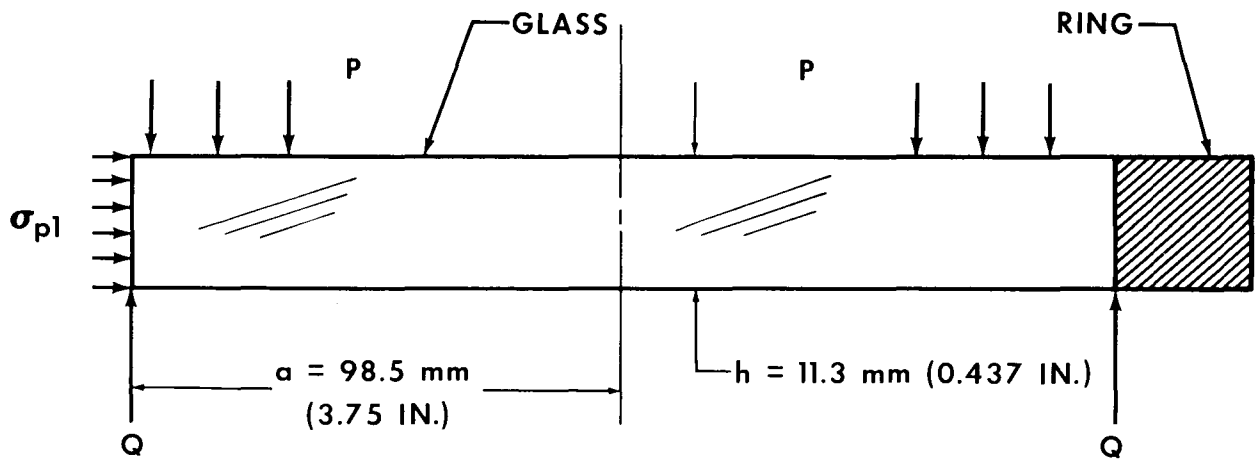


Figure 2. - Force diagram for test with compression ring.



Figure 3. - Test window.

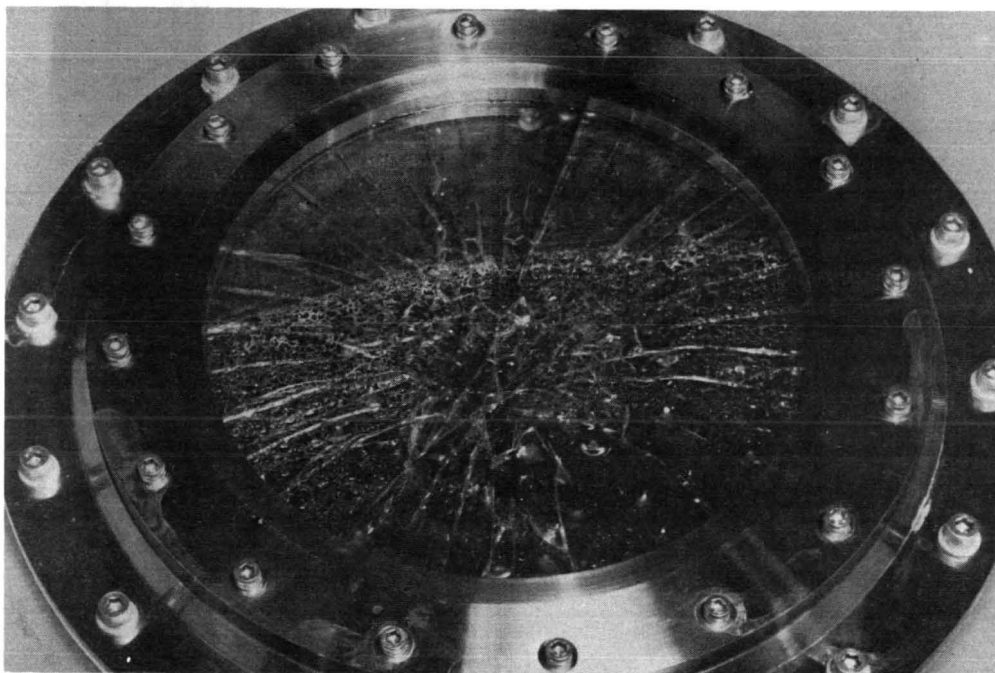


Figure 4. - Test window after failure.

## APOLLO COUCH ENERGY ABSORBERS

By Clarence J. Wesselski\* and Ralph E. Drexel\*

### ABSTRACT

Load attenuators for the Apollo spacecraft crew couch and the potential applications thereof are described in this report. Energy absorption is achieved through friction and cyclic deformation of material. In one concept, energy absorption is accomplished by rolling a compressed ring of metal between two surfaces. In another concept, energy is absorbed by forcing a plastically deformed washer along a rod. Among the design problems that had to be solved were material selection, fatigue life, ring slippage, lubrication, and friction loading.

### INTRODUCTION

Landing conditions and allowable stroking distances within the Apollo spacecraft necessitated that the crew couch struts (1) be designed to a close tolerance on the stroking force, (2) be designed to absorb energy in both directions, and (3) be designed to control the deceleration-onset rate to reduce the secondary impact of the crewman striking the couch.

The struts designed to meet these requirements incorporated two concepts of energy absorption: cyclic deformation of metal (ref. 1) and metal-to-metal friction (ref. 2). Impact protection of the Apollo crewman during land landing was accomplished by supporting the crew couch on load-attenuating struts (fig. 1). Cyclic deformation of metal (cyclic strut) is the principle energy absorber for the X-X and Z-Z struts. To overcome the overshoot problem inherent in constant-load absorbers, the low-onset device was added to the cyclic strut (fig. 2). The load/time characteristics of the two types of struts are shown in figures 3 and 4. Although the initial onset rate of loading up to "breakout" was approximately the same for both struts, the primary difference between the two was the breakout. As shown in figure 4, this point is lower than the nominal stroke load, and the rate of loading is controllable between breakout and nominal. With this application, the maximum load was never higher than nominal.

The authors wish to acknowledge the efforts of Ronald C. Gulacte and David L. Platus, Mechanics Research, Inc., Los Angeles, California, for the initial design and predevelopment of the cyclic strut; C. Bartik and J. Kragh, North American Rockwell Corporation, Los Angeles Division, Los Angeles, California, for the final design,

---

\*NASA Manned Spacecraft Center, Houston, Tex.

evaluation, and performance testing of the cyclic strut; and W. H. Keathley, NASA Manned Spacecraft Center, Houston, Texas, for development testing of the low-onset-rate energy absorber.

## PRINCIPLE OF OPERATION

### Cyclic Strut

The concept of continuous material deformation in the plastic range for energy absorption is used in the cyclic strut. Material is deformed by rolling a ring of metal (reaction ring) between an inner and an outer tube (fig. 5). When the space between the tubes is less than the diameter of the ring, the ring is forced "out-of-round," thus absorbing energy as it rolls. Because the ring is free to roll in either direction, load attenuation occurs for compression or tension and at any position of the strut. The reaction load was controlled by varying the number of reaction rings installed. Heat-treated, high-strength bearing rings are located at each end of the gang of reaction rings to maintain concentricity of the tubes and to control the deflection of the reaction rings.

### Low-Onset Device

The low-onset device consists of a slender, hard rod of very uniform diameter onto which has been pressed a series of washers. The washers are forced onto the straight portion of the rod, thus causing the washer to be deformed plastically and elastically and thereby maintaining a "squeeze" on the rod. When the washer is forced to slide along the rod, drag occurs from metal-to-metal friction and energy is absorbed.

The total load (or total energy consumed) is the cumulative effect of all the washers stroking along the rod. If spaces are left between the washers, the load is increased each time a washer is picked up and pushed along the rod. This incremental loading produces an approximate ramp function of the applied force, which, for a given mass, reduces the deceleration-onset rate as shown in figure 4. Thus, the deceleration-onset rate of a mass can be controlled by selecting the appropriate washer spacing, and the magnitude of the deceleration can be controlled by selecting the proper number of washers. The energy-absorption capacity of this device is very great. Conventional brakes, for example, absorb approximately  $58 \text{ W/cm}^2$  of contact area, while this device absorbs  $1250 \text{ W/cm}^2$ .

## DESIGN AND DEVELOPMENT

In the initial design of the struts, the stroking-load levels were calculated for attenuating a rigid single mass; final values were determined by full-scale impact testing of the Apollo command module and the couch/strut system. Strut loads were verified by impact tests and on a controllable stroking machine to determine the precise load levels during development.

## Cyclic Strut

Parameters for the reaction-ring elements necessary for the design of the strut, which are deformed into the plastic-deformation range of the material, are defined in reference 3. The parameters evolved from a consideration of the mechanics of the cyclic plastic deformation of a thin-walled ring or of tube elements; a first-order correction was applied to account for the effect of wall thickness. The parameters were substantiated by predevelopment tests.

The selection of a material for cyclic-strut reaction rings was based on the amount of energy per unit volume of steel that could be absorbed for a given stroke distance. A series of screening tests was conducted on different materials, and the most efficient material in terms of energy absorption was found to be 18 nickel maraging steel.

During design-verification testing of the struts, several failures were noted with regard to ring slippage, and a program was undertaken to identify the failure mode. The conclusion from testing was to grit-blast both the inner and outer tubes of the strut and the ring tractive surface for an optimal friction surface. Also, the ratio of squeeze force to roll force should be selected so that the sliding-friction force is always greater than the roll force.

A strong tendency was observed for highly deflected reaction rings assembled on bracelets to deflect in a preferential manner (to not load share) that caused the tubes to become eccentric. The reaction-ring material tended to "neck down" and deform locally on the rings at first flexure, while reaction rings on opposite sides of the bracelet were not deflected evenly. The solution for this problem was as follows.

1. Hold the tubes centered with additional bearing bracelets.
2. Limit the energy absorption of reaction rings so that the slope of the load-deflection curve gives a reliable centering force, as determined by test.
3. Size the tube-wall thickness by testing so that the reaction rings that had been cycled would hold the tubes concentric.

The final design of the cyclic strut was held to a breakout load of 10 percent over nominal and a stroking load of  $\pm 5$  percent of nominal. The total stroking life of the cyclic struts was proved to be a minimum of 254 centimeters of stroke, which allowed preinstallation testing to determine the actual stroking-load value.

## Low-Onset Device .

The low-onset device used for the Apollo spacecraft is shown in figure 6. This device consisted of a slender, straight, smooth, and relatively hard rod 46.45 centimeters long and 9.5 millimeters in diameter, with 76 washers on 0.304-centimeter centers for tension stroking and 26 washers on 0.174-centimeter centers for compression stroking.

To maintain consistent loading as the washers slid along the rod, the diameter of the rod was held to  $\pm 0.012$  millimeter, with the variations in diameter from end to end not to exceed 0.0025 millimeter. The material selected for this design was Inconel 718, which is a relatively new nickel-chromium base alloy having excellent mechanical, thermal, and friction properties. The rod was also heat-treated to a 40 Rockwell C hardness and surface-ground and polished to a fine finish.

The proper amount of "squeeze" by the washer on the rod was obtained by machining the inside diameter of the washer 2-1/2 percent smaller than the rod diameter. The washer was sized to an inside diameter of 9.30 millimeters, an outside diameter of 15.9 millimeters, and a thickness of 1.0 millimeter. The overall tolerances of the washers were maintained at  $\pm 0.025$  millimeter.

For the washers, several materials were considered, but only 304 and 416 stainless steel were tested. The 416 stainless steel was determined to be satisfactory. After machining from process-annealed stock, the washers were fully annealed and then cooled at an appropriate rate for 416 stainless steel. Annealing and cooling must be done in an inert-gas atmosphere.

The selection and application of the correct lubricant was also necessary for this energy absorber to function properly, because it is a friction device. Several oils and greases were tried but discarded because of high-stick-slip tendencies. A spray-type dry-film lubricant worked successfully with high repeatability.

Before assembly, the rod and washers had to be completely degreased with Freon and then handled only with gloves to avoid contamination. Lubricant had to be sprayed thoroughly onto the rod before each washer was installed, and the assembly had to be sprayed thoroughly again before it was installed in the strut.

An approximate solution for the stroking load of the washer can be found by considering the deformation of a thick-walled cylinder for a perfectly plastic material. The internal pressure  $p$  necessary to deform the entire cylinder plastically is given (ref. 4) in terms of the yield stress  $\sigma_y$  and the natural logarithm of the ratio of the outside and inside radii  $b/a$  as

$$p = \sigma_y \ln b/a \quad (1)$$

This solution can be applied without much loss of accuracy to the washer. As shown in figure 7, the force  $F$  required to stroke the washer along the rod of diameter  $d$  and thickness  $h$  is then

$$F = \mu p d h \quad (2)$$

where  $\mu$  is the coefficient of friction. For the values  $a = 4.65$  millimeters,  $b = 7.93$  millimeters,  $d = 9.53$  millimeters, and  $h = 1$  millimeter,  $\sigma_y = 276 \text{ N/mm}^2$ .

The pressure and stroking load are  $148 \text{ N/mm}^2$  and  $4500 \mu\text{N}$ , respectively. For boundary lubrication under carefully controlled conditions, the coefficient of friction generally ranges from 0.05 to 0.15, in which case the stroking load is between 225 and 675 newtons.

Preliminary testing of the low-onset device was conducted on a simple, single-mass system to determine the feasibility, best design features (materials and lubricants), and preliminary-design data. More advanced testing was conducted by using a two-mass system that closely simulated spacecraft landing impacts.

A typical load-stroke curve resulting from a full complement of 76 washers is shown in figure 8. As shown, the load is initially higher than desired; in midstroke, it is lower than desired. The load then rises at the end of the stroke. This performance is indicative of the velocity effects on the coefficient of friction but does not degrade the basic ability to absorb energy.

### POTENTIAL APPLICATION

These energy absorbers could be applied specifically to the automobile industry. As automobile bumpers, two 40 295-newton struts would attenuate a 2055-kilogram vehicle within 15.24 centimeters at a velocity of 10.9 m/sec and maintain the acceleration on the passengers at the level acceptable for spacecraft landing. With the application of a low-onset device to automobile struts, the deceleration-onset rate could be controlled, which would decrease the difference in velocity between the passenger and the vehicle, thereby reducing the secondary impact. By installing a low-onset device on the passenger seat, the secondary impact could be reduced further.

Other potential applications for the energy absorber are telescoping steering columns, vehicle seats, packaging of delicate instruments, and air dropping of cargo.

### CONCLUDING REMARKS

The cyclic concepts described herein allow energy absorbers to be fabricated with precise stroking loads and with the added advantages of pretesting and absorption in both tension and compression.

The low-onset device is a simple device that is readily assembled for any desired load level and rate of onset. The combination of a cyclic strut and a low-onset device results in a strut that will start stroking at a level lower than the nominal stroke level and will build up to maximum stroke value at a desired rate. This combination allows impact loading to be applied without initial overshoot.

## DISCUSSION

G. W. H. Stevens:

With reference to the problem of slippage of the central rod over the rings, one would expect that, at some level of acceleration, the inertia of the rings would have an influence on the slippage. Is there any information on this point?

Drexel:

The inertia does have an influence on ring slippage; however, because the inertia could not be changed, grit blasting the rings and properly selecting the squeeze force eliminated slippage up to an onset rate of loading 1.5 times our expected rate. The inertia does have an effect on the overshoot of initial load. Our tests resulted in 10-percent overshoot at a  $2.5 \times 10^6$  lb/sec onset rate and in 20-percent overshoot at a  $4.8 \times 10^6$  lb/sec onset rate.

G. W. H. Stevens:

Can you give any information on the efficiency, specific energy absorption, of both ring and low-onset shock-absorber units (that is, work done per full stroke against the weight of units)?

Drexel:

Cyclic attenuators have been tested successfully up to a force value of 16 000 pounds with a weight of 14.5 pounds. The cyclic attenuator has a total cumulative stroking life of 100 inches (tension and compression) while maintaining the force value within 5 percent of the nominal stroke value. Attenuators have been tested to 200 inches of stroking before the force value fell below the 5-percent margin. Based on the 100-inch stroke life, the efficiency of the largest unit we have tested is 9195 ft-lb/lb. The low-onset device used in our application absorbed 26 000 inch-pounds and weighed 1.5 pounds. This, of course, does not include the weight of a mechanism to actuate the device because this weight is included in the cyclic attenuator. For our applications, the device has an efficiency of 1450 ft-lb/lb for a single tension stroke.

M. M. Creel:

Have tests been conducted to determine the effect of long-term aging or corrosion (that is, metal to metal fusion) on the low-onset device?

Drexel:

No specific tests have been conducted on unprotected attenuators. The spacecraft attenuators are assembled in an inert atmosphere and are sealed. Tests have been conducted on a sealed unit after 2.5 years of storage, and the resulting stroking force was within the allowable limits, indicating no effect from aging.

## REFERENCES

1. Gulacte, Ronald C.; and Platus, David L.: Cyclic Deformation Crew Attenuator Strut. U. S. Patent 3 435 919.
2. Keathley, William H.; Wesselski, Clarence J.: Low Onset Rate Energy Absorber. U. S. Patent 3 603 433.
3. Platus, David L.: Cyclic Deformation Crew Attenuator Struts for the Apollo Command Module. Shock and Vibration Bull. no. 38, part III, November 1968.
4. Timoshenko, S.: Strength of Materials. Part II, Advanced Theory and Problems. Third ed., D. Van Nostrand Co., Inc., 1956, pp. 386-392.

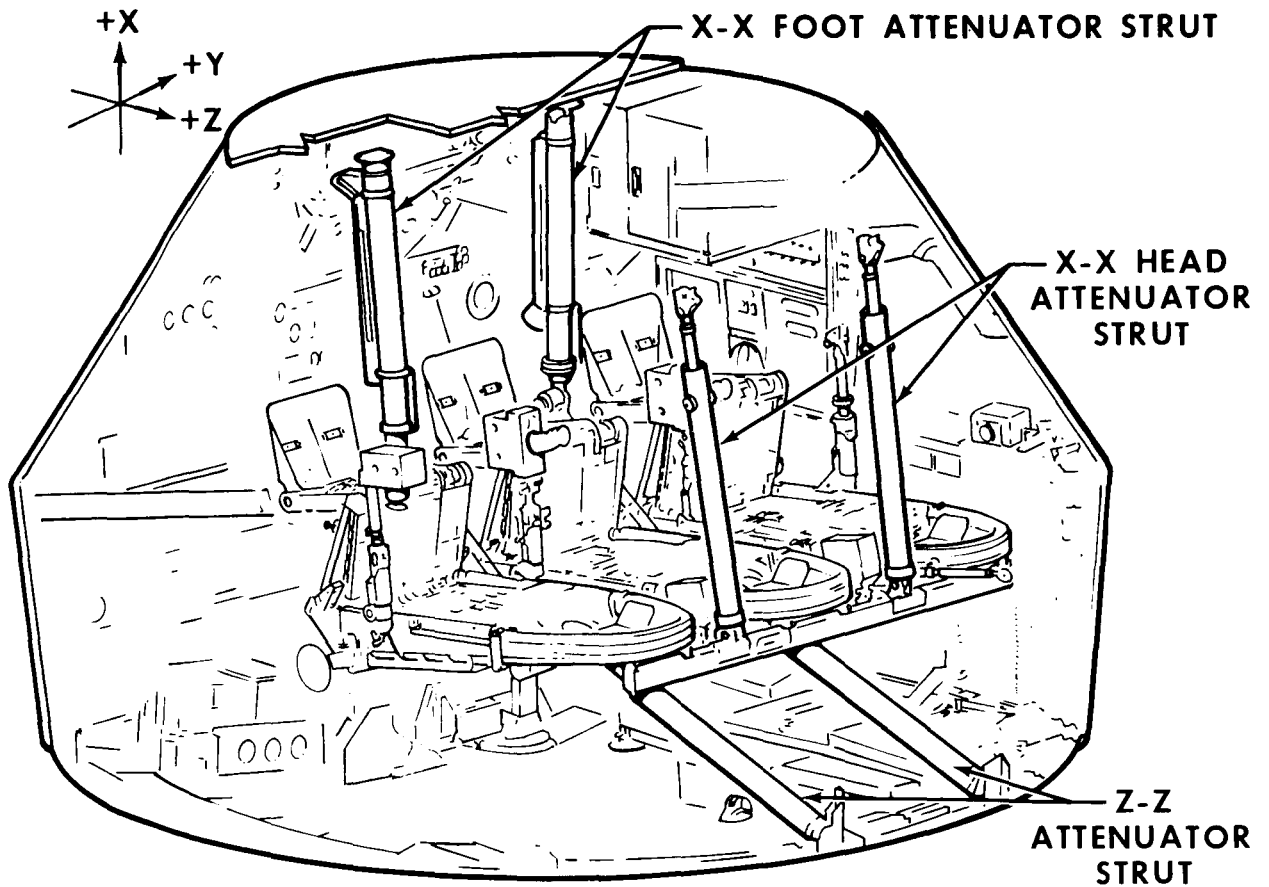


Figure 1. - Apollo load-attenuation-strut configuration.

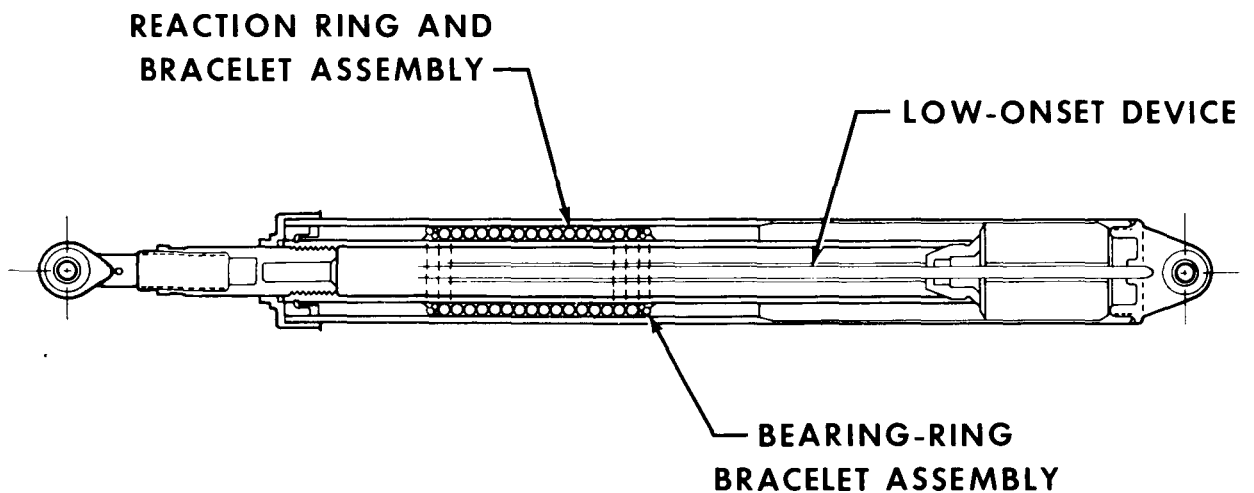


Figure 2. - Configuration of Z-Z axis cyclic-deformation-strut assembly combined with low-onset device.

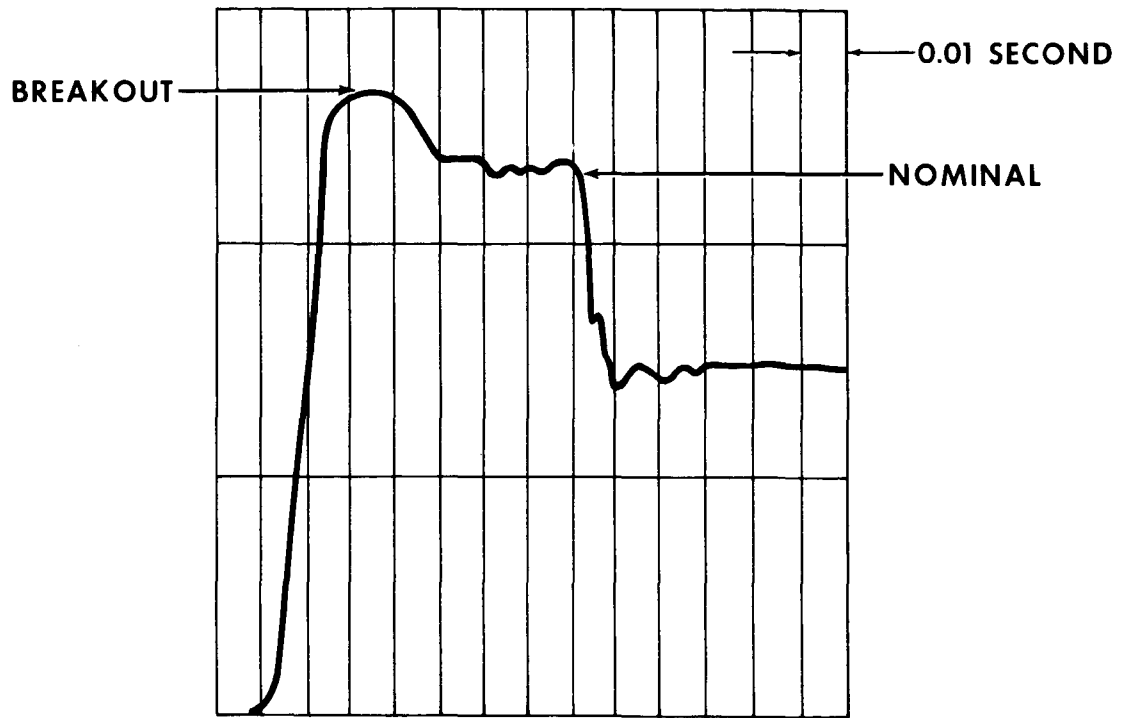


Figure 3. - Cyclic-strut load/time characteristic.

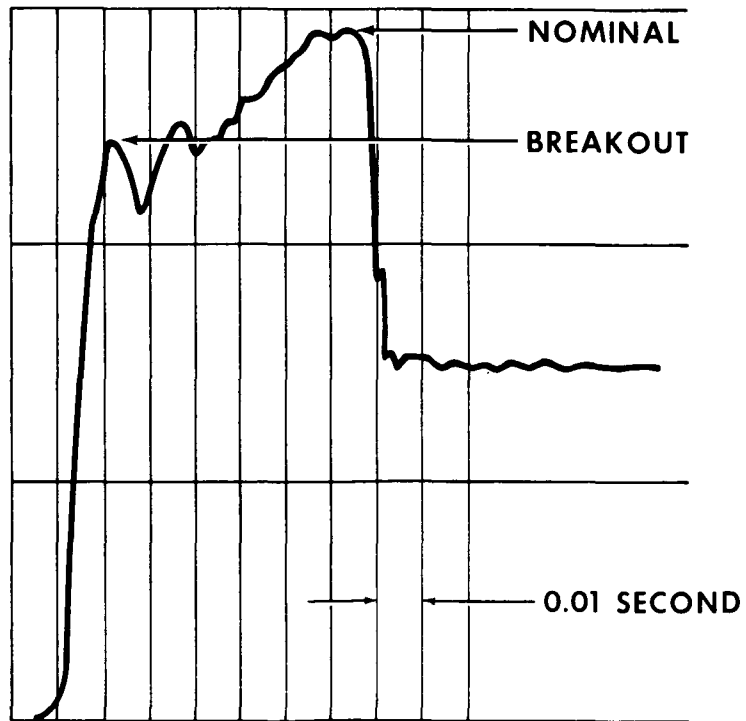


Figure 4. - Combined cyclic-strut and low-onset-device load/time characteristic.

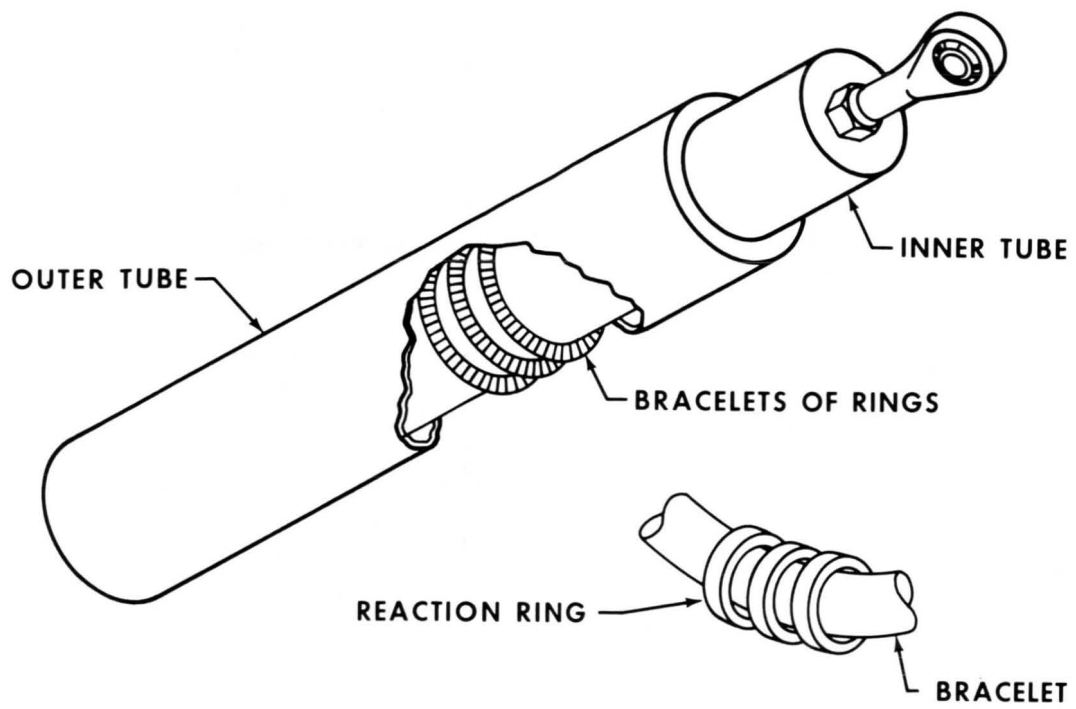


Figure 5. - Cyclic-deformation crew attenuator strut.

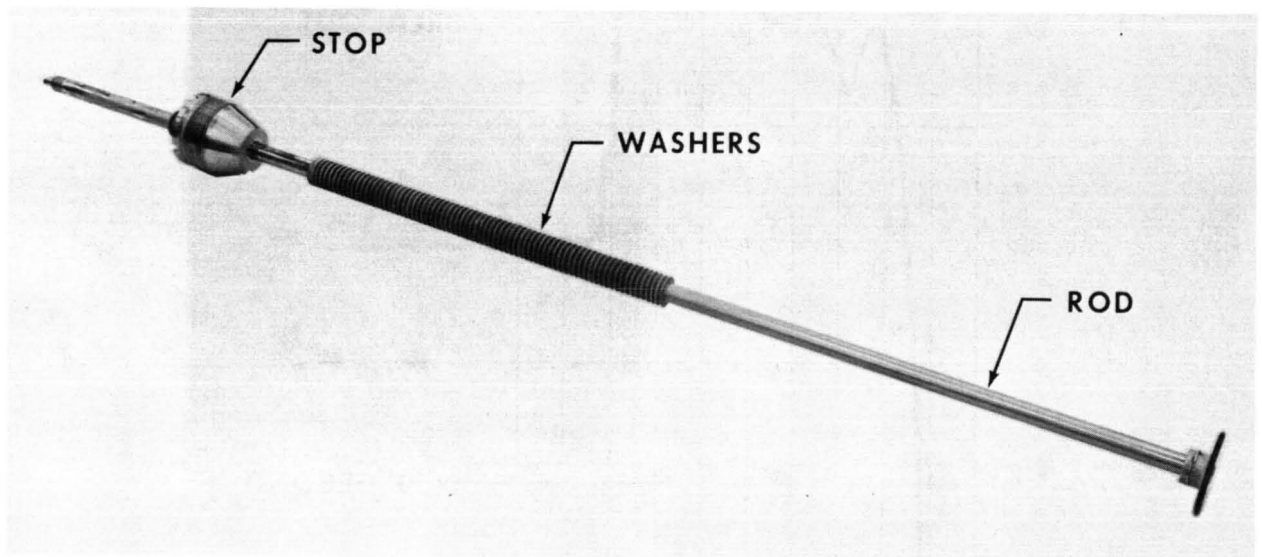


Figure 6. - Apollo low-onset device.

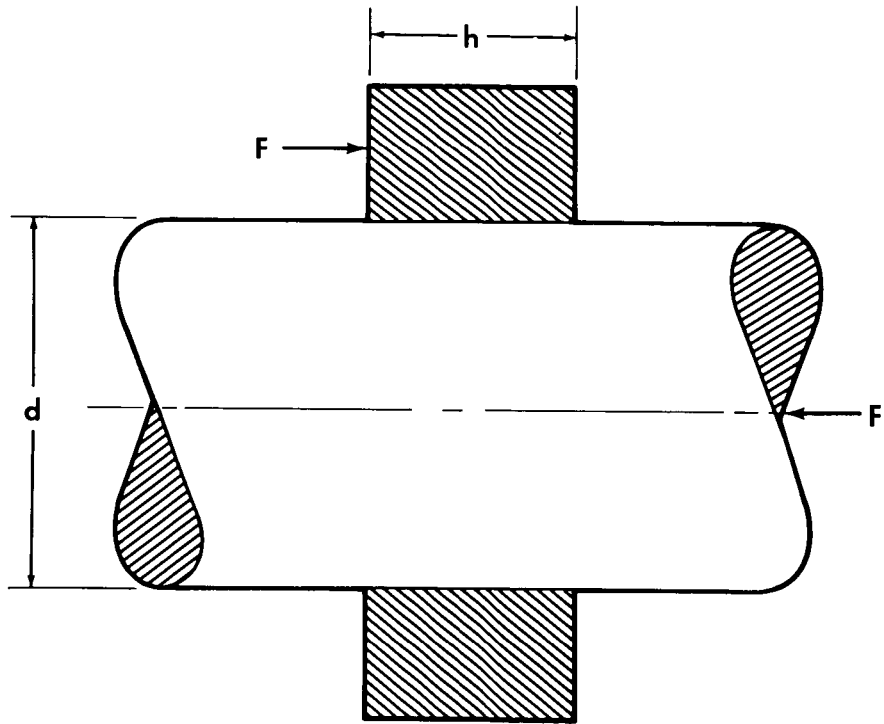


Figure 7. - Rod and washer geometry.

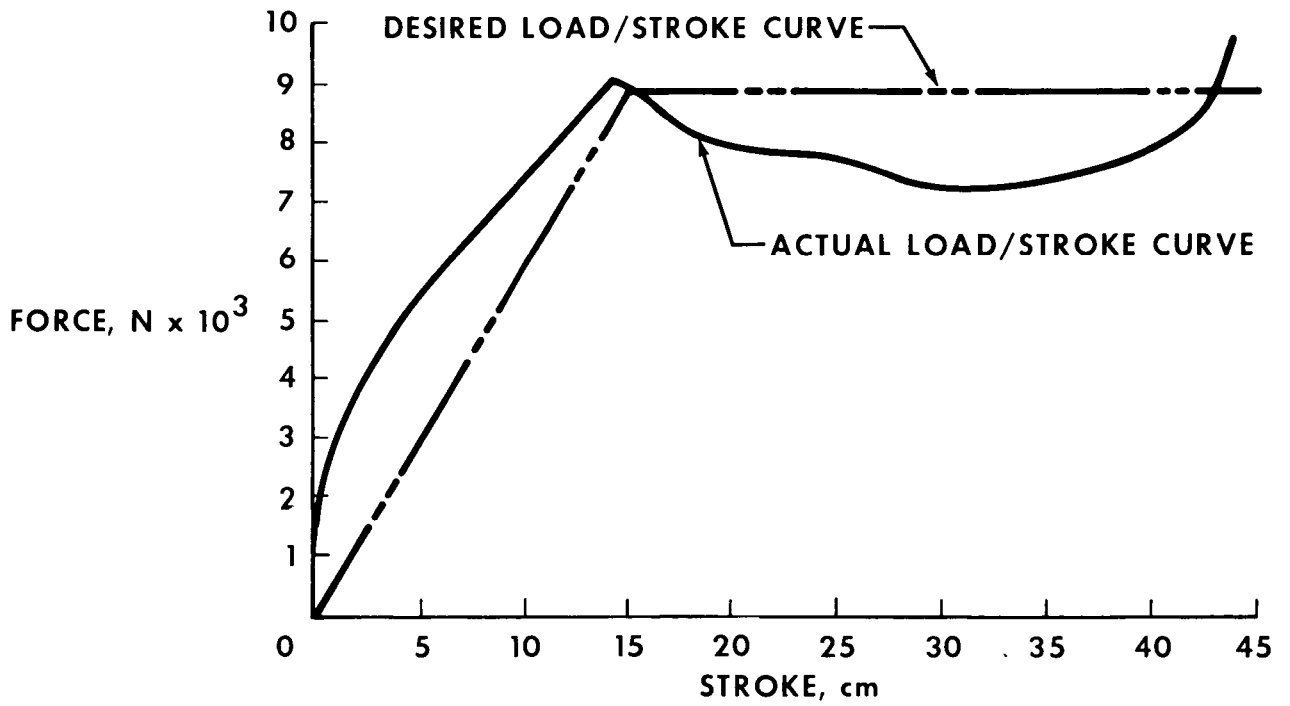


Figure 8. - Load as a function of stroke.

**Page intentionally left blank**

## THE LUNAR CART

By Glenn C. Miller\*

### ABSTRACT

A need was defined for expanded experiment-carrying capability for the lunar-surface crewmen, to be used between the Apollo 11 capability and the lunar roving vehicle capability. Methods used on earth to satisfy similar requirements were studied. A two-wheeled cart was built and tested to expected mission requirements and environments. The vehicle was used successfully on Apollo 14.

### INTRODUCTION

After the first manned landing on the moon, the NASA Manned Spacecraft Center needed to expand the capability of the crewmen to carry experiments and associated tools a greater distance from the lunar-landing site. The lunar rover was to be used on later missions, but in the interim, a simple light device was desired to bridge the gap in mobility range for the Apollo experiments. The basic requirement was to carry a maximum of 163.30 kilograms (360 pounds) of equipment up to 3352.8 meters (11 000 feet) from the landing site. The weight limit for this capability was 13.61 kilograms (30 pounds). There were 30 items of potential payload, and they varied widely in size, shape, material, and weight; thus, no standardized mounting procedures could be used.

### STUDY OF POTENTIAL CANDIDATES

Various devices used on earth to satisfy similar requirements were examined. This examination resulted in the following list: the travois, the suitcase, the pallet, and the single-, dual-, and four-wheeled vehicles. Each of these devices was an expression of the materials and resources available for the situation under which they had evolved on earth. Because each device was successful on earth, presumably, it would work on the moon.

The travois was conceived to carry heavy loads, but it disregarded efficient power utilization (fig. 1). Basically, the suitcase was designed to protect transported objects and to reduce many items to one item (fig. 2). A pallet, an excellent device for carrying many different things, accommodated a diverse and changeable payload (fig. 3). The wheelbarrow was a means of transporting heavy loads or diverse and

---

\*NASA Manned Spacecraft Center, Houston, Tex.

changeable loads for short distances; it reduced the lifting load and minimized the rolling friction by utilizing the wheel (fig. 4). The two-wheeled cart, a more stable wheelbarrow, reduced the wheel-bearing pressure for each wheel (fig. 5). The four-wheeled wagon was a very stable vehicle having low surface-contact pressure/wheel (fig. 6). The wagon was inherently heavier and less maneuverable than were the one- or two-wheeled vehicles. The single-, dual-, and four-wheeled vehicles and a pallet were chosen for testing.

## SELECTION OF CONCEPT

A test vehicle was constructed to observe the options. The payload of 163.30 kilograms (360 pounds) became the prime criterion in the final selection of a test vehicle. To keep the loaded wheelbarrow stable, the crewman had to grip the handles constantly; thus, he was fighting continually the desire of the pressurized glove to remain extended. Within several minutes, his forearms became so tired that he had to rest. Also, the decision was made that the crewman should pull rather than push the vehicle. If the wheel became lodged in a hole or deep soil when the crewman was pushing the vehicle, he could be catapulted over the vehicle; however, if the wheel hit an immovable object when the crewman was pulling the vehicle, it was pulled from the crewman's grasp. The two-wheeled cart was a solution to the stability problem of the wheelbarrow and considerably reduced the arm fatigue; therefore, the heavier four-wheeled vehicle was eliminated from further consideration. Thus, the two-wheeled cart, which contained a pallet as the body of the cart, became the final selection.

## TYPE OF WHEEL

The rubber tire was selected because of its widespread use on earth. The rubber tire did not present a temperature problem. Previously, rubber tires were tested, under load, to 202.59° K (-95° F) before they failed; the predicted minimum operational temperature on the lunar surface was 238.70° K (-30° F). The principal problems with the rubber tire were the ability of the tire to hold air in a vacuum and the tear resistance of the tire on the lunar surface.

## DEVELOPMENT AND QUALIFICATION

### Vehicle/Crew Interface

To define the crew interface, 1/6g testing was conducted. The first configuration had two handles that caused problems: the rolling gait of the crewman imparted the same roll to the cart, and the fact that two handles required two hands disturbed the gait. By switching to one handle, both problems were eliminated (fig. 7).

The next interface problem, the tiring of the crewman's arm from gripping the handle, was solved by going to a triangular grip (fig. 8). The dimension of the triangle base was greater than the gloved hand; however, the altitude of the triangle was less

than the gloved hand. This fact allowed the crewman to insert his hand on the grip; with a 90° rotation of his hand, the glove was wedged into the triangle. In this fashion, the crewman could pull the cart without gripping the handle.

In testing the vehicle, the fact was noted that the two legs, which provided the desired static stability, would hit the ground often. To solve this problem, a hinged joint was added, allowing the lower half of the leg to rotate when it hit a rock or the ground (fig. 9). A spring in the joint then forced the lower half of the leg to return to vertical. The joint had a slot to accept a pin in the lower leg when the leg was set on the ground; this action locked the joint for the desired static stability.

The proper height of the pallet above the ground was determined with a suited test subject. The wheel diameter and cross section were defined by measuring the pull-force capability of the crewman at 1/6g and by matching this capability with the calculated pull force of various wheel combinations. The required pull force compared with the load is shown in figure 10. The crewman's capability for sustained pulling was approximately 26.69 newtons (6 pounds), and his instantaneous pull force was approximately 111.2 to 155.68 newtons (25 to 35 pounds). From these data and the experience of the suited test subjects, the conclusion was reached that the crewman could pull as much as 163.30 kilograms (360 pounds) of vehicle, but that this action would have considerable effect on his oxygen and water usage and would reduce his total extravehicular-activity time on the moon. The vehicle payload was reduced by eliminating one experiment; the payload and the vehicle weight then became 61.24 kilograms (135 pounds). On the slopes of Cone Crater (a significant lunar-terrain goal for Apollo 14), the crewmen had to use the full 26.69-newton (6 pound) pull-force capability as opposed to the 3.34-newton (0.75 pound) capability on level surfaces. However, by trading the pulling job between crewmen and by remembering that the downhill portion of the traverse would be considerably easier, the decision was reached that the vehicle could be pulled without affecting the mission time on the lunar surface.

### Vehicle/Environment Interface

The critical environments affecting the vehicle were heat, atmosphere, vibration, and the lunar surface. The environment-critical parts of the vehicle were the rubber tires, the wheel bearings, and the overall structure of the vehicle.

Wheel-bearing thermal drag. - The wheel-bearing test was accomplished by cold soaking the wheel assembly to 216.48° K (-70° F) in a vacuum chamber, heating the wheel hub to 366.48° K (200° F), and measuring the thermal gradients and the drag of the bearings. A simulated lunar soil (a mixture of red crushed volcanic scoria and air-floated clay) was poured on the bearing dust cover at the same time. The peak drag, 342.04 gram-centimeters (4.75 inch-ounces), was well within limits.

Launch and landing vibration. - This test was performed as part of a requalification test of the modular equipment stowage assembly (MESA) to which the lunar vehicle was to be attached for the ride to the moon.

Thermal vacuum. - This test was performed to simulate the entire thermal mission. The vehicle was placed in a vacuum chamber in thermal wrappings on a pallet simulating the MESA. The temperature of the walls and floor were lowered to simulate deep space and the lunar surface at the sun angle anticipated for the landing site during

the time between landing and vehicle deployment. In this portion of the test, the vehicle-tire temperatures fell below the limit temperature of 216.48° K (-70° F); therefore, in the actual mission, the vehicle was deployed earlier and set aside in the sun until it was to be used. Later in this test, a suited subject deployed the vehicle inside the chamber. The maximum temperature of the vehicle structure and tires (≈366.48° K (≈200° F)) was recorded as anticipated; however, the temperature was not exceeded.

Thermal-vacuum endurance. - This test was devised to duplicate the travel ability of the vehicle on the lunar surface (fig. 11). A wooden cylinder 76.20 centimeters in diameter and 182.88 centimeters long (30 inches in diameter and 72 inches long) was coated with sand embedded in epoxy. A contour was cut in the drum so that one revolution of the drum represented 25.40 linear centimeters (10 linear feet) of an average lunar surface. Several rocks, varying from 2.54 to 10.16 centimeters (1 to 4 inches) in diameter, were bolted to the surface of the drum and were placed in groups by size along the length of the cylinder. The cylinder was mounted on an axle in the chamber, and the test vehicle was supported from the ceiling of the chamber at an angle of 8.3° from the vertical to provide the 1/6g force of the cart normal to the cylinder. The cylinder was run at a speed of 0.305 m/sec (1 ft/sec) for 2 minutes; the tire temperature was 216.48° K (-70° F) to simulate the condition at the beginning of a traverse. Then, the cylinder was run at a speed of 1.07 m/sec (3.5 ft/sec), and the tire temperature was 366.48° K (200° F). The second run was conducted on an area without rocks (150 revolutions), on an area with several 3.81-centimeter (1.5 inch) rocks (300 revolutions), on an area with 6.35-centimeter (2.5 inch) rocks (10 revolutions), and finally, on an area with 10.16-centimeter (4.0 inch) rocks (3 revolutions). This test was equivalent to 1411.22 meters (4630 feet) of horizontal travel. The last section of the run was done at 255.37° K (0° F), the predicted temperature of the tire in motion. This run was varied over the cylinder on the same basis and totaled 999 revolutions (3044.95 meters (9990 feet)) of travel.

### Vehicle/Payload Interface

By mission time, 23 metal, cloth, and plastic equipment items were mounted on the pallet of the vehicle (fig. 12). Four cameras, the hand-tool carrier, lunar-soil-sample bags, lunar-atmosphere-sample containers, and a lunar-surface magnetometer were included. Springs, clips, bags, straps, and existing protrusions on the items to be mounted were used to hold down the items. All interfaces were compatible with restrictions imposed on the crewmen in a pressurized garment.

### The Rubber Tire

The tire specifications are shown in table I. The first tire that was delivered met these specifications except for pressure loss. The primary problem was the permeability of the synthetic natural rubber tubes. Standard tubes are made of butyl rubber and are good to 233.15° K (-40° F); thus, the synthetic material was used. An increase in thickness from  $2.54 \times 10^{-2}$  to  $15.24 \times 10^{-2}$  centimeters (0.01 to 0.06 inch) and a  $10.16 \times 10^{-3}$ -centimeter (4 mil) layer of polyurethane solved this problem. Six weeks

before launch, when the cart was stowed on the launch vehicle, the tires were inflated in a vacuum bell jar to  $10.34 \times 10^3 \text{ N/m}^2$  (1.5 psia). Just before inflation, the tires were baked at  $366.48^\circ \text{ K}$  ( $200^\circ \text{ F}$ ) for 24 hours to reduce the outgassing.

### CONCLUDING REMARKS

Used on the Apollo 14 mission, the MET (fig. 13) successfully met all requirements. The slopes of Cone Crater, the fully loaded MET (foreground), and the lunar module (background) are illustrated in figure 14.

### DISCUSSION

J. Schmuecker:

What design changes were made as a result of the testing, particularly structural changes as a result of environmental tests? If there were no changes or if the changes were minor, in retrospect was the extent of the test program justified?

Miller:

The wheel-support hinge was thickened after hinge failure in tests. This could have been discovered without the vacuum or temperature environment that were part of the structural tests. Tire-tube thickness was changed as a result of environmental testing. The tire-inflation procedure was changed also. The mission time line changed as a result of environmental testing. I feel that the tests were justified.

R. J. Peterson:

What type of bearings are used for the wheels and how are they lubricated? Did you use seals to exclude contaminants?

Miller:

Bearings were standard BEMOL roller bearings with a Feuralon retainer ring that provided dry-film lubrication. We designed a dust cover to exclude contaminants.

TABLE I. - TIRE SPECIFICATIONS

Color . . . . .	Black
Size, width by height, cm (in.) . . . . .	10.16 by 40.64 (4 by 16)
Inflation pressure, N/m <sup>2</sup> (psia) . . . . .	10.34 × 10 <sup>3</sup> to 20.68 × 10 <sup>3</sup> (1.5 to 3)
Deflection under load, percent . . . . .	30
Allowable pressure loss:	
6 weeks in 101.34 × 10 <sup>3</sup> N/m <sup>2</sup> (14.7 psi) ambient and 2 weeks in vacuum, N/m <sup>2</sup> (psia) . . . . .	0.69 (0.1)
Abrasion and wear, meters (feet) of travel over simulated lunar surface . . . . .	6096 (20 000)
Outgassing, percent weight loss after baking in a vacuum chamber for 72 hr at 394.26° K (250° F) . . . . .	>4.3
Operating temperature environment, °K (°F) . . . . .	208.15 to 394.26 (-85 to 250)

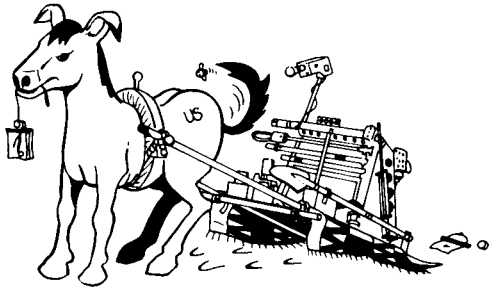


Figure 1. - The travois.

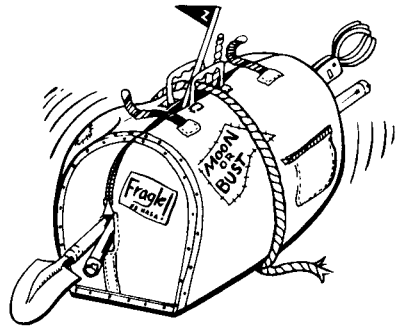


Figure 2. - The suitcase.

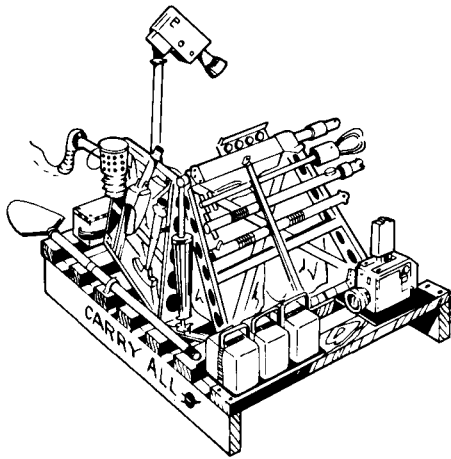


Figure 3. - The pallet.

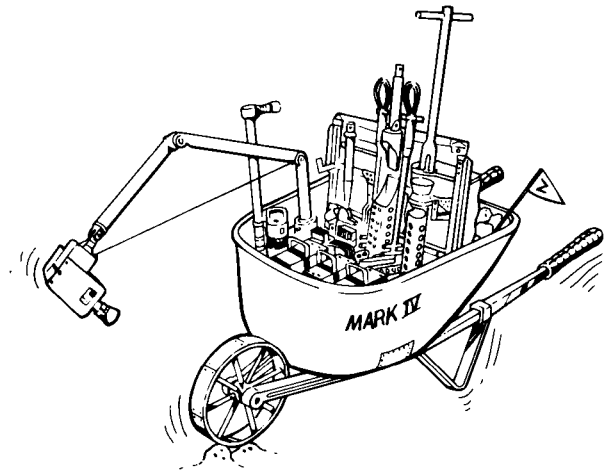


Figure 4. - The wheelbarrow.

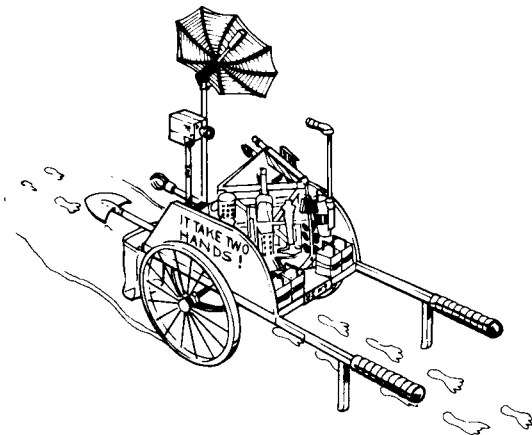


Figure 5. - The cart.

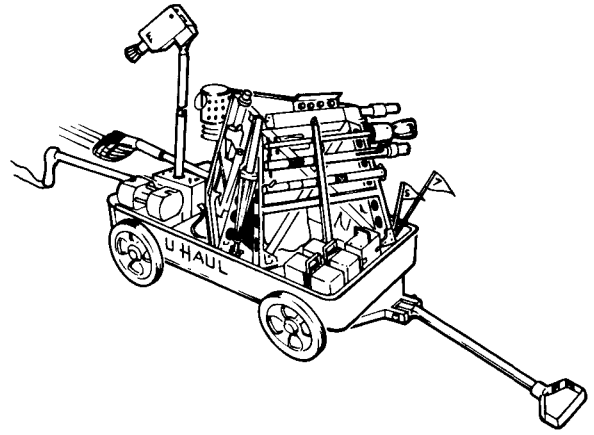


Figure 6. - The wagon.



Figure 7. - Cart with one handle.

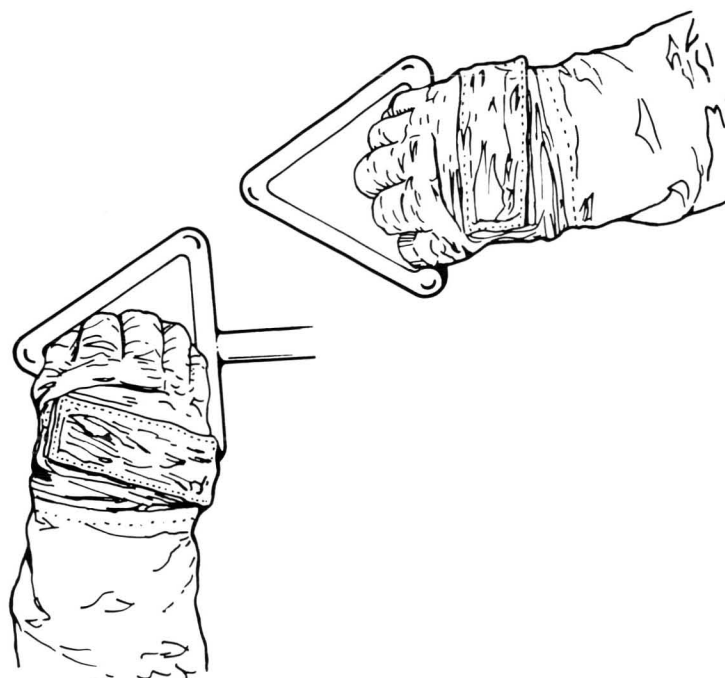


Figure 8. - Handgrip.

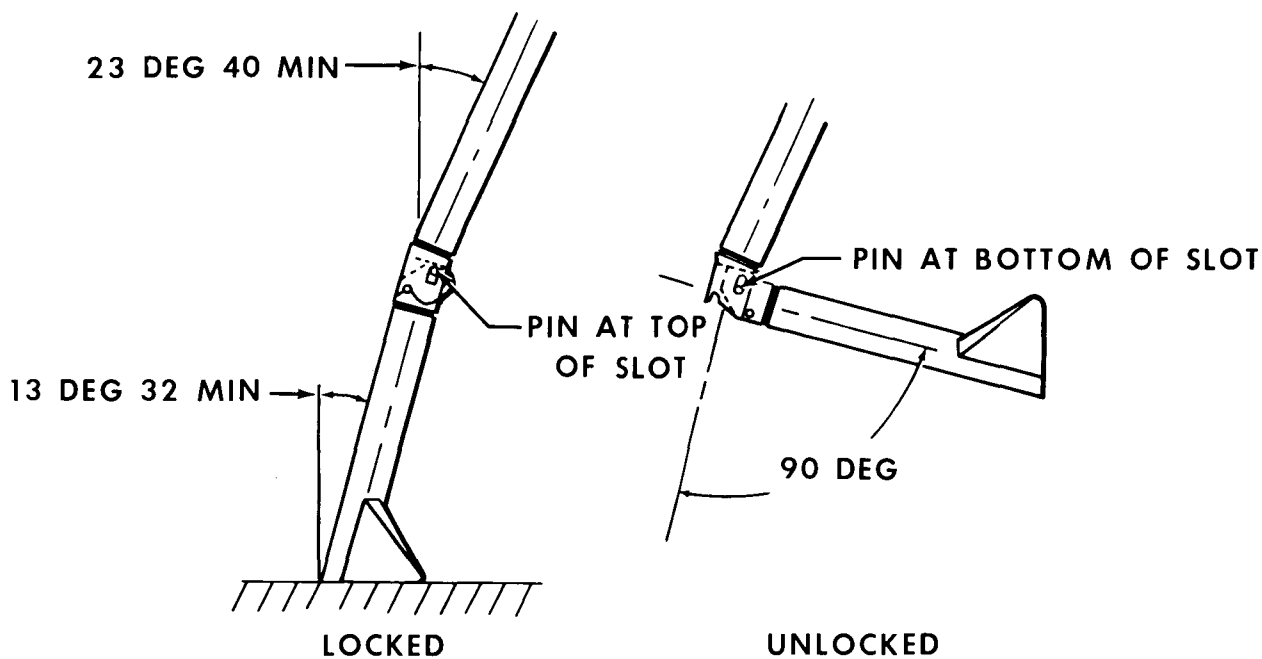


Figure 9. - Articulate leg.

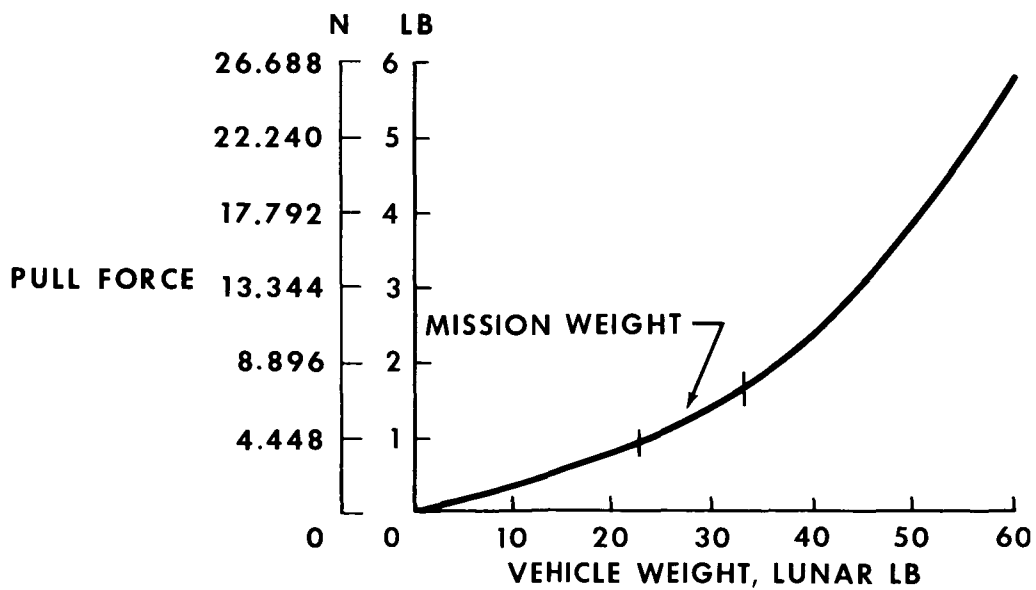


Figure 10. - Pull force compared with weight.

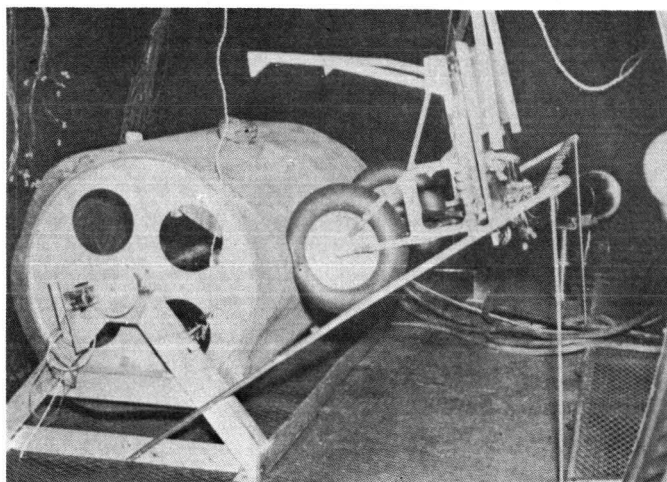


Figure 11. - Thermal-vacuum endurance test.

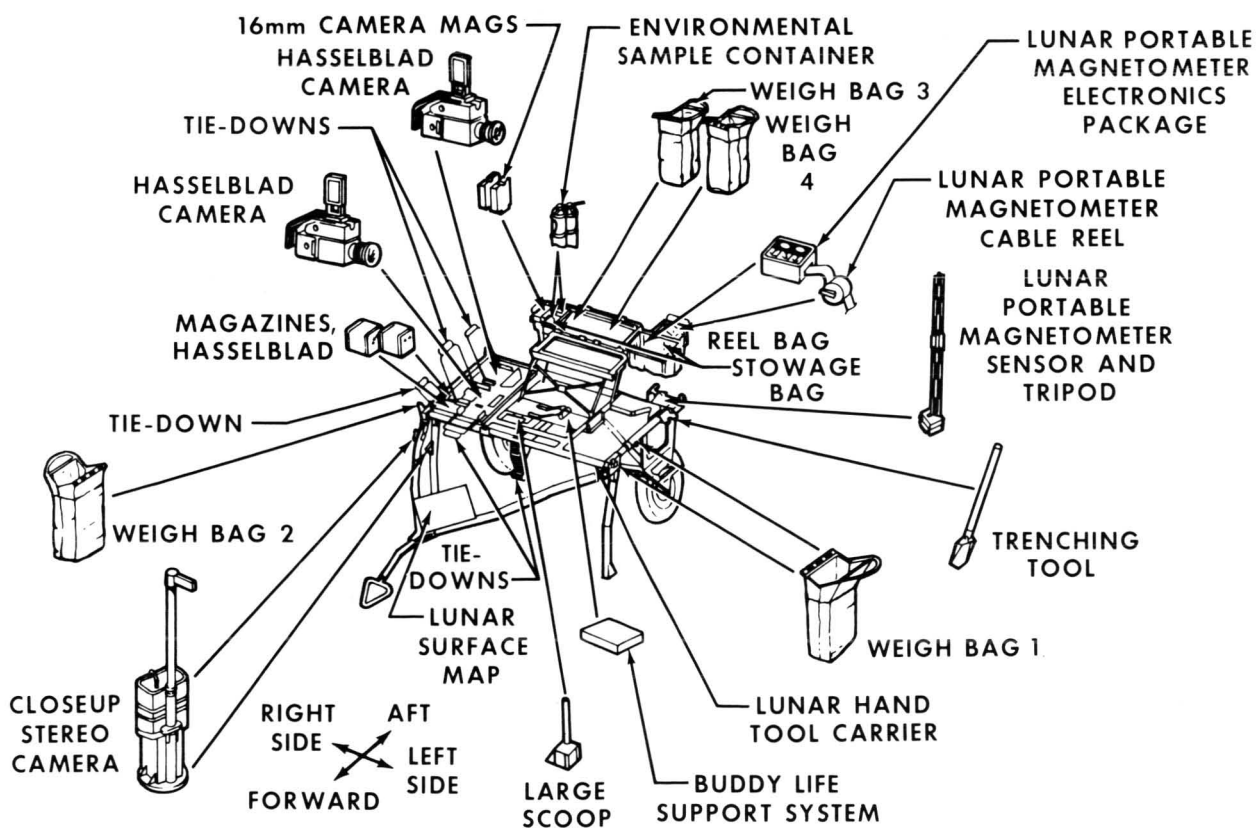


Figure 12. - Modular equipment transporter and equipment.

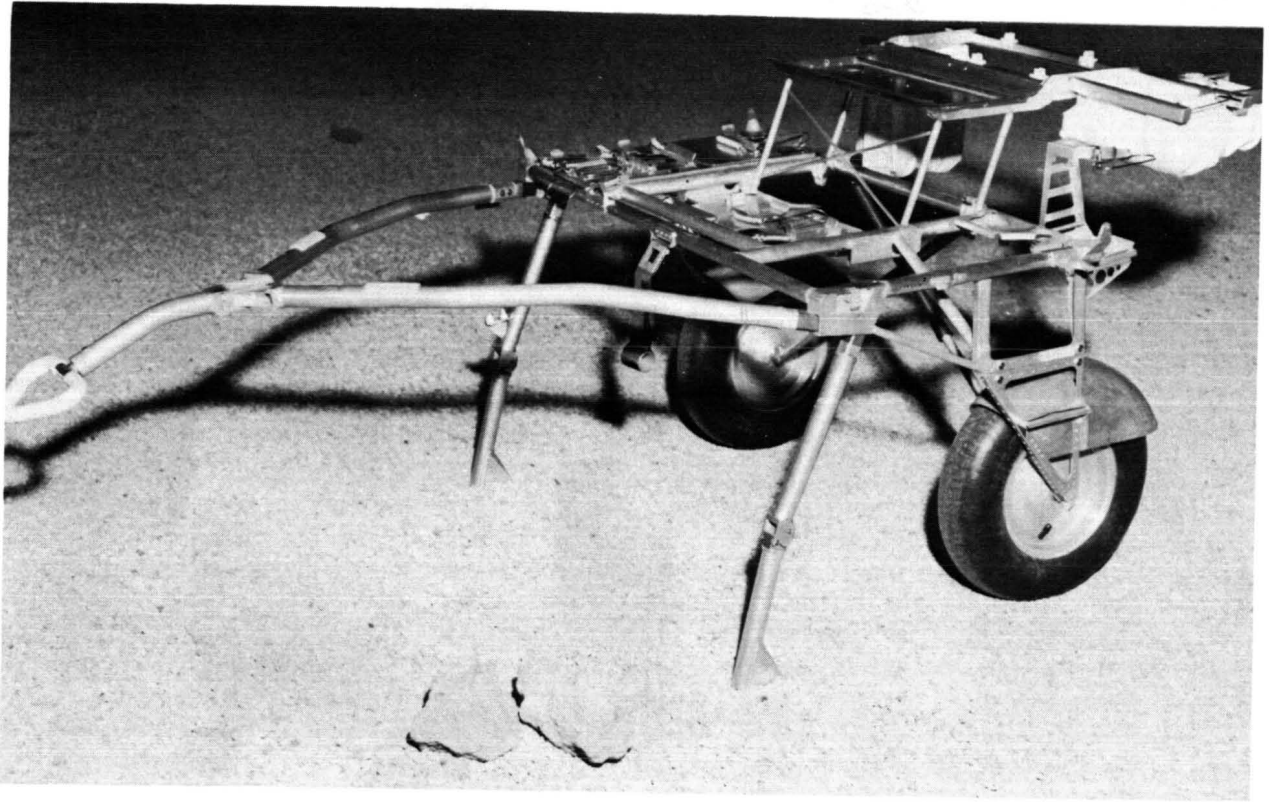


Figure 13. - Modular equipment transporter.

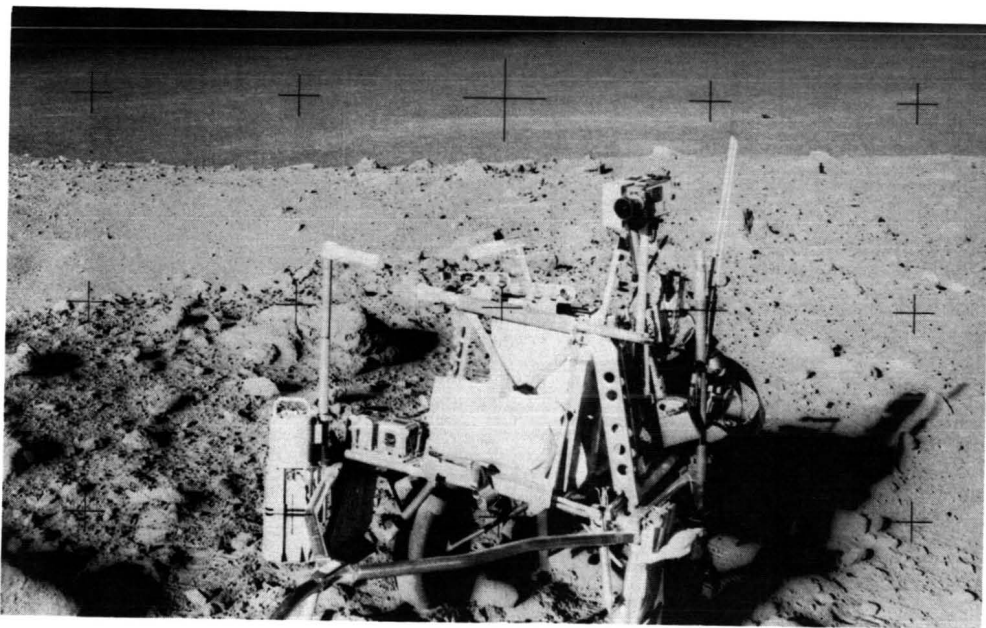


Figure 14. - Fully loaded modular equipment transporter at Cone Crater.

**Page intentionally left blank**

## LIQUID PUMP FOR ASTRONAUT COOLING

By Maurice A. Carson\*

### ABSTRACT

The Apollo portable life support system water-recirculation pump used for astronaut cooling is described in this report. The problems associated with an early centrifugal pump and how these problems were overcome by the use of a new diaphragm pump are discussed. Performance comparisons of the two pump designs are given. Developmental problems and flight results with the diaphragm pump are discussed.

### INTRODUCTION

Early in the Apollo Program, tests and engineering analyses revealed that gas ventilation alone provided inadequate body cooling for the astronaut performing extravehicular work. As a result, a liquid cooling system was incorporated into the extravehicular mobility unit (EMU) to circulate water through a network of tubing sewn into an undergarment worn by the astronaut. The water is cooled by a heat sink located within the portable life support system (PLSS). A simplified schematic of the cooling system is shown in figure 1. As indicated in figure 1, the cooling system is a completely closed loop. The rate of flow through the liquid cooling garment is constant, and a comfortable fluid temperature is maintained by partial water bypass of the heat exchanger.

### REQUIREMENTS

Design requirements established for the cooling system pump were as follows.

1. Flow rate: 1.82 liters/min
2. Pressure rise:  $0.37 \text{ kg/cm}^2$
3. Inlet pressure:  $1.31 \text{ kg/cm}^2$
4. Inlet temperature:  $289.15^\circ \text{ K}$  ( $16^\circ \text{ C}$ )
5. Input voltage: 16.8 V dc

---

\*NASA Manned Spacecraft Center, Houston, Tex.

6. Input power: 11.0 watts
7. Weight: 1.1 kilograms (maximum)
8. Operating environment: 0 to  $1.013 \times 10^5$  N/m<sup>2</sup> (0 to 1.0 atmosphere)

In addition, the usual Apollo environmental, safety, reliability, and compactness requirements were imposed.

Generally, commercially available pumps were unable to satisfy the requirements for one or more of the following reasons.

1. The overall efficiency was too low for the 11.0-watt power limitation.
2. The envelope and weight exceeded established limits.
3. When subjected to design limit requirements, reliability was too low to be qualifiable.

The conclusion was reached that the best method of meeting the established criteria was to design a new pump for the stated requirements.

## DESCRIPTION

### Centrifugal Pump Design

The initial PLSS pump design featured a brushless direct current motor mated to a centrifugal pump. As shown in figure 2, the pump impeller was an integral part of the motor armature. This simple pumping concept proved in developmental tests to be highly inefficient, requiring an average power input of 28 watts to achieve the specified flow rate and hydraulic head. It was estimated that "tuning" type design changes to the basic unit would have a negligible effect on the overall power requirement.

Other problems associated with this pump that would have necessitated redesign were in the following areas.

1. Bearings: The dry-film-lubricated bearings had an average lifespan of approximately 150 hours; the requirement was 500 hours and a target design life of 5000 hours. Replacement with a long-life bearing having the capability to accept the high thrust and radial loads would have necessitated a housing redesign.
2. Corrosion: The primary pump materials, alodined aluminum and steel, had significant corrosion problems. Elimination of this problem would have required a materials-replacement effort.
3. Electronics: Developmental testing indicated that the electronics module was unable to accept mission vibration and shock loads. A redesign would have required denser packaging and potted electronics.

Considering these problem areas as a group, the principal reason for deciding on a new pump was that of power. Solutions for the other problems were readily available, but it was considered impossible to approach the 11.0-watt input-power requirement with a centrifugal pump.

### Diaphragm Pump Design

The approach selected for a new pump was a double-acting, positive-displacement, diaphragm-type unit that was under development at the time. The input power for this development pump was within the specification requirements; further, isolation of the motor from the water promised to eliminate bearing and corrosion problems. The pump, shown in the cutaway view (fig. 3) and in the isometric projection (fig. 4), consists of two diaphragms at the end of a walking beam that is supported by a torsion rod. Inlet and outlet check valves are provided for each diaphragm chamber. Part of the walking-beam structure is the armature of a two-position solenoid. A permanent magnet forms part of the motor frame, as shown in figure 3. When the pump is not energized, the armature rests against one leg of the permanent magnet, and two of the four air gaps are closed. Energizing the coil weakens the magnetic flux across the closed air gaps and strengthens the magnetic flux across the open air gaps. Energy stored in the torsion rod accelerates the armature toward the center position when the magnetic force at the closed air gaps is neutralized. Thus, the position of the bistable solenoid armature changes with the electromagnetic field polarity established by the current direction through the coil. This displacement of the walking beam causes one diaphragm chamber to discharge fluid while the other chamber takes in fluid. Upon reversal of the current, the opposite air gaps are closed and the diaphragms are displaced in the opposite direction to deliver a pulse of flow through the check valves.

The integrated electronics control circuit consists of an amplifier section, which directs current to the electromagnetic coil, and a timing-inverter section, which sets the frequency with which the current is reversed through the coil. By suitably matching the spring constant of the spring-mass system to the electronic timing section, the frequency of the electromagnetic field reversals can be tuned to the natural resonance of the spring-mass system. By using energy stored in the torsion bar to augment the electromagnetic force on the walking beam, a significant pump input power reduction is achieved. The physical envelope of this pump is shown in figure 5.

The significant problems that occurred during development of this pump and the solutions of the problems are as follows.

1. Check valves: The valve seats, which were fabricated from a Teflon-based material, tended to deform conically under pressure loading, causing leakage (thus low pumping head). The problem was solved by changing the seat to 6061-T6 aluminum for increased structural rigidity.

2. Diaphragms: Water leakage occurred in some units through the Dacron diaphragm as a result of cracks in the butyl rubber coating material. The problem was traced to a manufacturing technique whereby a liquid butyl compound was applied to both sides of the Dacron fabric followed by a single operation to mold the convolute contour and cure the butyl. This combination form-and-cure operation had the potential for causing the Dacron fabric to migrate to the inside radius of the diaphragm contour.

The problem was solved by performing 100 percent inspection under a 30× magnification and rejecting the diaphragms that showed thin spots, tears, abrasions, or fibers protruding through the elastomer.

3. Torsion bar: In an early test unit, a fracture of the torsion bar was attributed to residual tensile stresses in the bar caused by soldering at the ends of the bar at the subassembly level. The problem was eliminated by redesigning to a pin and clamp arrangement rather than soldering the end shoulders in place.

4. Electronics: During motor testing, it was discovered that incoming voltage spikes of a microsecond duration were sufficient to burn out transistors in the inverter module. These spikes could be generated by electromagnetic interferences on the line or by transients during other PLSS switching functions. The problem was solved by redesign of the PLSS electrical circuitry. The pump was isolated from other components by an electromagnetic interference filter, and a high-speed switching diode was placed across the spike-producing switch to capture spikes at the source.

All of these problems occurred during the ground-based test operations. The pump operation on all Apollo flights has been without problems.

### Performance

As noted previously, the first approach to liquid pumping in the PLSS was rejected, principally because of high input power requirements. With the design change to the diaphragm pump, the specification input power requirement was met. An input power decrease of 18.3 watts for an equivalent output was realized. Defining overall efficiency as output work/input power, overall efficiency for the centrifugal and diaphragm pumps at design point conditions is 3.9 and 11.3 percent, respectively.

Considering that, on Apollo missions, three dual extravehicular activity periods of 7 hours duration each per flight were anticipated and considering the fact that the PLSS power supply is not spacecraft rechargeable, the power reduction achieved with the diaphragm pump resulted in a considerable weight advantage for both the PLSS and the lunar module. At a nominal battery weight of 110 W-hr/kg, the battery weight saving for each PLSS was 1.15 kilograms and for each lunar module was 6.9 kilograms. This neglects any possible structural increases required by a heavier battery. Also, the diaphragm pump was lighter and smaller than the centrifugal unit. Weight was reduced by 0.19 kilogram, and volume was decreased by 6 percent. The performance differences between the units are summarized in table I.

### CONCLUDING REMARKS

The diaphragm pump has been proven on several Apollo flights to be a highly reliable device for pumping water through the astronaut liquid cooling garment. By implementation of this unit, the power objectives established in the portable life support system specifications were met. Performance within the power specification resulted in a significant weight reduction for both the portable life support system and the lunar module. The diaphragm pump also proved to be lighter and more compact than the predecessor centrifugal pump.

## DISCUSSION

J. H. Parks:

You stated that, essentially, the purer the water, the more corrosive its action. Could you elaborate on that statement?

Carson:

The pure water referred to meant deaerated water used in the portable life support system. Because deaerated water lacks dissolved oxygen, it is a reducing environment for the natural passive oxide film which forms on metals and, thereby, causes a greater corrosive attack on certain alloys.

**TABLE I. - DESIGN POINT PERFORMANCE COMPARISON  
BETWEEN CENTRIFUGAL AND DIAPHRAGM PUMPS**

Characteristic	Centrifugal pump	Diaphragm pump
Voltage, Vdc . . . . .	16.8 ± 0.8	16.8 ± 0.8
Flow rate, liters/min . . . . .	1.82	1.82
Pressure rise, kg/cm <sup>2</sup> . . . . .	0.37	0.37
Power consumption, W . . . . .	28	9.7
Weight, kg . . . . .	0.8	0.61
Envelope, cm . . . . .	8.8 diameter by 9.3	10.1 by 5.6 by 8.6
Overall efficiency, percent . . .	3.9	11.3

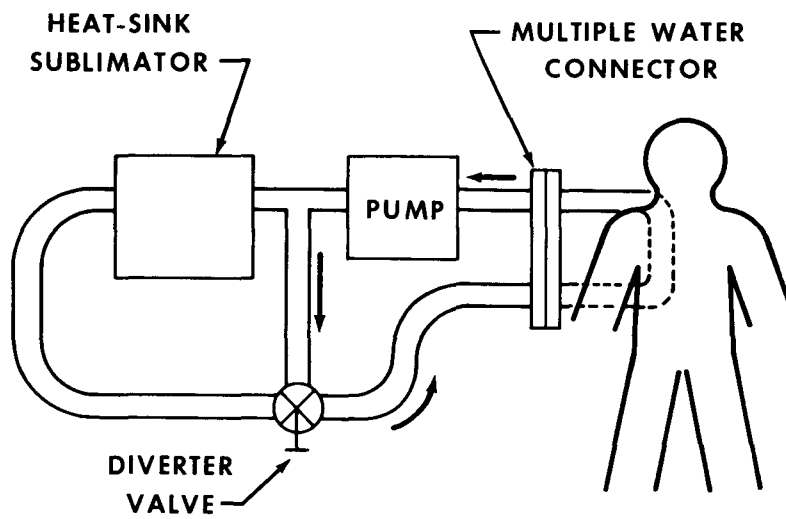


Figure 1. - The PLSS cooling-loop schematic.

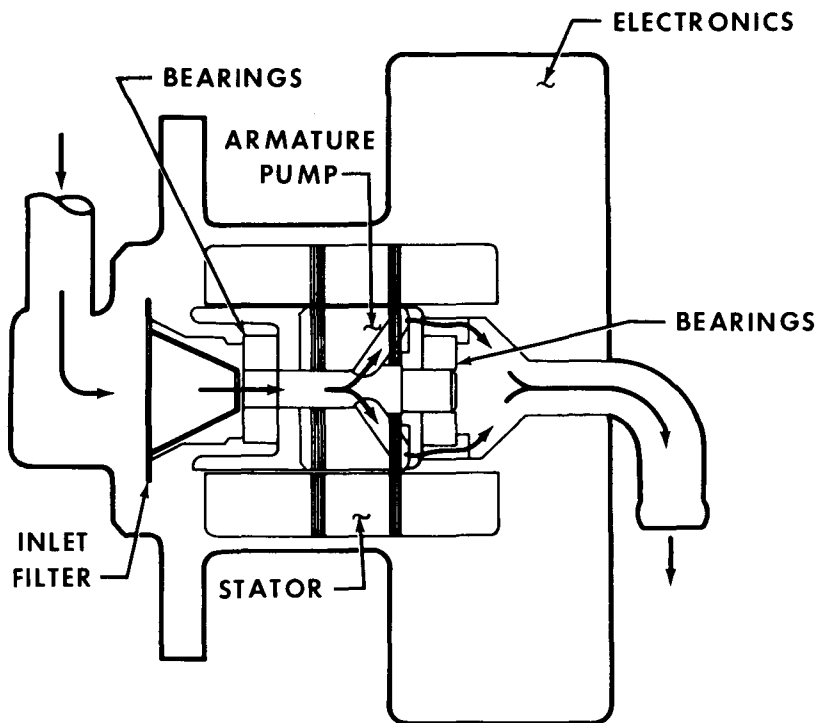


Figure 2. - Centrifugal pump schematic.

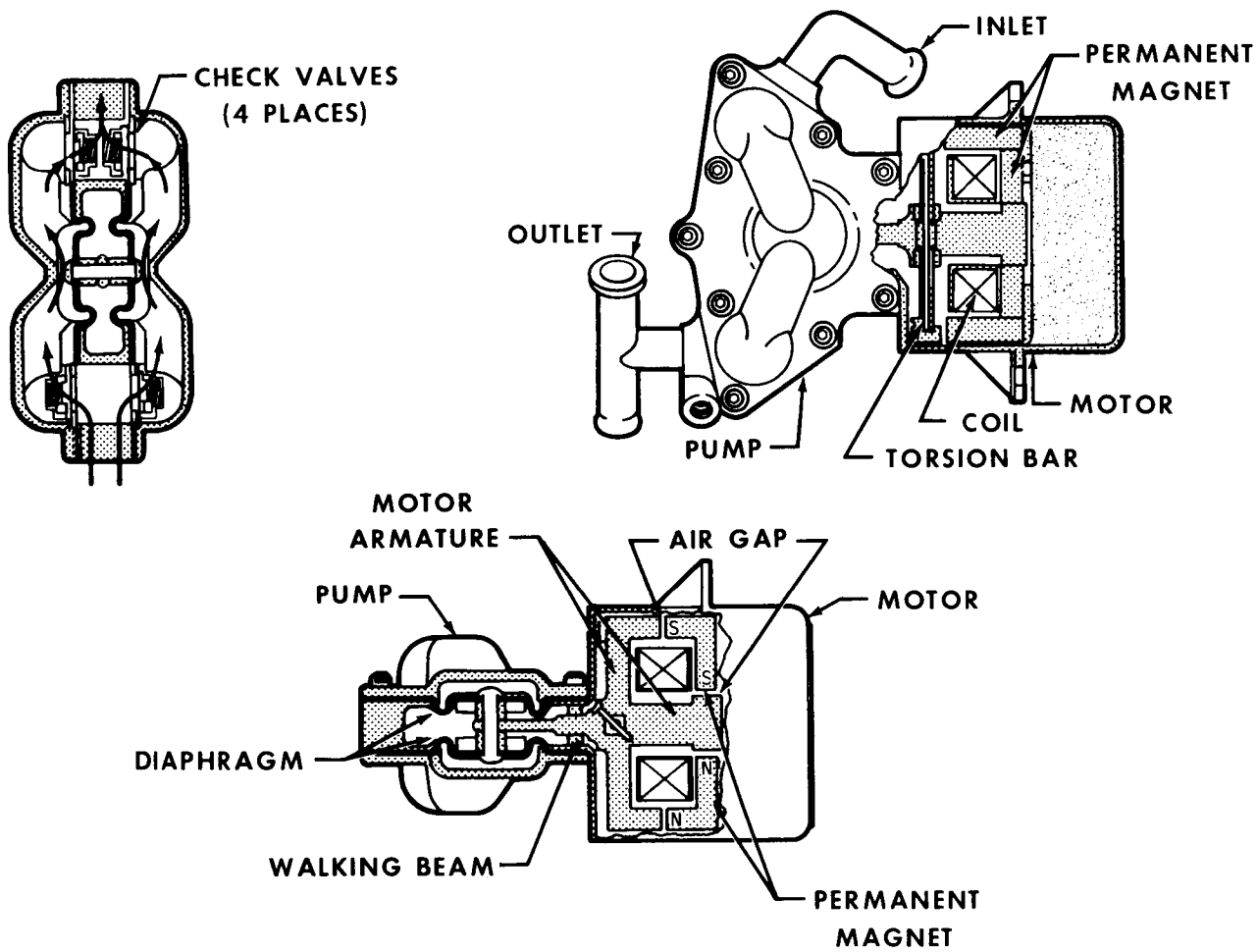


Figure 3. - Diaphragm pump cutaway.

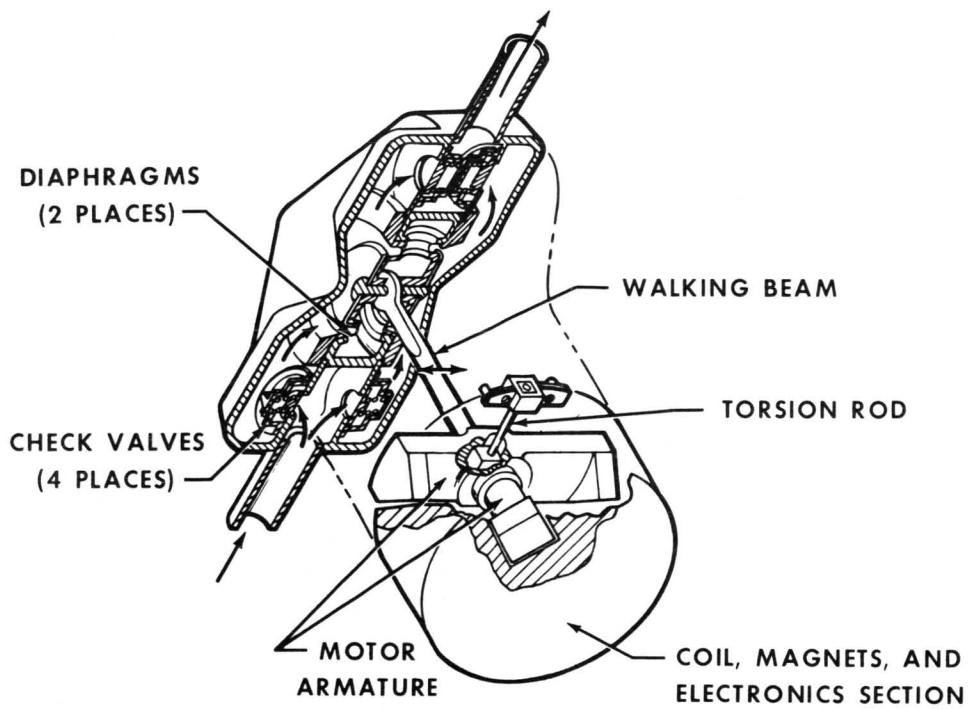


Figure 4. - Diaphragm pump isometric projection.

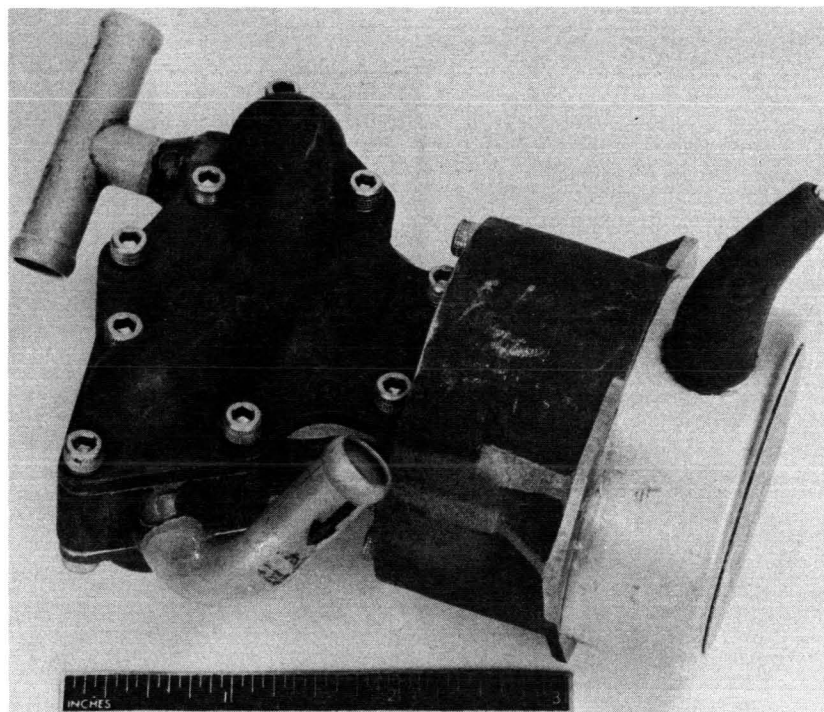


Figure 5. - Diaphragm pump.

**Page intentionally left blank**

73N18884

## THE APOLLO 14 DOCKING ANOMALY

By Robert D. Langley\*

### ABSTRACT

Six docking attempts were required to achieve initial latch engagement during the Apollo 14 translunar docking event. Although subsequent performance of the docking hardware was normal, the docking probe was retained for a thorough postflight investigation. Pertinent design details of the docking system, the mission events related to the anomaly, and a discussion of the postflight investigation of the cause of the anomaly are presented in this report.

### INTRODUCTION

The Apollo lunar-landing missions require that two docking maneuvers be performed: the first is called transposition or translunar docking and the second is referred to as lunar-orbit docking. Because the required dockings had been performed successfully on five previous Apollo missions, docking had become a routine procedure until the Apollo 14 docking anomaly. The Apollo 14 translunar docking required six attempts to achieve capture-latch engagement. Although subsequent mission operations were normal, the docking probe was returned to earth with the spacecraft so that a detailed investigation could be conducted. The purpose of this paper is to present a limited description of the docking mechanism, the associated mission events, and a discussion of the investigation and findings.

The material presented in this paper was derived from the Apollo 14 Mission Anomaly Report prepared by the NASA Manned Spacecraft Center Mission Evaluation Team.

### DOCKING SYSTEM DESCRIPTION

The Apollo docking system consists primarily of the probe, mounted on the forward end of the command module (CM), and the drogue, mounted within the lunar module (LM) tunnel (figs. 1 and 2). The docking probe consists of numerous subassemblies; however, a description of only the capture-latch assembly is presented because the Apollo 14 docking anomaly is associated with that area.

---

\*NASA Manned Spacecraft Center, Houston, Tex.

The probe capture-latch assembly (fig. 3) is contained within the self-centering, gimbal-mounted probe head and serves as the method for achieving initial coupling between the CM and LM. The assembly consists of three hooks that are pin mounted to the probe head and that are spring loaded so that the hook protrudes beyond the surface of the probe head. Opposite each of the hook pivot points is a two-piece toggle link that connects the hook to a fixed point on the probe head. When the hook is extended, as shown in figure 3, the toggle link pins are almost in line, providing a means of locking the hook.

Latch locking and release are determined by the axial position of a single, symmetrical spider that is spring loaded to the full-forward, locked position. In this position, a roller on the spider rests beneath each of the hook toggle links so that the hooks cannot be depressed. To unlock the latches, the spider must be moved aft and retained until subsequent latch lock is required.

Spider retention and release (fig. 4) are achieved by means of triggers located within each of the latch hooks. When the spider is moved aft of the triggers and released, pins located on the outer tip of the spider bear against the back face of the trigger and prevent forward travel of the spider. To release the spider, all three triggers must be depressed because one or more triggers will retain the spider in the aft (unlocked) position. The spider can be moved from the forward (locked) to the aft (unlocked) position by manually depressing the plunger in the probe head or by rotating the torque shaft. When the torque shaft is rotated, either by manually actuating the capture-latch release handle or by powering the torque motors in the actuator assembly (fig. 5), the rollers turn in the cam slots and force the cam and the spider aft. When power is removed from the torque motors, the torsion spring on the torque shaft rotates the shaft back and allows the spider to move forward until cocked; that is, the spider pins ride against the back of the triggers.

## APOLLO 14 MISSION SEQUENCE

Functional checkout of the Apollo 14 docking probe was completed in August 1970, and the retracted docking probe was installed in the CM docking ring on November 8, 1970. At that time, a tension-tie mechanism was installed between the probe head and the launch escape system (LES) boost protective cover to provide a system compatible with LES abort requirements (fig. 6). As shown in figure 6, the tension-tie installation places the capture latches in a mechanically cocked launch configuration.

On January 31, 1971, after a rain shower, the Apollo 14 spacecraft was launched from the NASA John F. Kennedy Space Center; as part of the normal boost phase of the flight, the LES was jettisoned. This event sheared the pins that attached the tension tie to the probe head, allowing the tension tie to remain with the jettisoned LES and leave an exposed, intact, docking probe. As part of the earth-orbit spacecraft-checkout activity, the crewmen extended the docking probe by operating a switch on the CM main-display panel. This extension sequence also applied power to the probe direct current torque motors to rotate the torque shaft. The crewmen verified proper extension by observing a talkback indicator on the same panel. The spacecraft was then injected into a translunar flight trajectory by firing the S-IVB booster engine.

The transposition and docking events (fig. 7) were initiated by separation of the command and service module (CSM) from the adapter and ejection of the adapter panels that house the LM. Then, the crew translated the CSM approximately 30 meters (100 feet) away from the LM and turned the CSM 180° with a pitch maneuver to align the CSM and LM in preparation for the docking. Before initiating a CSM/LM closure rate, the crew placed one of the docking switches to the retract position and certified that the probe capture latches were still in the cocked configuration. The CM pilot then experienced five unsuccessful docking attempts.

After docking, the crew examined the probe and drogue and no abnormal operations could be observed; however, there were marks on the drogue, as is shown in figure 8. Although subsequent docking functions were completely normal, the docking probe was returned with the CM.

### ANOMALY INVESTIGATION

The initial phase of the anomaly investigation consisted of activity to reduce the list of possible failure modes based on flight data and the crew debriefing. A summary of the docking attempts is presented in table I. The first attempt consisted of four distinct probe/drogue contacts near the drogue apex, whereas each succeeding attempt consisted of withdrawal of the CM and subsequent initiation of a new closure rate. These data support the conclusion that the contact conditions were normal for all docking attempts and capture-latch engagement should have been achieved for the five unsuccessful attempts.

The second conclusion, which is that the capture latches were not in the locked configuration during the unsuccessful attempts, is based on the following reasons.

1. The probe-status talkback displays functioned properly before and after the unsuccessful attempts, indicating proper switch operation and power to the talkback circuits. The talkback displays always indicated that the capture latches were in the cocked position during the unsuccessful attempts.

2. Electrical power to the motors is not required because the system is cocked before flight and the initial capture operation is strictly mechanical and must be triggered by the drogue. Conversely, a review of flight electrical data showed that there was no unexplained current usage during the docking maneuvers because power to the probe torque motors would have retained the latches in the cocked position.

3. Each of the six marks on the drogue resulted from separate contacts by the probe head (fig. 8). A docking impact with locked capture latches should result in three double marks (to match the latch hooks) within 2.54 centimeters (1 inch) of the drogue socket.

Because the latches were not locked, apparently the anomaly was caused by failure of the capture-latch spider to reach the locked position. Therefore, the investigative activity was focused on the items that could influence the position of the spider. The results are summarized as follows.

## Analysis

As a result of rain on the launch day, it was possible that water could have entered the probe head and frozen during the boost phase of flight. A maximum of 30 grams of ice could have formed; however, this amount would sublime within 15 minutes, well before the docking event that occurred approximately 3-1/2 hours after launch.

A trajectory analysis, based on Apollo 14 flight-acceleration data, was conducted to determine if the tension-tie shear-pin remnants could have reentered the capture-latch area. This analysis, which was verified by tests, showed that, if the remnants separated from the tension tie, impact would be well out of the capture-latch area.

The mating parts and surfaces of the capture-latch assembly were analyzed to determine if a worst-case tolerance accumulation combined with a 11° K (20° F) thermal gradient would produce interference. In all cases there were no metal-to-metal interferences.

## Ancillary Testing

Because improper shearing of the tension-tie shear pins could prevent movement of the capture-latch plunger, various design combinations of pins were shear tested. In each test, the shear was clear, regardless of the allowable pin-to-hole dimensional combination. In addition, the shock load associated with pin shearing had no effect on performance of the latch mechanism.

As part of the acceptance testing of each probe, a capture-latch timing test is performed to record spider travel as a function of time. To determine if shelf life degrades the latch mechanism, a timing test was performed on a probe that had been idle for approximately 5 months (similar to the Apollo 14 probe). The results were compared with previous time traces, and there was no evidence of degradation.

Coincidental with the Apollo 14 investigation, acceptance testing was being performed on the Apollo 16 docking probe when the capture latches failed in a manner symptomatic of the Apollo 14 anomaly. It was determined that, for a given torque-shaft alignment and the lateral load resulting from the torsion spring (fig. 9), the ball end of the shaft would fall into the cam slot. Then, a friction lock would occur between the ball and pin, preventing the ball from riding out of the cam slot. This, in turn, would prevent subsequent movement of the cam and spider train. Upon disassembly, the torque-shaft ball was found to be galled severely.

## Apollo 14 Docking-Probe Inspection and Tests

A visual inspection of the probe head revealed several small scratches and burrs on the inner wall of the tension-tie bushing (fig. 10). The scratches were caused by an object moving in the aft direction; the burrs were the material buildup. This burring could have been caused by a foreign particle lodged between the plunger and the wall of the bushing because the initial motion of the plunger is in the aft direction when the

capture hooks are depressed. Therefore, foreign particles in the area of the capture-latch plunger were considered a potential failure mode.

During disassembly of the probe, 12 contaminant particles were found. Three of the particles, which were foreign to the probe, were iron oxide, double-back tape, and cadmium particles. The largest of the 12 particles was 0.15 centimeter (0.060 inch) long, and, of those particles large enough to cause mechanical interference, none were hard enough to prevent operation of the mechanism.

After the Apollo 16 probe capture-latch problem, attempts were made to duplicate the problem on the Apollo 14 probe. With the latch assembly in a horizontal position so that the weight of the shaft added to torsion-spring lateral load, one malfunction was experienced during 60 latch cycles. This also remained a potential failure mode.

Tests were conducted to measure capture-latch timing, torque motor output, friction drag, and spring forces. The results were compared with preflight measurements and no significant degradation was noted.

A detailed inspection of each latch-assembly component did not reveal any wear, damage, or out-of-tolerance parts that could be related to the problem.

#### CONCLUDING REMARKS

The cause of the Apollo 14 docking anomaly was either (1) foreign material (that was subsequently lost) restricting mechanical operation or (2) jamming of the cam. To ensure proper performance for future systems, cleanliness requirements were improved and a design change was implemented to prevent jamming of the cam. Since then, the Apollo 15 and 16 missions have been completed successfully without recurrence of the docking problem.

#### DISCUSSION

W. W. Weber:

How were the supporting tests correlated with the actual failure environment (for example, zero gravity)? By vertical or horizontal positioning?

Langley:

During postflight testing of the Apollo 14 docking probe, the failure could not be reproduced with the probe in the vertical position (simulating zero gravity). The failure could only be produced with the probe horizontal, so that the weight of the torque shaft produced additional side loading (one failure in 60 activations).

TABLE I. - RELATED DATA AND FILM INVESTIGATION RESULTS

Docking attempt	Estimated velocity, m/sec (ft/sec) (a)	Socket contact time, sec (b)	+X thrusting after contact, sec	Comments
1A	0.03 (0.1)	1.55	None	No thruster activity Contact moderately close to apex
1B	0.043 (0.14 max.)	1.65	None	Contact close to apex
1C	0.043 (0.14 max.)	1.4	0.55	Contact close to apex
1D	0.088 (0.29 max.)	2.35	1.95	Contact close to apex
2	0.122 to 0.152 (0.4 to 0.5)	1.7	None	Contact close to apex
3	0.122 (0.4)	2.45	None	Contact close to apex
4	0.122 to 0.152 (0.4 to 0.5)	6.5	6.2	Contact close to apex
5	0.076 (0.25)	2.9	None	Contact close to apex
6	0.061 (0.2)	In and hard docked	14.3	Contact moderately close to apex Retract cycle began 6.9 seconds after contact Initial latch triggered 11.8 seconds after contact

<sup>a</sup>The system is designed to capture with closing velocities between 0.030 and 0.305 m/sec (0.1 and 1.0 ft/sec) and with initial probe contact within 0.305 meter (12 inches) of the center of the drogue. These criteria were met on all docking attempts.

<sup>b</sup>The maximum capture-latch response time is 80 milliseconds.

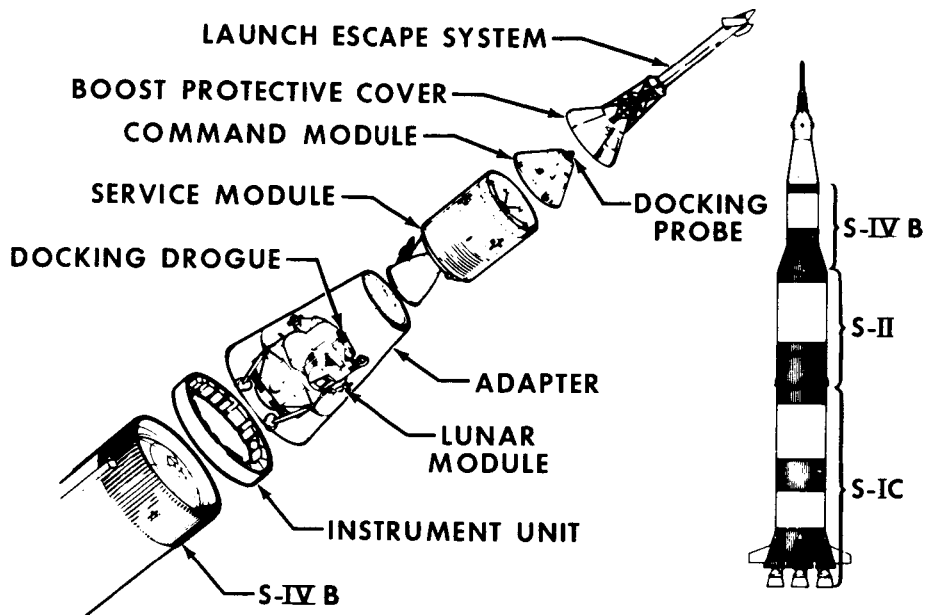


Figure 1. - The Apollo spacecraft.

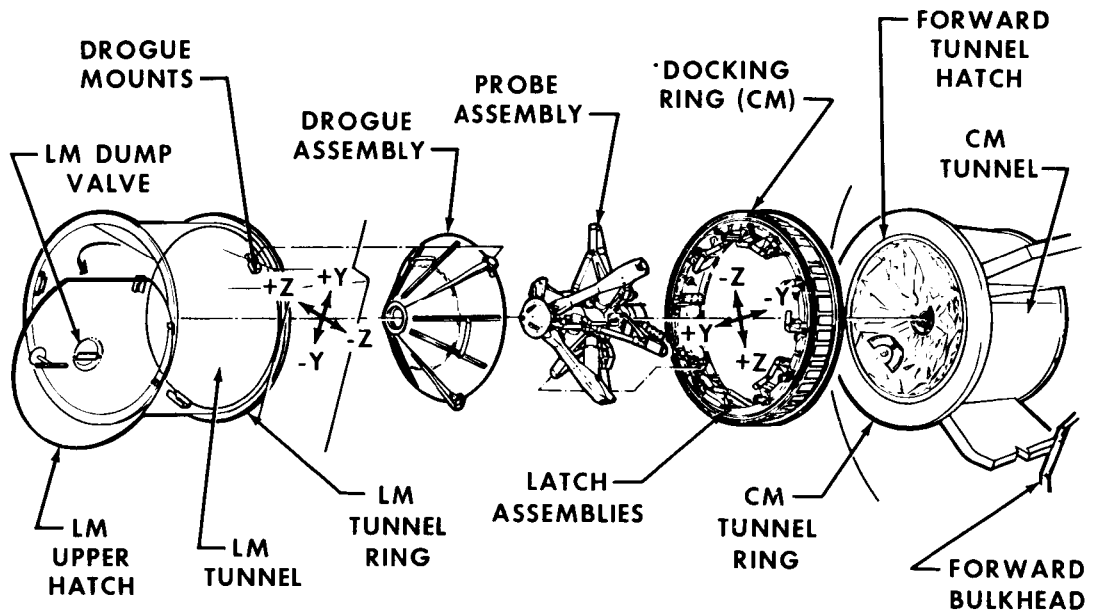


Figure 2. - Major assemblies of the docking system.

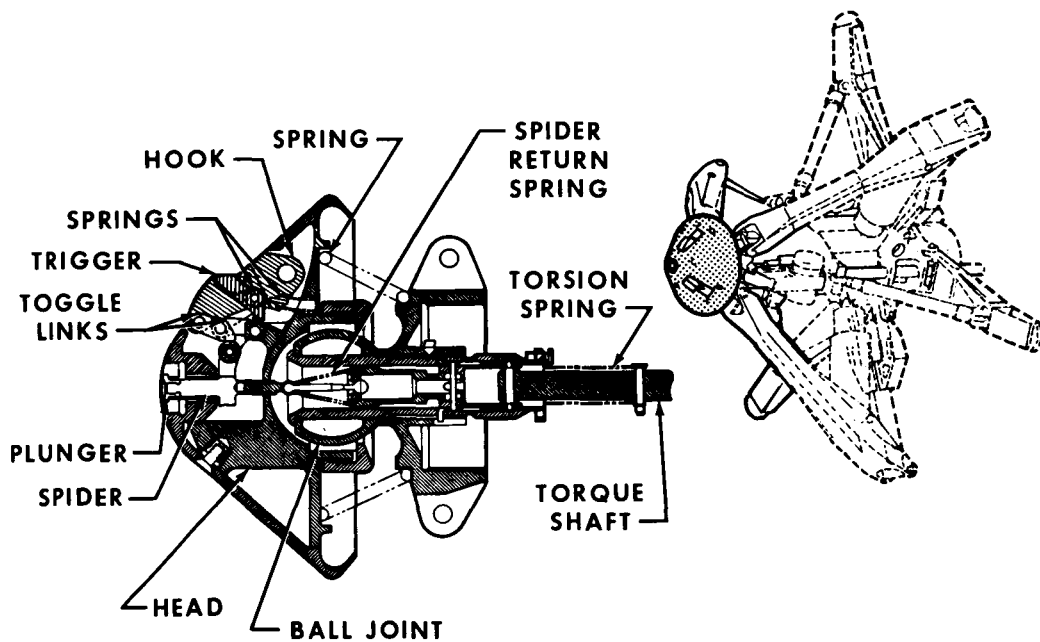


Figure 3. - Probe capture-latch assembly shown in locked position.

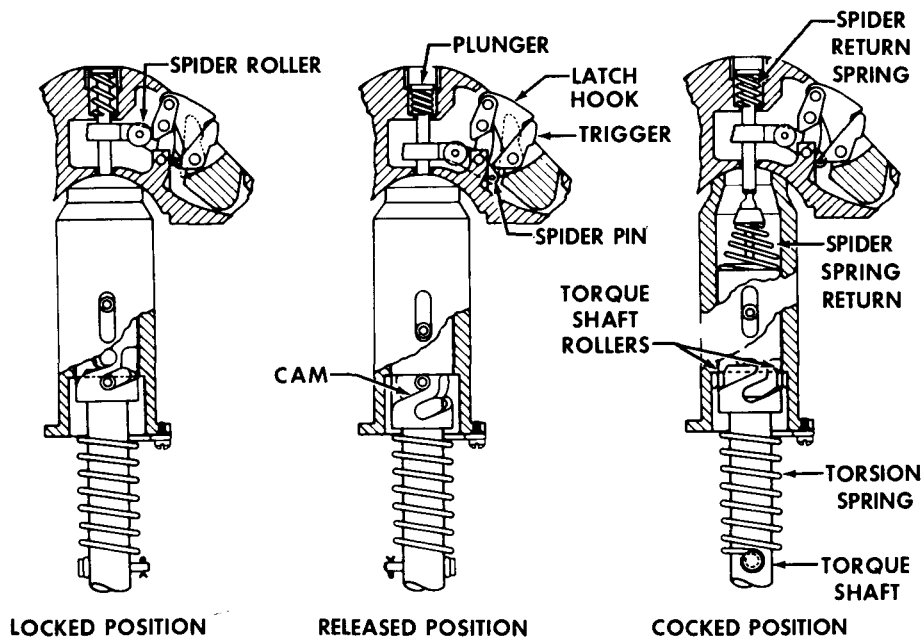


Figure 4. - Relationship of probe latch and cam mechanism.

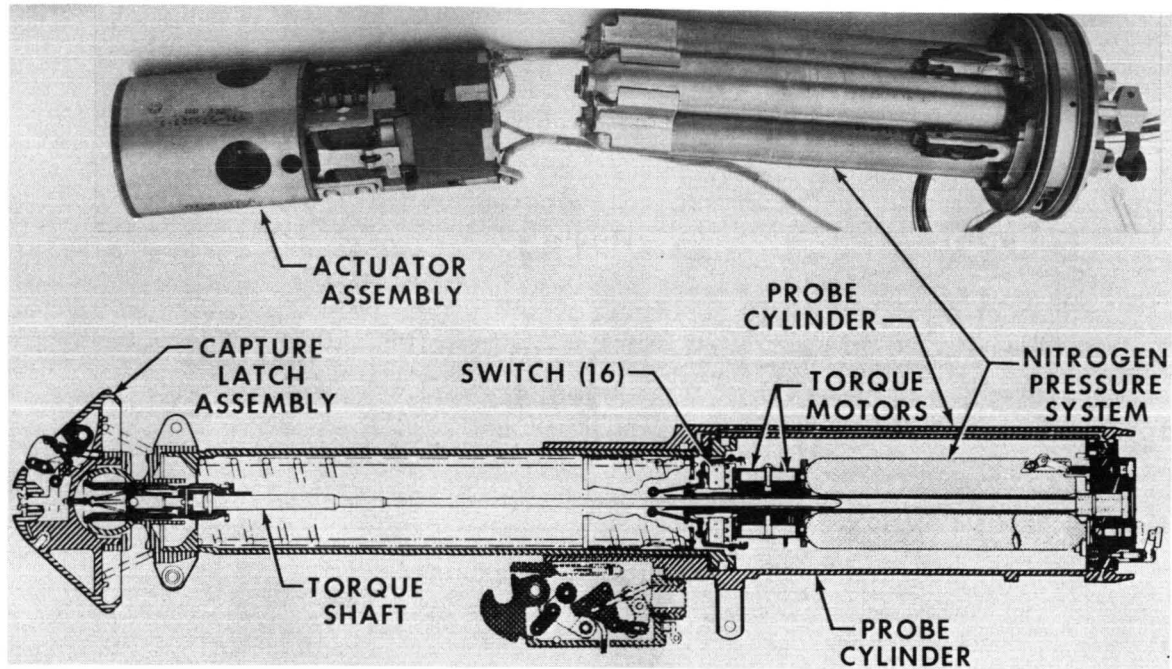


Figure 5. - Cutaway of probe assembly in extended and cocked position.

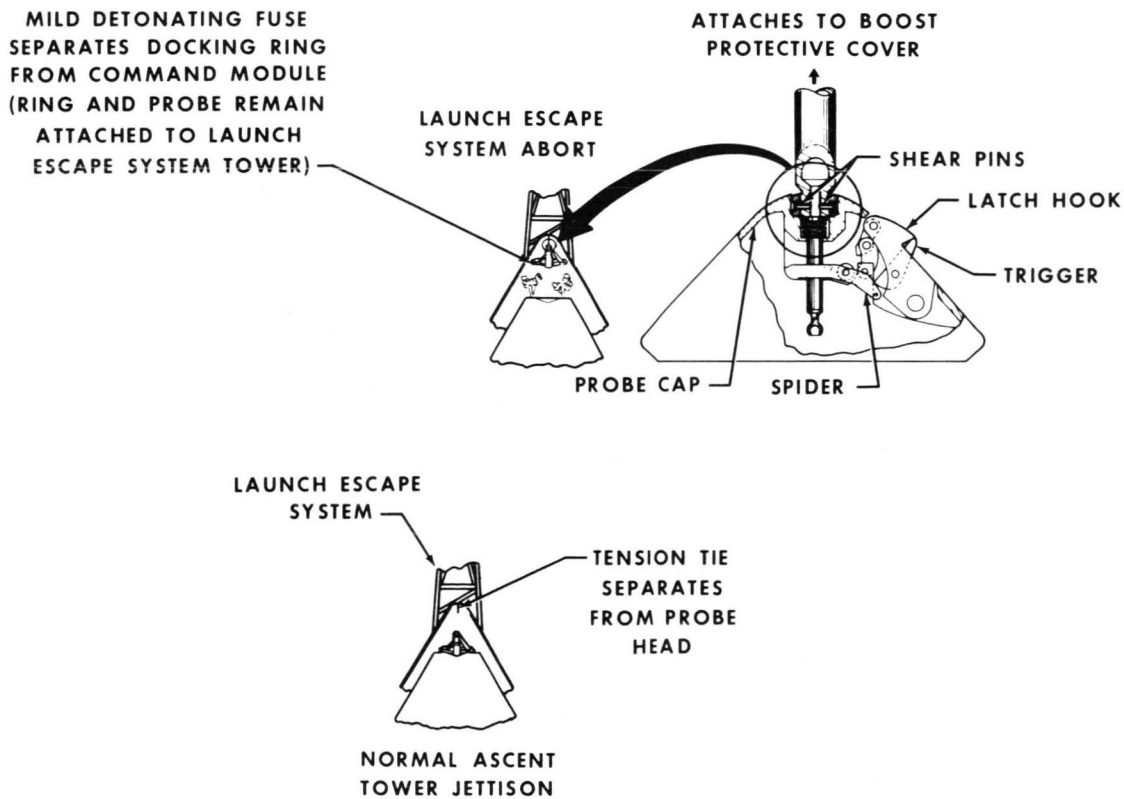


Figure 6. - Tension-tie operation.

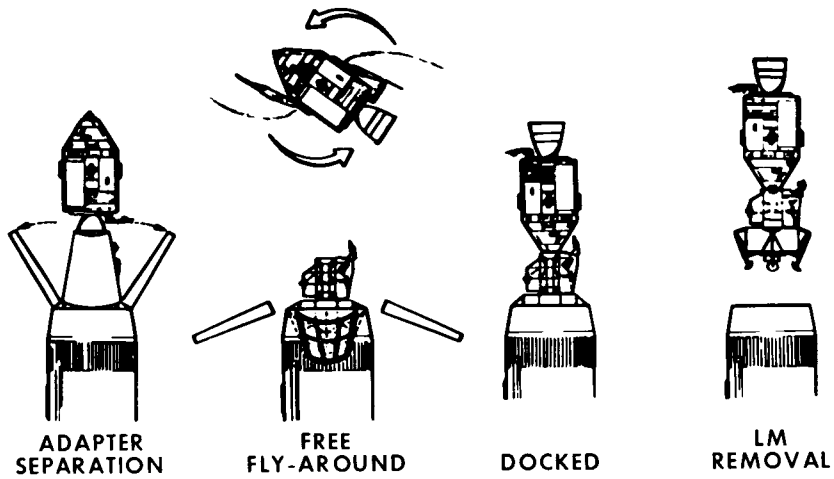


Figure 7. - Transposition and docking.

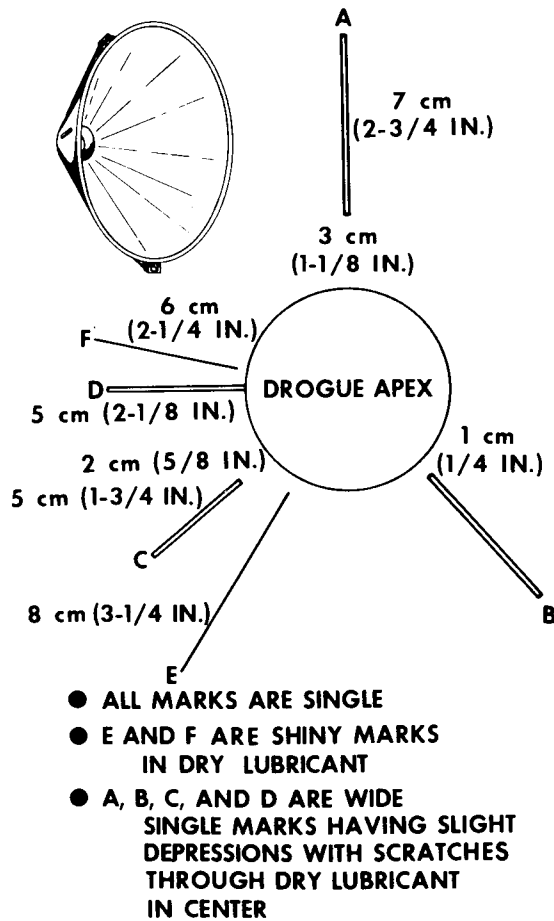


Figure 8. - Drogue assembly and location of radial marks.

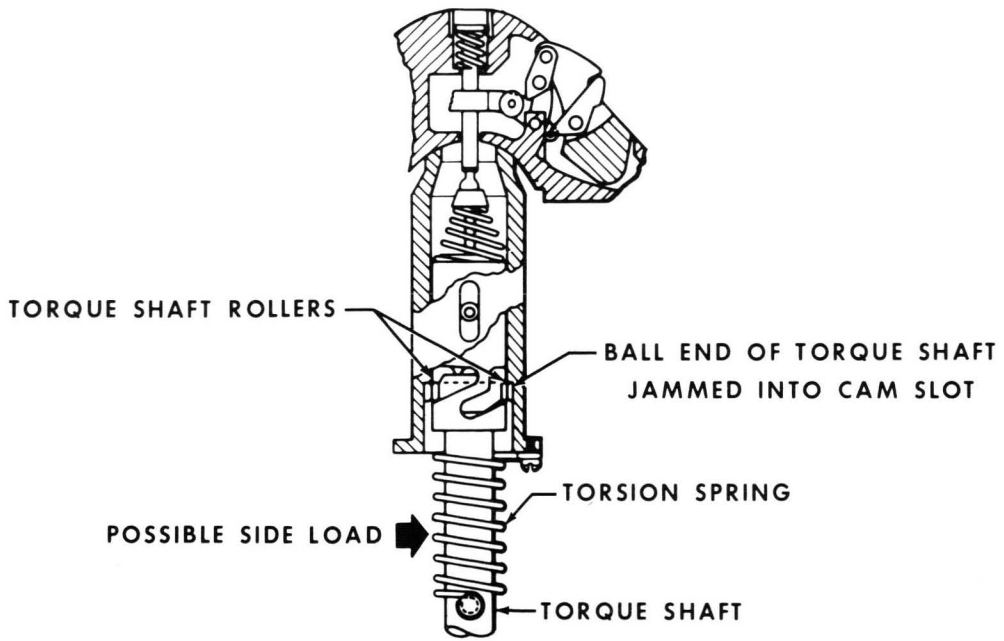


Figure 9. - Side-load reaction on torque-shaft operation.

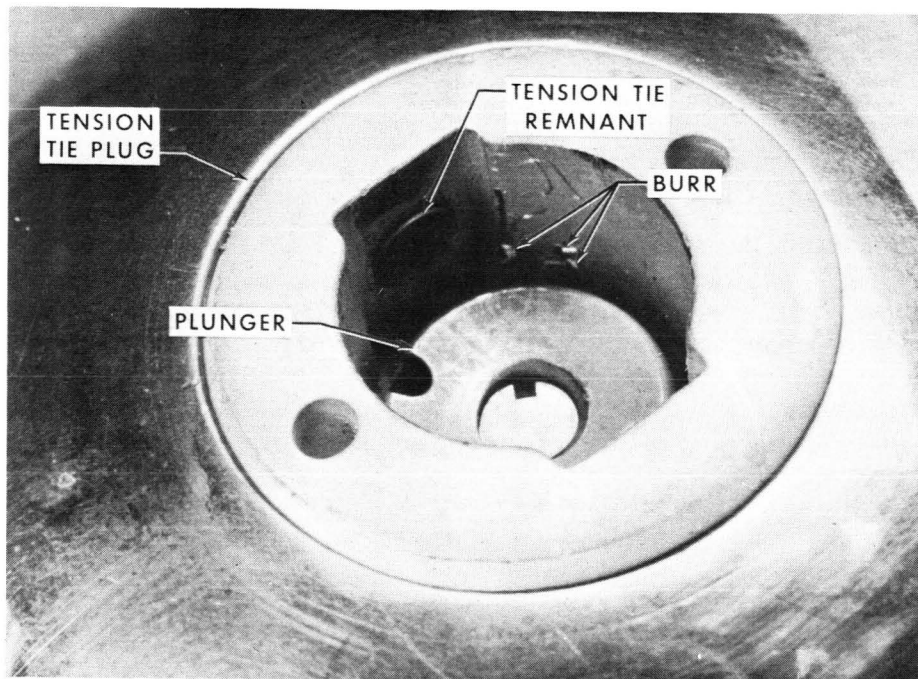


Figure 10. - Scratches and burrs adjacent to capture-latch plunger.

**Page intentionally left blank**

## DYNAMIC TESTING OF DOCKING SYSTEM HARDWARE

By Wade D. Dorland\*

### ABSTRACT

Extensive dynamic testing has been conducted to verify the flight readiness of the Apollo docking hardware. Testing was performed on a unique six degree-of-freedom motion simulator controlled by a computer that calculated the associated spacecraft motions. The test system and the results obtained by subjecting flight-type docking hardware to actual impact loads and resultant spacecraft dynamics are described.

### INTRODUCTION

During manned space operations in which two or more spacecraft rendezvous and dock for transfer of crew and cargo, the docking system hardware plays a critical role in achieving a successful mission. Because the docking system must perform flawlessly, its capability to perform reliably first must be verified in operational ground tests tailored to qualify the system for flight. In the Apollo Program, the dynamic ground testing was performed by means of a unique test system at the NASA Manned Spacecraft Center (MSC). Designated as the dynamic docking test system (DDTS), the system tests flight-type docking hardware on a six degree-of-freedom motion device combined with a computer that simulates the two docking spacecraft. This technique was employed in an extensive testing program to verify that the Apollo docking system design achieved the requirements of both Apollo and Skylab missions. The purpose of this paper is to describe the DDTS and the test results obtained with it.

### APOLLO DOCKING SYSTEM PERFORMANCE REQUIREMENTS

Because a complete description of the Apollo docking system is provided in references 1 and 2, the description in this paper will be confined to the essential elements of the docking-hardware performance. To achieve the requirements of the Apollo lunar-landing mission, a unique mechanism was needed to accomplish linkup of the Apollo modules in space. This mechanism, called the Apollo docking system, consists of a conical drogue mounted on the lunar module (LM) and a probe and latches mounted on the command module (CM) (fig. 1).

---

\*NASA Manned Spacecraft Center, Houston, Tex.

In an Apollo mission, a docking procedure involves the following sequence: The CM (active vehicle) approaches the LM (target vehicle). Contact is made; that is, the probe impacts the conical-drogue surface, slides to the apex, and latches (or captures) the drogue. The two modules are then aligned, drawn together, and securely connected.

A lunar-landing mission requires two docking maneuvers: translunar docking (TLD) on the way from earth orbit to lunar orbit and lunar-orbit docking (LOD), which occurs when the LM ascent stage rejoins the orbiting CM after the lunar-surface excursion. These two dockings include diverse dynamic conditions. The TLD requires the docking hardware to absorb high energy and to carry large component loads as a result of docking two very heavy spacecraft. Conversely, light spacecraft are involved in LOD, which requires excellent capture performance.

For these two dockings, the docking hardware had to be tested considering several design requirements.

1. The hardware functions had to accommodate the following initial contact (IC) conditions: axial (closing) velocity  $V_X$  of 0.03 to 0.30 m/sec (0.1 to 1.0 ft/sec), radial (transverse) velocity  $V_L$  of 0 to 0.15 m/sec (0 to 0.5 ft/sec), angular velocity  $\dot{\Theta}$  of 0 to 1.0 deg/sec, radial alignment (miss) of 0 to 0.30 m/sec (0 to 1.0 foot), any combination of pitch and yaw alignment of  $0^\circ$  to  $10^\circ$ , and a roll alignment of  $\pm 10^\circ$  (fig. 4(a)).

2. The command service module (CSM) would be the active (closing) vehicle for TLD, and either the CSM or LM could be the active vehicle for LOD.

3. The hardware had to function over a temperature range of  $366.48^\circ$  to  $219.26^\circ$  K ( $200^\circ$  to  $-65^\circ$  F).

Subsequently, another set of requirements was developed for use in docking the Apollo CSM to the Skylab space station. Because these requirements were similar to those for the Apollo TLD, testing primarily was intended to assure that no redesign of the Apollo docking system was required for the Skylab missions.

A test program was established to verify the docking-hardware capabilities. The most difficult aspect of this test program involved the problem of validating the ability of the docking hardware to carry the dynamic impact loads, to capture, and to provide a stable alignment of the spacecraft. The unique test system used for these dynamic tests is described in the following sections.

## DOCKING TEST SYSTEM DESCRIPTION

### Concept

To perform dynamic docking tests, several alternate concepts were considered. One of the concepts incorporated pendulum-supported-mass-representative spacecraft and another concept involved an air-bearing-supported-mass-representative spacecraft. However, these arrangements had such inherent undesirable limitations as high frictional loads and only two translational degrees of freedom.

Accordingly, a new test technique was sought that would overcome the inherent limitations of using full-mass-representative spacecraft in the testing, even though such a technique involved an indeterminate degree of technical risk. The idea was to simulate the spacecraft mathematically in a computer, input a set of initial docking-impact conditions, program the equations describing the motions (three in translation and three in rotation) of each simulated spacecraft, and solve the equations in real time. These solutions could then be used to derive electronic command signals that would be used to control forces and motions of a set of actuators (one for each of the six degrees of freedom, three translational and three rotational). Although unique challenges were encountered during the implementation of the concept, the task was accomplished successfully. This concept is used in the dynamic docking test system, as described in the following paragraphs.

### Basic Systems

The DDTS consists of two basic systems: a motion-generating device (fig. 2) and a large-scale hybrid computer (fig. 3). The docking hardware under test is installed in the motion device and is subjected to impact, force, and motion of a prescribed docking condition. The simulator has hydraulic actuators and bearings, along with mechanical pivots and guides, which provide the capability to move the test article in all six relative degrees of freedom. Furthermore, the device is designed to provide a motion envelope large enough to accommodate the Apollo docking hardware and the excursions resulting from the contact conditions as described previously. Within the computer, rigid-body mass properties and attitude control system characteristics for both vehicles are simulated mathematically. Compensation for electrohydraulic phase lags, coordinate system translation (coordinate references on the test device differ from spacecraft coordinate references), force-to-motion transformation, and gravity effects also are included in the computer.

In a test operation, the actuators are commanded to move the probe and drogue so that the required impact conditions (that is, translational and rotational alignments and velocities) exist at impact. As the docking-hardware components impact, the resulting loads are sensed by load cells and are transmitted instantly to the computer as input data to the equations of motion that produce the individual spacecraft dynamic responses. Operating as a real-time closed-loop system, this equipment generates the same impact loads and relative-motion dynamics that would occur between two actual full-sized spacecraft docking in a zero-g environment.

This simulation technique allows virtually any configuration of docking spacecraft to be evaluated with a given set of docking hardware. The vehicle mass properties and geometry, attitude control system characteristics, relative locations of the docking interfaces, and initial dynamic docking conditions all can be changed in minutes simply by inputting a new set of computer data cards. In addition, provisions have been incorporated to test the docking hardware over a wide range of temperatures (from  $394.26^{\circ}$  to  $199.81^{\circ}$  K ( $250^{\circ}$  to  $-100^{\circ}$  F)) so that thermal effects on the performance of the docking hardware can be evaluated.

## Auxiliary Test Equipment

The complete facility includes two 30-channel data-acquisition systems and several subsystems (for example, hydraulic power pack, control console, closed-circuit television, intercom, and simulator-to-computer transmission lines). The latter three subsystems were considered necessary because space limitations necessitated locating the simulator and computer in two buildings approximately 402 meters (0.25 mile) apart. Thirty of the data-acquisition channels record computer outputs that describe simulated-spacecraft-relative-motion dynamics, and the other 30 channels record docking-hardware-component loads and kinematic strokes. Provisions are included in the facility to accommodate test-mechanism control and display panels and energy sources (for example, gas bottles for the probe). A test team includes five to 10 people, depending on the degree of documentation and data recording required by a specific series of test runs.

### Activation and Checkout

Because the facility design incorporated several innovative concepts, numerous problems in activation and checkout were expected and encountered. The DDTS incorporated a previously untried approach which used a computer-operated servomechanism that included digital computations in the control loop; the complexity of checking out this approach was compounded because six independent, but coupled, high-force servos operated simultaneously over a frequency range of 0 to 10 hertz. System stability was the most severe recurring problem associated with the operation of the DDTS.

Checkout involved an extensive series of closed-loop runs, starting with one active servo; subsequently, the number of active channels was increased gradually until the system with all six servos had been exercised under a full range of operating conditions. This checkout was intended to culminate in a series of runs using actual probe and drogue test hardware. Concurrently, an elaborate kinematic mathematical model of the spacecraft and docking mechanism was implemented. This model was generated to serve several objectives; but, initially, a comparison of results with the DDTS results for specified contact conditions was intended to verify validity of the DDTS performance or to "calibrate" the facility (fig. 4).

In the checkout operations, many small modifications that could improve the phase and gain margins in the control loops were identified. Eventually, an elaborate stability analysis was implemented to evaluate destabilizing effects and to propose stability remedies. Ultimately, analog calculations were substituted for the real-time control-loop digital segment, and this arrangement was used for subsequent operations.

### The DDTS Capabilities

The capability of the DDTS to produce prescribed impact conditions (including more than 20 cases) was demonstrated repeatedly. Early problems with reliability of the DDTS equipment largely were eliminated so that test productively easily could surpass available data-processing and evaluation capability. The computer implementation evolved to a general configuration that used all analog components for the real-time computations during a run. The digital section was employed to set up and check out

the computer system before closed-loop runs were made with the simulator and to monitor analog operations during these runs.

Throughout the program, simulator improvements were incorporated to extend performance and mitigate the inherent limitations of the equipment. The salient limitation that had the most significant effect on testing was the total-system-stability margin, which was limited by the basic characteristics of the computer-controlled servo actuators. The use of all analog real-time computations in the control loop eliminated the major destabilizing characteristic. Accordingly, at the completion of the Apollo/Skylab test program, only two stability limitations existed.

1. Near the end of retraction, when probe-ring-to-drogue-ring contact had been established, the inherent stability margins were reduced to negligible values, thus allowing unstable divergent oscillation. After a few (but dramatic) oscillatory cycles, automatic interlocks disabled the device.

2. Under conditions in which the hydraulic actuators produced low-force, short-stroke (that is, high resolution) motions, the static friction of the actuators produced severe motion distortion that effectively nullified evaluation of the docking-hardware performance.

The DDTS can provide excellent tests of impact, capture, and most of the probe-retract cycle. The stability limitations discussed previously only affected the test by causing extraneous motions during the last part of the retract cycle. (These limitations are expected to be effectively eliminated during a DDTS upgrading currently underway.) Accordingly, the DDTS provided a versatile test tool to verify flight worthiness of the Apollo docking hardware.

## DOCKING HARDWARE TESTS

### Test Sequence

Testing of the Apollo docking system included four distinct phases.

Flight qualification. - The purpose of the flight-qualification phase was to certify that the docking system would function properly and reliably before the system was committed to flight operations. This phase was to prove that the design met all nominal mission requirements and that a demonstrated reserve capability existed to handle various foreseeable mission anomalies.

Parametric system testing. - The objective of the parametric system testing was to demonstrate docking system capabilities as affected by failures in the docking system or the spacecraft maneuvering system. Also, this phase was to evaluate the capture limits of the system and to increase confidence in the system capabilities.

Skylab verification. - The Skylab verification testing certified the capability of the Apollo docking system to meet the Skylab mission requirements, which introduced both different spacecraft masses and a new attitude control system. Also, off-normal high-load and capture stability capabilities required to cover the three Skylab spacecraft configurations were to be demonstrated.

Anomaly investigation. - Testing was performed in support of the Apollo 14 docking anomaly discussed in reference 2.

### Test Results

As a result of the docking system tests (including more than 1000 runs), extensive data have been accumulated. In general, the testing produced conclusive evidence that the load-carrying and energy-absorption capability of the system fulfilled the design requirements and provided a significant margin over all known mission needs. However, significant docking-hardware problems were disclosed. Major probe deficiencies produced important changes, as follows.

Unreliable capture latch operation. - Because inability to capture completely negated the docking-hardware effectiveness, this problem received extensive corrective action and had substantial ramifications. For example, the probe-component functions were critically interrelated, and additional rework was necessary when DDTS testing showed that the initial alterations were insufficient. Furthermore, the entire probe inventory (including several flight end items) had to be reworked because this problem had been unrevealed through all previous development. Ultimately, the probe underwent a redesign and substantial changes in assembly and checkout procedures. The reworked configuration provided acceptable capture performance.

Probe binding under lateral loading. - The problem of probe binding, which only occurred when significant side loads were imposed on the probe, was resolved with rework, including the use of an additional lubricated bushing in the assembly.

Minor deficiencies included drogue susceptibility to impact damage when contact occurred near intercostal joints and excessive scoring (or scratching) of drogue surface by sharp edges on capture latches. Although the drogue demonstrated an exceptional capability to absorb impacts in the presence of severe damage to its inner surface, both of these problems were remedied partially by minor rework.

A variety of capabilities was confirmed by other test results. The tests under adverse motion conditions (that is, the two spacecraft pitching away from each other) showed excellent docking-hardware capture performance. Retraction and alignment functions were shown repeatedly to be more than adequate. Furthermore, the runs at high ( $366.48^{\circ}$  K ( $200^{\circ}$  F)) and low ( $219.26^{\circ}$  K ( $-65^{\circ}$  F)) temperatures demonstrated that the hardware performance was adequate for expected temperature extremes. Finally, the docking hardware demonstrated a substantial capability to accomplish capture and latching with damaged attenuators, malfunctioning spacecraft attitude control systems, or unusual spacecraft masses (for example, Skylab configuration).

When the docking capture anomaly occurred during the Apollo 14 mission, the DDTS was used to evaluate contingency lunar-orbit docking procedures. During the lunar-stay portion of this mission, 32 runs were performed on the DDTS. These runs ascertained that other procedures could be used to perform a successful docking should the capture latch anomaly recur. Subsequently, other contingent docking procedures were identified, and an additional 93 DDTS runs were performed to increase confidence in the docking system before the Apollo 15 mission.

## CONCLUDING REMARKS

The unique and complex functions of the Apollo docking system necessitated the development of a dynamic testing capability, which in turn, provided a significant advance in dynamic test technology. This test system was used to produce a substantial demonstration of the dynamic performance capability and reliability of the Apollo docking hardware. Early testing identified needed probe and drogue improvements, and later tests subsequently verified the capability of the reworked docking hardware to meet Apollo and Skylab mission requirements. Currently, application of this facility, with major revisions to the actuation portion of the system, is being planned for testing the next generation of docking systems. These systems, one for the U.S./U.S.S.R. rendezvous missions and another for the space shuttle, also will be subjected to verification through intensive testing by the Manned Spacecraft Center dynamic docking test system.

This paper can only provide a limited description of the complex and extensive development efforts invested in the dynamic docking test system. The information presented in the following sections is essentially a summary obtained from the comprehensive MSC and contractor documentation produced in the course of the program by the various groups that participated in the activation and operation of the simulator. Special credit is due to C. Alan Kirkpatrick, MSC, who has handled the project operations since their inception.

## REFERENCES

1. Langley, Robert D.: Apollo Experience Report. The Docking System. NASA TND-6854, 1972.
2. Langley, Robert D.: The Apollo 14 Docking Anomaly. Proceedings of the 7th Aerospace Mechanisms Symposium, Sept. 7 and 8, 1972. NASA TM X-58094, 1972.

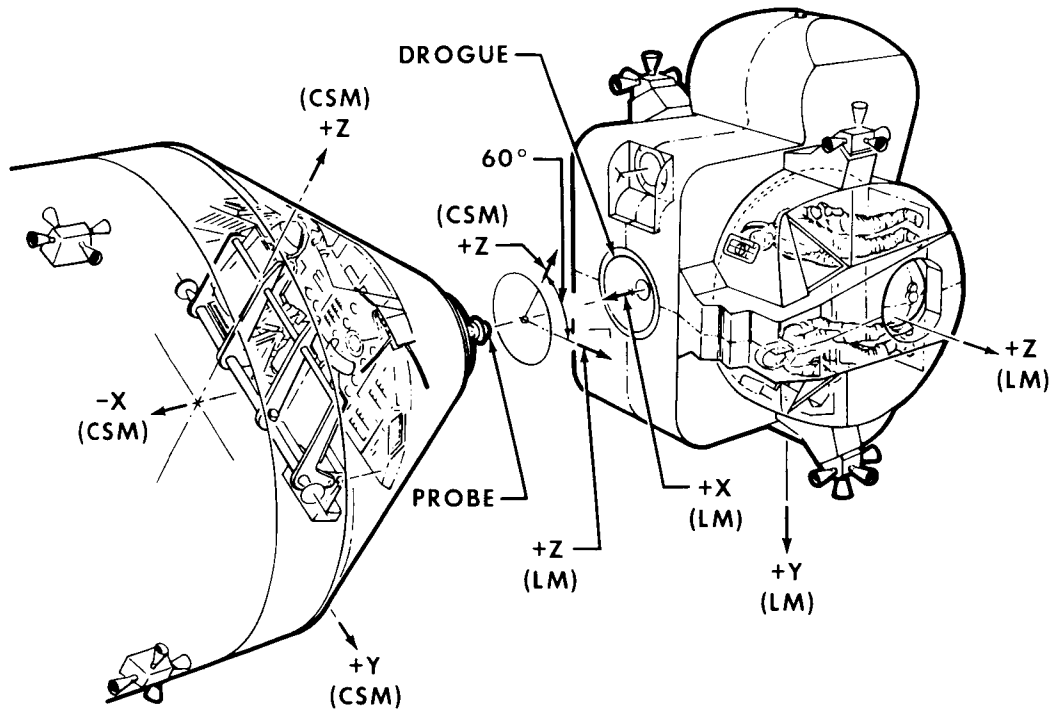


Figure 1. - The CSM/LM orientation before contact.

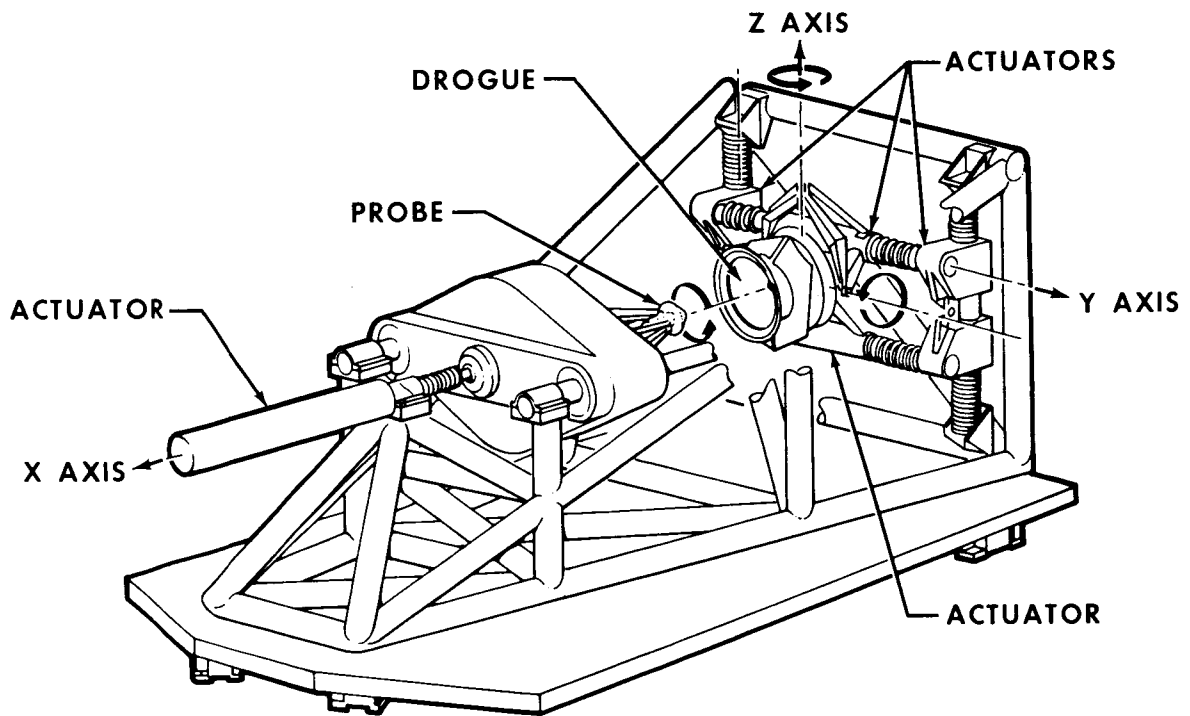


Figure 2. - Perspective of DDTS motion simulator.

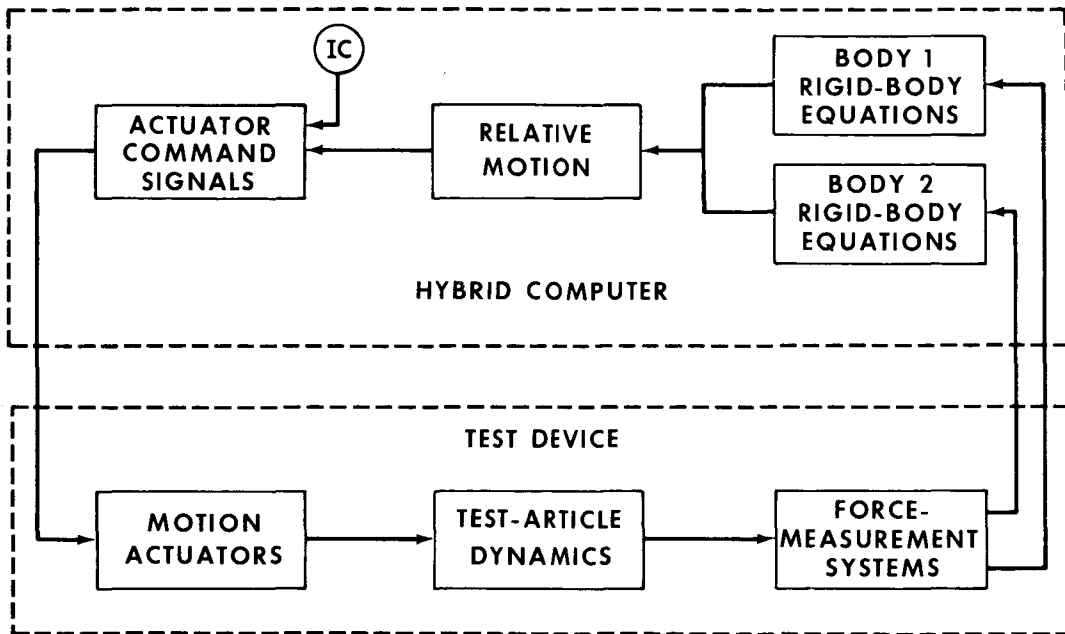
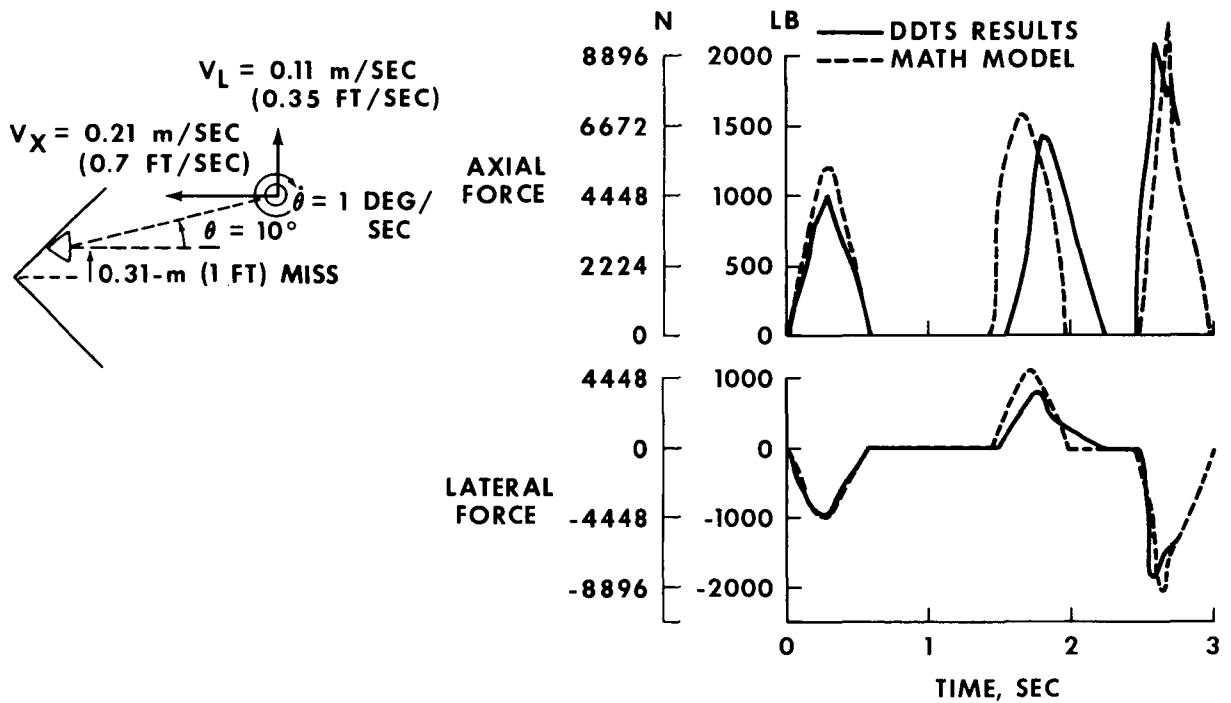


Figure 3. - Basic DDTS block diagram.



(a) Initial contact conditions.

(b) Force history.

Figure 4. - Typical docking system forces.

**Page intentionally left blank**

## SESSION IV

**Page intentionally left blank**

73N/8886

## PLY-TEAR WEBBING ENERGY ABSORBER

By Geoffrey W. H. Stevens\*

### ABSTRACT

Ply-tear webbing is essentially two plain webbings that are bound together by a portion of the warps and that can be torn apart and do work by breaking the binders. Nylon webbings have been woven to range in tear force from 1 to 10 kilonewtons. This force is substantially independent of speed, which was as high as 100 m/sec in some cases. A specific energy absorption of 90 J/g has been achieved in the dry state. However, lower rated webbings that absorb approximately 40 J/g are recommended for use in practice where it is acceptable.

### INTRODUCTION

In aeronautical and aerospace engineering, the requirement frequently arises to use an energy absorber of high specific energy. The requirement has arisen particularly in airdrop equipment and aerodynamic decelerators. Some success in the technical solution has been achieved by the invention of a textile construction known as ply-tear webbing (refs. 1 and 2).

Among the materials with the highest specific strain energies are the fiber-forming polymers, having energies of approximately 300 J/g ( $10^5$  ft-lb per lb). However, initial interest in these was concentrated on such undrawn and plasticized polymers as undrawn nylon, low-density polythene, and plasticized polyvinylchloride. Many of these materials can be worked by propagating a draw-neck through each filament, but some disadvantages are encountered. For example, stable drawing without fracture is restricted to a modest temperature range, and the speed of drawing also is limited (ref. 3). Therefore, it is desirable to ease these restrictions.

Although for a limited temperature range the specific energy to break can be higher for an undrawn than a drawn polymer, a drawn polymer maintains a usefully high value for a much wider temperature range (refs. 4 and 5). Some advantage should be gained if a method of using the material efficiently can be found; for example, breaking the fibers in many places, as in tearing a woven structure. This is the philosophy behind the invention of ply-tear webbing, in which a proportion of warp threads are repeatedly broken. The additional benefit of work by friction is obtained because the tearing of a woven structure of the type developed involves slippage of the weave.

---

\*Royal Aircraft Establishment; Farnborough, Hampshire, England.

The purpose of this paper is to describe some of the webbings developed and to give an account of their physical properties. Some discussion of the factors in the use of webbings in an energy absorber is given, and the simple case of the mechanics, such as taking up the surplus energy in a cable release, is illustrated.

Acknowledgements are made to the Aircraft and Armament Experimental Establishment, Boscombe Down; to Hunting Engineering, Ltd.; to W. Ribbons, Ltd.; and to the Royal Aircraft Establishment, Farnborough, in particular to Mr. John E. Swallow and his staff of the Materials Department for quotations from their work and the use of illustrations of successful applications. Moreover, a special acknowledgement is made to W. Ribbons, Ltd., and the Irvin Industries, Inc., for making it possible for this paper to be presented personally by the author.

### SYMBOLS

$B$	binder strength
$c_1, c_2$	velocity of propagation of strain disturbances
$e_1, e_2$	initial strain in cables
$F, F_{\min}, F_{\max}$	tear force
$k$	logarithmic factor for change of tension of a binder around a weft
$L$	length of cable
$M_1, M_2$	coupling masses
$m_1, m_2$	cable masses per unit length
$N$	number of binders
$S$	tear distance
$t$	time
$T, T_1, T_2$	initial tensions in cable
$v, v_1, v_2$	instantaneous velocity of end of cable

## BASIC PLY-TEAR WEBBING

Ply-tear webbing can be woven on a loom with either one or, preferably, two shuttles. The warps are programmed by the "Dobby" mechanism into three sets: one for one ply or back, one for the other, and a third to provide the binders. On a twin-shuttle loom, each ply has its own weft; however, on a single-shuttle loom, the top and bottom plys are woven in sequence, four picks at a time, by a common weft between each bind. Therefore, in webbing woven on a single-shuttle loom, the weft also must break with the binders as the plys are torn apart; and, in all cases, the weft must be strong enough to withstand the pull of the binder. Although there are many possible variations of pattern, the basic construction is illustrated in figure 1. A sample of webbing for this construction is shown in figure 2. Because of the need for free ply ends to provide a means of attachment in a mechanism, all development has been concentrated on twin-shuttle looms.

Most of the webbings on which there is quantitative technical data (table I) have been based on 93 tex nylon yarn (ICI Type 242). However, a research program on the various factors in construction has been carried out (ref. 6), and this program has covered the use of polyester and nomex for binders. Moreover, most webbings have been woven and evaluated at 45-millimeter width because this width is standard in aeronautical equipment.

## PROPERTIES OF PLY-TEAR WEBBING

When ply-tear webbing is torn slowly in a Dennison machine, a cyclic pattern of tear force is obtained, as shown in figure 3. A severalfold variation of force from minimum to maximum occurs. The force falls sharply on breakage and then builds up steadily as the binders slip through the weave until they are stressed to breaking point again. It appears that all the binders across the weave are being nearly equally loaded at the same time.

When the webbing is being torn at speed, such as in a drop test or in a catapult test, a much smoother tear is often experienced. A flash photograph of a sample of webbing tearing at 35 m/sec is illustrated in figure 4; the tear force in a drop test is shown in figure 5. Fluctuations of force in drop tests can be as large as those illustrated in figure 3; they are of audio frequency and responsible for the real noise of tearing. It appears that this noise phenomenon is much influenced by the mechanism or test machine in which the material is torn and by the elasticity of the free length of ply between the anchor and the point of tearing. For example, with sufficiently short leads in the Dennison test machine, irregular breakage of binders that gives an apparently more uniform tear force than that illustrated in figure 3 has been observed.

Detailed technical data on ply-tear webbings can be found in references 1, 2, and 6. The two earlier reports explored the physical envelope for the engineering use of ply-tear webbings. The work established the magnitude and the tear force and also established the important fact that the mean tear force was substantially independent of

the speed of tearing. Separation speeds up to 10 m/sec were achieved in drop tests (ref. 6) and up to 110 m/sec in catapult tests (ref. 7). If there was any trend in the magnitude of the tear force with tear speed, it was for an increase with increase of speed.

Three widths of nylon webbing (29, 44, and 50 millimeters) were available for the preliminary work, and all were similar in construction; that is, twofold warps laid in pairs and a threefold weft. For these three webbings, the mean tear forces in dynamic tests were approximately 2.7, 4.7, and 5.6 kilonewtons, respectively. The specific energy absorption is approximately 90 J/g. More work can be done when these webbings are soaked in water or light oil, (ref. 2), but then the safety margin in the backing strength becomes unacceptably low. Conversely, a resin impregnation reduces the tear force and the work done because the binders are prevented from slipping in the weave and doing work by interweave friction.

The level of work done per gram of binder yarn is very high. These yarns constitute approximately 19 percent of the weight of the types of webbing evaluated. Therefore, the specific working capacity of a ply-tear webbing, in terms of binder weight, is approximately 450 J/g, which is more than half the specific energy required to fuse nylon (ref. 1). Thus, it is unlikely that webbings of higher specific energy will be developed. In fact, more recent work suggests that if a requirement exists for operation in wet conditions or for achieving a smooth tear force, a lower efficiency webbing may have to be accepted.

The more recent work (ref. 6) by John Swallow and his assistants has been more systematic and covers 12 webbing constructions (table II), in which variations have been selected in accordance with the requirements of a properly factored experiment. A number of the constructions broke without tearing in certain circumstances. Within the levels tested, the efficiency at a given binder strength was highest at lower warp count, higher velocity, larger falling mass, and in wet conditions. However, the circumstances leading to higher efficiency were those giving the highest probability of webbing breakage without tearing. A safe limit for all the conditions examined indicated a maximum efficiency (specific energy absorption) of about 40 J/g at a maximum binder mass fraction of 0.08 and weft fraction of 0.3. For webbings of a given specific mass, the efficiency was linearly related to the tear force developed, which, in turn, was linearly related to the total binder strength. High correlation coefficients (0.98) were noted. The amplitudes of the oscillations, particularly the low frequency ones, are roughly correlated through the origin with the magnitude of the tear forces, with no evident separation between the types (nylon, polyester, and nomex) of binder material.

## MECHANISM OF TEARING

The mechanism of tearing, particularly the influence of interyarn friction and the rate of tearing, is inadequately understood and has been made the subject of a research agreement with the Department of Textile Studies, the University of Manchester Institute of Science and Technology. It has been established that ply-tear webbing can be torn very fast, and experimental methods for high-speed tearing probably will involve

considerable difficulty and expense. Therefore, a good theoretical background is required before the experimental work is extended. Four major questions need to be answered.

1. What are the factors that limit the maximum rate of tearing?
2. How is the efficiency of a ply-tear webbing affected at the highest speeds of tearing?
3. At what speeds do the inertial forces become significant?
4. How can fluctuations of tear force be limited and for what penalties?

A simple illustration of how frictional forces may act in the process of tearing and determine the interval between breakages is shown in figure 6. For the binder to break, a tension has to be built up by the process of the free end of the binder being pulled through the weave. The computation of the tension between the point A of maximum stress shown in figure 6 and the free end arises from a combination of arithmetic and logarithmic increments of force at each point where the yarn is pulling through the backing. The illustration in figure 6 has been simplified by showing only logarithmic components of force. If  $F$  is the force being applied to the webbing backing, then the tension in the backing will fall between points Z and Y and, further, between Y and X. The binders within the untorn ply will be in tension, and it is impossible to represent the true equilibrium of forces without introducing the inertial forces, which cannot be neglected in the understanding of high-speed tearing.

When the binders at A have reached their maximum tension and are about to break, the maximum tear force  $F$  transmitted across the two plys is given by

$$F_{\max} = NB(1 + k + k^2 + k^3) \quad (1)$$

After breakage, the tension in the link at A falls to zero. In the next link to the right, the slippage of the binder reverses and the tension falls to  $k^3B$ , so that the tensions in this link and the fourth link to the right balance the tension in the third link as it is pulled out. Thus, the tear force falls to a minimum value

$$F_{\min} = NB(k^3 + k^2 + k^3) \quad (2)$$

The ratio of these two forces is

$$\frac{F_{\min}}{F_{\max}} = \frac{k^3 + k^2 + k^3}{1 + k + k^2 + k^3} \quad (3)$$

An example numerical value (ref. 1) of this ratio is 0.40, and a value of  $k$  that fits this ratio is 0.64, corresponding to a 0.14 value for the coefficient of friction of binder over weft. Therefore, the observation that binder breakages occur, on the average, every four links is consistent with a realistic coefficient of friction between weft and binder.

## USE OF PLY-TEAR WEBBING IN MECHANISMS

Ply-tear webbing is an expendable material and, as such, must be compared with a fuel. Apart from its mechanical performance, its economic performance must be examined. Although the gross cost of the energy absorber should be used as a basis of comparison, it is possible to give some guide to the net economic efficiency of the material. Such an estimation is not easy because work has been concentrated mostly on only development weaving, which has been done on conventional looms to give a guide. With the heavy webbing used in pattern WR 1058, the economic performance is approximately  $1 \times 10^4$  J per dollar. Such a figure is useful when assessing the feasibility of high-capacity systems because in many smaller systems, the net cost of the energy-absorbing material is swamped by the costs of engineering the mechanism.

The material was conceived for use in the working elements of an erectable shock absorber. Although a working model was built and underwent sufficient tests to show that the material was viable in this context, the requirement was not urgent and development in other applications has overtaken this work.

Ply-tear webbing first was successfully used to absorb the surplus energy in a partly rigid aerodynamic decelerator. This was the retarder for conventional armament. The application is illustrated in figure 7, which shows two rigging strops that have been looped up by attaching a piece of ply-tear webbing across the loop.

In the mediumweight-supplies dropping parachute platform for the airborne forces, without ply-tear webbing, damage occurred to the release mechanism because the extractor parachute was required first to break a shear wire on the emergency release mechanism before it pulled on the platform. The strain energy in the cable was transferred to kinetic energy in the coupling, causing it to strike other parts of the equipment violently and become damaged. Thus, to check the accelerations of separation, ply-tear webbing had to be placed in parallel with the slack cable connecting the components of the release mechanism. In figures 8 and 9, the link before and after tearing, respectively, is shown.

In human engineering, ply-tear webbing has excellent potential for use in crash and safety harnesses. Because tear forces are so predictable, it is possible to design for the known deceleration tolerances of the human body. Thus, in the example of the automobile seat belt, it is possible to design to take advantage of the full available stroke in a system and be acceptable at all speeds up to that which uses all the stroke. In the case of aircraft and helicopters, in which the occupant requires a harness for normal flight conditions, a case can be made for considering a ply-tear mounting of the whole seat in the airframe. However, a successful application to an industrial safety harness has been developed in England.

Ply-tear webbing is being used successfully and with quantitative precision for both main and emergency decelerators on dynamic test facilities. It is used on the Royal Aircraft Establishment rocket track and at other British research establishments.

## DESIGN PROCEDURES FOR PLY-TEAR WEBBING

In many applications, it is sufficient to look at the equation of energy and work done, which, in a ply-tear webbing of a given pattern, is proportional to the weight of webbing torn. This weight can be obtained in one long length or in several shorter lengths in parallel, giving a higher total tear force. Thus, in arresting a moving body of known mass, the permissible deceleration will determine the force, and the kinetic energy will determine the weight of webbing required. The stroke is explicitly determined. When a body is falling under gravity and the tear force is equal to the weight of the body, then the latter should fall at constant velocity.

The case of the ply-tear link across a coupling in long cables requires an examination of the speed of separation when the coupling parts. The mechanics of the problem is best illustrated with reference to figure 10. The two parts of the coupling have masses  $M_1$  and  $M_2$ , which are attached, respectively, to elastic cables. The time interval between release and the moment when the first relaxation of strain returns to the coupling is considered. During this time, the motion of the masses is determined by the magnitude of strain  $e$  in the cables and the velocity  $c$ , with which the rate of change of strain travels. The velocities of separation of the massive parts during the initial time interval, before any reflection of strain relaxation occurs, are shown in figure 10. If the coupling masses are small, the separation velocities will quickly approach the asymptotic values  $e_1/c_1$  and  $e_2/c_2$ , respectively. At the ultimate strains for steel and nylon cables, these velocities are approximately 50 and 275 m/sec, respectively, typical of the accidental breakage situation. When working at a safety factor of three, the velocities are approximately 15 and 90 m/sec, respectively.

In many practical cases, the mass on one side of the coupling is much larger than on the other side, so that the simple case of the movement of one member with respect to a fixed mass is appropriate. This simpler case will be chosen to illustrate the effect of inserting a ply-tear link. The tension  $T_1$  in the cable is proportional to strain and can be written  $m_1 e_1 c_1^2$  or  $m_1 c_1 v_1$ . If only a partial relaxation occurs, as when the acceleration of the mass is restrained by a tear force  $F$ , the instantaneous velocity  $v$  is determined by the following equation of motion

$$T - mcv = M\dot{v} + F \quad (4)$$

for which the solution, for the condition  $v = 0$  when  $t = 0$ , is

$$v = \frac{(T_1 - F) \left( 1 - \exp \frac{-m_1 c_1 t}{M_1} \right)}{m_1 c_1} \quad (5)$$

This equation holds for a time  $2L/c_1$ . The corresponding tear distance  $S$  is

$$S = \left[ \frac{2 - \left( 1 - \exp \frac{-2m_1 L}{M_1} \right) M_1}{m_1 L} \right] \left( \frac{(T_1 - F)L}{m_1 c_1^2} \right) \quad (6)$$

It is seen that  $v$  can only be substantially reduced by making  $F$  nearly equal to  $T_1$  and that the length of tear webbing required is correspondingly made shorter. The work done by this tear link is

$$FS = \left[ \frac{2 - \left( 1 - \exp \frac{-2m_1 L}{M_1} \right) M_1}{m_1 L} \right] \left( \frac{(T_1 - F)FL}{m_1 c_1^2} \right) \quad (7)$$

which is a maximum for a single link when  $F = T_1/2$ . The total strain energy in the cable before release is  $LT_1^2/2m_1c_1^2$ , so that the fraction of it absorbed by a single link is

$$\frac{1}{2} \left[ \frac{2 - \left( 1 - \exp \frac{-2m_1 L}{M_1} \right) M_1}{m_1 L} \right] \quad (8)$$

Thus, when  $M_1$  is finite, a single link of  $F = T_1/2$  cannot absorb all the energy, and the remainder must be released as kinetic energy in the cable and coupling.

The significance of the ratio of the coupling mass to the total cable mass can be illustrated with reference to a numerical example. The case of a nylon cable of 30-kilonewton breaking force tensioned to 10 kilonewtons is considered. A cable of

this type of breaking force would have a mass per unit length of about 0.1 kg/m. The coupling mass is assumed to be 1 kilogram. The velocity of propagation of strain disturbances in woven nylon cables is approximately 1000 m/sec. For convenience, the unstrained length of the cable is chosen at 10 meters, for which it is implicit that the extension is 1 meter for the loading conditions stated. For these data, the total length of cable will weigh the same as the coupling mass; thus, by the time a strain disturbance has traveled the length of the cable and back to the coupling, the value of the exponential term is 0.135. On substituting numerical values in equations (5) and (8), the separation velocity is still 43 m/sec, and 56 percent of the energy has been absorbed. Of the residual energy, 19 percent is in the coupling mass and 25 percent in the cable. The length of tear will be approximately 0.56 meter, and this value can be exceeded slightly by virtue of the inertia of the coupling.

An improvement in energy absorption can be obtained with two parallel tear links, one of 4.2 kilonewtons tearing for 0.34 meter and another of 2.8 kilonewtons tearing for 0.80 meter. Therefore, a total tear force of 7 kilonewtons acts over the first 0.34 meter, and a reduced force acts over the remainder of the stroke. This system would absorb 70 percent of the energy.

The practical problem of setting the tear force at a high proportion of the initial tension concerns the peaks in the tear force. An initial peak in the tear force is unlikely if a little slack occurs in the link, although a final peak, as seen in figure 5, can occur. This fact requires caution in the design of a system with a low residual retention of energy.

## PRACTICAL FACTORS AFFECTING PREMATURE BREAKAGE

It has been observed that the backing ply of a wet nylon webbing may break prematurely, whereas it is quite safe in the dry state (ref. 6). The reaction of the wet backing is caused by two factors: first, the wet backing is 15 percent weaker than in the dry state, and, second, the tear force is greater because the binders are kept cooler and are stronger.

Another factor leading to premature breakage is an impact on the ply backing while tearing is taking place. Even the impact of the section of untorn ply against the backing has caused a breakage at the point of tearing. Thus, it is important to control the motion of the untorn webbing by a scheme as illustrated in figure 11, where it is stowed in a satchel. The untorn webbing is laid in flakes parallel to the backing so that the transverse motion is minimized. The actual article is shown in figure 12.

If the tear link is in a mechanism that can rotate during tearing, care must be taken in the layout so that no part of the mechanism can strike the link during the subsequent motion because the shock loads arising from such impacts are difficult to predict. If an impact on the webbing cannot be avoided, then the tear strength/backing strength ratio must be reduced and be satisfied with a tear webbing of lower specific energy.

## CONCLUDING REMARKS

Ply-tear webbings have now been available for approximately 5 years, and during this time, a number of successful applications have been found. An important property of a tear webbing is that the tear force is independent of the tear speed, so that design calculations for an energy absorbing mechanism can be kept simple. The material is primarily appropriate to long-stroke shock absorbers. Satisfactory tearing of nylon webbings has been achieved at separation speeds slightly in excess of 100 m/sec, but the maximum separation practicable and at what efficiency level is yet to be established.

## REFERENCES

1. Stevens, G. W. H.: Ply-Tear Webbing as an Energy Absorber. TR 68164, Royal Aircraft Establishment (Farnborough, Hampshire, England), 1968.
2. Longrigg, J. C. H.: Tests of Ply-Tear Webbing. TR 69012, Royal Aircraft Establishment (Farnborough, Hampshire, England), 1969.
3. Stevens, G. W. H.; and Bluett, F. C.: A Technique for Studying High Velocity Drawing of Polymers. Current Paper 1061, Aeronautical Research Council, Her Majesty's Stationery Office (London).
4. Baker, A.: The Mechanical Properties and Porosity of Parachute Fabrics. Report Chem 507, Royal Aircraft Establishment (Farnborough, Hampshire, England), 1956.
5. Vincent, P. I.: The Strength of Plastics. Plastics, vol. 28, parts 11-13. IPC Industrial Press, 1963.
6. Swallow, J. E.; Webb, M.; and Watts, Shirley A.: The Energy-Absorbing Efficiency of Ply-Tear Webbings of Various Constructions. TR 72051, Royal Aircraft Establishment (Farnborough, Hampshire, England), 1972.
7. Bluett, F. C.; and Longrigg, J. C. H.: The RAE Nylon Rope Catapult. TR 69108, Royal Aircraft Establishment (Farnborough, Hampshire, England), 1969.

TABLE I. - SUMMARY OF PLY-TEAR WEBBINGS

Type number	Warps				Weft		Width, mm	Weight, g/m	Tear force		Backing strength		Specific tear energy, J/g	Application
	Single ply		Binders		Count tex	Picks, 10 mm			Slow, kN	Dynamic, kN	Nominal, kN	Test, kN		
	Count tex	Number	Count tex	Number										
WR 1017	93×2	104	93×2	22	93×2	10	45	75.7	2.70	1.52	12.5	9.6	57	Industrial safety harness Motor industries research Rocket track decelerator
WR 1018	93×2	104	93×2	22	93×2	Single shuttle 20	45	77	3.12	2.25	12.5	--	63	Royal Aircraft Establishment research and development
WR 1058/1	93×2	50×2	93×2	44	93×3	7.5	29	73	5.0	2.7	--	--	--	Weapon retarder tail Erectable shock absorber
WR 1054	93×2	80×2	93×2	72	93×3	7.5	45	121	8.2	4.7	20.2	14.4	83	Airdrop platform Automotive seatbelt
WR 1058/2	93×2	92×2	93×2	84	93×3	7.5	52	133	9.6	5.6	22.1	19.9	87	Royal Aircraft Establishment research and development
WR 1127	93×2	80×2	<sup>a</sup> 93×3 93×2	36 36	93×3	7.5	45	124	7.9	--	20.2	17.0	--	Irvin Industries, Inc. Log transporter
WR 1146	93×2	92×2	<sup>a</sup> 93×3 93×2	36 36	93×3	7.5	50	145	--	--	22.1	--	--	Irvin research and development
WR 1147	93×3	100	93	88	93×3	7.5	48	105	3.35	--	18.8	--	--	Automotive seatbelts
WR 1147/6	93×2	100	<sup>a</sup> 93 47	44 44	93×3	7.5	48	99	3.9	2.9	18.8	14.2	63	Automotive research and development
WR 1147T/6	110×3	100	<sup>a</sup> 93 47	44 44	110×3	7.5	48	117	2.65	--	--	--	--	Polyester research and development
WR 6157	93×6	92	93×3	84	93×4	--	52	185	--	--	33.1	--	--	

<sup>a</sup>The heavy and light binders alternate across the width of the webbing.

TABLE II. - CONSTRUCTION OF EXPERIMENTAL WEBBINGS

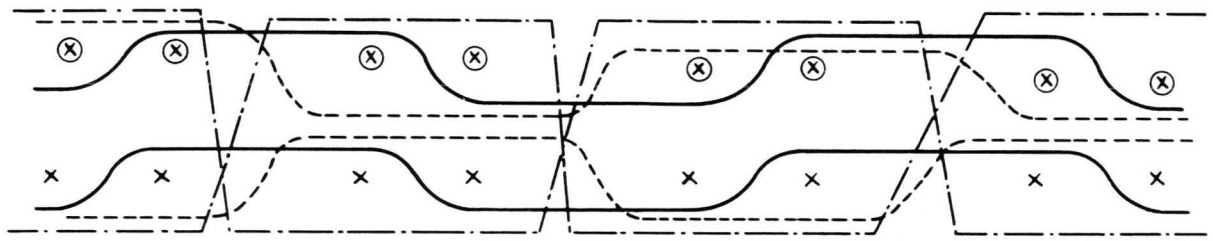
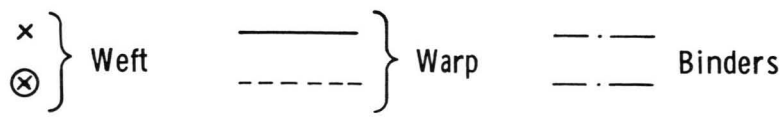
Factor	Webbing number											
	1	2	3	4	5	6	7	8	9	10	11	12
Nominal warp count <sup>a</sup> tex	93	93	93	93	93	93	93×2	93×2	93×2	93×2	93×2	93×2
Nominal weft count <sup>a</sup> tex	93×2	93×2	93×2	93×3	93×3	93×3	93×2	93×2	93×2	93×3	93×3	93×3
Nominal binder count <sup>a</sup> tex	93×2	22×4×2	110×2	93	22×4	110	93	22×4	110	93×2	22×4×2	110×2
Binder material	A <sup>b</sup>	B <sup>c</sup>	C <sup>d</sup>	A	B	C	A	B	C	A	B	C
Number of binder pairs	22	16	11	22	16	11	16	11	22	16	11	22

<sup>a</sup>In accordance with BC 946:1970, single to fold designation.

<sup>b</sup>A = nylon.

<sup>c</sup>B = Nomex.

<sup>d</sup>C = polyester.



Note: Section along warp normal to weft

Figure 1. - Construction of ply-tear-webbing weaving sequence.

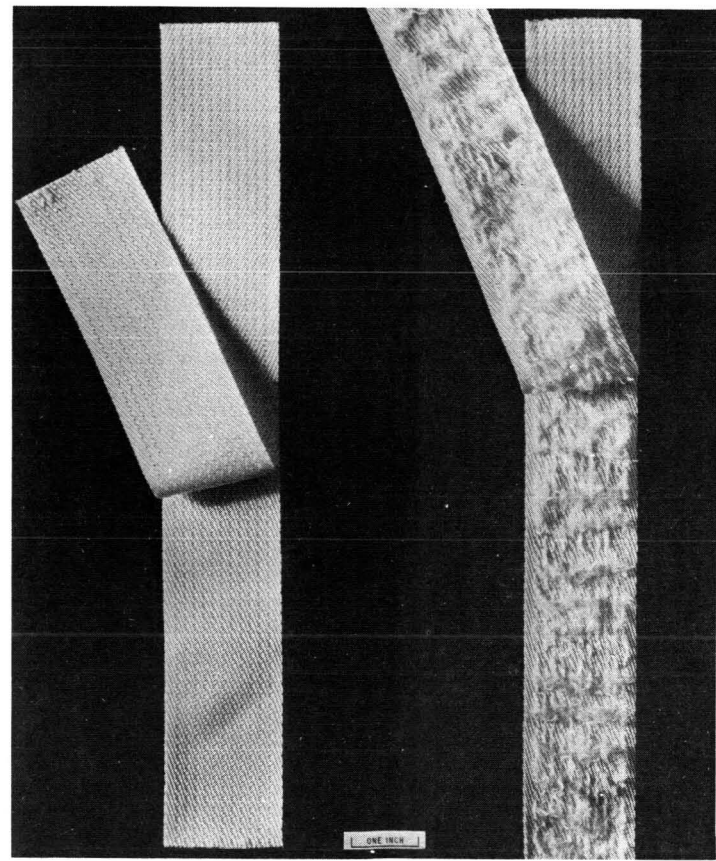


Figure 2. - Ply-tear webbing type WR 1017.

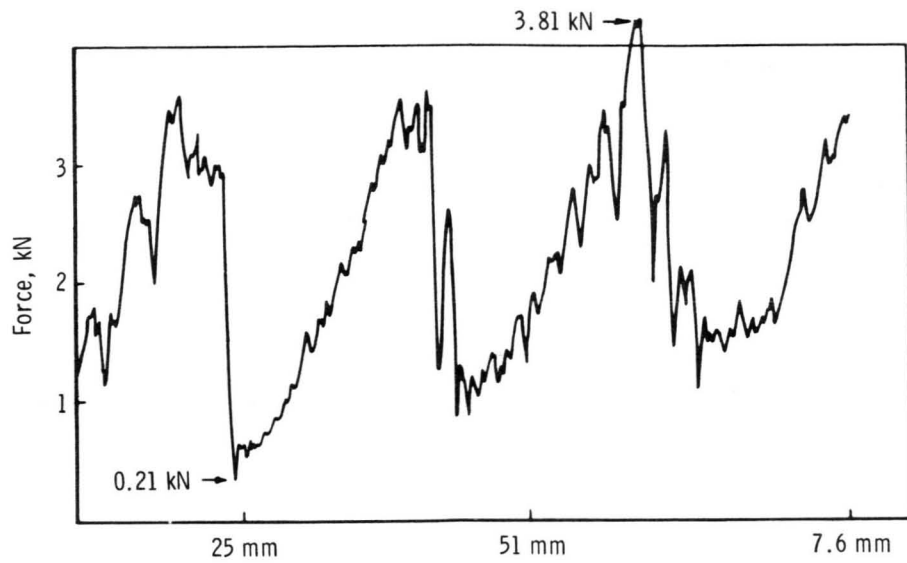


Figure 3. - Nylon webbing WR 1017 slow-speed tearing on a Dennison machine.

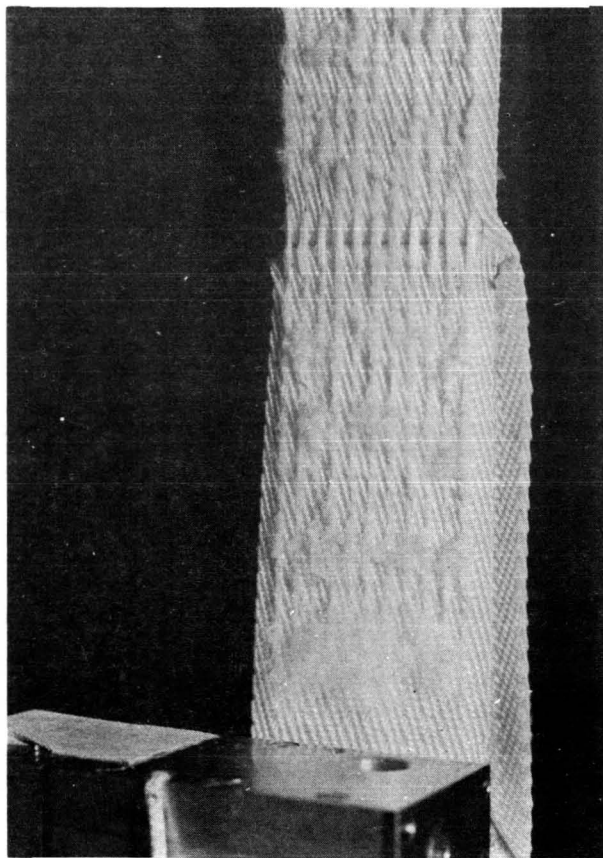
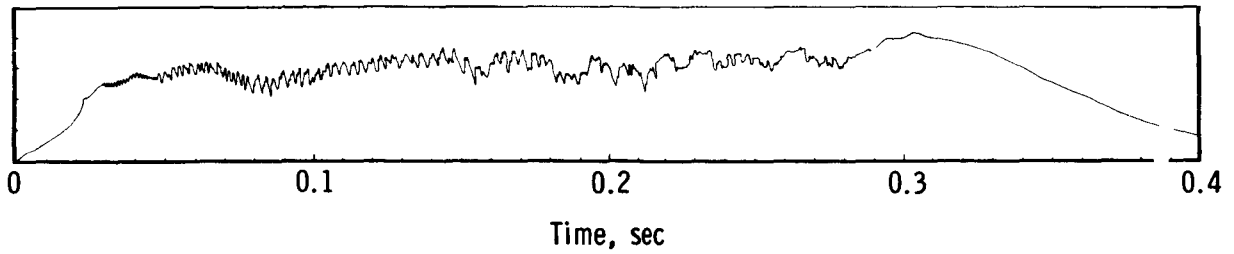


Figure 4. - Type WR 1017 webbing tearing at a rate of 35 m/sec.



Descent velocity at start of tear, m/sec . . . 10  
 Free-fall distance, m . . . . . 4.9  
 Weight of dummy, kg . . . . . 83.5  
 Mean retardation, g . . . . . 4  
 Full scale of force, kN . . . . . 6.7

Figure 5. - Force/time record of retardation of a dummy by ply-tear safety harness.

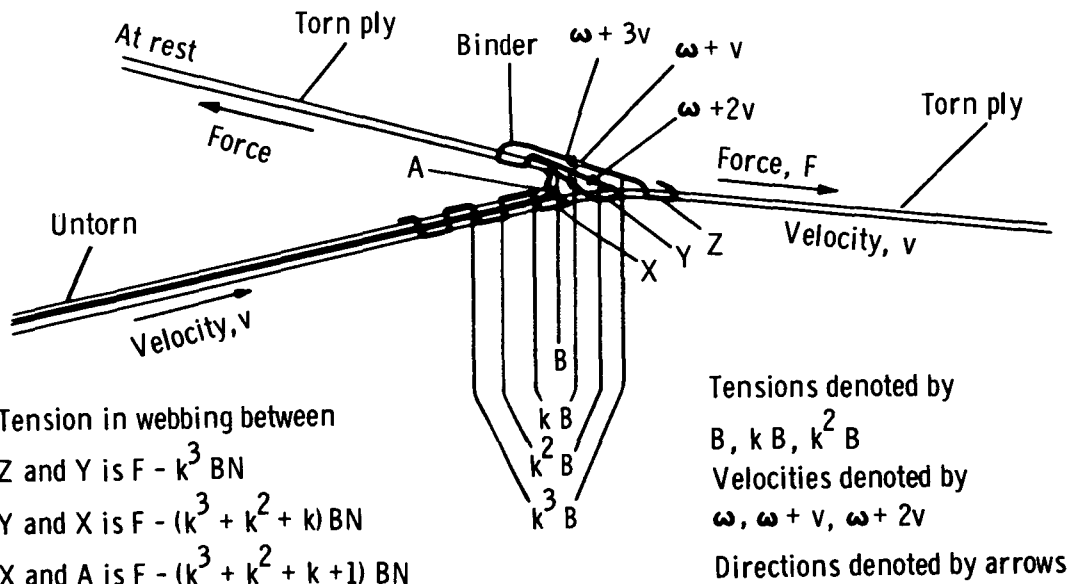


Figure 6. - Analysis of tearing forces.

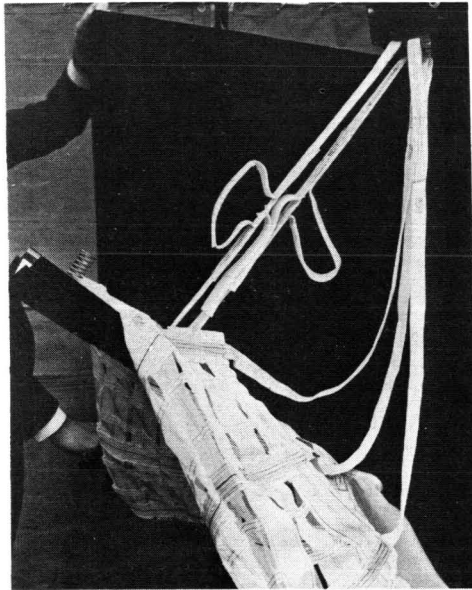


Figure 7. - Ply-tear webbing links retarder unit for bomb.

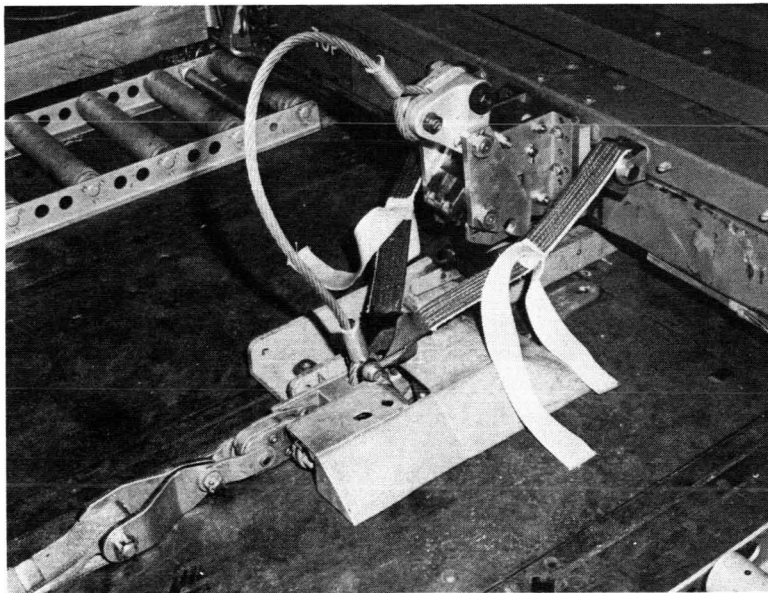


Figure 8. - Mediumweight-supplies dropping system (ply-tear link across extractor parachute emergency release).

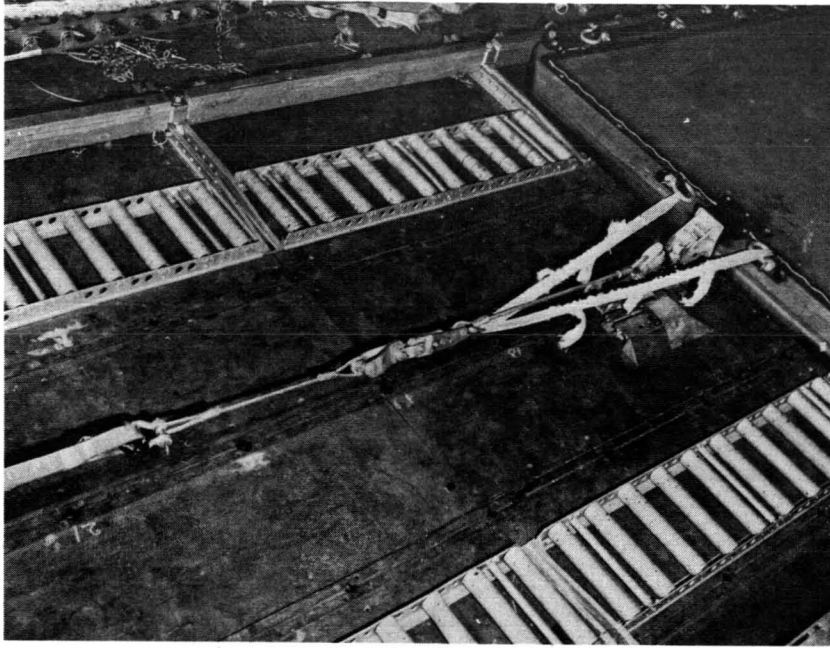


Figure 9. - Mediumweight-supplies dropping system (link torn and supplies platform under extraction load).

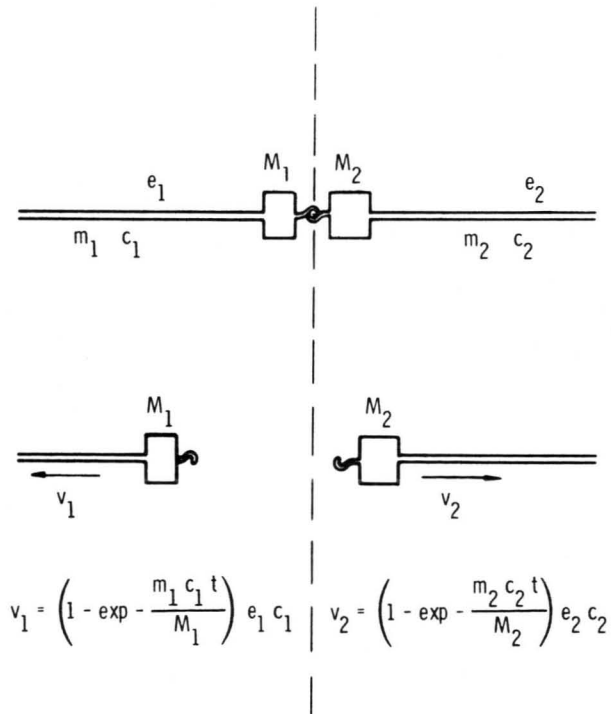


Figure 10. - Motion of masses and elastic cables after instant of release.

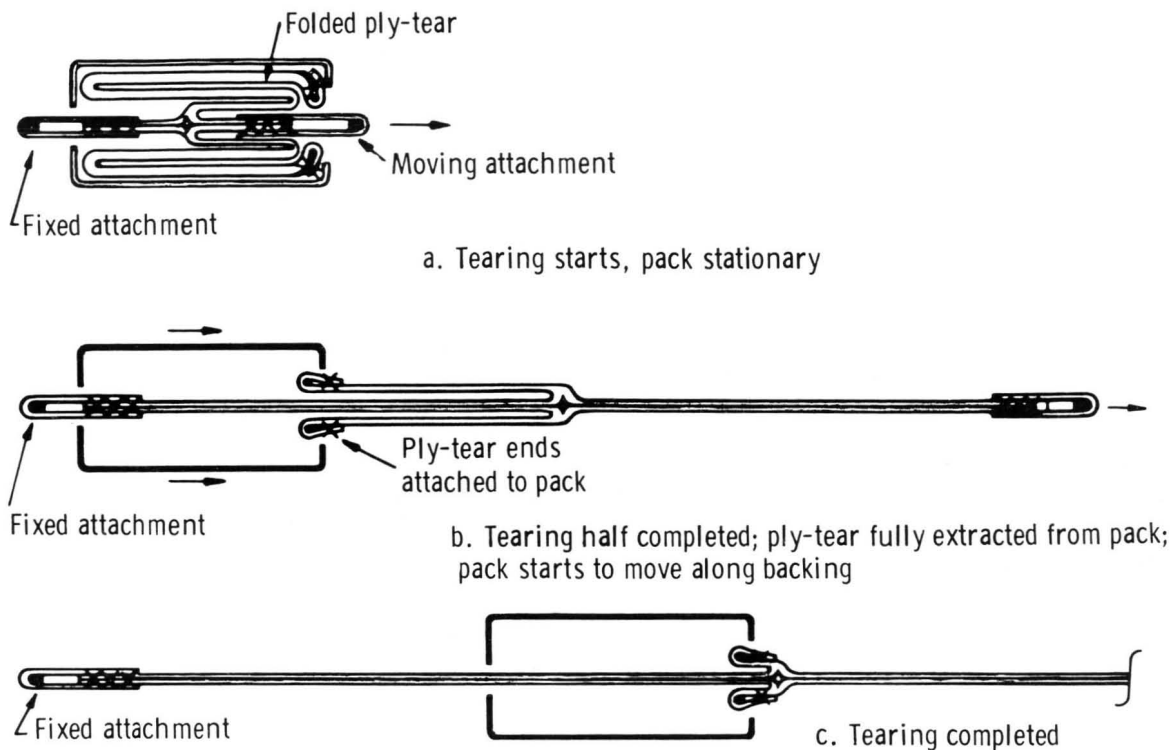


Figure 11. - Ply-tear webbing pack design to restrain untorn webbing ends.

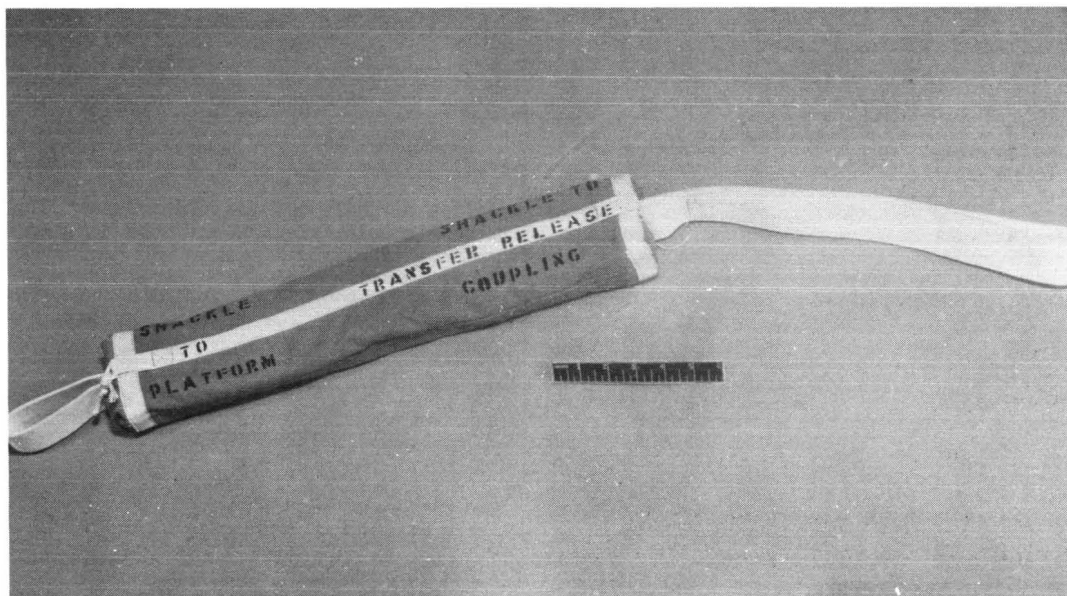


Figure 12. - Ply-tear webbing pack design for heavyweight-supply-dropping application (mean tear force, 9 kilonewtons; extension, 8.4 meters from 1.1 meters).

## FLEXIBLE SOLAR-ARRAY MECHANISM

By Merlyn C. Olson\*

### ABSTRACT

One of the key elements of the flexible rolled-up solar array system is a mechanism to deploy, retract, and store the flexible solar-cell arrays. The selection of components, the design of the mechanism assembly, and the tests that were performed are discussed in this paper. During 6 months in orbit, all mission objectives were satisfied, and inflight performance has shown good correlation with preflight analyses and tests.

### INTRODUCTION

Several advanced space-technology experiments were placed in a circular orbit on October 17, 1971. One of these experiments was a flexible rolled-up solar array (FRUSA) (fig. 1). This unique, self-contained power system consisted of the following components.

1. A pair of drum-mounted, 4.88- by 1.68-meter (16 by 5-1/2 foot), extendible/retractable, flexible solar-cell arrays
2. An orientation mechanism and control that maintains the array in a sun-pointing attitude
3. A power conditioning and storage subsystem to provide regulated ac and dc voltages, to control battery charging, and to furnish housekeeping power before deployment and during eclipses
4. An instrumentation system to monitor structural, thermal, and system performance

The objectives of the FRUSA experiment were the following.

1. Demonstrate solar-array-assembly deployment and flexible-solar-cell-array extension and retraction in an orbital environment for a 1.5-kilowatt system
2. Demonstrate solar-array-assembly tracking and lockon performance in an orbital environment

---

\*Hughes Aircraft Company, El Segundo, Calif.

3. Demonstrate power-generation capability in an orbital environment for a period of up to 1 year

4. Verify dynamic behavior of the array system

5. Provide reference measurements with calibrated solar cells and modules

The subject of this paper is the development, qualification, and flight performance of the drum mechanism of the FRUSA system. The drum mechanism is a key unit used to deploy, retract, and store the flexible solar panels.

### DRUM-MECHANISM REQUIREMENTS

The drum mechanism is required to perform the following functions.

1. Store the solar arrays during the launch phase of the mission and during any retracted mode of operation

2. Extend and retract the solar-array panels in orbit

3. Provide equal tension across the width of the panel during extension and retraction and during fully extended operation

4. Transfer electrical power between the solar panels and the spacecraft

The mechanism must perform the functions in accordance with the following conditions.

1. Boost environment: 19.5g root mean square broadband random plus up to 8g sinusoidal

2. Flight dynamic environment: 0.1 g

3. Orbit environment: 1 year at 643.6 kilometers (400 miles) to synchronous altitude

4. Extension/retraction cycles

In orbit: 10 cycles

Ground test: 25 cycles

5. Array-storage-volume goal:  $2 \text{ ft}^3/\text{kW}$

6. Power output: 1.5 kilowatts at synchronous altitude

7. Weight goal (including panel): 15.88 kg/kW (35 lb/kW)

## MECHANISM DESCRIPTION

The drum mechanism, shown with the solar panels in figure 2 and with the parts identified in figure 3, consists of several major elements. The elements include an extendible-boom-actuator unit, a boom-length-compensator mechanism, a storage-drum assembly, a panel-tension drive, and power- and data-transfer assemblies.

### Extendible-Boom-Actuator Unit

The boom-actuator unit, shown in figure 4 with a shortened torque tube, is a completely dry-lubricated device consisting of two actuators that store and form the 2.18-centimeter-diameter (0.86 inch diameter) stainless-steel Bi-Stem booms; a single 115-V ac, 400-hertz motor/gearhead to extend and retract booms; and an inter-connecting torque tube between master and slave units to allow for a single motor drive unit.

Each of the four booms is approximately 4.88 meters (16 feet) long and deploys at a rate of approximately 1.27 cm/sec (0.5 in/sec). Microswitches are employed to indicate full extension or retraction. A strain-gage installation is built into one of the boom guidance assemblies to measure boom bending.

### Boom-Length-Compensator Mechanism

The boom-length-compensator mechanism (fig. 5) is used to ensure uniform tension on the solar panels in the event of uneven extension or retraction of the individual booms. This unevenness can develop because the extension rates of the individual booms are different (as a result of lost motion and friction within the actuator) or because each of the two panels extends to a different length (as a result of the dual-panel/single-drum design). Although the latter problem can be partially resolved by the use of different length booms on each side of the drum, exact compensation is difficult because of the variations in the effective thicknesses of the panel and cushion. The lost motion and friction variations within the cassettes could be corrected by sprocket drives, servo systems, and so forth. Because these approaches all involved complex modifications to existing flight-proven boom designs, the decision was made to compensate for the differences in boom lengths by designing a mechanism on the boom tips.

In the mechanism design, dry-lubricated ball bearings are used in the pulleys and rollers. A cobalt-alloy (Elgiloy or Havar) tape is used between the boom tips. Calibrated strain gages on the tape provide a direct readout of tension in the solar panels.

### Storage-Drum Assembly

A thin-wall magnesium cylinder, 20.32 centimeters (8 inches) in diameter and 177.80 centimeters (70 inches) long, is used for the storage drum. The end plates are a titanium/aluminum honeycomb structure.

The bearings used in the storage drum are as follows.

1. Type: angular contact
2. Material: 440C stainless steel
3. Bore: 5.8730 to 5.8738 centimeters (2.3122 to 2.3125 inches)
4. Lubrication: burnished molybdenum sulfide ( $\text{MoS}_2$ ) plus Duroid 5813 retainer
5. Preload: 35.58 to 53.38 newtons (8 to 12 pounds)

The installation shown in figure 6 was designed to provide low torque operation over the expected temperature ranges, with temperature differentials between housing/shaft and inboard/outboard bearing pairs. Axial differential expansion is accommodated by allowing one pair of bearings complete axial freedom. In the case of differential temperatures between the inner and outer races of particular pairs, a combination of wavy washer springs and matched materials for housing, shaft, and bearings is used.

#### Panel-Tension Drive

A constant-torque Negator spring drive is used to provide tension on the panels during extension and retraction. The Negator spring is a coiled stainless-steel band wound on spools to produce a torque essentially constant over the entire travel range. However, because of the changing radii in the drum and Negator spools, the tape is modified by contouring. The contouring consists of varying the tape width with length to produce a slightly negative spring constant. Total two-panel tension provided by this drive arrangement over the entire travel and temperature range was  $44.48 \pm 11.12$  newtons ( $10 \pm 2.5$  pounds).

#### Panel-Cushion Takeup Drive

The cushion required to protect the solar cells in the stowed condition, particularly during launch, is made of embossed Kapton. The function of the cushion takeup is to roll up and store the cushion when the panels are deployed and to deploy the cushion between the two panels during the retraction cycle. The cushion tension provided by this drive is between 4.448 and 11.12 newtons (1 and 2.5 pounds).

The system chosen for this task is a Negator motor drive operating directly on the takeup reel, independent of the storage drum. As in the case of the panel-tension drive, this motor is a coiled metal band wound on spools to produce a torque essentially constant over the entire travel range. It was selected over a dc or ac motor and pulley drive for this function primarily because of its simplicity, low cost, low weight, and high reliability.

## Power- and Data-Transfer Assemblies

Transfer of power and data signals within the storage drum is accomplished by means of flexible flat cables. These cables employ copper conductors with  $2.54 \times 10^{-5}$ -meter (1 mil) Kapton insulation. Transition to conventional round wires is made at the hub of the drum to allow use of conventional connectors at the spacecraft interface. For the power cables, a printed circuit board is used as an interface with the panel-wiring bus (fig. 7). The data cable at the opposite end of the drum is soldered directly to the flat solar-panel conductors. The cables are wound up on the center spar of the drum when the panels are fully retracted. As the panels extend, the cables unwind and then rewind in the opposite direction. This feature permits shorter cable lengths and, therefore, lower power losses.

An extensive tradeoff study was performed to evaluate this system with respect to a slipring/brush arrangement. The final results of this study are summarized in table I.

## COMPONENT-EVALUATION TESTS

The component-evaluation phase of the program included functional and environmental tests of boom-actuator units; bearing, Negator, and flexible-cable installation; and the boom-length-compensator mechanism.

### Boom-Actuator Units

An engineering model of the boom actuator was subjected to the following series of functional and environmental tests.

1. Sinusoidal vibration tests
2. Thermal extension/retraction tests
3. Boom synchronization, straightness, alinement, and bending evaluation
4. Boom-bending instrumentation calibration

A single-boom breadboard model of the actuator unit was also built and subjected to a life-test program. This program consisted of 314 extensions and retractions under ambient conditions with simulated tip loading. The successful demonstration of 314 cycles represents a capability to perform 35 cycles (25 on ground and 10 in orbit) with a 90-percent confidence level.

## Bearing, Negator, and Flexible-Cable Development Tests

The development program on the drum bearings, panel-tension drive, flexible cable, and cushion reel drive was conducted in a dry-nitrogen environment and included the following conditions.

1. Drum bearings at room temperature and at  $172.04^{\circ}$  and  $383.15^{\circ}$  K ( $-150^{\circ}$  and  $230^{\circ}$  F)
2. Drum bearings and simulated flexible flat cable at room temperature and at  $172.04^{\circ}$  and  $383.15^{\circ}$  K ( $-150^{\circ}$  and  $230^{\circ}$  F)
3. Cushion reel drive at room temperature
4. Complete system (drum bearings, drum drive, cushion reel drive, and flexible cable) at room temperature and at  $172.04^{\circ}$  and  $383.15^{\circ}$  K ( $-150^{\circ}$  and  $230^{\circ}$  F)
5. Drum bearings with inner-race temperature  $2.78^{\circ}$  to  $16.67^{\circ}$  K ( $5^{\circ}$  to  $30^{\circ}$  F) higher than outer races

The test results indicated adequate margins for all components tested when operating in the expected thermal environment. The significant results and conclusions were as follows.

1. Drum-bearing torque levels for essentially uniform temperature distribution (no temperature gradients between inner and outer race) were  $0.15 \times 10^6$ ,  $0.25 \times 10^6$ , and  $0.31 \times 10^6$  dyne-cm (0.13, 0.22, and 0.27 in/lb) per pair for room temperature,  $172.04^{\circ}$  K ( $-150^{\circ}$  F) and  $383.15^{\circ}$  K ( $230^{\circ}$  F), respectively.
2. Drum-bearing torque for the expected  $5^{\circ}$  to  $10^{\circ}$  differential between inner and outer races was approximately  $0.23 \times 10^6$  dyne-cm (0.20 in/lb) per pair. For  $\Delta T = 16.67^{\circ}$  K ( $30^{\circ}$  F), the torque was  $0.39 \times 10^6$  dyne-cm (0.35 in/lb), still within the allowable limit of  $1.13 \times 10^6$  dyne-cm (1 in/lb).
3. Flexible-cable torque levels, based on a simulated cable with representative Kapton/copper, were estimated to be approximately  $2.26 \times 10^6$  dyne-cm (2.0 in/lb), maximum. This includes two pairs of data cables and two pairs of power cables at  $172.04^{\circ}$  K ( $-150^{\circ}$  F).
4. Cushion tension, provided by cushion reel drive, would be between 4.45 and 11.12 newtons (1.0 and 2.5 pounds). The larger value corresponds to the empty-reel condition, in which the largest tension is required for proper rollup of the cushion.
5. Drum Negators, when contoured to compensate for changing drum diameters, would provide total panel-tension levels (two panels) between approximately 35.38 and 35.58 newtons (8 and 12 pounds) (fig. 8). Based on panel rollup tests and the allowable boom loads, this range of panel tension was considered acceptable.

A contoured Negator was subjected to more than 4450 cycles at room temperature before a bending-fatigue failure occurred. This number of cycles represents a large margin over the 2500-cycle vendor guarantee and the 35-cycle (10 flight and 25 pre-flight ground test) life required for the experiment. Measurements made after approximately 4000 cycles revealed no apparent change in the Negator torque characteristics over a typical cycle. These measurements also verified that the contouring operation achieved the features desired.

### Boom-Length-Compensator Development Tests

The development test program on the boom-length-compensator devices was performed at room temperature and at 188.70° and 408.15° K (-120° and 275° F). Results of the tests indicated the maximum difference between the panel tension from one edge to the other was less than 4.45 newtons (1 pound). This value was considered well within the difference allowable for satisfactory rollup of the flexible arrays.

### ASSEMBLY ENGINEERING AND QUALIFICATION TESTS

Functional engineering tests of the drum mechanism with a solar panel were performed on a water-table-deployment installation (figs. 9 and 10). A total of 20 complete cycles were run with the following data and information obtained.

1. Motion-picture coverage at various locations to evaluate deployment characteristics of booms, panel, and so forth
2. Qualitative data on panel and cushion rollup features
3. Specific information on size, number of turns, and so forth, for panel drum and cushion reel
4. Operation of 400-hertz drive electronics with boom-actuator motor
5. Evaluation of water-table and float-insertion procedures
6. Static measurements of boom synchronization

The system operated well with no significant design changes required. The following were specific observations on the functional performance.

1. Boom synchronization appeared to be good, with less than  $\pm 5.08$  centimeters ( $\pm 2$  inches) differential.
2. Cushion and panel windup was satisfactory, with only a small amount of lateral translation or "walking" noted during panel windup.
3. Float insertion and water-table operation was quite smooth, with only minor changes required in the table or procedure.

4. Operation of limit switches in boom-actuator unit was not proper, and redesign was initiated.

5. Booms had a tendency to self-extend approximately 15.24 centimeters (6 inches) after full retraction. To prevent a possible oscillatory mode, a slight modification in motor-drive electronics was incorporated.

The qualification model of the drum mechanisms was subjected to functional tests, solar thermal-vacuum tests, and the launch environments as indicated in table II. No major failures were observed during exposure to the environmental tests.

## FLIGHT TESTS

On the ninth vehicle orbit, the solar panels of the FRUSA system were deployed by the drum mechanism. Because array extension on the ground was influenced by the water-table/float system and gravity, this rollout provided the first real demonstration of the zero-g mechanical and dynamic performance of the drum-mechanism design. The accelerometers mounted on the boom tips recorded the data shown in table III during the extension. The start of the extension saturated the accelerometers with sensitive axes (u, w) in the plane of the panel. During rollout to the fully extended panel length of 4.88 meters (16 feet), the accelerations averaged approximately 15 to 30 milli-g peak. Termination of the rollout did not generate any noticeable dynamic excitation.

The duration of the initial panel extension was 294 seconds, which agrees with the extension periods measured on the water table in ground testing. Actuator-motor current levels also were approximately the same as ground-test values. The nominal tension in each of the panels as monitored by the strain gages on the boom-length-compensator mechanism was approximately 26.24 newtons (5.9 pounds). This value at full extension agrees with the nominal setting of the panel tension as defined by ground testing.

The accelerometer data, along with the boom-bending instrumentation, revealed a boom/panel system fundamental frequency of approximately 0.25 Hz and an effective damping factor of approximately 2 percent. Analytical prediction of the first mode frequency was 0.20 Hz. Analysis of flight data to this point indicates that the system is exceptionally stable. No significant dynamic interaction with the Agena control system has been noted for either the active gas or the gravity gradient modes of operation.

A total of 10 complete extensions and retractions had been performed successfully by the beginning of 1972. Several extension/retraction cycles were performed during eclipse conditions in which drum temperatures reach 233.15° K (-40° F) and the panel temperatures go as low as 188.70° K (-120° F). No measurable degradation in solar-panel power output was observed after the 10 cycles.

## CONCLUDING REMARKS

The successful operation of the drum mechanism on the flexible rolled-up solar array experiment aided in demonstrating the feasibility of the system. In addition, the agreement between analysis and ground tests and orbital dynamic performance enhances the confidence in the design approach and techniques for larger and more advanced power systems using this concept.

TABLE I. - COMPARISON OF SLIPRINGS AND FLEXIBLE CABLE  
FOR 1500-WATT SYSTEM

Parameter	Flexible cable	Slipring/brush arrangement	Difference
Weight	<sup>a</sup> 0.15 kg (0.34 lb)	<sup>a</sup> 0.68 kg (1.50 lb)	<sup>a</sup> -0.53 kg (-1.16 lb)
Reliability	Higher	Lower	--
Voltage drop	.22 V	.11 V	+0.11 V
Power loss	11.5 W (0.77 percent of total)	5.75 W	+5.75 W
Torque about drum axis	Lower	Higher	--
Growth factor	Equal	Equal	--

<sup>a</sup>Includes cells necessary to compensate for larger power loss.

**Page intentionally left blank**

TABLE III. - DRUM-MECHANISM EXTENSION DYNAMICS

Acceleration sensing axis	Peak accelerations, milli-g		
	Start of extension	During extension	End of extension
U direction	(Saturated)	59.1	18.3
V direction	70.4	32.2	23.5
W direction	(Saturated)	27.0	13.9

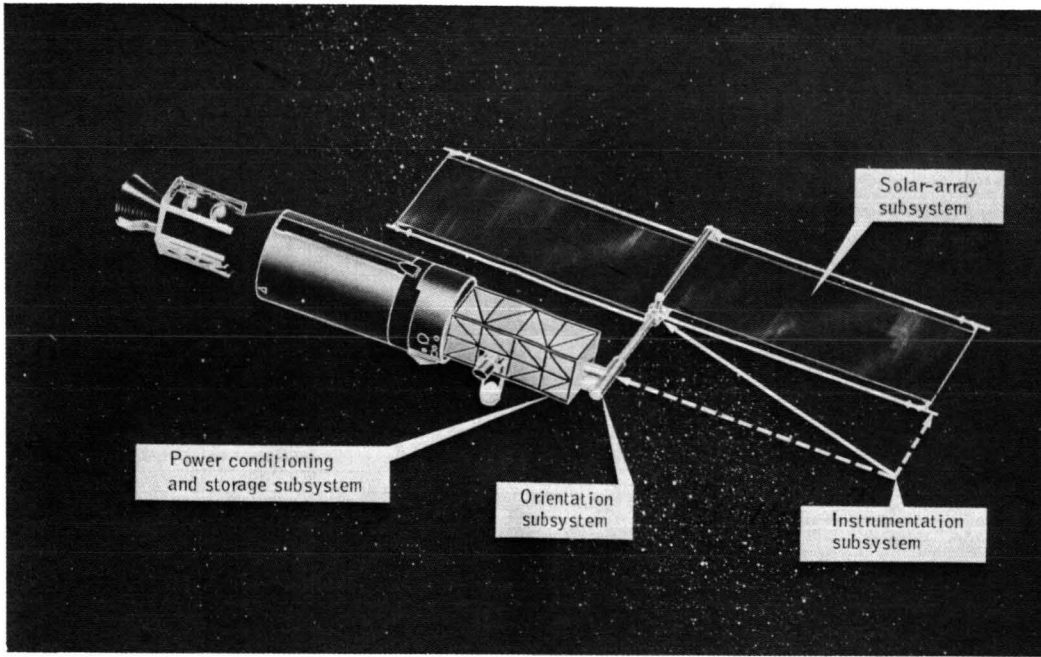


Figure 1. - The FRUSA system.

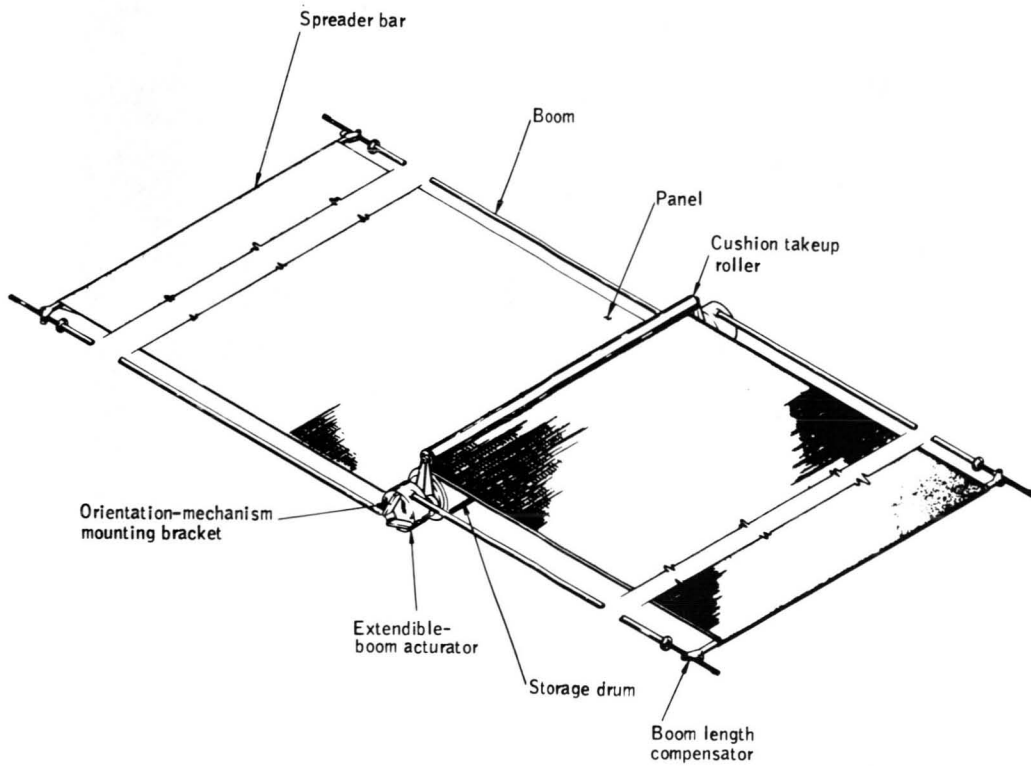


Figure 2. - Drum mechanism and solar panels.

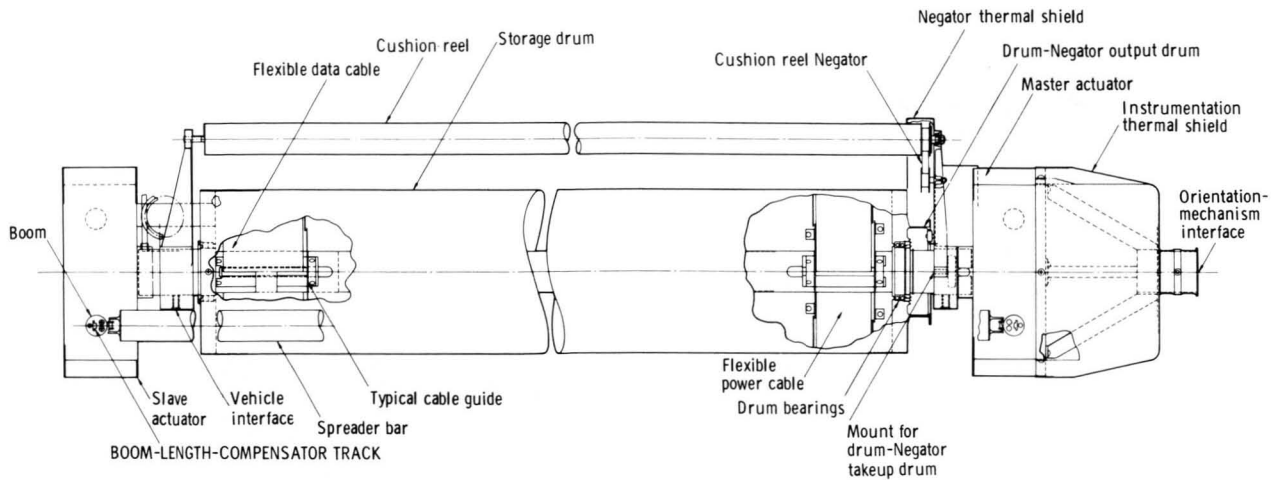


Figure 3. - Drum-mechanism details.

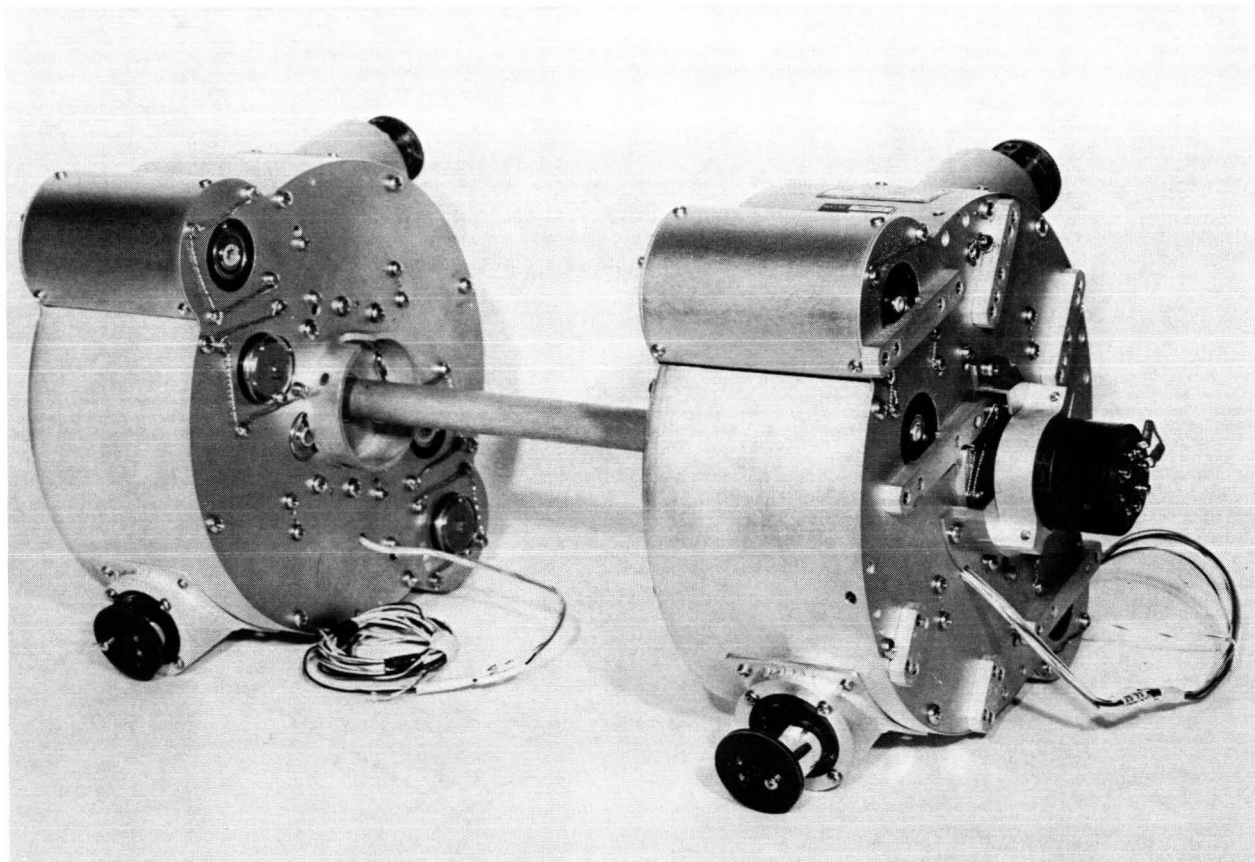


Figure 4. - Extendible-boom-actuator unit.

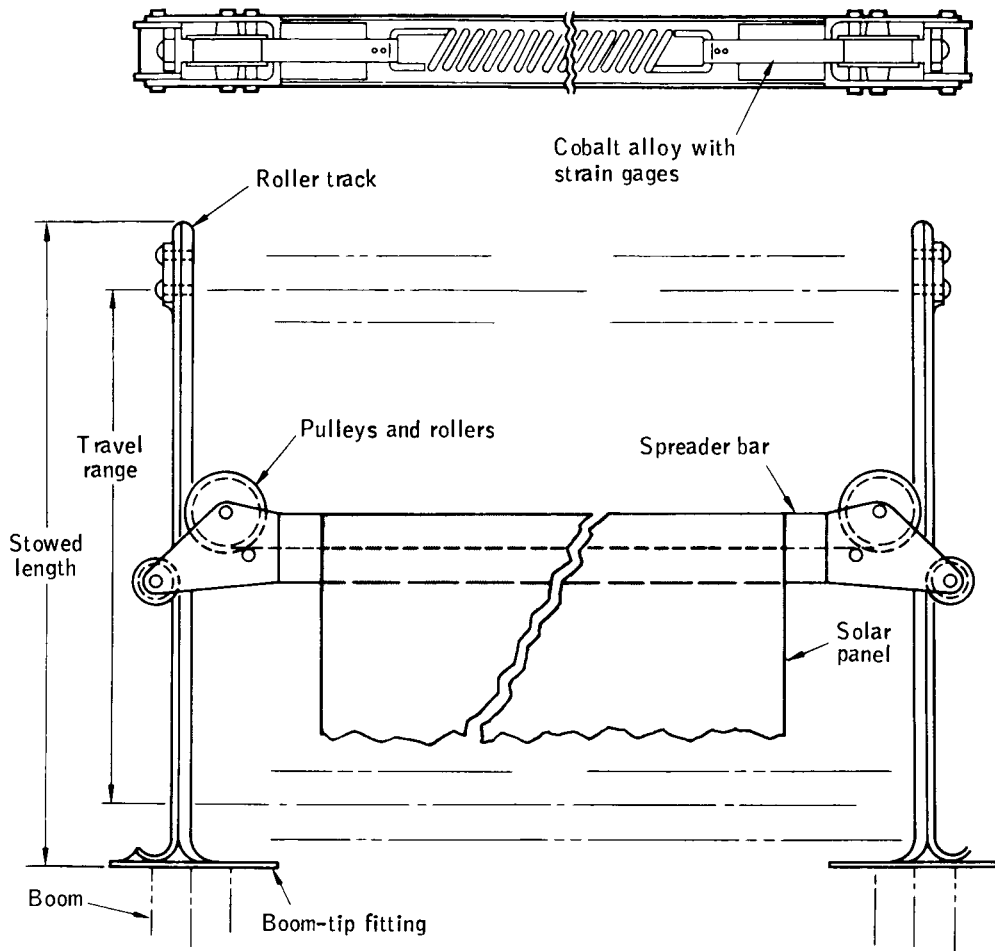


Figure 5. - Boom-length compensator.

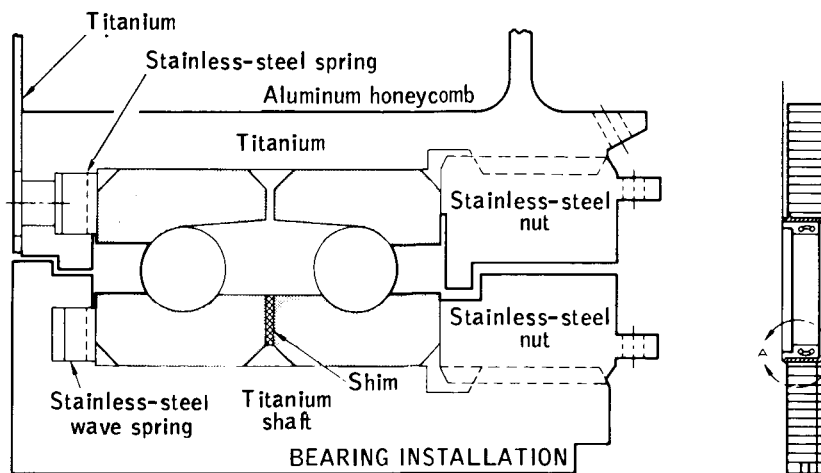


Figure 6. - Drum end plate and bearing installation.

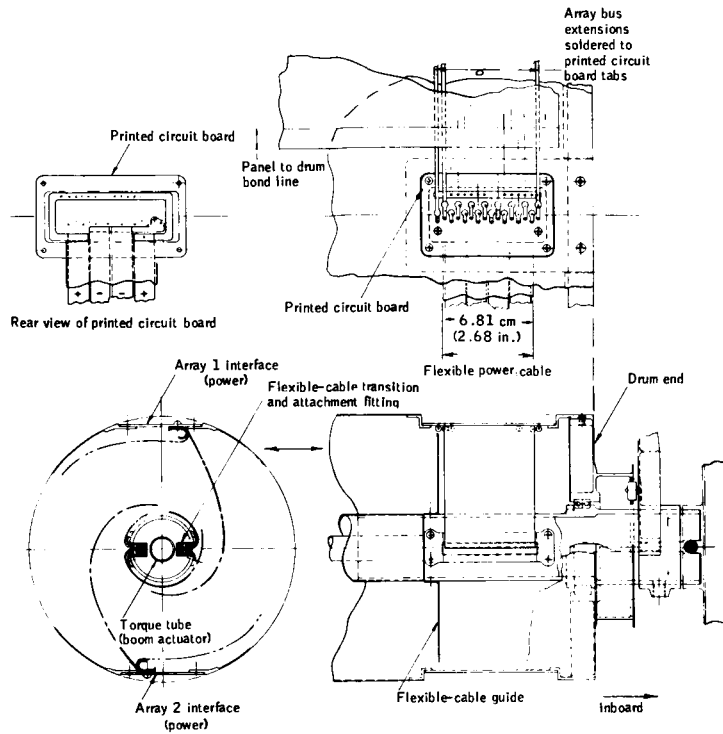


Figure 7. - Flexible-power-cable arrangement.

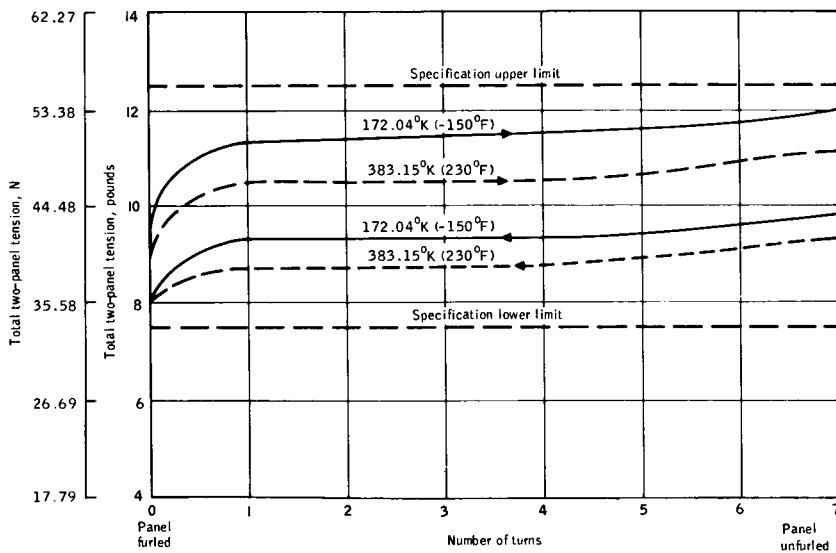


Figure 8. - Estimated average two-panel tension based on development test data.

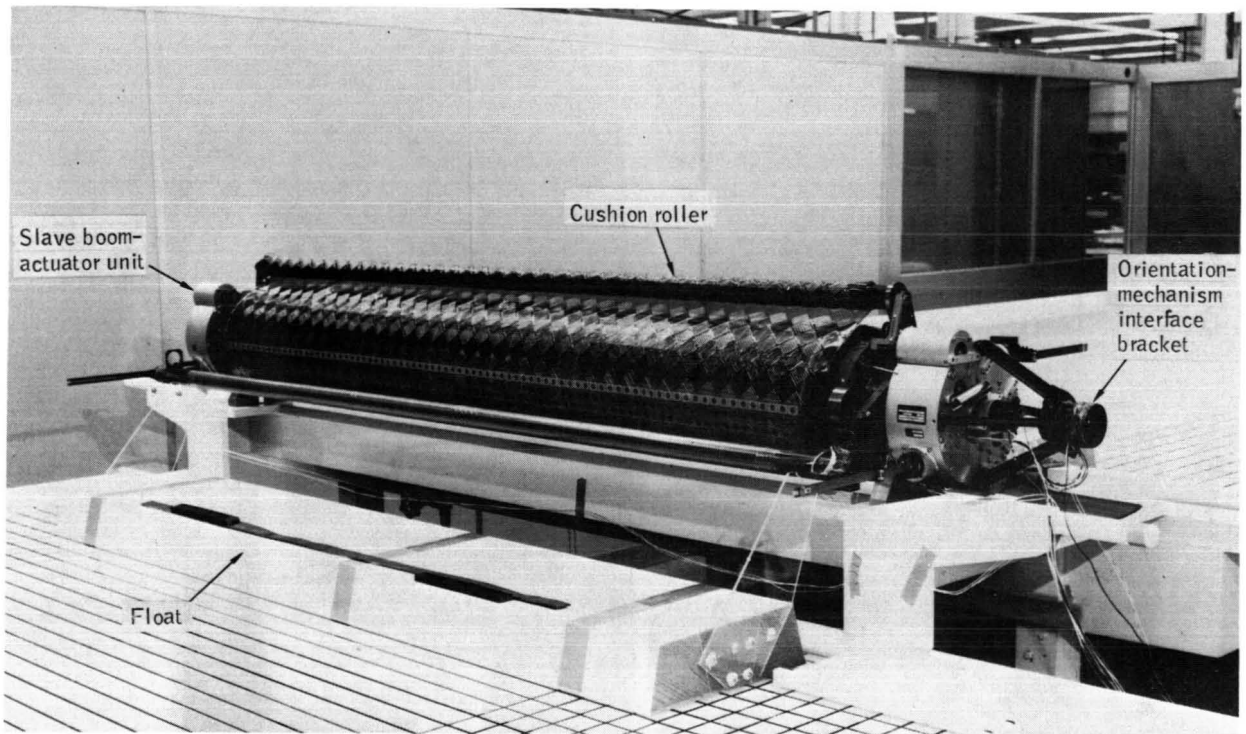


Figure 9. - Drum mechanism and panels mounted on water table for engineering tests.

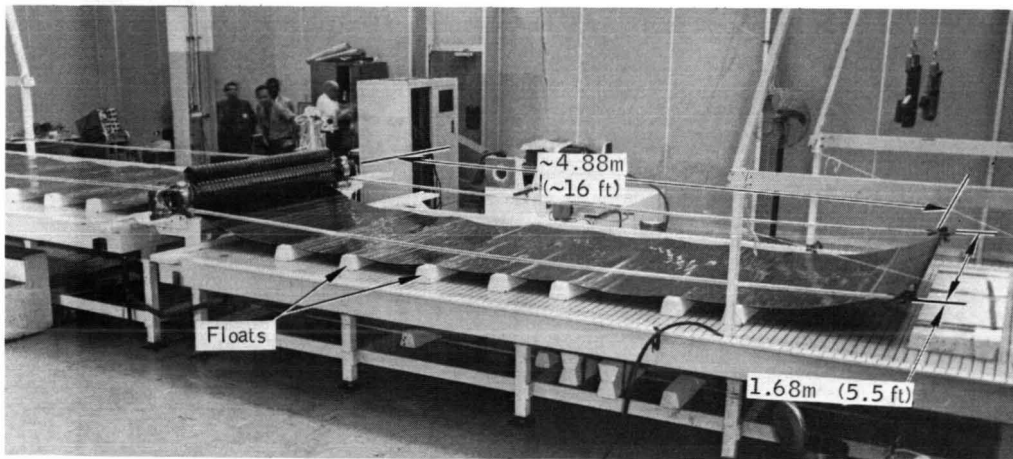


Figure 10. - Drum mechanism and panels deployed on water table.

**Page intentionally left blank**

73N18888

## SCANNING MIRROR FOR INFRARED SENSORS

By Richard H. Anderson and Sidney B. Bernstein\*

### ABSTRACT

A high-resolution, long-life, angle-encoded scanning mirror, built for application in an infrared attitude sensor, is described in this report. The mirror uses a Moire' fringe type optical encoder and a unique torsion-bar suspension together with a magnetic drive to meet stringent operational and environmental requirements at a minimum weight and with minimum power consumption. Details of the specifications, design, and construction are presented with an analysis of the mirror suspension that allows accurate prediction of performance. The emphasis is on mechanical design considerations, and brief discussions are included on the encoder and magnetic drive to provide a complete view of the mirror system and its capabilities.

### INTRODUCTION

The encoded scanning mirror is a fully integrated assembly that incorporates a controlled torsional-pendulum scanner that is coupled optically to an angle encoder that has an 87-microradian resolution over a scan angle of 0.35 radian. The mirror suspension uses a one-piece torsion bar to scan at a rate of 3.5 hertz in the resonant torsional-vibration mode. Also, the design allows the mirror to survive a severe initial shock and vibration environment, in which a 60-g level in shock and a 40-g level in vibration can be reached, without caging.

The sensor requirements specified that operation would be in deep space in a zero-g environment, with the enclosure temperature varying from 233° to 338° K, for a minimum operational life of 20 000 hours without the need for maintenance. Furthermore, the entire mirror assembly was limited in weight to 0.680 kilogram and in power consumption to 0.5 watt. Thus, to satisfy all of the requirements, an inherently simple mirror was needed.

Standard flex pivots, coupled with a magnetic drive, were investigated and rejected because their stiffness and radial runout over the  $\pm 0.22$  radian scan angle would not satisfy the system requirements. In general, a servo-driven pivoted mirror would be heavier and would consume more power than was allowed by specification. In addition, the pivot design would be complex in order to limit the radial runout over the life

---

\*Lockheed Missiles and Space Co., Sunnyvale, Calif.

of the mirror to 3.05 micrometers in 0.44 radian of mirror rotation (the tolerance for reliable encoder operation). Therefore, it was decided that the torsional-pendulum concept, which was mechanically simple and required little drive power, could be developed into a viable scanning mirror ideally suited for this application.

In the torsional-pendulum design, the basic parameters are the scan frequency, the scan amplitude, and the moment of inertia of the suspended mirror. The moment of inertia is a function of the geometry, whereas the frequency and amplitude are determined by the sensor-system requirements. Given constraints on the configuration of the torsion bar and its material or fabrication, the higher the frequency (for a given moment of inertia) the smaller the scan amplitude must be to keep the torsional shear stress developed in the bar below the endurance limit. However, if the moment of inertia can be altered, large scan amplitudes (with increasing frequency) still can be obtained without sacrificing reliability or life. This freedom in design through the manipulation of the suspension parameters allows this type of mirror to be applied in a whole spectrum of sensors that have different system requirements. Interplay between these parameters will be made more evident in the section on the suspension analysis.

Nine encoded scanning mirrors have been built and are flight qualified within project specifications. All of these mirrors have passed the environmental-testing program that is to be described in this report.

#### SYMBOLS

A	cross-sectional area of active section of torsion bar
d	diameter of active section of torsion bar
E	modulus of elasticity
$f_n$	natural frequency of suspended mirror
g	gravitational acceleration
G	shear modulus
I	area moment of inertia of active section of torsion bar
J	mass moment of inertia of suspended mirror without weights
$J_s$	mass moment of inertia of complete suspended mirror
k	torsional spring constant of active section of torsion bar
L	length of active section of torsion bar
$l_w$	length of trim weights (4.128 centimeters)

P	tensile preload force
Q	$\frac{1}{2 \times \text{damping factor}} = \frac{\pi}{\text{logarithmic decrement}}$
R <sub>0</sub>	half width of mirror (3.969 centimeters)
t <sub>w</sub>	thickness of trim weights (0.478 centimeter)
W	weight of complete suspended mirror
w <sub>W</sub>	width of trim weights
δ <sub>m</sub>	maximum transverse deflection of bar
δ <sub>0</sub>	maximum deflection of bar without preload (WL <sup>3</sup> /24EI)
ρ̄	mass density of Mallory 1000 (17.28 × 10 <sup>-3</sup> g-sec <sup>2</sup> /cm <sup>4</sup> )
σ <sub>m</sub>	maximum normal stress in active section of torsion bar
τ <sub>m</sub>	maximum torsional shear stress in active section of torsion bar
φ	angle of twist of the torsion bar

### GENERAL DESCRIPTION OF ENCODED SCANNING MIRROR

The encoded scanning mirror assembly is shown in figures 1 and 2. The mirror (8.89 by 5.72 centimeters) is gold plated on one side and is suspended within the frame by a one-piece torsion bar, the ends of which are captured by the tension nuts and clamps. The glass encoder reticle plate is attached directly to the mirror by means of the encoder hub. Below the reticle plate and attached to one side of the frame is the encoder illumination source. The remainder of the encoder optics are contained within the encoder housing that forms the base leg of the frame. Behind the mirror (supported by the housing) are the magnet coils that drive the mirror. The frame is closed on the side opposite the encoder housing by an infrared telescope support plate.

The mirror is driven by the magnetic interaction between the short permanent magnets that are mounted on the back of the mirror and the coils. Only one of the coils is used to start and drive the mirror. The other coil senses the mirror motion and generates a synchronous feedback signal to the input of the electronic control circuit.

The mirror and its suspension form a torsional pendulum that has a mechanical Q of approximately 2500 in vacuum. This pendulum is tuned by using trim weights to a frequency of 3.5 hertz. The very high Q ensures a sharp resonance that is free of

any perturbing influences from nonlinearities in the drive system and reduces the required drive power to only 0.5 milliwatt.

The sag of the torsion bar, caused by the mirror load, is limited by applying a tensile preload to the bar with the tension nuts. Excessive transverse deflection under high inertial loads is prevented by mechanical stops located at the bumper and the end of the encoder hub. These stops are Teflon bushings that contact the rigid end hubs of the torsion bar when the mirror deflects beyond 0.254 millimeter. Because the mirror "floats" during normal operation, there are no frictional surfaces in the system. Therefore, mechanical wear is eliminated.

The mirror mates with the torsion bar at its center hub. Mating is achieved primarily by chemical bonding with Loctite. This method of attachment is desirable here, because the thinness of the mirror wall in this area precludes the use of mechanical fasteners that would distort the mirror face.

The angular swing amplitude is limited by the mirror stops located at each end of the coil mounting plate. Nominally, contact with the stops will occur at 0.235 radian of swing. The face of the stop is made of sponge rubber to cushion the impacts resulting from vibration-induced torsional oscillation. During normal operation, there is no contact between the mirror and the stop because of the amplitude control exercised by the drive electronics.

Initially, the mirror is excited by the passage of the drive-amplifier noise current through the drive coil. The magnetic interaction causes the mirror to move slightly. This motion is sensed by the pickup coil that generates a synchronous signal to the drive-amplifier input. In turn, this increases the current to the drive coil, thereby increasing the mirror motion. Because the suspended mirror is a torsional pendulum, the amplitude of swing builds up rapidly. When the pickup coil signal reaches a preset value, a control circuit in the drive electronics is activated, stopping the drive current in order to maintain the mirror amplitude at 0.218 radian. Any change in this amplitude is compensated for automatically by the circuit.

### ANALYSIS OF THE MIRROR SUSPENSION

The addition of trim weights in the mirror-suspension design was necessary to increase the mass moment of inertia so that the 3.5-hertz scan frequency can be obtained with a torsion bar of reasonable diameter. The following calculations show the iterations required for design. In actual production, all width dimensions for the weights were calculated from actual measurements of the torsion-bar diameter. Then, a matched pair was machined and used with the specific bar. Of the 11 mirrors assembled, all had a natural frequency within 0.1 hertz of the nominal value, demonstrating the validity of the design procedure.

The natural frequency of a torsional pendulum of the type being considered (fig. 3(a)) is given by

$$f_n = \frac{1}{2\pi} \sqrt{\frac{2k}{J_s}} \quad (1)$$

where  $k = \pi G d^4 / 32 L$ . If  $f_n$ ,  $J_s$ ,  $G$ , and  $L$  are known, the required diameter of the active section of the torsion bar can be calculated from the formula

$$d = \left( \frac{64 \pi f_n^2 L J_s}{G} \right)^{1/4} \quad (2)$$

It is assumed here that the torsion bar is symmetrical in configuration (that is, the active sections are the same).

The value of  $J_s$  computed for the suspended mirror minus the trim weights is  $J_s \equiv J = 0.397 \text{ g-cm-sec}^2$ . Then, substituting this value along with  $L = 3.016$  centimeters,  $G = 8.86 \times 10^5 \text{ kg/cm}^2$  (shear modulus for Elgiloy, the torsion bar material), and  $f_n = 3.5$  hertz into equation (2), the value  $d = 0.432$  millimeter. This value is too small for practical fabrication of the bar as a one-piece unit. However, it is possible to fabricate (on a production basis) sections that have a diameter of 0.533 millimeter. Then, by using the trim weights to increase  $J_s$ , the frequency can be maintained.

The trim weights are located at the outer edges of the mirror to minimize their weight and to significantly increase  $J_s$ . Further gains are obtained by making the weights from a heavy material like Mallory 1000 (which has a density of  $17 \text{ g/cm}^3$ ).

Selection of  $d = 0.533$  millimeter raises the value of  $k$  to  $0.234 \text{ kg-cm}$ . Therefore, for  $f_n = 3.5$  hertz,  $J_s$  must now be equal to  $0.968 \text{ g-cm-sec}^2$ . The required  $J_s$  is 2.44 times greater than  $J$ . If a rectangular shape of length  $l_w$  and thickness  $t_w$  is selected for the weights, the required weight width (for example, the dimension in the mirror radial direction) can be calculated by using the formula

$$w_W = R_o \left\{ \left[ 1 + \frac{3(J_s - J)}{2 \bar{\rho} t_w l_w R_o^3} \right]^{1/3} - 1 \right\} = 0.470 \text{ cm} \quad (3)$$

This width is certainly acceptable within the design envelope, and the suspended mirror weight is increased by only 35 percent.

The final configuration of the torsion bar is shown in figure 3(b). The overall length was determined by the allowable size of the mirror assembly. The hub lengths

were dictated by the mirror-mating and deflection-limiting requirements, and the large fillets at each end of the active sections reduce the stress concentrations at the changes in section to a minimum.

The torsion bar is preloaded to control the transverse sag under the weight of the mirror. A suitable analytic model for calculating the stresses and deflection is shown in figure 4. It is reasonable to assume that the hubs are perfectly rigid and the mirror weight acts as a concentrated load at the center of a bar of length  $2L$ .

The maximum transverse deflection will occur at the center and represents the actual mirror deflection. Its value can be calculated from the approximate formula

$$\delta_m = \frac{\delta_o}{1 + (PL^2/\pi^2 EI)} \quad (4)$$

Solving equation (4) for  $P$ , with  $\delta_m$  limited to 0.102 millimeter and  $W = 0.121$  kilogram, gives the required preload  $P = 13.99$  kilograms.

The normal stress in the torsion bar is the algebraic sum of the axial and bending stresses induced by the  $P$  and  $W$  loads. The maximum normal stress is given by

$$\sigma_m = \frac{P}{A} + \frac{Wd}{4I} \sqrt{\frac{EI}{P}} \quad (5)$$

At room temperature,  $\sigma_m = 7.252 \times 10^3$  kg/cm<sup>2</sup>. Over the operating temperature range, caused by changes in the mirror-frame dimensions, this stress can increase by as much as  $1.645 \times 10^3$  kg/cm<sup>2</sup>. The proportional limit for Elgiloy (based on tests) is  $5.455 \times 10^3$  kg/cm<sup>2</sup> in the non-heat-treated case and  $11.998 \times 10^3$  kg/cm<sup>2</sup> when heat-treated. Clearly, to preserve the elastic behavior of the torsion bar under load, it is essential that only heat-treated bars be used.

The stresses that developed in the torsion bar when the mirror was subjected to a 60-g level of both transverse and axial inertial loading were analyzed. It was found that if, in the transverse case, the deflection was not limited by the mechanical stops, failure would occur because the ultimate strength of Elgiloy would be exceeded. However, in the purely axial case, the stress would not exceed the proportional limit. The maximum allowable transverse deflection before the proportional limit is exceeded in a worst case situation has been questioned. Knowing this, the maximum clearance between the Teflon bushings and the torsion-bar hubs could be established. By means of analysis, it was shown that, without an axial load component, the maximum deflection would be 0.711 millimeter. However, when both a 60-g axial component and a transverse component were acting simultaneously to stress the bar to its proportional limit,

only a 0.127-millimeter deflection would be tolerable. To establish this amount of clearance in the mechanical stops is impractical. Therefore, it was decided that, if the clearance was 0.254 millimeter, the likelihood of failure would be small in any actual situation that was within the performance specifications. This judgment was upheld throughout the environmental testing of the complete mirror assembly.

The maximum torsional shear stress was investigated to ascertain whether this stress would exceed the estimated torsional endurance limit of Elgiloy. Using the formula

$$\tau_m = \frac{Gd}{2L} \varphi \quad (6)$$

it was found that  $\tau_m = 1.709 \times 10^3 \text{ kg/cm}^2$  for  $\varphi = 0.218$  radian. A conservative estimate of the endurance limit indicated a value of  $2.285 \times 10^3 \text{ kg/cm}^2$  when the bar was preloaded at the level  $P = 13.99$  kilograms. Without preload, tests have indicated that the endurance limit is raised to  $4.218 \times 10^3 \text{ kg/cm}^2$ . Therefore, it is seen that torsional fatigue failure, caused by overstressing, does not appear probable under normal operating conditions. The life tests, discussed in the next section, supports this conclusion.

## TORSION-BAR CONSIDERATIONS

Torsion-bar-grade Elgiloy was selected for the bar material because it has a very high proportional limit, shear strength, and torsional endurance. Furthermore, it is nonmagnetic and highly corrosion resistant; it also has low thermal conductivity, low torsional hysteresis loss, a modulus of elasticity equivalent to steel, and a notch sensitivity of approximately zero. The grade chosen is select in that it is free of macroscopic inhomogeneities and core pipe throughout its volume.

When the mirror development began, the physical properties for Elgiloy wire were not available. Therefore, it was desirable to perform a series of tests on specimens conforming to the torsion-bar design in support of the theoretical calculations and strength estimates. Tests were conducted on both heat-treated and "as received" specimens for comparison purposes and to establish the true advantage of heat-treating the bars. The results of the project are summarized in table I.

In general, machining Elgiloy is not difficult if carbide-tipped tools are used. However, to machine a rod to the torsion-bar configuration, a special lathe setup is required. The tool pressure on the workpiece is high; therefore, a backup rest that travels with the cutter is necessary when machining the thin active sections. A technique was developed that facilitates the fabrication of as many as four torsion bars in 1 man-day.

The bars are machined to within 51 micrometers of the final diameter. Finishing to specifications is achieved by electropolishing. This process not only allows precise control of the final diameter but facilitates removal of all surface marks, minimizing the chance of failure for this reason.

The reliability of the bar has been proven in both environmental tests and in accelerated life tests. The environmental tests were conducted on complete mirror assemblies and consisted of subjecting them, along three mutually perpendicular axes, to the following environments: a 30-g sustained acceleration for 300 seconds, a 60-g half-sine-wave shock for 8 milliseconds (three impacts), 25-g sinusoidal vibrations to 400 hertz followed by 40 g to 2000 hertz, random vibration for 180 seconds, and temperature cycling while operating in the range 233° to 338° K. In no case did the suspension fail with these flight-quality mirrors.

The accelerated life test involved torquing 12 preloaded bars at a frequency of 60 hertz, for a minimum of  $10^9$  cycles of scan or to failure, whichever occurred first. Three of the bars were torqued through 0.524 radian and the remainder through 0.436 radian, simulating the actual mirror operation. Ten of the bars were operated over  $2.5 \times 10^9$  cycles and the other two were operated over  $1.9 \times 10^9$  cycles before the test was voluntarily terminated with no failures. The discrepancy in cycles is caused by a test-apparatus problem that resulted in the failure of two bars. The results of this test are indicative that, if the design torsional stress is kept below  $2.11 \times 10^3 \text{ kg/cm}^2$ , there will be no fatigue failure caused by overstressing.

## ENCODER-SYSTEM DESIGN AND OPERATION

The optical angle encoder system was unique in that the nature of the application and the limitations imposed by the space and weight requirements called for complete integration of the encoder with the basic mirror assembly design. A schematic of the encoder system is shown in figure 5(a). The light from a miniature lamp is divided into two beams by the optics contained in the illuminator assembly. One beam illuminates the encoder reticle with collimated light and the other beam is focused into a bright line at the center reference reticle. These reticles are printed photographically on the reticle plate which is fastened rigidly to the mirror.

The encoder reticle is made up of a series of evenly spaced lines that radiate from the mirror axis. This pattern is imaged onto a similar pattern at the fixed reticle by the image-transfer optics. Behind the fixed reticle, four silicon detectors form a quadrature array that has two output channels. If there are  $n$  lines in  $2\pi$  radians on the encoder reticle, the fixed reticle contains  $n + 1$  lines. The fixed reticle pattern is skewed slightly with respect to the encoder pattern in order to generate Moire' fringes (at the detectors) as the mirror moves. The fringe width is adjusted to the width of one detector and the detectors are wired back-to-back in alternate pairs. The result of this arrangement is the same as having an encoder with full disks of  $n$  and  $n + 1$  lines and detectors at  $\frac{\pi}{2}$ ,  $\pi$ ,  $\frac{3\pi}{2}$ , and  $2\pi$  radians.

The A channel is connected to the detectors corresponding to the  $\pi$  and  $2\pi$  points, and the B channel is connected to the other two detectors. Each pair of detectors produces a sinusoidal signal, the period of which corresponds to 0.698 milliradian of scan angle, with a  $\frac{\pi}{2}$  radian phase difference between them. The direct-current component of the signals is eliminated by the back-to-back wiring arrangement. These signals enter the encoder logic circuit where the B signal is added to and subtracted from the A signal to produce sum and difference signals that are  $\frac{\pi}{4}$  and  $\frac{3\pi}{4}$  radians out of phase with A (fig. 4(b)). The four signals A, B, A + B, and A - B are combined logically to produce data pulses every  $\frac{\pi}{4}$  radian within each period. A factor of 8 subdivision is achieved, thereby increasing the encoder resolution to 87 microradians.

The center reference reticle appears as two rows of arc segments, alternately clear and opaque about the center lines (fig. 5(a)). The pattern illumination is projected through a narrow slit and falls on two silicon detectors located behind each row. These detectors are wired back-to-back to eliminate the direct-current component. As the mirror moves through its center position the signal from the detectors reverses polarity. Then, this signal is combined logically with one of the encoder pulses to obtain a center reference data pulse that is accurate to within 87 microradians of the center of the mirror scan.

A considerable amount of encoder testing has been performed to demonstrate the adequacy of the design. The glass reticle plate, mounted in the hub, has been shock tested to the 100-g level. The complete working assembly has been temperature cycled without any loss in performance, and the accuracy has been measured over 0.35 radian of scan angle and was indicative that each data pulse was in its true location to within 17.5 microradians.

### CONCLUDING REMARKS

The feasibility of constructing a flight-qualified encoded scanning mirror based on the torsional-pendulum concept has been shown. In all respects, the environmental and operational requirements have been met or exceeded by the application of valid engineering analysis to the mirror suspension and encoder system and the development of special fabrication techniques that ensure reliable torsion-bar performance. The latter represents the most important achievement in actually realizing a mirror of this type.

Since the development of the flight-qualified torsion bar and mirror assembly, several new designs that use the same basic concepts have been created to satisfy other configuration requirements that involve differences in frequency, scan angle, and moment of inertia. All of these new designs have been analyzable along the lines outlined here, with the predicted results achieved during manufacture and test.

TABLE I. - MECHANICAL PROPERTIES OF 0.533-MILLIMETER-DIAMETER TORSION-BAR-GRADE ELGILOY WIRE

Property	Specimen <sup>a</sup>	
	As received	Heat treated <sup>b</sup>
Ultimate tensile strength, $\text{kg/cm}^2 \times 10^3$	17.08	18.77
Yield strength, 0.2-percent offset, $\text{kg/cm}^2 \times 10^3$	13.99	18.56
Elongation, percent	2	1.27
Proportional limit, $\text{kg/cm}^2 \times 10^3$	5.455	11.998
Elastic modulus, $\text{kg/cm}^2 \times 10^3$	2066.8	2087.9
Hardness, $R_c$	39	45
Ultimate torsional shear strength, $\text{kg/cm}^2 \times 10^3$	14.20	16.24
Torsional shear yield strength, $\text{kg/cm}^2 \times 10^3$	8.29	12.44
Torsional shear proportional limit, $\text{kg/cm}^2 \times 10^3$	4.22	9.07
Shear modulus, $\text{kg/cm}^2 \times 10^3$	773.3	885.8

<sup>a</sup>Test specimens conformed to one active section of the torsion bar; specimens were not electropolished; gage length = 3.05 cm.

<sup>b</sup>Conformed to manufacturing specifications.

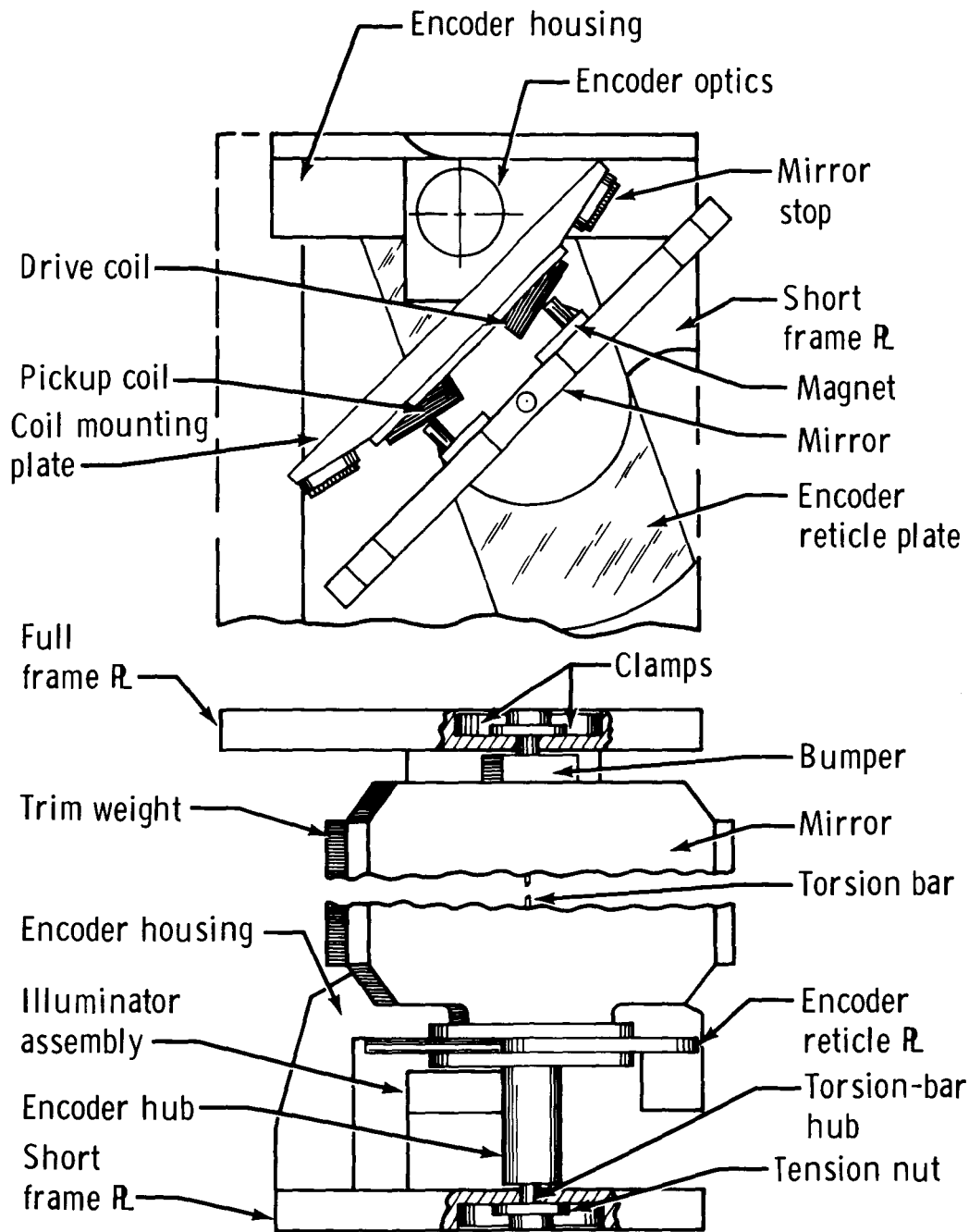


Figure 1. - Encoded scanning mirror configuration.

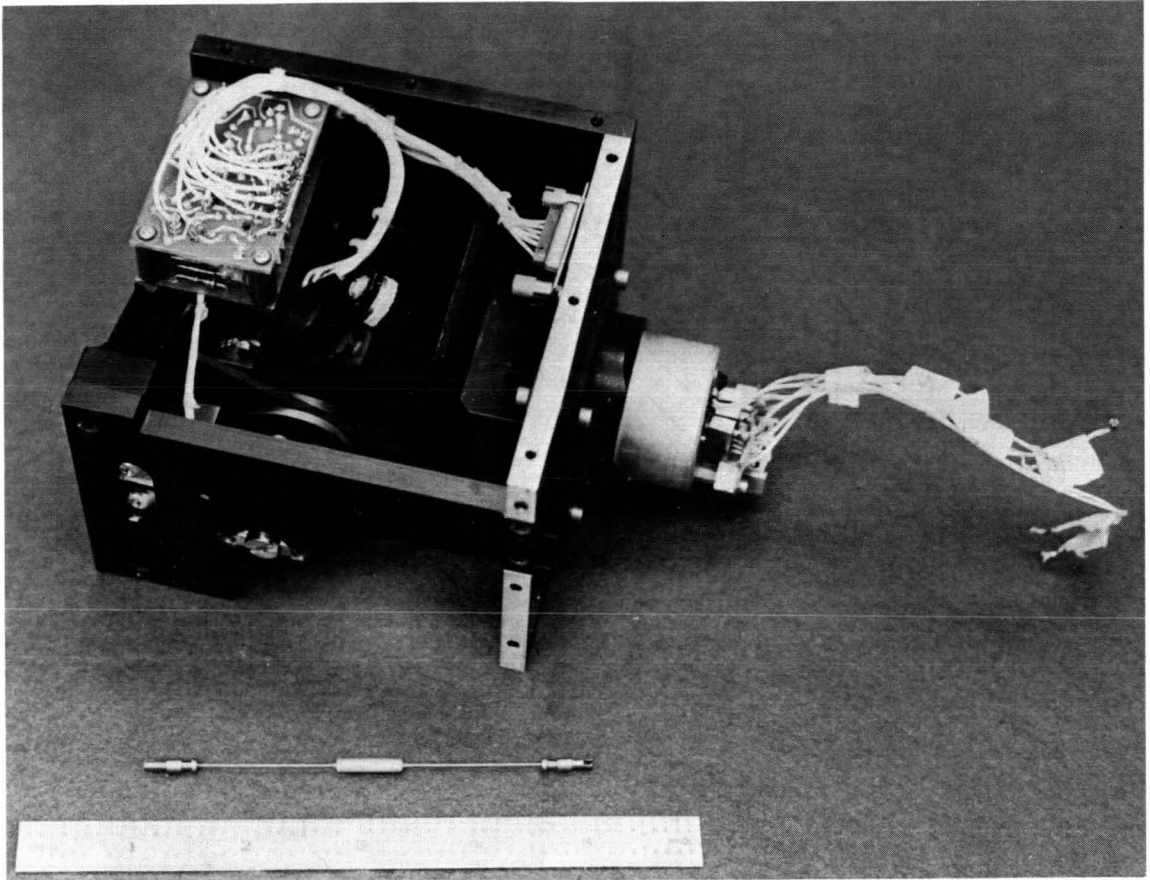
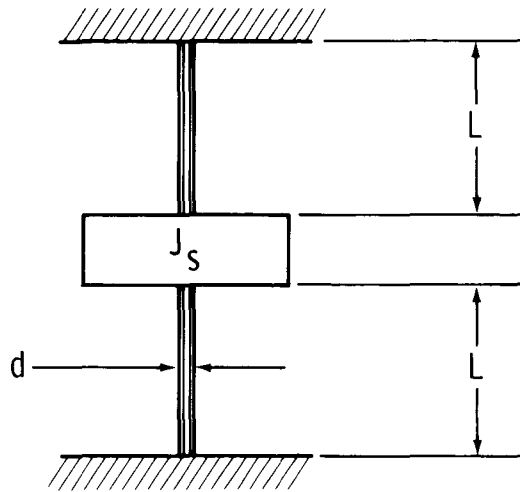
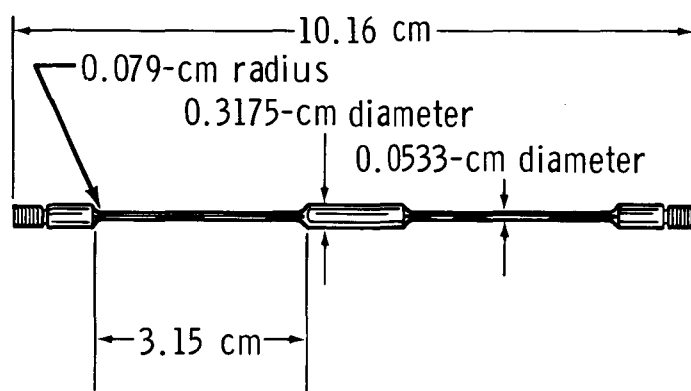


Figure 2. - Encoded scanning mirror assembly and torsion bar.



(a) Torsional-pendulum model for suspended mirror.



(b) Final torsion-bar configuration.

Figure 3. - Torsional-pendulum model and torsion-bar configuration for suspended mirror.

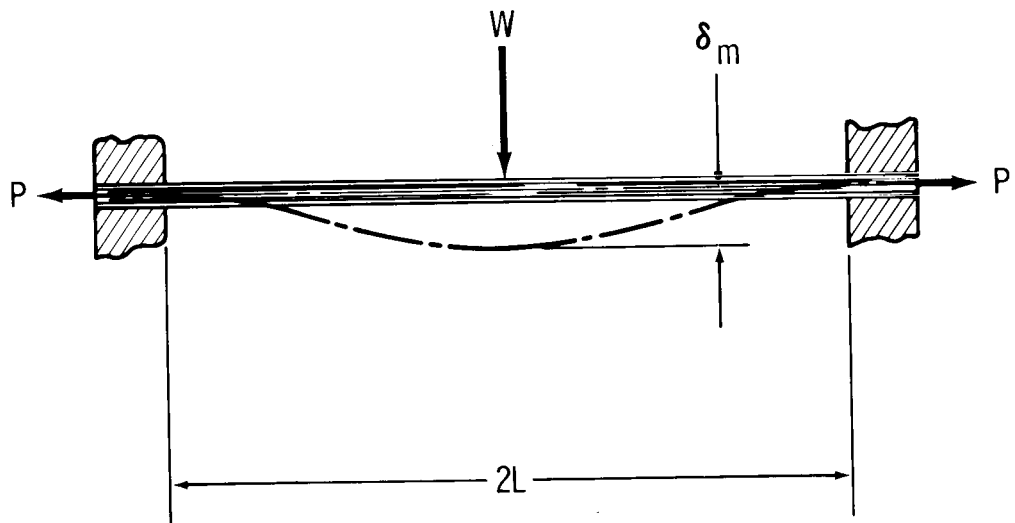
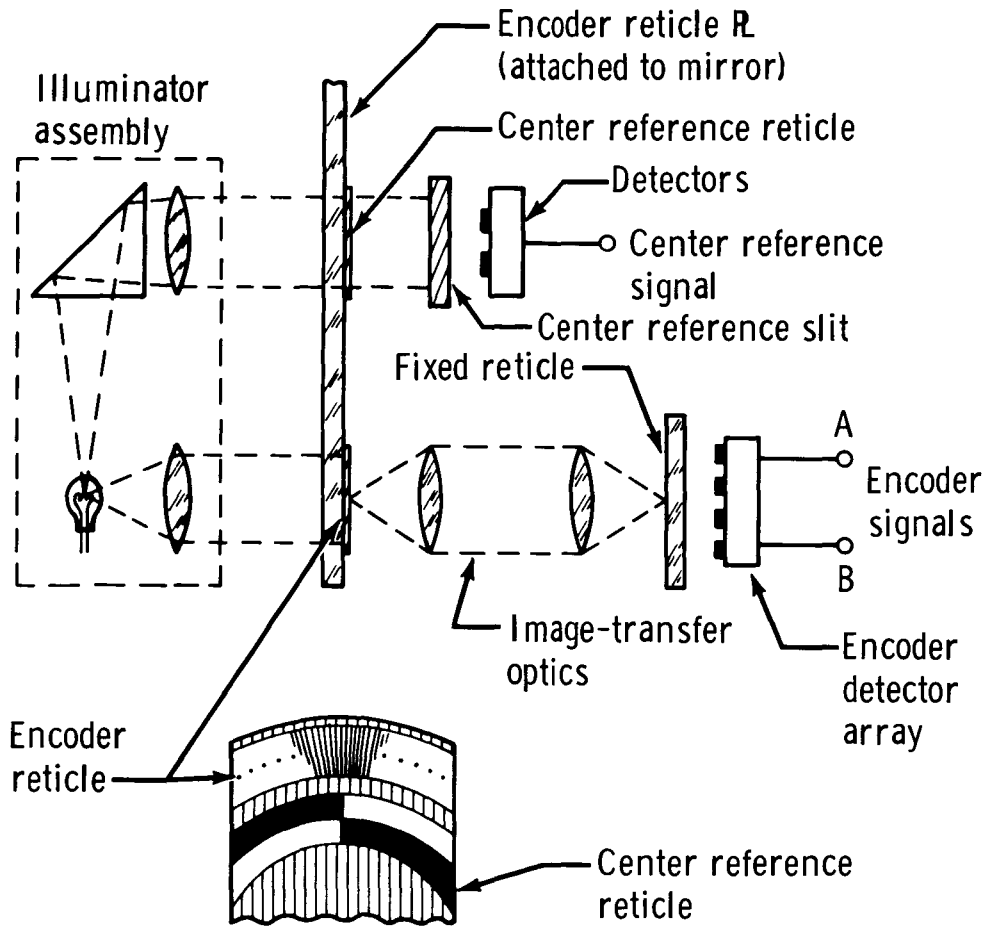
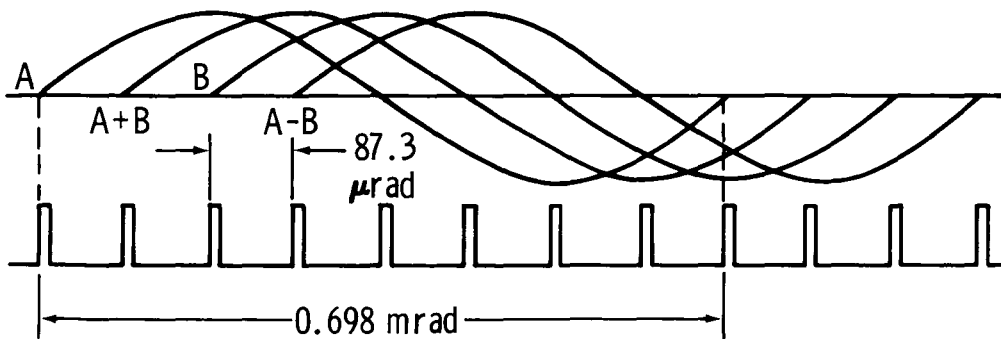


Figure 4. - Analytical model of torsion bar for stress and deflection calculations.



(a) Encoder system.



(b) Encoder-pulse formation.

Figure 5. - Optical-angle encoder system and pulse formation.

**Page intentionally left blank**

## MANIPULATOR TECHNOLOGY FOR THE SPACE SHUTTLE

By E. Glenn Burroughs\*

### ABSTRACT

A shuttle-attached manipulator is currently proposed as the payload-handling device for the space shuttle. Basic requirements for the manipulator involve length, force, compliance, and control. In this report, approaches for studying control methods are presented and simulation methods are discussed. Basic details about the two earth-based manipulators selected for simulation experiments are related to the test methods. Preliminary data from one test are shown as an example of the direction of the testing. A computer-generated simulation is explained, and the relationship of the three simulations to the design problems is discussed.

### INTRODUCTION

The orbital delivery system for space flight in the future will be the space shuttle. The current design for the shuttle orbiter vehicle specifies a payload bay having dimensions of 4.57 by 18.29 meters (15 by 60 feet) and having provisions for handling payloads. The payloads will have a wide variety of sizes, weights, and shapes. Examples of the handling functions to be performed are deployment, capture and retrieval, and stowage of the payloads. The various payloads may be handled either by individual manipulative devices, each designed to perform simple functions, or by a general-purpose manipulator designed to span the range of handling functions. In this report, a preliminary design for a shuttle-attached manipulator (SAM), which is a general-purpose manipulator, is described.

No manipulators have been used in space, except for such simple devices as the Surveyor surface-sampler scoop. However, the technology of earth-based manipulators provides an adequate base from which to design the SAM. Significant aspects of the SAM design deviate from earth-based manipulator designs; thus, a logical program to extend the technological base toward the design of the SAM is necessary. The salient parts of this program and the reasoning used in the extension of the technology are discussed in this report.

---

\*NASA Manned Spacecraft Center, Houston, Tex.

## DESIGN REQUIREMENTS

A conceptual drawing of a SAM and its installation in a shuttle is shown in figure 1. The shuttle payloads identified in current mission models can be as small as a few cubic feet and weigh as little as several hundred pounds or can be as large as 4.57 meters (15 feet) in diameter and 18.29 meters (60 feet) in length and weigh as much as 29 478 kilograms (65 000 pounds). The desirability of grasping a heavy module near its center of gravity and the need to grab a small satellite located toward the aft end of the payload bay establish a minimum length of approximately 9.14 meters (30 feet) for the SAM. Apparently, there is no requirement for the length to exceed 18.29 meters (60 feet). Current plans are for a SAM to be 9.14 to 12.19 meters (30 to 40 feet) in length because, with a SAM of this length, 90 percent of all the payloads in the traffic model located anywhere in the payload bay can be reached, and 100 percent of the payloads can be reached if the smaller satellites are not located far aft. The shorter lengths are lighter and easier to control. The degrees of freedom of the SAM are distributed so that they correspond anthropomorphically to a shoulder, elbow, and wrist.

### Tip Force

The minimum tip force required for the SAM is primarily a function of the arm length, the payload weight, and the ability of the operator and his control system to control acceleration and velocity safely. The minimum tip force of 44.48 newtons (10 pounds), used with a maximum length arm, is required to provide sufficient energy to complete many operations within a reasonable time. The energy also is required to stop the heavy payloads at residual closing velocities. Arms shorter than the maximum length require larger force because the available stopping and starting distances decrease, and the accelerations must be increased to supply equivalent energy. The maximum useful force is more difficult to establish. Because the heaviest payload imposes design constraints on minimum force, the selection of a force level only marginally greater than the minimum will result in a low-weight system. An upper limit of 444.82 newtons (100 pounds) was established, based on combinations of the heaviest payloads and the shortest arms.

### Compliance

Compliance in the SAM is defined as the amount of tip deflection per unit of tip force. Compliance is caused by the flexure of the arm structure, the elastic deflection and tolerances within the joints, and the electronic response of the servocontrols. As in other orbiter systems, the weight of the SAM must be minimized. The values of stiffness (the reciprocal of compliance) postulated in preliminary designs are sufficiently high that the design of the arm structure is controlled by stiffness instead of by stress. Consequently, it would be desirable to allow more compliance (less stiffness), use higher stress levels, and reduce weight. Just as too little compliance increases weight, excess compliance decreases safety and lessens positioning accuracy. The compliance value of 0.06 cm/N (0.1 in/lb) was used in the preliminary designs because it would produce conservatively high weight and better-than-adequate positioning. Recent experiments that will be described have produced data indicating that more compliance is tolerable.

Currently, electric actuators are planned for use in the SAM. Conditioned electric power will be available on the orbiter, whereas hydraulic power sources probably will not be active during payload-handling periods. Electric motors also will be more easily space qualified than hydraulics because of contamination restrictions.

### Control System

The effect of man in the servocontrol loop is difficult to assess, particularly because partial computer control probably will be used. In preliminary designs, two desirable modes of computer operation have been identified. In the first mode, active when man is in primary control, system status is monitored by computer, and collision avoidance is ensured by the computation of the position of the arm with respect to all fixed objects. Automatic collision avoidance is particularly desirable with respect to the position of the elbow. Requiring the operator to be constantly aware of the elbow and wrist, points that are at least 4.57 meters (15 feet) apart, reduces his capability to operate the secondary television and information systems while also operating the arm. In the second computer mode, the computer operates the arm and the man is in monitor status. This mode will be used only in situations in which all bodies are at known locations. The reason for using full computer control is to make precise operation of a controller for a long timespan unnecessary. Examples of operations in which the second mode is used are deploying the arm from the stowed position, stowing the arm, and translating a payload between positions near (but not in contact with) other bodies. These operations do not need precise position control from a safety standpoint but do require careful force control to minimize operation times. The operator can prepare the peripheral systems for the next operation to be completed while the computer is in control.

The type of hand controller to be used by the operator for his real-time control is being studied. A variety of types of controllers probably would be suitable. Examples of candidate controllers are hand controllers, joysticks, buttons, and master-slave devices. The current work is to determine which controller offers the best combination of safety, reliability, utility, and weight penalty.

### SIMULATION METHODS

The design requirements for reach and force were developed by means of a simple analysis of the payload-handling functions and dynamics. The determination of tolerable levels of compliance and optimal computer and controller mechanization is not susceptible to analysis because man adds an active part to the control equations. Consequently, empirical methods are being used, and the obvious approach is to build and test a SAM. The force levels previously mentioned were in a zero-g environment, but a limited study has indicated that simulating zero-g performance in a one-g field for a SAM is not practical early in the design process.

A review of manipulator technology reveals that there is no manipulator system currently using a combination of reach, force, compliance, and complex control that even approximates the SAM. The remaining approach is to find systems that approximate some characteristics of the SAM and to use appropriate testing to extrapolate their performance. Thus, the performance of the SAM is approximated by a series of

simulations using current systems with the man in operational control. This approach is relatively economical and allows the performance of the SAM to be demonstrated by experiment instead of by analysis very early in the design process.

## Manipulative Systems

A wide variety of manipulative systems are available for experiment. The systems range from such large but nonadvanced devices as derricks to extremely complex, anthropomorphic systems used in materials handling. The force level of the SAM appears to offer no difficult problems, and the length per se is just a design detail. The experimentation must facilitate information acquisition regarding compliance and control in a remotely controlled, dextrous system. The materials-handling devices that have great dexterity embody the most complicated and versatile control systems. Two manipulators, an E-2 and a CAM 1400, were good choices for study because of performance capability and availability.

The E-2 (fig. 2) is an anthropomorphic, bilateral, six-degree-of-freedom, master-slave, electric manipulator. The motions and distribution of the degrees of freedom of the E-2 arm are anthropomorphic. The controller (master) is a duplicate of the working arm (slave); operations are performed by moving the handle of the master through the motions and with the forces desired of the slave. Bilateral refers to the fact that force feedback generated at the master arm is equal to the working force of the slave arm. A useful test is possible with the E-2, even though the slave arm has approximately one-tenth the effective reach of the SAM. The purpose of the test is to demonstrate the ability of a man to control high-inertia dynamics by the application of small forces and to quantify his response to different compliances. The massive body to be controlled with 26.69 newtons (6 pounds) of available force is a 181.44-kilogram (400 pound) weight suspended from a 6.71-meter (22 foot) pendulum (fig. 2). The weight swings in the plane containing the slave arm and is released from a position 0.61 meters (2 feet) from rest on the far side from the arm. The slave arm captures the weight at the point of closest approach and brings it to a rest as soon as possible. A potentiometer used as a position transducer measures the lateral displacement of the weight from rest for recording on an oscillograph. In figure 3, the data record of the position transducer for one test run of one operator is shown. Different compliances are introduced by making adjustments to the servoamplifiers between runs. The operator reacts essentially the same to servocompliance as to structural compliance of the SAM. Four different compliance values were used. Each of the nine operators made practice runs before making test runs. The data point for each combination of compliance and operator is the average of several consistent runs. In figure 4, the overall average for all operators at each compliance is shown. The significance of the curve is that it shows that operators can adapt to almost any compliance of interest to the SAM design and that only small performance changes result.

The CAM 1400 is an anthropomorphic, bilateral, five-degree-of-freedom, master-slave, electrohydraulic manipulator (fig. 5). The CAM is not bilateral master-slave in all five degrees of freedom. The three degrees of freedom, two at the shoulder and one at the elbow, that translate the end point of the arm are controlled by a master arm that kinematically resembles the slave and that has 22.24 newtons (5 pounds) of force feedback. The remaining degrees of freedom, which position the wrist motions, are controlled by one constant-rate switch and one position potentiometer. A more

significant difference between the E-2 and the CAM is that the E-2 has an effective reach of 0.91 meter (3 feet) and the CAM has an effective reach of 6.71 meters (22 feet). The CAM will be used in conjunction with a 5.49- by 10.67-meter (18 by 35 foot) air-bearing surface, air-bearing freebodies, and television systems to simulate all major handling functions of the SAM. Examples of tests are tracking and grasping a moving small satellite, payload stowage and deployment, and payload inspection. In tests presently being conducted, the CAM moves a 3175.1-kilogram (7000 pound) weight mounted on air bearings through a maze in order to evaluate positioning capability and the effects of compliance changes. Compliance will be varied as it was in the E-2 tests, and performance data will be taken. Other tests will be used to evaluate television systems and interactions between direct vision and television. The combination of buttons, potentiometers, and master-slave control methods also will give early indication of operator preference of control types.

### Computer-Generated Scene

At the NASA Manned Spacecraft Center, a computer-generated scene, which is a method of simulation not incorporating an actual manipulator, is being used to resolve problems involving control methods. The scene is composed of points, lines, and colors. A typical scene, shown in figure 6, consists of the cargo bay area of the orbiter vehicle, the SAM, and a large payload module. The computer program can handle rigid-body dynamics for the bodies and is capable of imposing such restrictions as rate limiting. The scene is displayed on a television screen. Force feedback is not available currently. A variety of controllers can be used because only programming changes are needed to interface the physical controller with the simulation. Controllers covering the range from a button box to a master arm without feedback will be used.

### CONCLUDING REMARKS

The technology base necessary for the design of the SAM is being derived from simulations using earth-based manipulator equipment and computer simulation. These simulations are being used to give operators the subjective feel of a space manipulator and to generate design data. Two hardware simulations, using the E-2 and the CAM, and the computer simulation form an experiment program that covers the characteristics of the SAM that need definition early. The computer scene generator will provide control-system definition, and the E-2 experiments have provided needed data on compliance and man-control interaction. The CAM experiments will allow exploration of compliance, man-control interactions, vision-control interactions, and even such procedures and limited hardware work as evaluation of arm terminal devices. By the use of this program early in the SAM design, the gap between the technology of earth-based manipulators and the technology needed for the SAM can be bridged efficiently.

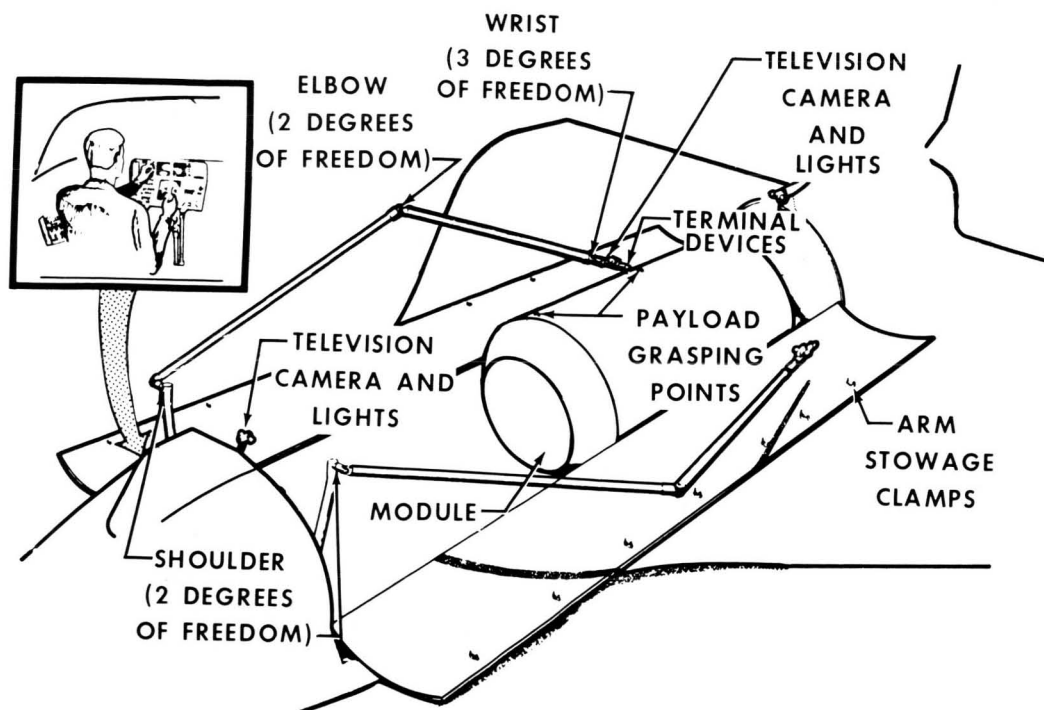


Figure 1. - The SAM installation.

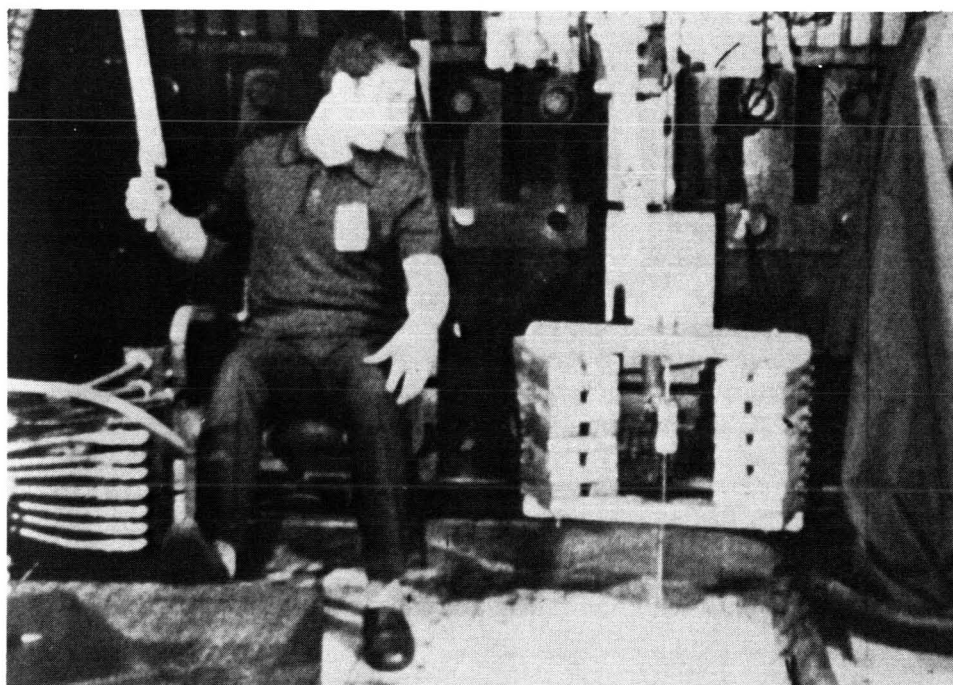


Figure 2. - The pendulum test setup.

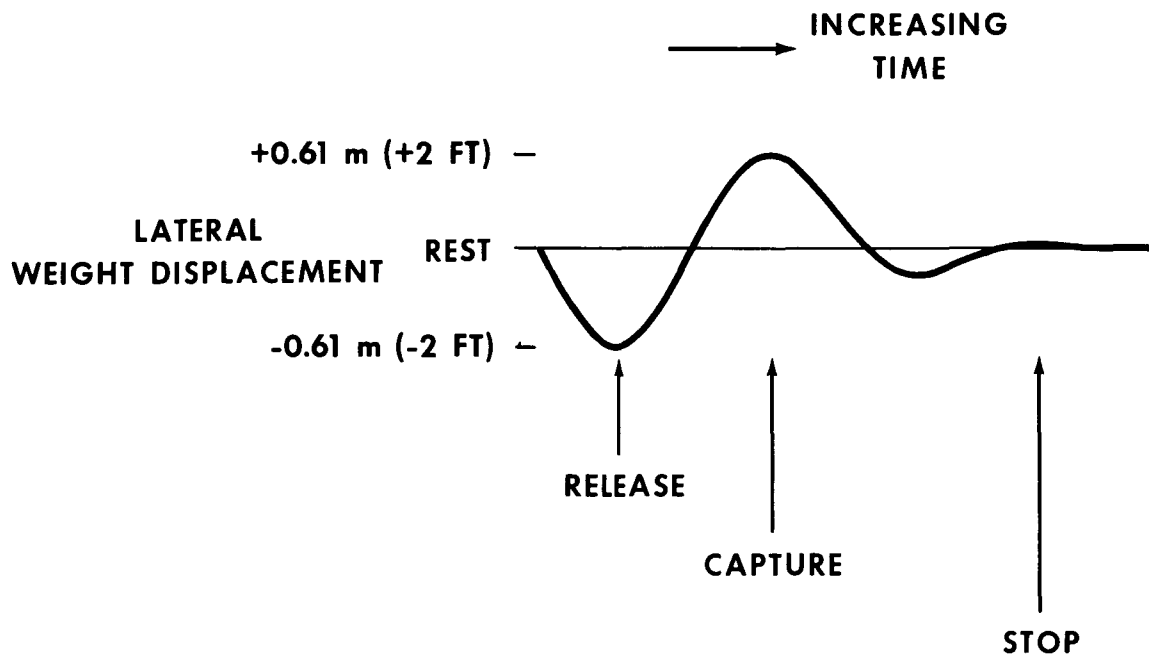


Figure 3. - Sample test data.

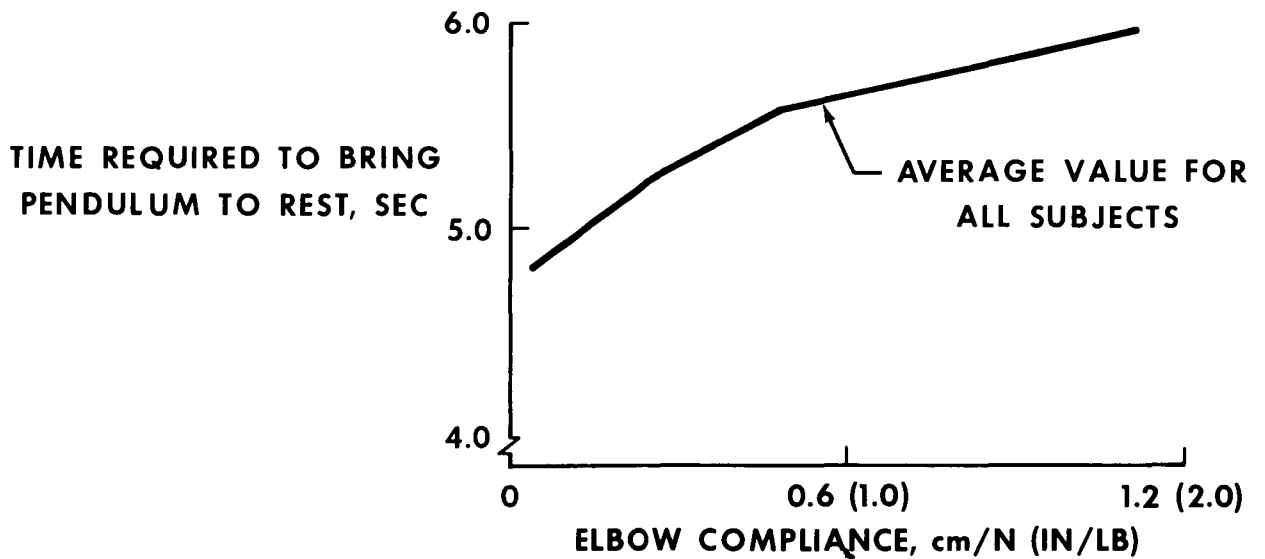


Figure 4. - The effect of compliance on performance.

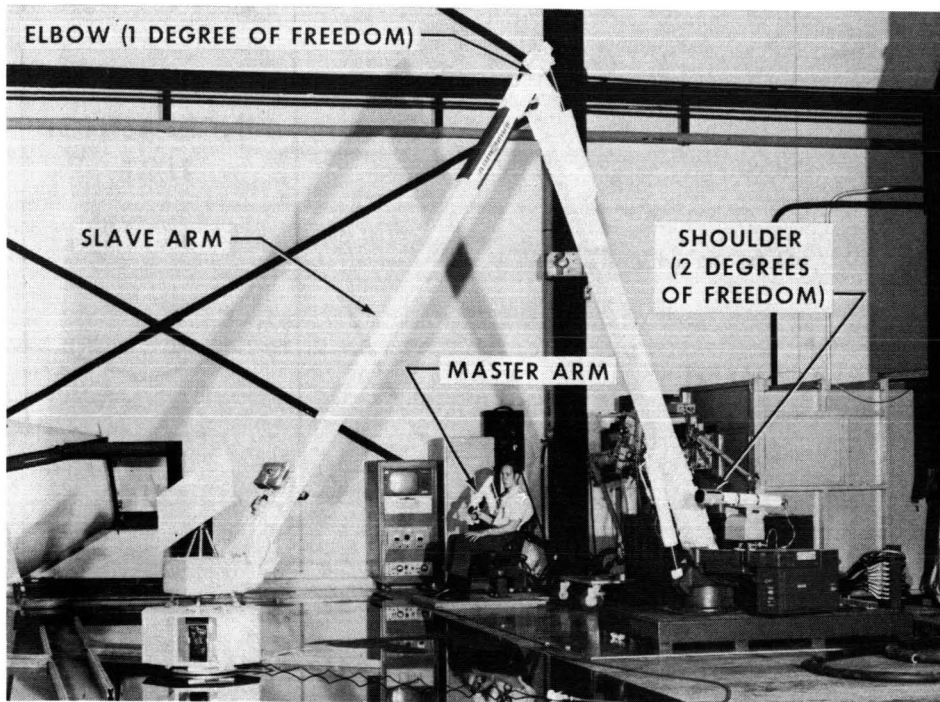


Figure 5. - The CAM 1400.

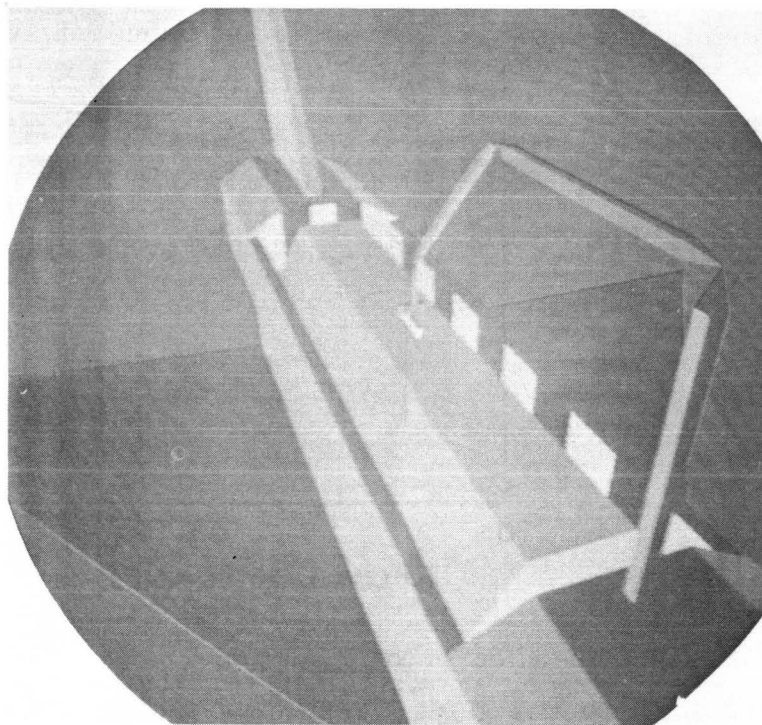


Figure 6. - The computer-generated scene.

73N18890

## A FLYING EJECTION SEAT

By R. H. Hollrock\* and J. J. Barzda\*

### ABSTRACT

To increase aircrewmembers' chances for safe rescue in combat zones, the armed forces are investigating advanced escape and rescue concepts that will provide independent flight after ejection and thus reduce the risk of capture. One of the candidate concepts is discussed in this paper; namely, a stowable autogyro that serves as the crewman's seat during normal operations and automatically converts to a flight vehicle after ejection. Discussed are (1) the mechanism subsystems that the concept embodies to meet the weight and cockpit-packaging constraints and (2) tests that demonstrated the technical feasibility of the stowage, deployment, and flight operation of the rotor lift system.

### INTRODUCTION

The United States Navy and Air Force envision an advanced aircrew-escape/rescue capability (AERCAB) that will provide independent flight after ejection, provide the crewman with a means of flight to areas better controlled by friendly forces, and permit rescue in safer, more accessible sites than is often the case at present. Thus, an aircrewman's chances for safe rescue will be increased, particularly in combat zones. The concept is proposed initially for fighter/attack aircraft.

Primary performance goals for AERCAB are shown in figure 1. The cruise altitude is just above the range of small-arms fire. The AERCAB design objectives also specify that (1) current escape capabilities/envelopes will not be compromised, (2) deployment and conversion will be fully automatic, (3) the system must be capable of operation in adverse weather, and (4) retrofit into A-7 and F-4 aircraft is highly desirable.

Four proposed concepts are being demonstrated and evaluated for eventual selection as the operational system. One concept is a parawing system propelled by a turbofan engine installed on the back of the ejection seat. Fuel cells are located on both sides of the seat. The parawing is deployed and flown with the crewman in a face-down position. In the second concept, a "Princeton sailing," a deployable fixed wing, is used to provide lift. The craft contains a turbofan engine and a telescoping tail boom.

---

\*Kaman Aerospace Corporation, Bloomfield, Conn.

Fuel is stored in bladders inside the hollow leading-edge wing spars. The wings and tail surfaces are deployed by parachute at or near flight velocities. These two concepts are depicted in figure 2. In a third concept, a rigid, deployable metal wing is used. Submitted after other concepts had begun to be tested, the rigid wing is still in early development. The fourth candidate concept is the Stowable Aircrew Vehicle Escape ROTOSEAT (SAVER), the primary subject of this paper. ROTOSEAT and SAVER are registered for exclusive use by Kaman Aerospace Corporation.

## SAVER AERCAB

### System Description

The SAVER is a compact autogyro that folds and stows into the aircraft cockpit to serve as the crewman's seat during normal operations. In an emergency, the SAVER ejects with the crewman and converts to the flight-vehicle configuration. The configurations are depicted in figure 3, showing the full-scale wind-tunnel model. At the end of the flight, the crewman is separated from the SAVER and parachutes to the ground. All events from ejection through conversion and autogyro flight to the final parachute descent are automatic. The crewman only needs to pull the ejection-initiation control. In flight, he may override the automatic flight control and programmed events if he desires. The SAVER includes an alternate parachute mode of escape for low altitudes and speeds, retaining current escape envelopes. The parachute-mode functions are also performed automatically. The applicable escape mode is determined and initiated by means of an onboard selector. The SAVER is designed for retrofit in the A-7 and F-4 aircraft; it fits between the cockpit control consoles and mounts on the existing seat-mounting bulkheads. The major structure of the aircraft is unaffected.

The SAVER provides 30 minutes of flight at a velocity of 51.4 m/sec at an altitude of 914 meters, just above the range of small-arms fire. The service ceiling is approximately 3000 meters. The maximum rate of climb is almost 5 m/sec. Propulsive power is provided by a small turbofan engine with a sea-level thrust rating of 1280 newtons.

### Deployment and Operation

The deployment/conversion sequences from ejection through rotor deployment into autogyro flight are shown in figure 4. The crewman pulls the face curtain or control to initiate ejection. Events are subsequently automatic. Current ejection-seat techniques, escape dynamics and velocities, and programming are applied in the ejection phase. After ejection, when the aircraft structure has been cleared safely, the extraction drogue parachute pulls the stowed blades aft and upwards to the trail position, rotates the seat into deployment alignment, and serves as the initial drogue parachute and stabilizer. Rotor-hub- and blade-tip-restraint bolts are then severed with squib cutters, and the deployment springs position the hub and blades into position for spinup. Aerodynamic torque about the shaft axis spins up the rotor assembly, and centrifugal force extends the telescoped blades to full span. The drogue parachute is jettisoned after full spinup. Conversion to the autogyro mode is initiated after deceleration to

near flight velocity. The rotor, engine, and tail surfaces are actuated to flight positions. The SAVER then makes a transition into powered autogyro flight after inflight startup of the engine and automatic flight-control guidance.

## Design

A major criterion in the preliminary design of the SAVER was that the folded vehicle fit into a fighter cockpit. In effect, the SAVER was designed in reverse order; that is, the packaged outline having been determined, unique mechanisms that folded and fitted within the envelope had to be devised and embodied into the SAVER to achieve the specified packaging, deployment, control, and flight goals. The system also is designed to rescue dazed, injured, and nonpilot crewmen in fair or adverse weather conditions. Rearward vision in the parent aircraft was to be minimally compromised.

The most unique subsystem mechanism is the rotor installation. When stowed, the installation forms a compact package 1.22 meters long and 0.2 meter wide and fits at the rear of the seat. When deployed, it forms a rotor 4.27 meters in diameter. To convert from a stowed package to a spinning rotor, special features that had to be included were the following.

1. Two-panel telescoping blades with integral blade-extension stops
2. A stretchable, energy-absorbing cable to control the stop-impact loads during blade extension
3. Double-hinged blade retention for spinning up the rotor, governing the speed of rotation, and folding the blade
4. A rotor spinup mechanism that, when severed by pyrotechnic cutters, set the hub-geometry for aerodynamic spinup of the rotor
5. A drogue parachute to extract and orient the rotor package through rotor spin-up, with a provision for jettisoning the parachute when the rotor attained operational speeds of rotation

The rotor-control system serves dual purposes. During the rotor-deployment phase, the system properly orients the rotor from behind the seat to the trailing decelerator position. After conversion to the autogyro mode, the control system becomes a direct rotor-tilt-control system, providing longitudinal and lateral tilt. The system may be operated both by the crewman and by an automatic flight-control system.

The automatic flight-control/navigation system positions the SAVER at flight altitude and flies it to a predetermined area without crewman input (in the event the crewman is injured or dazed or is a nonpilot). The system is programmed with the direction for return flight, and it heads and guides the vehicle in this direction; flies the SAVER upright in a safe, stable manner; and monitors terrain clearance. Control techniques and logic used in current autopilots, remotely piloted vehicles, droned helicopters, and unmanned spacecraft are utilized. The crewman may override automatic flight with a sidearm-formation stick if he so wishes.

Total-system compactness was achieved by integrating components and assigning dual functions where possible. The fins are stowed alongside the seat, take on the outline pattern of the seat panel, and are mounted on hinged booms, which also serve as the catapult/boost-rocket cases. Ejection guide rollers also are mounted on the boom tubes. A small horizontal stabilizer is mounted between the booms near the fins. The empennage is deployed into flight position by a pyrotechnic actuator.

The engine deployment is coupled with that of the tail. The propulsion engine, a small turbofan, is stowed behind the seat between the headrest and folded rotor. The turbofan design is based on current engine technology; for example, existing small gas turbines operating at SAVER-engine thrust-to-weight ratios, length-to-diameter ratios, and specific fuel consumptions. Inflight cartridge-impingement startup is planned.

The SAVER also includes a life-support system (in case of high-altitude ejection), survival gear, and a personnel-recovery parachute. The parachute, stowed in the headrest, is spread ballistically for fast action at low altitudes and speeds.

At the end of flight, the crewman is separated from the seat with a conventional lumbar inflatable bladder and descends with the parachute. To preclude subsequent flight into the descending crewman, the rotor blades are jettisoned with linear shaped charges near the root-end retention. Centrifugal force slings the blades clear of the crewman.

All functions throughout the ejection, rotor-deployment, conversion, and flight phases are programmed, timed, and initiated by a mode-selector/events programmer. A precision electroballistic sequencing and initiating system provides the control intelligence. If a malfunction occurs, sequencing diverts to the parachute mode of escape.

### Testing

Wind-tunnel and autogyro-mode flight tests with full-scale hardware have been performed to demonstrate technical feasibility. The wind-tunnel demonstrations were performed in September 1970 in the NASA Ames Research Center 12.2-by-24.4-meter facility with a full-scale SAVER preliminary-design-configuration model. The model was folded into the seat configuration and was designed to demonstrate the deployment/transition events. Successfully demonstrated in the tests were decelerator-mode rotor operation at speeds up to 93 m/sec; rotor extraction, spinup, and operation in seat wake at 82.5 m/sec; conversion from decelerator-mode to flight-mode configuration; and autogyro-mode operation at speeds up to 56 m/sec. Demonstration tests are shown in figure 5.

The model was then adapted to a powered, manned flight-test vehicle in the ground-takeoff/landing autogyro mode by the addition of landing gear, a propulsion system, manual flight control, and instrumentation. The autogyro-mode manned flights (fig. 6), completed in January 1972, were the first flight of a turbofan-powered autogyro and the first manned flight of a telescoping-blade rotor. Demonstrated in these flights were manned flight of the SAVER rotor, stable and controllable rotor and vehicle behavior, rotor lift capability 14 percent above design normality, flight of a trainer prototype, and adaptability of turbojet power to autogyro propulsion.

## CONCLUDING REMARKS

Aircrew-escape/rescue capability is being planned to increase the chances for the safe rescue of aircrewmembers by providing features that will reduce the risk of capture, facilitate location and rendezvous, reduce on-the-ground exposure time, and permit rescue in safer, more accessible areas.

The Stowable Aircrew Vehicle Escape ROTOSEAT autogyro aircrew-escape/rescue-capability candidate system meets the cockpit-stowage, aircraft-retrofit, and flight-performance requirements. Experimental demonstration tests have thus far indicated that this system is a viable and technically feasible approach. Inflight deployment, the planned next phase, will complete the military requirement for feasibility demonstration and evaluation.

## DISCUSSION

J. E. Price:

What is the minimum altitude at which the system will operate?

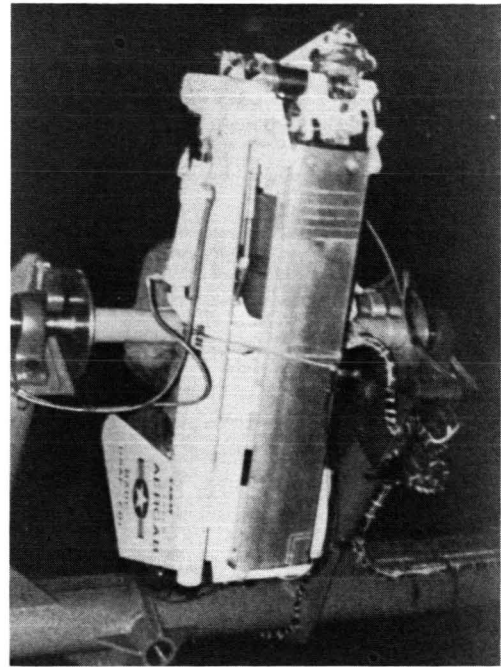
Barzda:

The SAVER is designed to convert to and operate in the AERCAB "flying ejection seat" mode when the ejection altitude is 1000 feet or more above the terrain. The "parachute mode" recovery will be initiated for ejections below the 1000-foot minimum altitude. The normal cruise altitude for the AERCAB is 3000 feet.

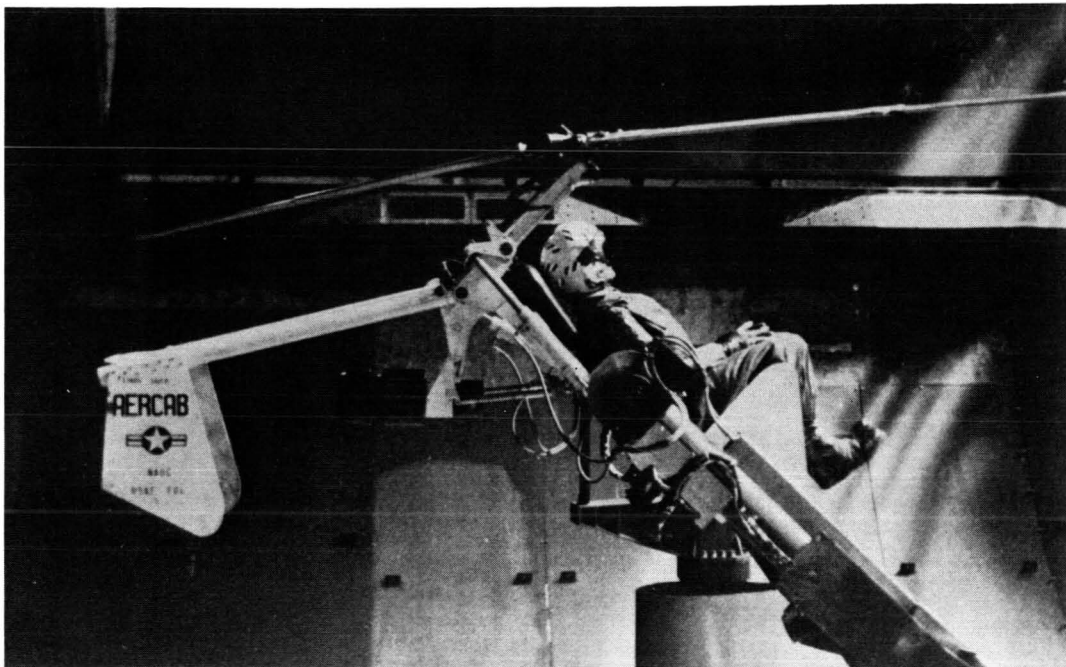




(a) Stowed-ejection-seat mode, front.

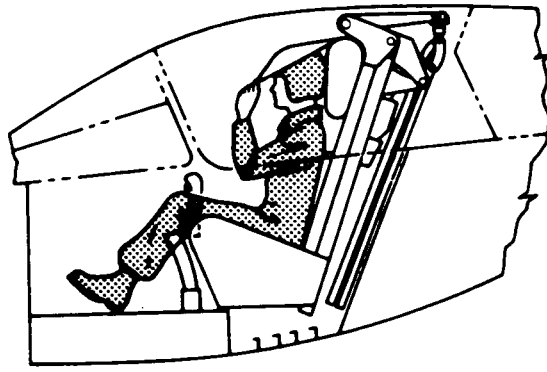


(b) Stowed-ejection-seat mode, rear.

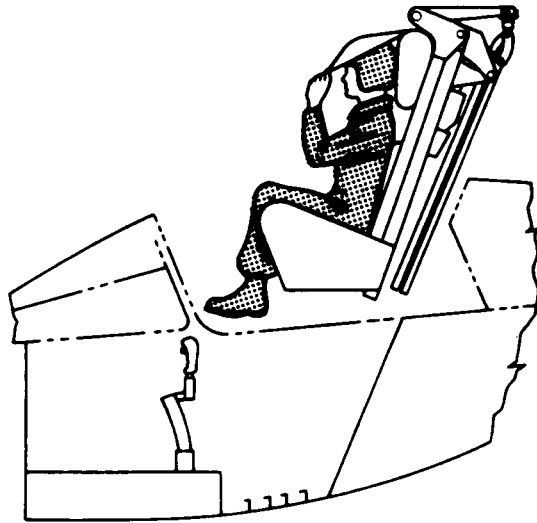


(c) Deployed-autogyro-flight mode.

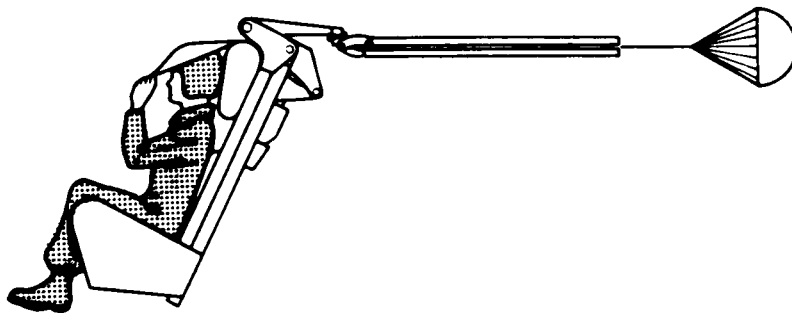
Figure 3. - The SAVER AERCAB.



(a) Initiation.

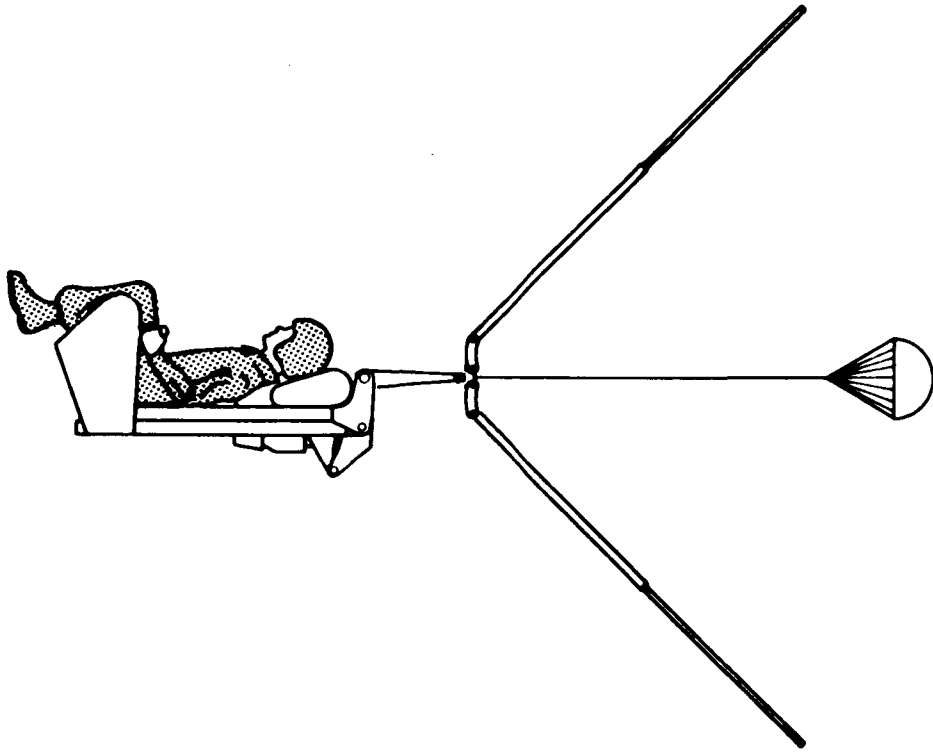


(b) Ejection.

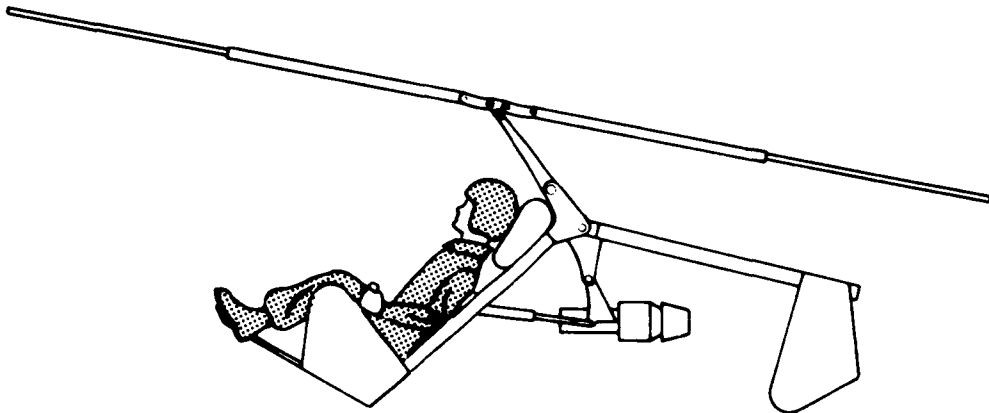


(c) Drogue-parachute deployment.

Figure 4. - The SAVER deployment sequence.

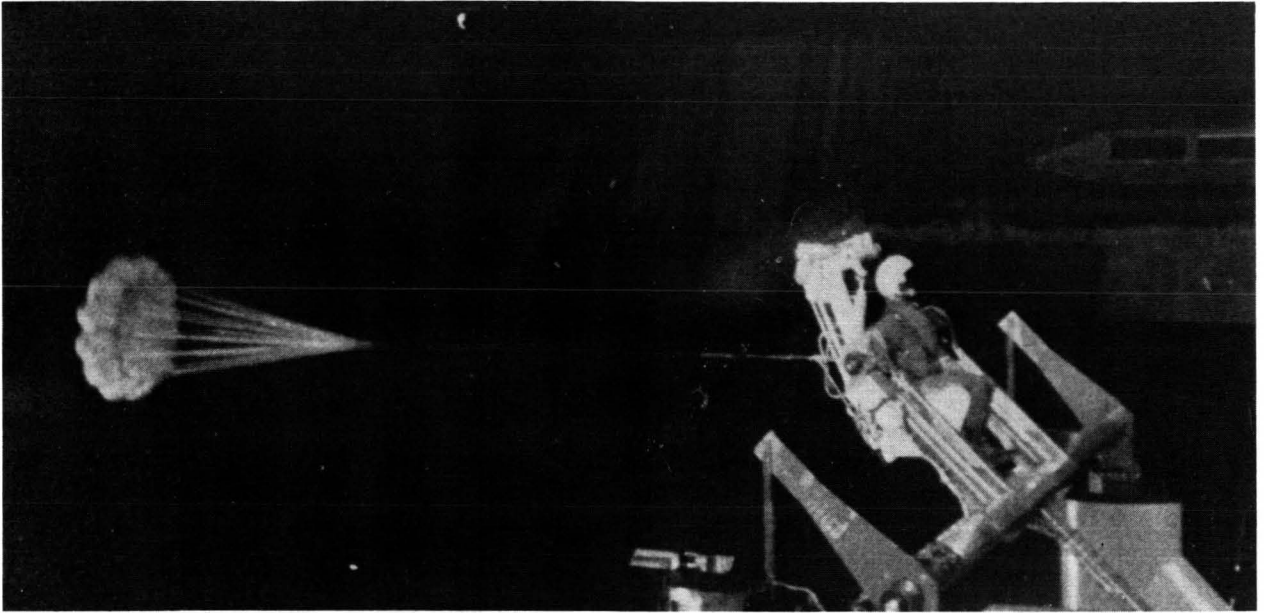


(d) Rotor deployment.

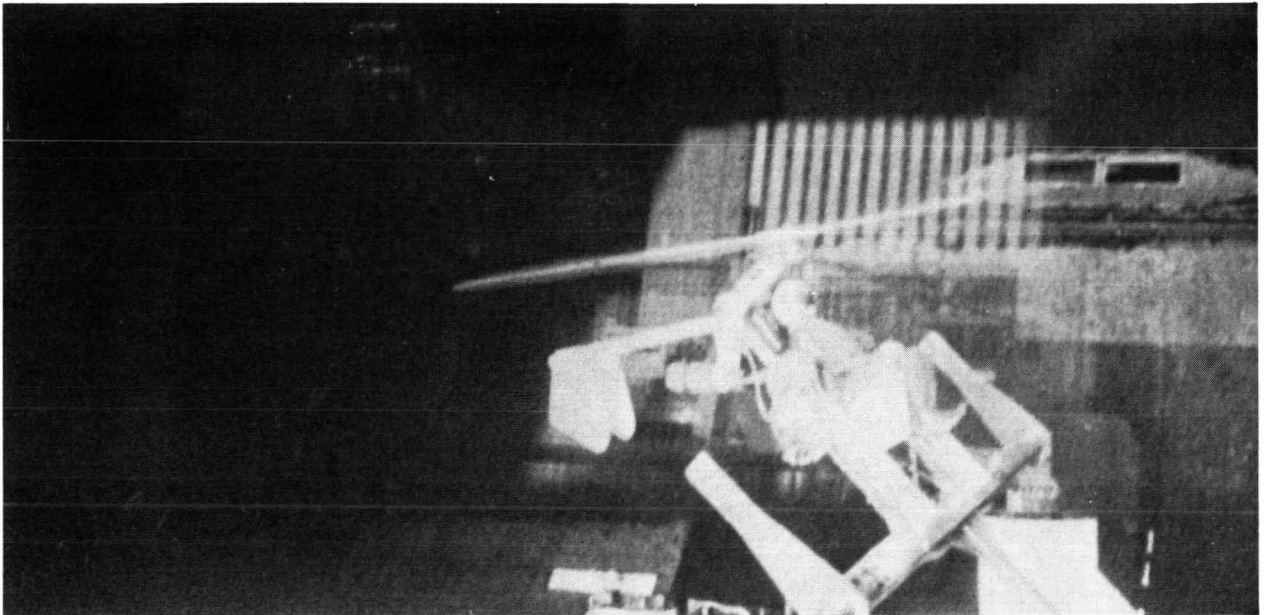


(e) Autogyro mode.

Figure 4. - Concluded.

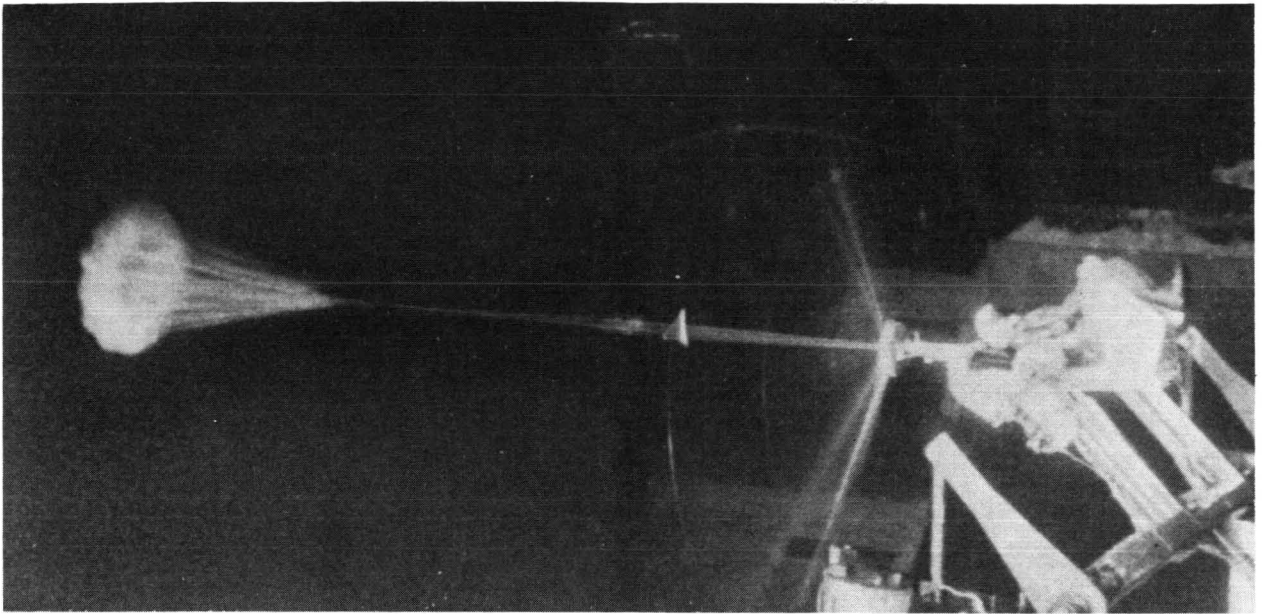


(a) Drogue-parachute deployment (82.5 m/sec).

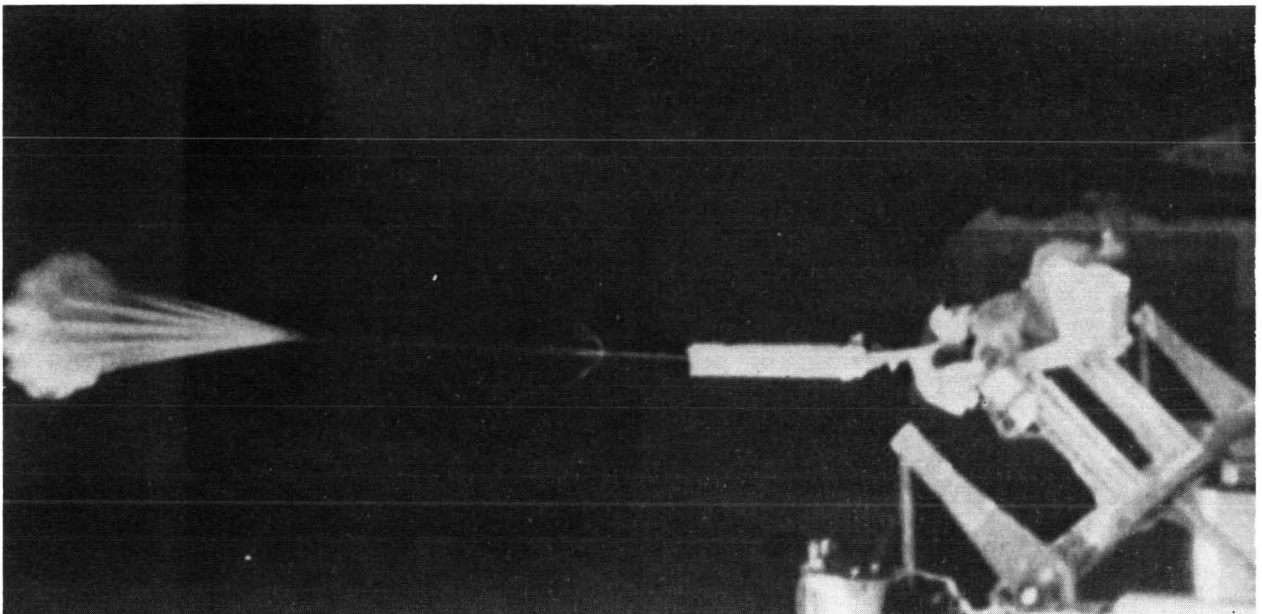


(b) Rotor extraction (82.5 m/sec).

Figure 5. - Full-scale-prototype feasibility demonstration of the SAVER.



(c) Rotor spinup (82.5 m/sec).



(d) Autogyro mode (56 m/sec).

Figure 5. - Concluded.



Figure 6. - Autogyro-mode manned flight of the SAVER.

A 928-M<sup>2</sup> (10 000 FT<sup>2</sup>) SOLAR ARRAY

By Dale E. Lindberg\*

## ABSTRACT

As the power requirements for space vehicles increases, the area of solar arrays that convert solar energy to usable electrical power increases. The requirements for a 928-m<sup>2</sup> (10 000 ft<sup>2</sup>) array, its design, and a full-scale demonstration of one quadrant (232 m<sup>2</sup> (2500 ft<sup>2</sup>)) deployed in a one-g field are described in this report.

## INTRODUCTION

Until the beginning of this program, all operational solar-array systems were designed in small sizes (the largest was 112 m<sup>2</sup> in area per vehicle) and were designed for low structural loadings (0.1-g level or less) in the deployed condition. The space station solar-array requirements were to design a deployable array of silicon solar cells 928 m<sup>2</sup> in area that was to be capable of articulation in two axes for sun tracking; the entire structure was to be packaged for deployment in the space shuttle cargo bay. The entire structure had to be retractable automatically into a 4.27-meter diameter by 15.25-meter length shuttle cargo envelope without recourse to astronaut extra-vehicular activity (EVA). Furthermore, high-on orbit loads had to be tolerated by the structure in the deployed condition because it was required that the entire space station rotate about a center displaced as much as 13.4 meters from the center of mass of the solar-array system, resulting in nonsymmetric gravity loadings that are an order of magnitude greater than those previously experienced in operational solar arrays.

After an evaluation of state-of-the-art solar-array and extendible-beam technology, design studies were conducted to evaluate several structural configurations, including calculation of weight penalties and assessment of system complexity. A two-boom system was selected that used an Astromast boom as a basic deployable structure. This boom and rigid truss members, which also functioned as ascent supporting members for the stowed solar array, were the main structural elements. A unique variable-tensioning system and an auxiliary guide-wire system were used for deployment of the flexible solar-array strips.

---

\*Lockheed Missiles and Space Company, Inc., Sunnyvale, Calif.

Full-scale hardware was fabricated and assembled into a 232-m<sup>2</sup> quadrant of the 928-m<sup>2</sup> array. The quadrant components were tested individually for function and were assembled for deployment-capability testing.

## DESIGN REQUIREMENTS

The following two ground rules were established at the beginning of the design phase to accommodate the development of a valid component-technology demonstration during a period of requirement definition. Maximum use was to be made of modularity so that changes could be made at the component and subcomponent levels and to facilitate straightforward size scaleup or scaledown. If a requirement conflict occurred, the most difficult requirement was to be adopted so that any subsequent changes or firming up in requirements would result in a less difficult design or fabrication problem and, thereby, not compromising the validity of the technology demonstrated in the program.

The NASA shuttle-launched space station requirements were used as a basis for the design. The shuttle requirements that were developed originally and the requirements derived using the noted ground rules are listed in table I. There were additional assumed requirements, listed in table II, which provided a basis for the solar-array design.

## STRUCTURAL DESIGN

### Configuration

A model of the space station solar-array baseline 928-m<sup>2</sup> design is shown in figure 1 in relation to a shuttle-launched space station concept. The test quadrant that was fabricated is shown in figures 1 and 2. The quadrant is 10.3 meters wide by 27.4 meters long. The orientation and power-transfer drive is built around a 1.53-meter power-boom section at the center root of the array.

The initial deployment sequence of the solar array, starting with the position of the stowed quadrants that are packaged within the 4.27-meter maximum envelope (a basic requirement of the design), is shown in figure 3. Initial outward deployment of the quadrants is accomplished by means of a jackscrew mechanism. After this phase of the deployment has been accomplished, the upper portion of the structure, the outboard support assembly (OSA), begins the deployment of the major array.

The major structural elements of the solar array and the next step in the deployment sequence are shown in figure 4. The two inboard solar-array strips, on each side of the boom, deploy to provide power for the artificial-gravity mode, which is the initial mode that is assumed to be used in the operational station. The inboard and outboard supports form the upper and lower supports for the packaged array during launch and contain the tensioning mechanisms that are required for proper support of

the arrays. Also, these support assemblies provide housings for the guide-wire assembly that is used for solar-array-strip alignment and to provide retraction capability for the strips. After all of the 10 solar-array strips have been deployed, subsequent retractions are completed with all solar-array strips and structures being retracted together, providing replaceability at the array level. An attachment point is provided for the support of the inboard support assembly during ascent and the artificial-gravity mode.

The deployed arrays, with guy tapes in place, are shown in figure 5. The inset shows more details of the packaged array before deployment.

### Extendible Truss Beam

The extendible truss beam (ETB) forms the primary structural element of the solar-array system. It is the actuation (deployment and retraction) device and the supporting structure for the flexible-substrate solar array. Because of its characteristics of high strength and stiffness as well as low weight and thermal bending, a truss beam was selected for this application. Although other truss-beam designs that have significantly lower parts counts and higher strength-to-weight ratios are available, the Astromast beam (figure 6) develops full strength and rigidity at any stage of deployment, is fully retractable, and represents the minimum developmental cost. In addition, this type of boom is versatile in that the deployed length and structural properties may be varied with little change to the basic design and hardware.

In the launch mode, the entire beam is stowed within a canister 0.61 meter in diameter and 1.32 meters in height. The upper external portion of this canister is a rotatable nut that has three sets of inward-facing rectangular threads. The internal (stationary) part of the canister supports the three vertical guideslots. The rollers extending from the beam-batten corners are guided by tracks and are engaged simultaneously between the vertical guideslots and the lands of the threaded nut. The beam deploys from or retracts into the canister when the nut is rotated by means of electric motors. Cams for latching and unlatching the diagonal linkages of the beam are fixed to the inner canister wall just below the rotating nut. The ETB is shown deployed in figure 7.

When extended to its full length (25.6 meters), the beam is composed of 66 bays (including two bays that remain inside the canister). A single bay consists of two fixed (upper and lower) tubular triangles (battens) joined at each of the vertices by vertical tubular compression members and by diagonal cable-tension members. Three of the six tension cables terminate at one end (bottom of the bay) in an "over-center" toggle-joint locking mechanism. The longerons and tubular batten members are deformed locally to minimize the stowed-package height. These deformations reduce the overall stowed height by approximately 30 percent, and reduce the strength of the members by approximately 25 percent.

The ETB was subjected to basic structural testing in the vertical position. Compression loads of as much as 19 670 newtons (2400 pounds) combined with a 271 meter-newtons (200 foot-pounds) bending moment were sustained without failure. Also, during testing, more than 2000 bays were extended and retracted successfully. The only major failure occurred when a pivot pin in the latching mechanism sheared after 882 bays had been extended.

## Guy-Tape Assembly

The guy-tape system minimizes the beam-bending loads and prevents cross-wrinkling of the substrates strips by limiting the inplane deflections of the truss beam to less than 25 centimeters. These deflections of the beam tip are caused by external loading on the array from station-docking, attitude-control, and artificial-gravity operation.

The guy-tape assembly consists of a 27.10-meter (1068 inch) winding tape and a reel motor for stowage and release of the tape. The reel motor (one for each quadrant of the array wing), to which one end of each tape is attached, is mounted near the outer end of its inboard-support assembly. The other end of each tape is fixed to the cap at the upper end of the truss beam by means of a pair of 0.294-centimeter-diameter stainless-steel-cable assemblies, each of which straddles the cap assembly. As the truss beam is deployed, the tapes unreel until a fixed position of the array wing is reached. The guy-stowage mechanism is shown in figure 8 installed on the inboard support assembly (ISA).

### Strip Tensioning and Deployment Mechanism

As was mentioned, the three outer strips of each solar-array quadrant are deployed after artificial-gravity operation has been completed and are tensioned to a constant value of 29.2 N/m (2 lb/ft) throughout the entire mission life. To accomplish this task, a simple motor-clutch system is mounted on the OSA (fig. 9) and is combined with a Negator reel-tensioning system on the inboard supports in order to provide a simple combined deployment drive and tensioning system for the zero-g strips. The two strips closest to the beam in each quadrant require much higher tensions during operation in artificial gravity. These strips are tensioned through the use of a pneumatic bellows system. During ascent, the unpressurized bellows are left open to the outboard atmosphere to prevent inadvertent actuation of the mechanism. After extension and before artificial-gravity operation, the bellows are pressurized to provide the increase in tension for the strips; tension is maintained until the station returns to a zero-g mode. Assuming the strip modulus of elasticity is constant with load, the tension during artificial-gravity operation will vary from 1220 newtons (275 pounds) to 1265 newtons (285 pounds) because of length changes that result from orbital temperature variations in the extendable beam and the strip (fig. 10). After the artificial-gravity mode, the bellows are depressurized and the system becomes a completely spring-loaded system for the remainder of the mission.

### Array Packaging and Deployment Assembly

Details of one array-strip packaging assembly, 20 of which are required for the solar-array baseline design, are shown in figure 11. The cover plate (top) and the base plate (bottom) of the strip package are honeycomb pallets that are lined on the inside with polyurethane foam. The plates are used to provide support normal to the stored modules and to provide contamination control during ground-based handling ascent and descent phases of the station mission. The sheet-metal sides on the packaging assembly are formed to deflect the retracting strip modules into the container for orderly stacking during the ground-based test. Also, the sides are used to control contamination and to contain the retracted strip during resupply operations.

Each strip cover plate has six adjustable preload screws (three near the front edge and three near the rear edge) to prevent slippage between stowed strip-module joints during launch and ascent. Separation-nut assemblies, at the front and rear center edges of the cover and base plate, form the tie points of the ISA and OSA, thereby supporting the container. These assemblies are detonated on command to release the preload screws and to permit system deployment.

Cushioning pads between alternate module layers (cell to cell surfaces) of a strip prevent possible cell damage during ground-based handling and ascent vibration. The pads are hinged, at the front edge of the ISA, to a spring-loaded double-hinge system to facilitate removal of the pads during deployment. A pair of guide wires, tensioned by negator motors and reels and passing through slots in alternate module joints, maintain control of the strips during deployment and retraction of the array. During extension and retraction tests, the simulated OSA was offset as much as  $10^\circ$  and the strip was extended and retracted successfully several times.

### GROUND-BASED TESTING

To demonstrate quadrant operation it was necessary to counterbalance all deployed fixed and variable weights and to balance the system tensions with an applied (but variable) moment at the beam cap. This setup was accomplished as shown in figure 12.

A 12.2-meter I-beam was supported from the test area ceiling 33.6 meters (110 feet) above the floor and was stabilized by means of a cable on each end tied to the floor. The beam was used to support the pulley systems for the deployed variable and fixed weights. A chain of various weights per meter was used in combination with fixed weights as the variable counterbalances.

A moment-reaction beam was used in conjunction with a cable to balance the quadrant tensions. The cable was attached to the overhead beam, passed around a pulley near the external beam support ETB cap, and over another pulley at the reaction beam tip, and then attached to a hydraulic cylinder at floor level. A leveling accelerometer was attached to the ETB cap and the reading was used to manually increase or decrease the tension in the cable, thereby maintaining the cap within  $0.5^\circ$  of level. Normally, after the tension was adjusted for a deployment cycle, no further adjustment was required in order to maintain a level cap.

Ten complete deployment cycles involving numerous short extensions and retractions were accomplished successfully. In addition, two cycles were accomplished that demonstrated the ability of the array system to extend and retract a single strip for replacement or additional power. During extensions or retractions, the air conditioning was shut down to ensure that no external loads were imparted to the array.

## CONCLUDING REMARKS

The following conclusions were formulated during the study program and the hardware demonstration. It is feasible to design, fabricate, and test solar arrays 928 m<sup>2</sup> in area that will withstand the loads of a spinning spacecraft. The design must be modular from the solar-cell strip to structural components to permit configuration versatility, component handling, and maintenance. The Astromast extendible truss beam is an excellent choice if high strength, low thermal bending, configuration versatility, and retraction are required of a beam. Vertical testing of large-area flexible-substrate arrays is a practical method of ground-based testing if adequate indoor facilities are available.

TABLE I. - BASELINE REQUIREMENTS FOR FIRST-LEVEL DESIGN

Requirement	Cargo	Module size, m	Artificial-g mode	Power level, kW	Module weight, kg	Launch mode	Resupply launch	Inclination, deg	Altitude, km
MSC-03696 (ground rule)	--	4.27 by 17.7	Not on first station	15 average, minimum	908	Shuttle	--	55	445 to 500
Derived	--	4.27 by 11.6	Capability for all stations	25 average, 100 maximum	--	--	Complete power module, no EVA	--	--
Assumed	--	--	At start of flight only	--	--	--	Replace strip by EVA	--	--

TABLE II. - BASELINE REQUIREMENTS FOR SECOND-LEVEL DESIGN

Item	Assumed requirement
Resupply accommodation	Main structure retractable (array strips retractable)
Artificial-g mode	Main structure fully deployable to 25.6 m with 4 strips/wing
Artificial-g mode	Maximum artificial-g radius of rotation displacement = 13.4 m
Array orientation	2-axis tracking $\pm 12^\circ$ point accuracy
Lowest possible level of resupply	Array strip (1.83 by 25.3 m) EVA required
Maintainability	Shirt-sleeve maintenance

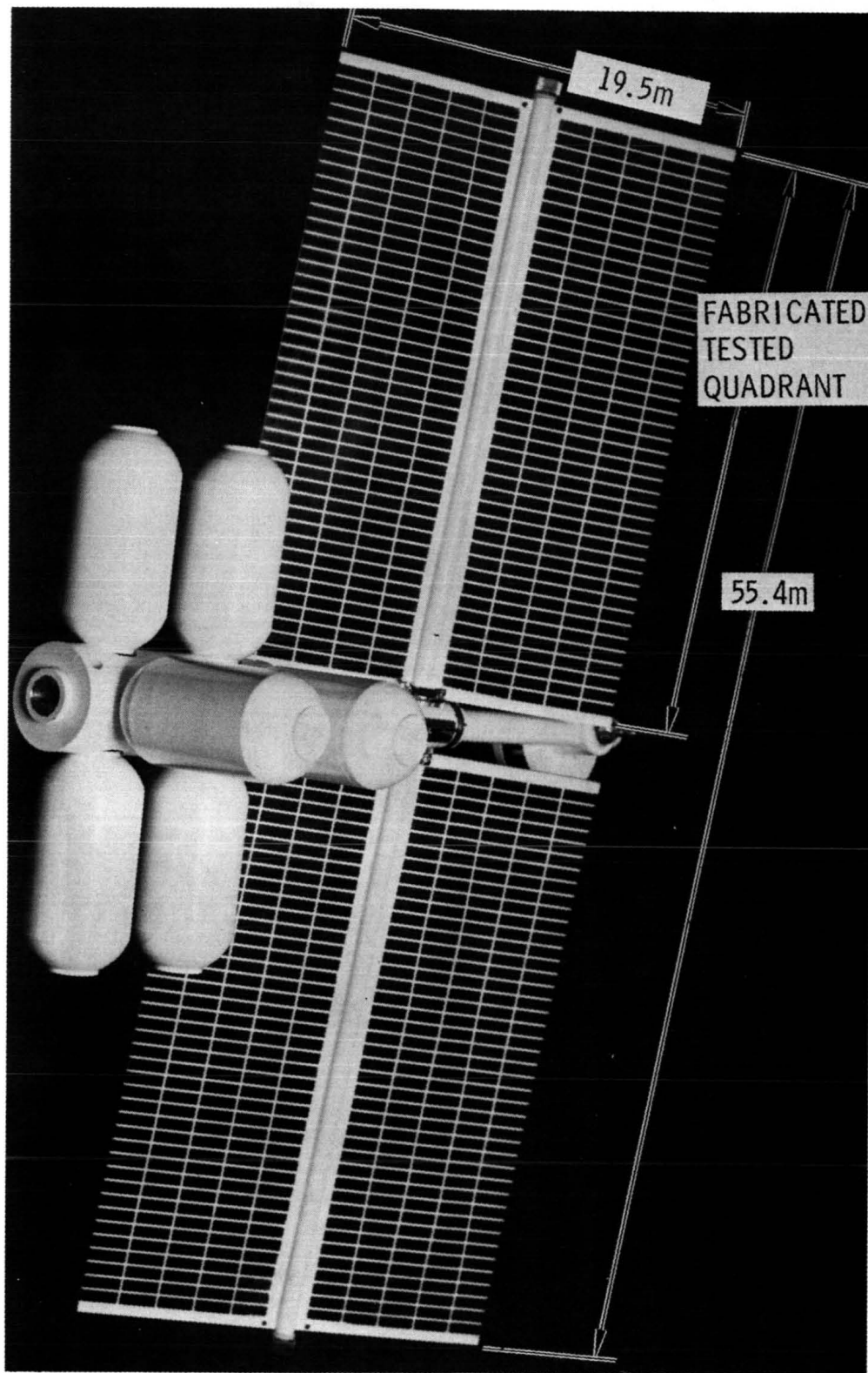


Figure 1. - Shuttle-launched station concept.

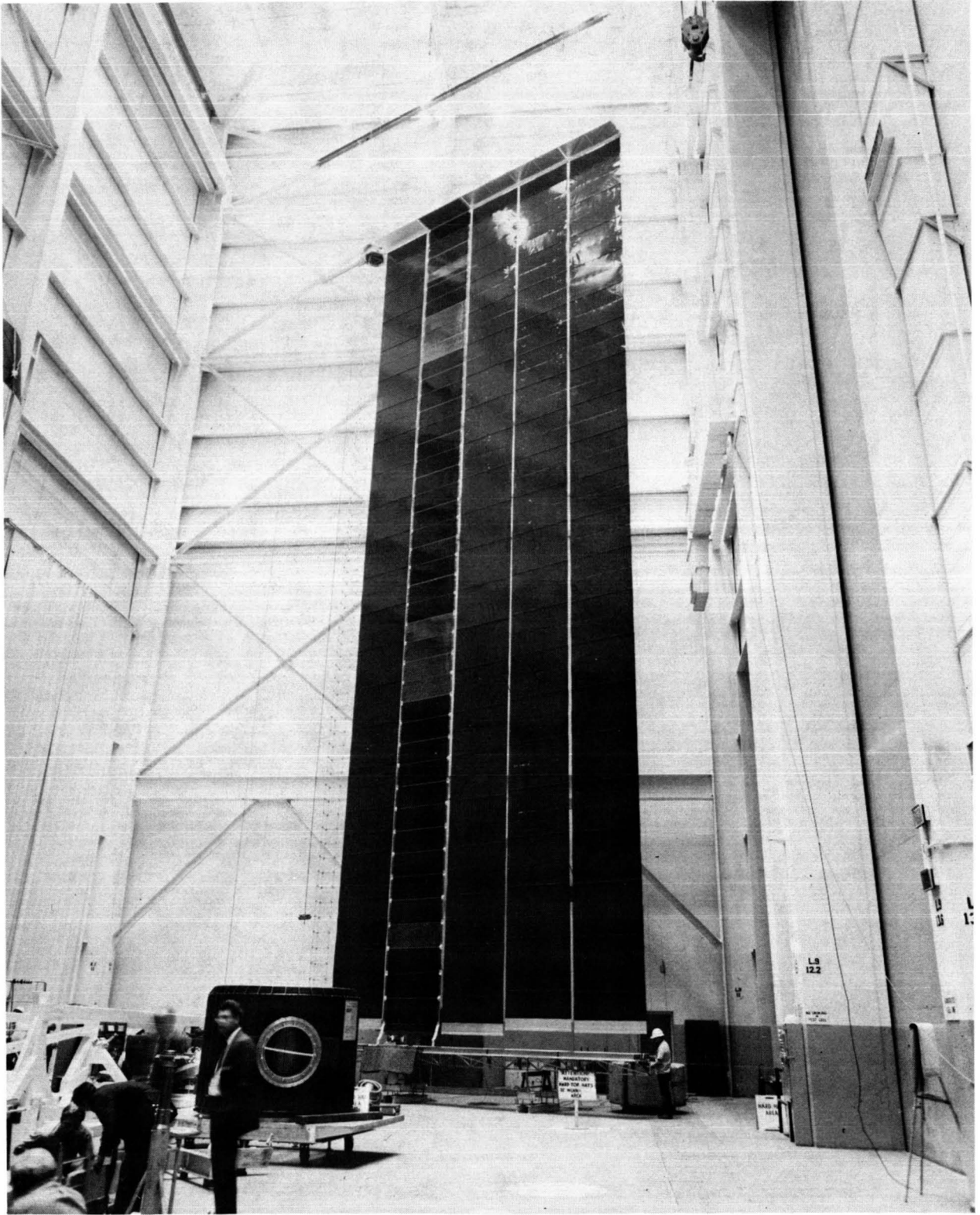


Figure 2. - Deployment-test quadrant.

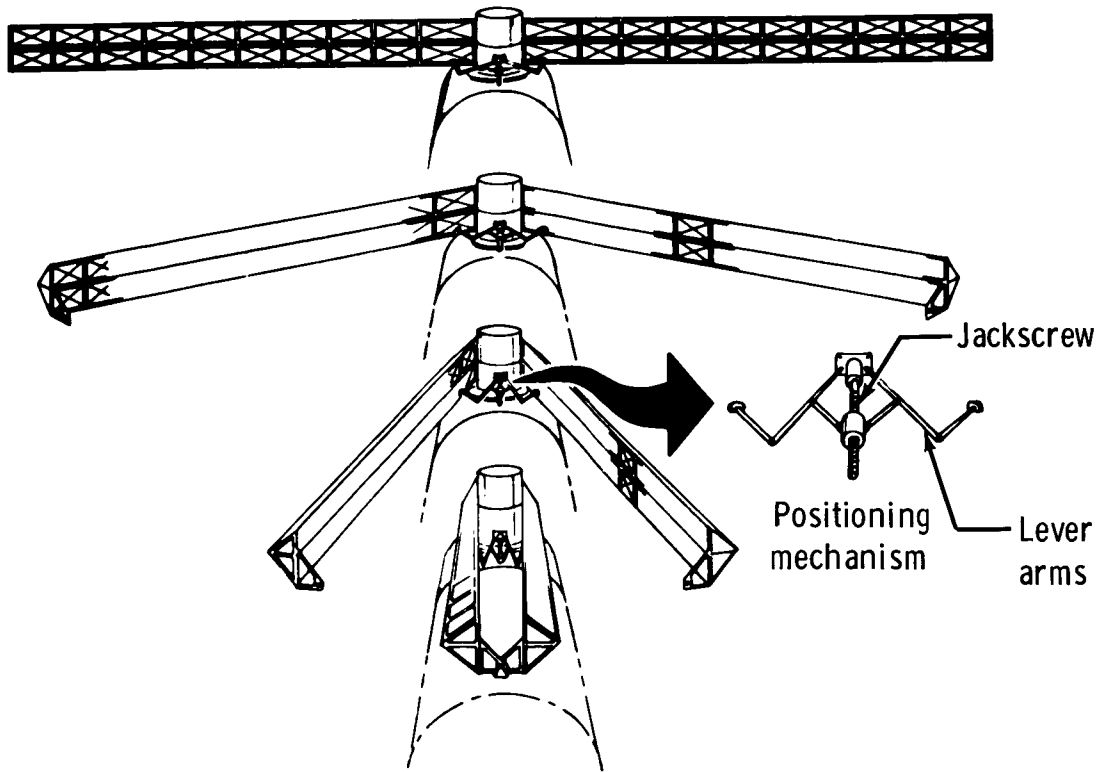


Figure 3. - Initial positioning of stowed quadrants.

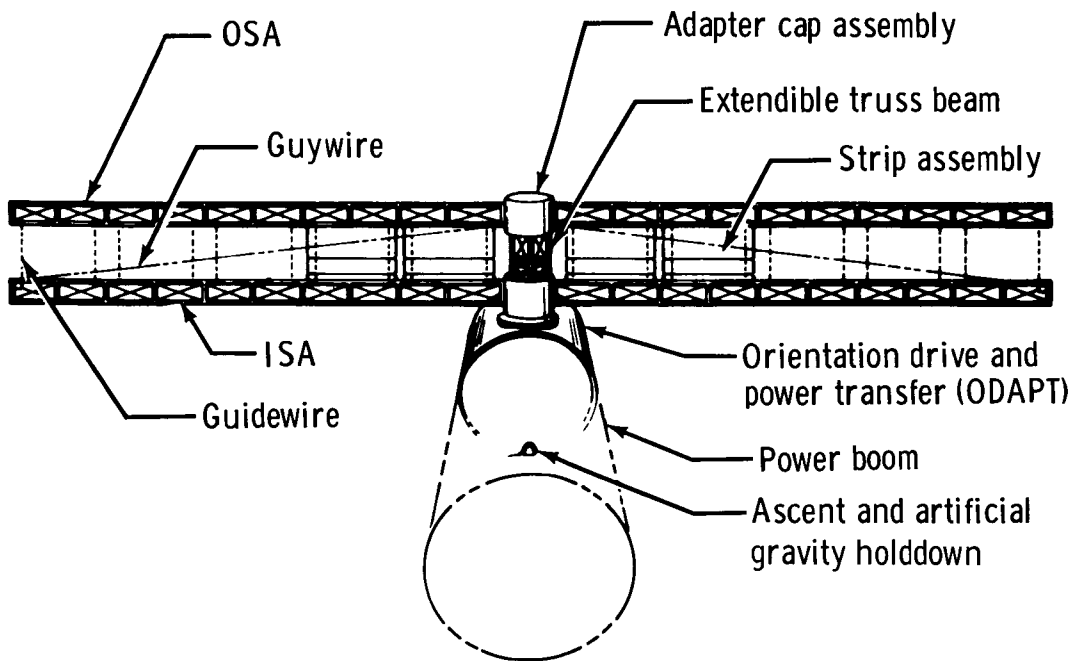


Figure 4. - Baseline structural elements.

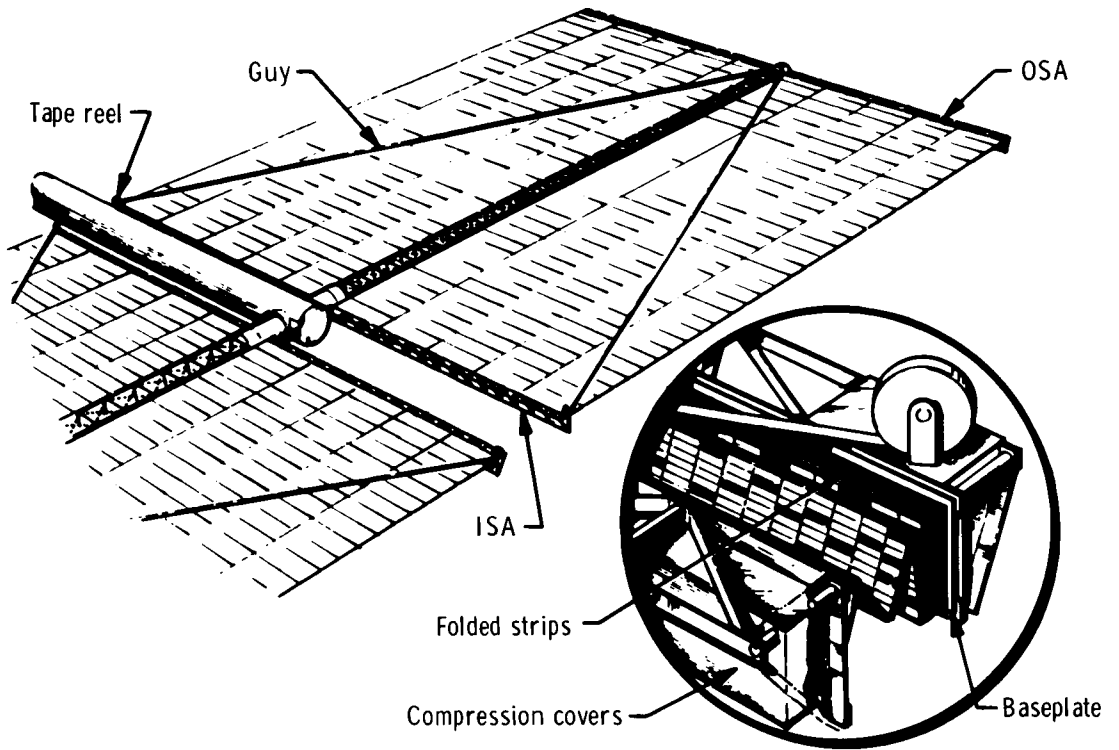


Figure 5. - Array wing.

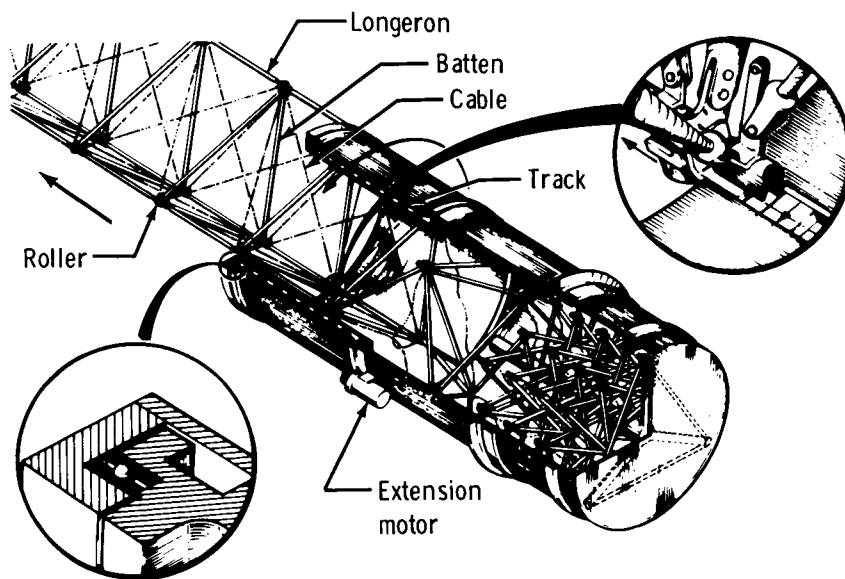


Figure 6. - Cutaway of the Astromast.



Figure 7. - Extendible truss beam.

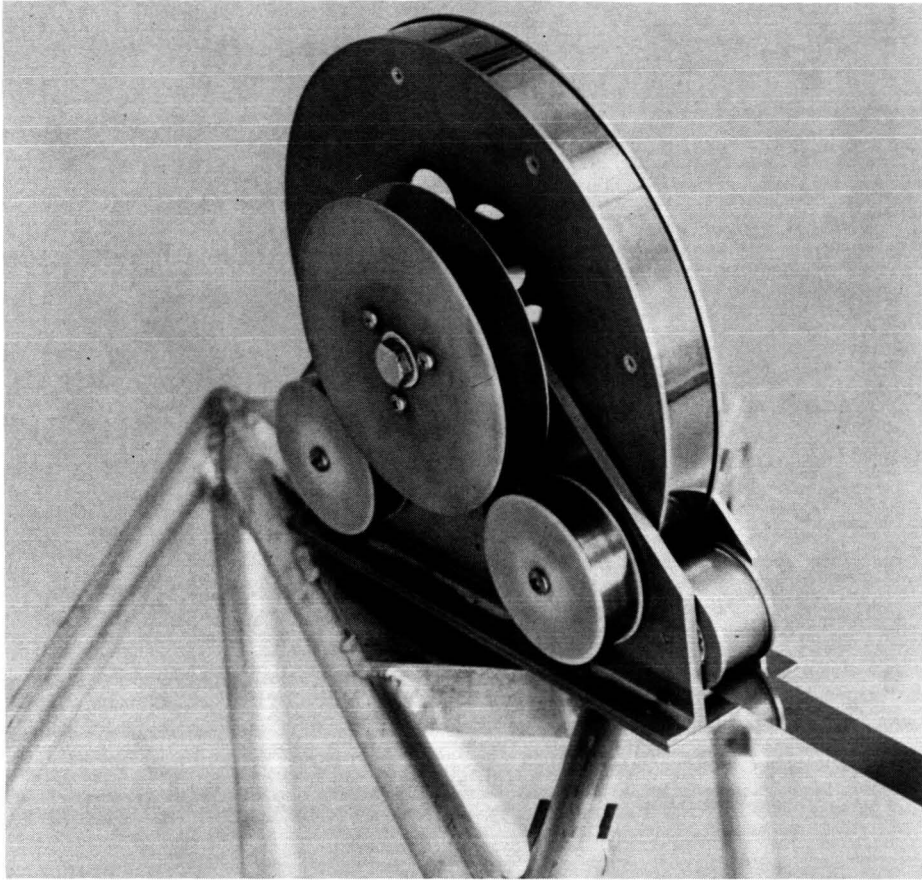


Figure 8. - Guy-tape stowage mechanism.

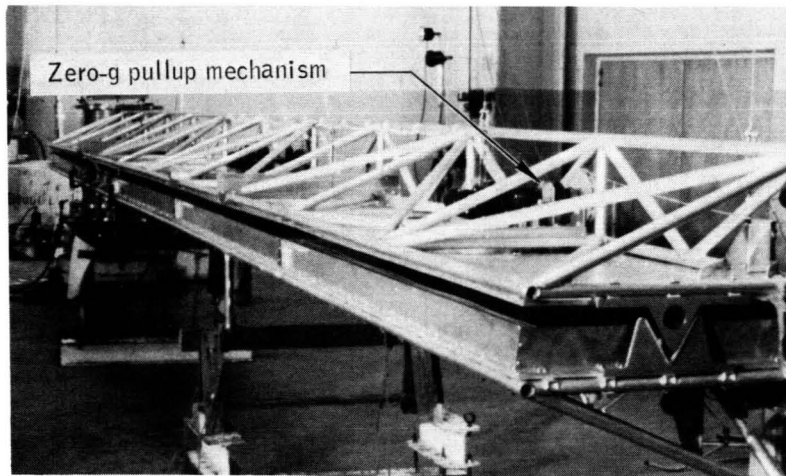


Figure 9. - Strip pullup mechanisms.

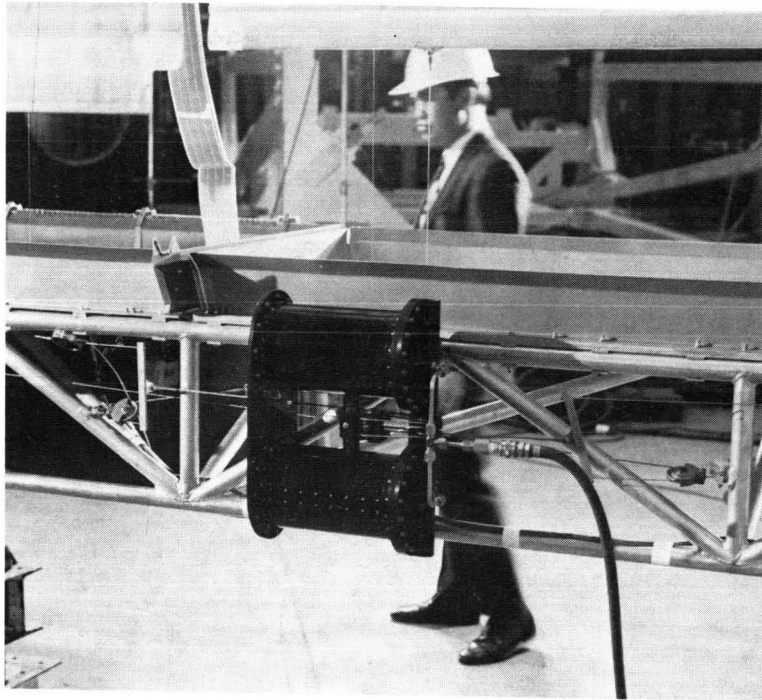


Figure 10. - Artificial-gravity tension mechanism.

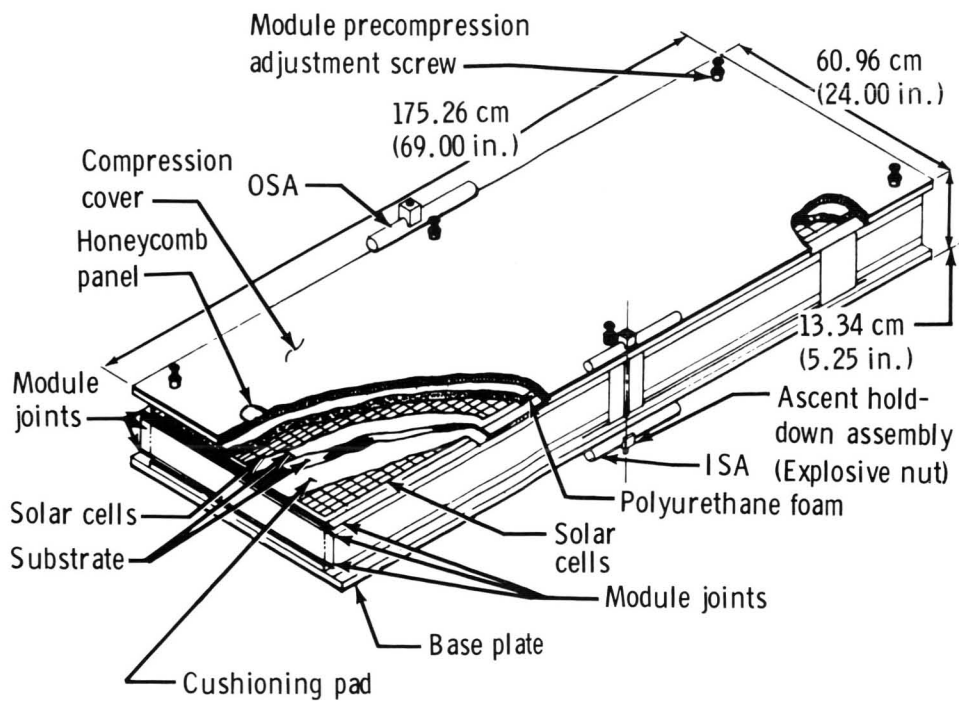


Figure 11. - Array packaging assembly.

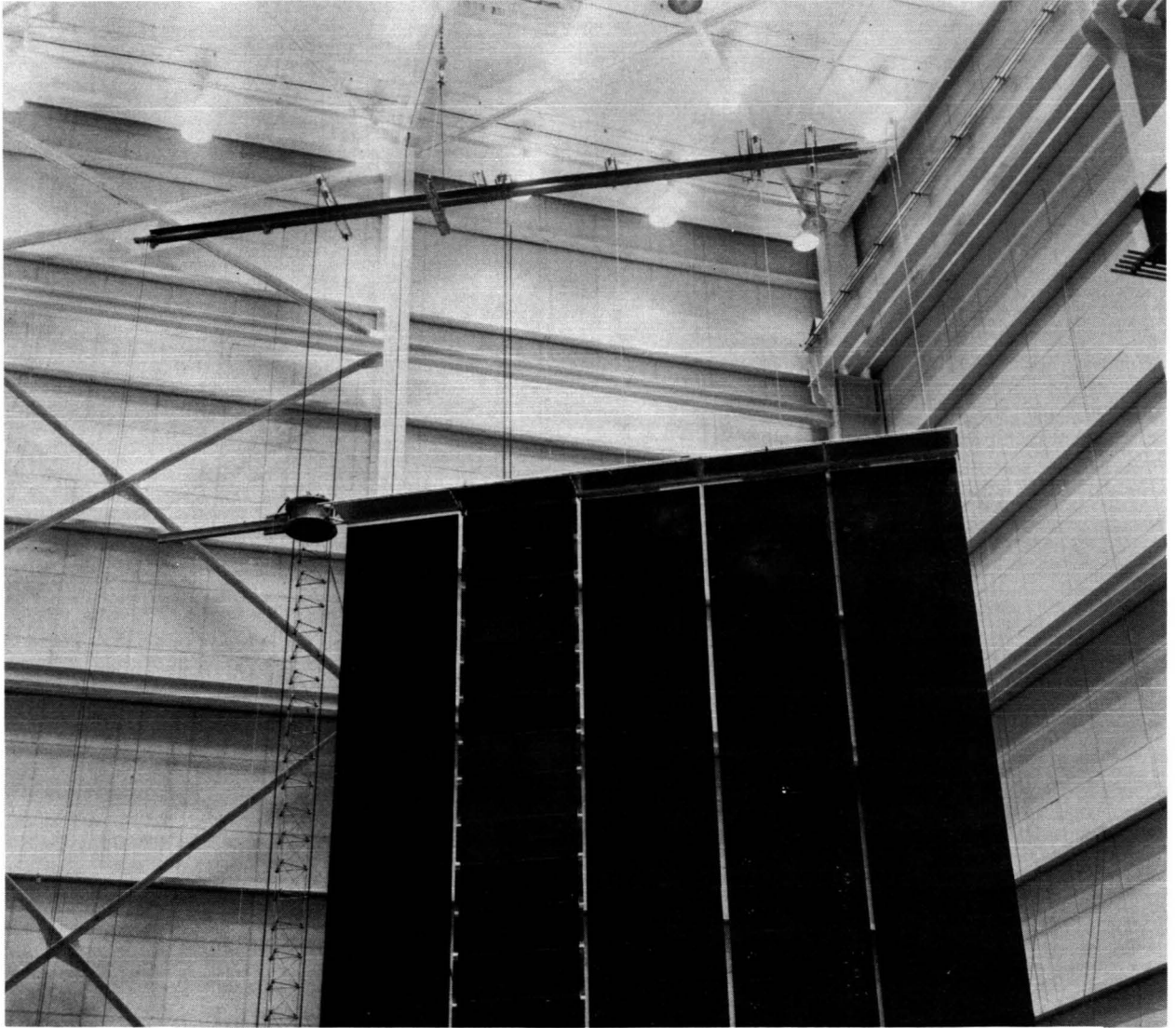


Figure 12. - Counterbalance support beam.

**ATTENDEES**

**Page intentionally left blank**

ATTENDEES OF THE  
7th AEROSPACE MECHANISMS SYMPOSIUM

Adair, H. L.  
Kentron Hawaii, Ltd.  
Bldg. VI, 1720 NASA Rd. 1  
Houston, Tex. 77058

Anderson, Thomas W. (EW)  
NASA Manned Spacecraft Center  
Houston, Tex. 77058

Balzen, Richard T.  
Tracor, Inc.  
6500 Tracor Lane  
Austin, Tex. 78721

Barzda, Justin J.  
Kaman Aerospace Corp.  
77 Overlook Drive  
Windsor, Conn. 06095

Bates, William V. (FC4)  
NASA Manned Spacecraft Center  
Houston, Tex. 77058

Beall, Roger R.  
Lockheed Missiles and Space Co., Inc.  
P. O. Box 504  
Sunnyvale, Calif. 94088

Beam, Benjamin H. (213-1)  
NASA Ames Research Center  
Moffett Field, Calif. 94035

Berg, Tom  
The Boeing Co.  
P. O. Box 58747  
Houston, Tex. 77058

Bernstein, S.  
Lockheed Missiles and Space Co., Inc.  
Org. 62-30, Bldg. 151  
P. O. Box 504  
Sunnyvale, Calif. 94088

Binge, Derek (116)  
RCA, Astro-Electronics Div.  
P. O. Box 800  
Princeton, N.J. 08540

Bomke, P. W.  
Jet Propulsion Laboratory  
4800 Oak Grove Drive  
Pasadena, Calif. 91103

Bond, A. C. (EA2)  
NASA Manned Spacecraft Center  
Houston, Tex. 77058

Brown, H.  
California Institute of Technology  
Pasadena, Calif. 91109

Brubaker, Lee M. (PA)  
NASA Manned Spacecraft Center  
Houston, Tex. 77058

Buchanan, J. S.  
220 Albans St.  
Houston, Tex. 77005

Bunson, George A.  
Santa Barbara Research Center  
75 Coromar Drive  
Goleta, Calif. 93017

Burroughs, E. G. (ES4)  
4016 Tilson Lane  
Houston, Tex. 77055

Bush, Kenneth S. (257)  
NASA Langley Research Center  
Hampton, Va. 23365

Campbell, Carlisle (EW5)  
NASA Manned Spacecraft Center  
Houston, Tex. 77058

Campbell, R. L.  
The Boeing Co.  
P. O. Box 58747  
Houston, Tex. 77058

Carlton, Robert L. (FC4)  
NASA Manned Spacecraft Center  
Houston, Tex. 77058

Carrier, David (TN4)  
NASA Manned Spacecraft Center  
Houston, Tex. 77058

Carson, Maurice A. (EC6)  
NASA Manned Spacecraft Center  
Houston, Tex. 77058

Casebolt, Barry J.  
Huntsville Times  
Huntsville, Ala. 35901

Chauvin, Leo T. (EA22)  
NASA Manned Spacecraft Center  
Houston, Tex. 77058

Cioni, Jim (EP5)  
NASA Manned Spacecraft Center  
Houston, Tex. 77058

Clark, Dianne (ES)  
NASA Manned Spacecraft Center  
Houston, Tex. 77058

Clark, Don. G. (FC4)  
NASA Manned Spacecraft Center  
Houston, Tex. 77058

Cole, Mark W., Jr. (314)  
NASA Langley Research Center  
Hampton, Va. 23365

Colovin, James E.  
Fairchild Corp.  
18611 Point Lookout Drive  
Houston, Tex. 77058

Conner, J. E.  
Lockheed Propulsion Co.  
16811 El Camino Real  
Houston, Tex. 77058

Cook, James E.  
University of Texas  
3819 Maple Avenue  
Dallas, Tex. 75219

Coston, Charles L.  
5526 Whispering Creek  
Houston, Tex. 77017

Cousins, T. E.  
Kentron Hawaii, Ltd.  
Bldg VI, 1720 NASA Rd. 1  
Houston, Tex. 77058

Creel, Morris M.  
Tracor, Inc.  
6500 Tracor Lane  
Austin, Tex. 78721

Curry, Kenneth C.  
Jet Propulsion Laboratory  
4800 Oak Grove Drive  
Pasadena, Calif. 91103

Dabbs, Danielle E.  
American Institute of Aeronautics and  
Astronautics  
4404 Memorial Drive, Apt. 2103  
Houston, Tex. 77007

Davidson, Richard B. (EW6)  
NASA Manned Spacecraft Center  
Houston, Tex. 77058

Davis, Stewart L. (EP)  
NASA Manned Spacecraft Center  
Houston, Tex. 77058

DeBrecht, John J.  
Singer-Link Co.  
506 S. Austin  
Webster, Tex. 77598

Dessert, Kenneth O., Jr.  
Northrop Services Incorporated  
210 Pecan Drive  
League City, Tex. 77573

Dickson, L. R. (ES64)  
NASA Manned Spacecraft Center  
Houston, Tex. 77058

Dodson, J. W. (PT2)  
NASA Manned Spacecraft Center  
Houston, Tex. 77058

Dorland, Wade D. (ES64)  
NASA Manned Spacecraft Center  
Houston, Tex. 77058

Downs, W. R. (ES)  
NASA Manned Spacecraft Center  
Houston, Tex. 77058

Drexel, Mildred  
10227 Old Orchard  
LaPorte, Tex. 77571

Drexel, Ralph (EC3)  
NASA Manned Spacecraft Center  
Houston, Tex. 77058

Eggleston, Jack M. (EA4)  
NASA Manned Spacecraft Center  
Houston, Tex. 77058

Faget, Maxime A. (EA)  
NASA Manned Spacecraft Center  
Houston, Tex. 77058

Fawcett, W. K.  
Lockheed Propulsion Co.  
P. O. Box 111  
Redlands, Calif. 92373

Fedor, O.  
NASA John F. Kennedy Space Center  
Kennedy Space Center, Fla. 32899

Ferger, H. L.  
The Aerospace Corp.  
1904 Via Arroyo  
Palos Verdes, Calif. 90274

Ferguson, Mary C. (FD3)  
NASA Manned Spacecraft Center  
Houston, Tex. 77058

Ferrera, J. D.  
Jet Propulsion Laboratory  
4800 Oak Grove Drive  
Pasadena, Calif. 91103

Fields, John B., Jr.  
Sperry Rand Corp.  
1715 Solomon Rd.  
Charlottesville, Va. 22901

Fisher, Ken  
Celesco Industries  
3333 Harbor Blvd.  
Costa Mesa, Calif. 92626

Fisher, Lewis R. (EK)  
NASA Manned Spacecraft Center  
Houston, Tex. 77058

Fogwell, J. W.  
Southwest Research Institute  
8500 Culebra Rd.  
P. O. Drawer 28510  
San Antonio, Tex. 78284

Foster, G. B., Jr. (PT3)  
NASA Manned Spacecraft Center  
Houston, Tex. 77058

Foster, Ralph H. (CD33)  
NASA Manned Spacecraft Center  
Houston, Tex. 77058

Foster, Robert W.  
McDonnell-Douglas Corp.  
15611 Wandering Trail  
Friendswood, Tex. 77546

Frazer, R. R. (MT)  
NASA Manned Spacecraft Center  
Houston, Tex. 77058

Frere, Fred (FC4)  
NASA Manned Spacecraft Center  
Houston, Tex. 77058

Frost, Richard H.  
Frost Engineering  
3900 S. Kalamath St.  
P. O. Box 1294  
Englewood, Colo. 80110

Gammon, Edward P. (PT3)  
NASA Manned Spacecraft Center  
Houston, Tex. 77058

Graves, John C.  
IBM Corp.  
Dept. K81, Bldg 5-2  
150 Sparkman Dr.  
Huntsville, Ala. 35805

Gelotte, Gustav A.  
The Boeing Co.  
4002 Highknoll  
Seabrook, Tex. 77586

Giesecke, Robert L. (ED2)  
NASA Manned Spacecraft Center  
Houston, Tex. 77058

Girala, Anthony S. (EW7)  
NASA Manned Spacecraft Center  
Houston, Tex. 77058

Glenn, Dean C. (EW7)  
NASA Manned Spacecraft Center  
Houston, Tex. 77058

Glynn, Philip C. (ES2)  
NASA Manned Spacecraft Center  
Houston, Tex. 77058

Gonzales, Norberto R. (EW7)  
NASA Manned Spacecraft Center  
Houston, Tex. 77058

Graves, Donald L. (HA-84)  
The Boeing Co.  
P. O. Box 58747  
Houston, Tex. 77058

Greek, B. F.  
Chemical & Engineering News  
P. O. Box 27620  
Houston, Tex. 77027

Groskopf, Ernest  
Spar Aerospace Products  
825 Caledonia Rd.  
Toronto, Canada

Gruby, Charles L. (FC4)  
NASA Manned Spacecraft Center  
Houston, Tex. 77058

Gudikunst, J. B.  
Hughes Aircraft Co.  
Centinela and Teale Streets  
Bldg 5, MS B-145  
Culver City, Calif. 90230

Guerin, A. R.  
The Singer Co.  
Kearfott Div.  
3300 W. Mockingbird Lane, Room 632  
Dallas, Tex. 75235

Hacker, Russell  
Stanford University  
1214 St. Josephs Avenue  
Los Altos, Calif. 94022

Hagel, Virginia T. (EM)  
NASA Manned Spacecraft Center  
Houston, Tex. 77058

Hallmark, William A.  
Martin Marietta Corp.  
1730 NASA Rd. 1, Suite 106  
Houston, Tex. 77058

Hamblett, Edward B., Jr. (PD)  
NASA Manned Spacecraft Center  
Houston, Tex. 77058

Hannigan, James E. (FC4)  
NASA Manned Spacecraft Center  
Houston, Tex. 77058

Hardy, P. B.  
Beech Aircraft  
Box 631  
Boulder, Colo. 80302

Harrington, Timothy G.  
Lockheed Missiles and Space Co., Inc.  
906 Forest Ridge Drive  
San Jose, Calif. 95129

Haynie, H. Theron  
The Boeing Co.  
5226 S. W. Dakota St.  
Seattle, Wash. 98116

Hazel, Frank J.  
RCA  
1275 Space Park Dr., Suite 106  
Houston, Tex. 77058

Heineman, W., Jr. (EW6)  
NASA Manned Spacecraft Center  
Houston, Tex. 77058

Herzl, G. G.  
Lockheed Missiles and Space Co., Inc.  
3400 Kenneth Drive  
Palo Alto, Calif. 94303

Hinricks, James T.  
Ball Brothers Research Corp.  
P. O. Box 1062  
Boulder, Colo. 80302

Hobokan, Andrew (MT)  
NASA Manned Spacecraft Center  
Houston, Tex. 77058

Hodge, Ralph D. (EW)  
NASA Manned Spacecraft Center  
Houston, Tex. 77058

Holder, Ben W. (ES2)  
NASA Manned Spacecraft Center  
Houston, Tex. 77058

Hollrock, Richard  
Kaman Aerospace Corp.  
Bloomfield, Conn. 06002

Horne, William A.  
American Institute of Aeronautics  
and Astronautics  
4106 Willow Hill Dr.  
Seabrook, Tex. 77586

Howey, Charles K.  
The Aerospace Corp.  
P. O. Box 92957  
Los Angeles, Calif. 90045

Hoyler, W. F. (MT)  
NASA Manned Spacecraft Center  
Houston, Tex. 77058

Hunter, Alex B., Jr.  
The Boeing Co.  
2111 Wimberly Rd.  
Huntsville, Ala. 35805

Idomir, Kenneth (EW)  
NASA Manned Spacecraft Center  
Houston, Tex. 77058

Jacobsen, S. E. (JM5)  
NASA Manned Spacecraft Center  
Houston, Tex. 77058

Jaderlund, W. W. (MT)  
NASA Manned Spacecraft Center  
Houston, Tex. 77058

James, Jack W.  
Ball Brothers Research Corp.  
P. O. Box 1062  
Boulder, Colo. 80302

Jenkins, Lyle M. (EW8)  
NASA Manned Spacecraft Center  
Houston, Tex. 77058

Jiongo, Edward M. (FM2)  
NASA Manned Spacecraft Center  
Houston, Tex. 77058

Johansen, David  
Weber Aircraft Co.  
2820 Ontario St.  
Burbank, Calif. 91505

Johnson, C. C. (EW)  
NASA Manned Spacecraft Center  
Houston, Tex. 77058

Jones, James C. (EW8)  
NASA Manned Spacecraft Center  
Houston, Tex. 77058

Jones, J. L.  
NASA Ames Research Center  
Moffett Field, Calif. 94035

Jordan, J. J.  
Singer Co.  
120 Oak Brook Center Mall  
Oakbrook, Ill. 60521

Katsuyama, G.  
Marubeni America Inc.  
3650 One Shell Plaza  
Houston, Tex. 77002

Keathley, William H. (EW7)  
NASA Manned Spacecraft Center  
Houston, Tex. 77058

Keim, Paul T. (CC4)  
NASA Manned Spacecraft Center  
Houston, Tex. 77058

Kerfoot, H. P.  
Lockheed Missiles and Space Co. , Inc.  
1111 Lockheed Way  
Sunnyvale, Calif. 94088

Kiker, John W. (EW5)  
NASA Manned Spacecraft Center  
Houston, Tex. 77058

Kilbourn, Max B. (FM2)  
NASA Manned Spacecraft Center  
Houston, Tex. 77058

Kirkpatrick, Donald L.  
General Electric Co.  
P. O. Box 8555, Room M2700  
Philadelphia, Pa. 19101

Klauss, Marion E. (Z11)  
Philco-Ford Corp.  
Western Development Laboratories  
3939 Fabian Way  
Palo Alto, Calif. 94303

Knight, Jack (FC4)  
NASA Manned Spacecraft Center  
Houston, Texas 77058

Korth, Kenneth G.  
Delco Electronics Div.  
General Motors Corp.  
18334 Hereford Lane  
Houston, Tex. 77058

Kraft, C. C. (AA)  
NASA Manned Spacecraft Center  
Houston, Tex. 77058

Kubly, Dan B.  
Jet Propulsion Laboratory  
4800 Oak Grove Drive  
Pasadena, Calif. 91103

Kueth, M. W.  
Martin Marietta Corp.  
P. O. Box 179  
Denver, Colo. 80201

Laine, Don  
Celesco Industries  
3333 Harbor Blvd.  
Costa Mesa, Calif. 92626

Langley, Betty  
109 Sherwood Drive  
Alvin, Tex. 77511

Langley, Robert D. (EW5)  
NASA Manned Spacecraft Center  
Houston, Tex. 77058

Lindberg, Dale E.  
Lockheed Missiles and Space Co. , Inc.  
259 LaHerran Drive  
Santa Clara, Calif. 95051

Lobb, John D. (PT14)  
NASA Manned Spacecraft Center  
Houston, Tex. 77058

Loden, Harold A. (FC4)  
NASA Manned Spacecraft Center  
Houston, Tex. 77058

Loftus, J. P., Jr. (AT)  
NASA Manned Spacecraft Center  
Houston, Tex. 77058

Lovell, Robert B.  
Lovell Enterprises  
646 El Rancho Dr.  
El Cajon, Calif. 92021

Lytton, John L.  
The Boeing Co.  
1420 Ramada  
Houston, Tex. 77058

Martin, F. T. (720.0)  
NASA Goddard Space Flight Center  
Greenbelt, Md. 20771

Mathias, Mike (CD43)  
NASA Manned Spacecraft Center  
Houston, Tex. 77058

McBarron, James W. ,II (EC9)  
NASA Manned Spacecraft Center  
Houston, Tex. 77058

McCullough, John E.  
Arthur D. Little Co.  
20-554 Acorn Park  
Cambridge, Md. 02140

McDonald, Herman D.  
Northrop Ventura  
800 NASA Blvd. , Apt. 290  
Webster, Tex. 77598

McIntire, Claude L.  
The Boeing Co.  
P. O. Box 58747  
Houston, Tex. 77058

McLane, J. C. , Jr. (EL)  
NASA Manned Spacecraft Center  
Houston, Tex. 77058

McManus, Ray S.  
Singer/Simulation Products Div.  
P. O. Box 58647  
Houston, Tex. 77058

Mechelay, Joseph E. (PT2)  
NASA Manned Spacecraft Center  
Houston, Tex. 77058

Merritt, Walter M. (FC4)  
NASA Manned Spacecraft Center  
Houston, Tex. 77058

Miller, Glenn C. (EW)  
NASA Manned Spacecraft Center  
Houston, Tex. 77058

Miller, Matthew N.  
Fairchild Stratots  
1800 Rosecrans Avenue  
Manhattan Beach, Calif. 90266

Minter, Larry V. (FC4)  
NASA Manned Spacecraft Center  
Houston, Tex. 77058

Naimer, Jack (EC7)  
NASA Manned Spacecraft Center  
Houston, Tex. 77058

Nemecek, Joseph J. (7129)  
U.S. Naval Research Laboratory  
Washington, D. C.

Neuschaefer, W. A.  
Martin Marietta Corp.  
1740 NASA Rd. 1  
Houston, Tex. 77058

Norma, L. S.  
Kentron Hawaii, Ltd.  
Bldg. VI, 1720 NASA Rd. 1  
Houston, Tex. 77058

Oakey, W. E.  
Southwest Research Institute  
8500 Culebra Road  
P. O. Drawer 28510  
San Antonio, Tex. 78284

Olson, Merlyn C.  
Hughes Aircraft Co.  
3379 Wade Street  
Los Angeles, Calif. 90066

Owen, David H. (EL)  
NASA Manned Spacecraft Center  
Houston, Tex. 77058

Pacey, J. J.  
LTV Aerospace Corp.  
P. O. Box 6267  
Dallas, Tex. 75222

Parks, James H. (114)  
NASA Langley Research Center  
Hampton, Va. 23365

Pearson, O. L. (EL2)  
NASA Manned Spacecraft Center  
Houston, Tex. 77058

Peters, Ronald A.  
Marubeni America, Inc.  
3650 One Shell Plaza  
Houston, Tex. 77002

Peters, William L. (FC4)  
NASA Manned Spacecraft Center  
Houston, Tex. 77058

Peterson, Rodney J. (MZ 6-73)  
General Dynamics Corp.  
1675 W. Mission  
Pomona, Calif. 91766

Pettit, E. M. (A3-830-BBG0-9)  
McDonnell-Douglas Astronautics Co.  
5301 Bolsa Avenue  
Huntington Beach, Calif. 92647

Phelps, Ellsworth, Jr. (EW6)  
NASA Manned Spacecraft Center  
Houston, Tex. 77058

Phillips, Jesse L. (EW8)  
NASA Manned Spacecraft Center  
Houston, Tex. 77058

Piercy, Norman A. (EW6)  
NASA Manned Spacecraft Center  
Houston, Tex. 77058

Pooch, R. J.  
Lockheed Propulsion Co.  
P. O. Box 111  
Redlands, Calif. 92373

Price, Jack  
The Boeing Co.  
950 Lefant Plaza  
Washington, D.C.

Quinn, William J. (D132)  
Hughes Aircraft Co.  
Bldg. 6  
Culver City, Calif. 90230

Ratcliff, Larry P. (EW7)  
NASA Manned Spacecraft Center  
Houston, Tex. 77058

Red, Arthur G.  
Spar Aerospace Products  
825 Caledonia Road  
Toronto 395  
Ontario, Canada

Rice, William E. (EA2)  
NASA Manned Spacecraft Center  
Houston, Tex. 77058

Riedel, John K.  
Lockheed Missiles and Space Co., Inc.  
1861 Waverley Street  
Palo Alto, Calif. 94303

Rinaldo, A. L.  
Lockheed Missiles and Space Co., Inc.  
1111 Lockheed Way  
Sunnyvale, Calif. 94088

Robertson, James A.  
General Dynamics Corp.  
1730 NASA Blvd., Suite 204  
Houston, Tex. 77058

Rogers, William F. (EW5)  
NASA Manned Spacecraft Center  
Houston, Tex. 77058

Ross, Thomas O. (EW7)  
NASA Manned Spacecraft Center  
Houston, Tex. 77058

Royce, R. S.  
Jilsco, Inc.  
8914 Randolph  
Houston, Tex. 77017

Rysavy, Gordon (EW6)  
NASA Manned Spacecraft Center  
Houston, Tex. 77058

Salcedo, D. E.  
Kentron Hawaii, Ltd.  
Bldg. VI, 1720 NASA Rd. 1  
Houston, Tex. 77058

Samuels, Ronald L.  
Airsupply Co./Spar  
2230 Michigan Avenue  
Santa Monica, Calif. 90404

Schliesing, John A. (ES2)  
NASA Manned Spacecraft Center  
Houston, Tex. 77058

Schmuecker, Jay  
Jet Propulsion Laboratory  
4800 Oak Grove Drive  
Pasadena, Calif. 91103

Schneider, Charles C. (EW8)  
NASA Manned Spacecraft Center  
Houston, Tex. 77058

Sechler, E. E. (205-50)  
California Institute of Technology  
Pasadena, Calif. 91109

Seger, R.  
Martin Marietta Corp.  
P. O. Box 179  
Denver, Colo. 80201

Seifert, Richard  
The Aerospace Corp.  
P. O. Box 95085  
Los Angeles, Calif. 90045

Shannon, James D. (FC4)  
NASA Manned Spacecraft Center  
Houston, Tex. 77058

Sharpless, Eric C.  
AMETEC/Hunter Spring  
1 Spring Avenue  
Batfield, Pa. 19440

Sherwin, H. G.  
Northrop Corp.  
Box 34416  
Houston, Tex. 77034

Shields, Dales R. (1610)  
Martin Marietta Corp.  
Box 179  
Denver, Colo. 80201

Simmons, Delford E. (7129.2)  
U.S. Naval Research Laboratory  
Washington, D.C. 20390

Simpkinson, Scott H. (PA)  
NASA Manned Spacecraft Center  
Houston, Tex. 77058

Slayton, D. K. (CA)  
NASA Manned Spacecraft Center  
Houston, Tex. 77058

Smith, H. Gaylan  
The Boeing Co.  
P. O. Box 58747  
Houston, Tex. 77058

Smith, P. Don (ES12)  
NASA Manned Spacecraft Center  
Houston, Tex. 77058

Smith, Richard F. (EW7)  
NASA Manned Spacecraft Center  
Houston, Tex. 77058

Snyder, Howard E.  
The Boeing Co.  
P. O. Box 58747  
Houston, Tex. 77058

Sova, Bill (EW6)  
NASA Manned Spacecraft Center  
Houston, Tex. 77058

Speight, Kevin M.  
General Electric Co.  
3008 Taft Road  
Norristown, Pa. 19403

Stap, John, Jr.  
Martin Marietta Corp.  
1730 NASA Blvd., Suite 106  
Houston, Tex. 77058

Starkey, Donald J. (157-110)  
Jet Propulsion Laboratory  
4800 Oak Grove Drive  
Pasadena, Calif. 91103

Steadman, B. E.  
Lockheed Missiles and Space Co., Inc.  
16811 El Camino Real  
Houston, Tex. 77058

Stellenwerf, W. A.  
Martin Marietta Corp.  
1730 NASA Blvd.  
Houston, Tex. 77058

Stevens, Doug  
Celesco Industries  
3333 Harbor Blvd.  
Costa Mesa, Calif. 92626

Stevens, G. W. H.  
Engineering Physics Dept.  
Royal Aircraft Establishment,  
Farnborough  
Hampshire 1  
England

Stewart, William A.  
American Institute of Aeronautics  
and Astronautics  
P. O. Box 57913  
Webster, Tex. 77598

Stott, Gary R.  
Lockheed Missiles and Space Co., Inc.  
1556 Mallard Way  
Sunnyvale, Calif. 94087

Straayer, Joe  
The Boeing Co.  
P. O. Box 58747  
Houston, Tex. 77058

Sturgis, J. D.  
Radiation, Inc.  
P. O. Box 37  
Melbourne, Fla. 32901

Suarez, S. M. (320.1)  
NASA Goddard Space Flight Center  
Greenbelt, Md. 20771

Swales, Frank  
Lockheed Missiles and Space Co., Inc.  
P. O. Box 504  
Sunnyvale, Calif. 94088

Swenson, Bill  
Bell Aerospace Co.  
1115 Gemini, Suite F  
Houston, Tex. 77058

Talas, Alfred (EL2)  
NASA Manned Spacecraft Center  
Houston, Tex. 77058

Taub, Willard M. (EW8)  
NASA Manned Spacecraft Center  
Houston, Tex. 77058

Tepley, L. R.  
Lockheed Missiles and Space Co., Inc.  
1111 Lockheed Way  
Sunnyvale, Calif. 94088

Thames, Paul S.  
Singer/Simulation Products Div.  
1700 Bay Area Blvd.  
Houston, Tex. 77058

Thayer, J. C.  
Champion Paper Co.  
P. O. Box 872  
Pasadena, Tex. 77501

Thirolf, R. G. (DE4)  
NASA Manned Spacecraft Center  
Houston, Tex. 77058

Thomson, Graham  
Hughes Aircraft Co.  
11356 Chenault Street  
Los Angeles, Calif. 90049

Trafton, Thomas W.  
The Aerospace Corp.  
P. O. Box 95085  
Los Angeles, Calif. 90045

Tweedt, Roger E.  
Hughes Aircraft Co.  
Centinela and Teale Streets  
Culver City, Calif. 90230

Vaccaro, James J.  
TRW Systems  
1 Spacepark Drive  
Houston, Tex. 77058

Vallandigham, Peter L.  
Sunstrand Aviation  
Rockford, Ill. 61101

Vaughan, N. B. (MT)  
NASA Manned Spacecraft Center  
Houston, Tex. 77058

Wade, A. L.  
Santa Barbara Research Center  
75 Coromar Drive  
Goleta, Calif. 93017

Walker, William H. (13-08)  
The Boeing Co.  
P. O. Box 3999  
Seattle, Wash. 98124

Walter, John K. S.  
Sandia Laboratories  
Division 1326  
P. O. Box 5800  
Albuquerque, N. Mex. 87115

Ward, B. W. (732.0)  
NASA Goddard Space Flight Center  
Greenbelt, Md. 20771

Webb, Granville L. (159)  
NASA Langley Research Center  
Hampton, Va. 23362

Weber, Winston W.  
Martin Marietta Corp.  
1730 NASA Rd. 1, Suite 106  
Houston, Tex. 77058

Webster, H. T.  
Weber Aircraft  
2820 Ontario Street  
Burbank, Calif. 91505

Welch, D. F.  
California Institute of Technology  
1201 E. California Blvd.  
Pasadena, Calif. 91109

Wesselski, Clarence J. (EW7)  
NASA Manned Spacecraft Center  
Houston, Tex. 77058

Weyman, Nick  
Spar Aerospace Products  
825 Caledonia Road  
Toronto, Ontario  
Canada

Wheeler, Bryce A. (B109)  
Hughes Aircraft Co.  
Centinela and Teale Streets  
Culver City, Calif. 90230

White, G. R.  
P. O. Box 27012  
Houston, Tex. 77027

White, Jim H.  
4195 Dundas Street W.  
Toronto 590, Ontario  
Canada

White, Robert D. (EW5)  
NASA Manned Spacecraft Center  
Houston, Tex. 77058

Whitmore, C. V. (FC4)  
NASA Manned Spacecraft Center  
Houston, Tex. 77058

Wible, Lee A. (FC4)  
NASA Manned Spacecraft Center  
Houston, Tex. 77058

Williams, John E. (EW8)  
NASA Manned Spacecraft Center  
Houston, Tex. 77058

Woods, Ace M.  
Chrysler Corp.  
1339 Riviera  
New Orleans, La.

Wrede, Karl J.  
Singer Co.  
P. O. Box 58551  
Houston, Tex. 77058

Wren, R. J. (ES12)  
NASA Manned Spacecraft Center  
Houston, Tex. 77058

ORGANIZATIONS REPRESENTED AT THE  
7th AEROSPACE MECHANISMS SYMPOSIUM

The Aerospace Corp.	IBM Corp.
Airsupply Co./Spar	Jet Propulsion Laboratory
American Institute of Aeronautics and Astronautics	Jilsco, Inc.
AMETEC/Hunter Spring	Kaman Aerospace Corp.
Arthur D. Little Co.	Kentron Hawaii, Ltd.
Ball Brothers Research Corp.	Lockheed Missiles and Space Co., Inc.
Beech Aircraft	Lockheed Propulsion Co.
Bell Aerospace Co.	Lovell Enterprises
The Boeing Co.	LTV Aerospace Corp.
California Institute of Technology	Martin Marietta Corp.
Celesco Industries	Marubeni America, Inc.
Champion Paper Co.	McDonnell-Douglas Astronautics Co.
Chemical and Engineering News	McDonnell-Douglas Corp.
Chrysler Corp.	NASA Ames Research Center
General Motors Corp., Delco Electronics Div.	NASA Goddard Space Flight Center
Fairchild Corp.	NASA John F. Kennedy Space Center
Fairchild Stratots	NASA Langley Research Center
Frost Engineering	NASA Manned Spacecraft Center
General Dynamics Corp.	Northrop Corp.
General Electric Co.	Northrop Ventura
Hughes Aircraft Co.	Northrop Services Incorporated
Huntsville Times	Philco-Ford Corp.
	Radiation, Inc.

RCA

RCA, Astro-Electronics Div.

Royal Aircraft Establishment,  
Engineering Physics Div.

Sandia Laboratories

Santa Barbara Research Center

Singer Co.

Singer-Link Co.

Singer/Simulation Products Div.

Southwest Research Institute

Spar Aerospace Products

Sperry Rand Corp.

Stanford University

Sunstrand Aviation

Tracor, Inc.

TRW Systems

University of Texas

U. S. Naval Research Laboratory

Weber Aircraft Co.